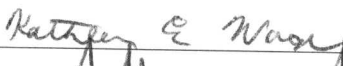
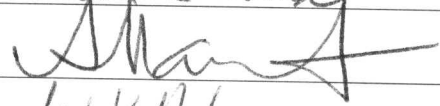

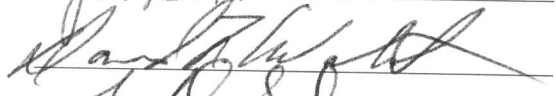

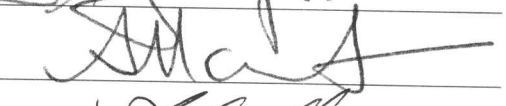



STRUCTURED COVARIANCE ESTIMATION FROM SPATIAL SPECTRA
FOR ADAPTIVE BEAMFORMING

by

Joseph James Schwarzwald
A Dissertation
Submitted to the
Graduate Faculty
of
George Mason University
In Partial fulfillment of
The Requirements for the Degree
of
Doctor of Philosophy
Electrical and Computer Engineering

Committee:

	Dr. Kathleen E. Wage, Dissertation Director
	Dr. Andrzej Z. Manitius, Committee Member
	Dr. Jill K. Nelson, Committee Member
	Dr. David F. Walnut, Committee Member
	Dr. Thomas J. Green, Jr., Committee Member
	Dr. Andrzej Z. Manitius, Department Chair
	Lloyd J. Griffiths, Dean, The Volgenau School of Information Technology and Engineering

Date: November 22, 2010

Fall Semester 2010
George Mason University
Fairfax, VA

Structured Covariance Estimation From Spatial Spectra For Adaptive Beamforming

A dissertation submitted in partial fulfillment of the requirements for the degree of
Doctor of Philosophy at George Mason University

By

Joseph James Schwarzwald
Master of Science Electrical Engineering
Johns Hopkins University, 2002
Bachelor of Electrical Engineering
The Catholic University of America, 1996

Director: Dr. Kathleen E. Wage, Professor
Department of Electrical and Computer Engineering

Fall Semester 2010
George Mason University
Fairfax, VA

Copyright © 2010 by Joseph James Schwarzwald
All Rights Reserved

Dedication

To Debbie

and Holly, Jason, Emma, and Robyn

Acknowledgments

I would like to thank my wife, Debbie, for her love and support. You have been my biggest fan, always understanding why this has been important to me, and supporting me through long nights, early mornings, and time away from home to get the job done right. We did it!

To our children, Holly, Jason, Emma, and Robyn, my hope is that this work inspires you. Always believe in and challenge yourselves, never settle for being average. Now that it is done, trips to the Caribou Coffee can be simply for relaxing cups of coffee and hot chocolate, without the simulations and technical writing.

I would like to thank Dr. Kathleen E. Wage, my advisor, for her patience, listening, and guidance. The research process is unpredictable, and your encouragement has helped me in maintaining a steady progress in seeing this through. I would also like to thank the members of my committee, Dr. Jill K. Nelson, Dr. Andre Z. Manitijs, and Dr. David F. Walnut, with special thanks to Dr. Thomas J. Green, Jr. for his time, insight and support.

Finally, I would like to thank my employer, Argon ST, for seeing the value in my academic pursuits and providing, more than anything, the gift of time. Without it, this would not be possible. Special thanks are deserved for Stuart Ware, who provided the down field blocking when I needed it, and for Joe Carlin, who sponsored the endeavor.

This work is supported by Argon ST, Internal R&D, R0227.



the view from the “usual studying place”
in Fenwick Library

Table of Contents

	Page
List of Tables	ix
List of Figures	x
Abstract	xiii
1 Introduction	1
1.1 Motivation	1
1.2 Adaptive Beamforming Algorithms	4
1.2.1 Snapshot Deficient Algorithms	4
1.2.2 Correlated Signal and Interference Algorithms	7
1.2.3 Structured Covariance Algorithms	8
1.2.4 Summary	10
1.3 Structured Covariance Based on Spatial Spectrum	11
1.4 Dissertation Outline	14
2 Background	15
2.1 Introduction	15
2.2 Notation	16
2.3 Data Models	17
2.3.1 Assumptions	17
2.3.2 General Model	17
2.4 Space-Time Random Processes	20
2.4.1 2^{nd} Order Characterization of Space-Time Random Processes	21
2.4.2 Cramér Spectral Representation	26
2.5 Optimal Beamforming	35
2.5.1 Minimum Variance Distortionless Response (MVDR)	35
2.5.2 Normalized SINR Loss	37
2.6 Spectral Estimation Techniques	38
2.6.1 Classical (nonparametric) Spectral Estimation	39
2.6.2 Multitaper Spectral Estimation (MTSE)	41

3	Structured Covariance Matrices	
	Based On Frequency Wavenumber Spectral Estimation	52
3.1	Introduction	52
3.2	Sensitivity of a Model Based Beamformer	53
	3.2.1 Single Plane Wave in Spatially White Noise	53
	3.2.2 Multiple Plane Waves in Spatially White Noise	61
3.3	Model For Covariance	64
	3.3.1 Estimating Visible Space Covariance, $\hat{\mathbf{R}}_{\text{vs}}$	66
	3.3.2 Visible and Virtual Space	67
	3.3.3 Regularly and Uniformly Spaced Array Geometry	68
	3.3.4 Positive Definiteness	72
3.4	Performance When Using Classical PSD Techniques	74
	3.4.1 Background	74
	3.4.2 Expected Value - Stationary Random Process	78
	3.4.3 Performance Based On Expected Value	80
	3.4.4 Prototype Power Pattern	81
	3.4.5 Prototype Window Normalized SINR Loss	84
3.5	Summary	91
4	Structured Covariance Estimation with Thomson's MTSE	92
4.1	Introduction	92
4.2	Covariance from Spatial Spectra (CSS) with MTSE	93
	4.2.1 Introduction	93
	4.2.2 Number of Tapers, D	94
	4.2.3 FFT and Zero-Padding	95
	4.2.4 Discrete Line Component Processing (Harmonic Analysis)	96
	4.2.5 Background / Continuous Spectrum	98
	4.2.6 Covariance Matrix Computation	99
	4.2.7 Composite Spectrum Generation	99
4.3	Performance Simulation	101
	4.3.1 Discrete Interference	101
	4.3.2 Spatially Spread Interference	108
	4.3.3 Mixed Spectra	116
	4.3.4 Impact of Harmonic Analysis	120
4.4	Summary	122
5	Correlated Signal and Interference	123

5.1	Introduction	123
5.2	Covariance for Correlated Signals	124
5.3	Expected Value	126
5.4	CSS Performance with Correlated Signal and Interference	129
5.4.1	Introduction	129
5.4.2	Relative Contribution of Correlated and Uncorrelated Components	131
5.4.3	Normalized SINR Loss w.r.t. Uncorrelated Ensemble Covariance	134
5.4.4	Effective SINR	139
5.5	Related Techniques	141
5.5.1	Redundancy Averaging	141
5.5.2	Covariance Matrix Tapers	143
5.5.3	Comparison Summary	143
5.6	Summary	144
6	Non-Ideal Array Manifold Response	146
6.1	Introduction	146
6.2	Types of Non-Ideal Array Manifold Responses	147
6.2.1	Random Errors	147
6.2.2	Deterministic Errors	149
6.3	Impact to Structured Covariance Matrix ABF Performance	151
6.4	Mitigation Techniques	156
6.4.1	Introduction	156
6.4.2	MMSE Unbiased Linear Estimate of Calibration Errors	157
6.4.3	Maximum Likelihood Estimate of Calibration Errors	162
6.4.4	Comments	164
6.4.5	Procedure	165
6.5	Performance Simulation	166
6.5.1	Random Errors	166
6.5.2	Deterministic Errors	174
6.5.3	Impact of Error Processing with Ideal Array Manifold Response	178
6.5.4	Performance Simulation Recap	183
6.5.5	Comparison - MTSE and MVDR Spectra	183
6.6	Summary	186
7	Extensions for Arbitrary Geometry	191
7.1	Introduction	191

7.2	Sensor Noise with Arbitrary Array Geometry	191
7.3	Positive Definiteness	196
7.3.1	Method 1	196
7.3.2	Method 2	198
7.4	Covariance from Spatial Spectra (CSS) with MTSE	199
7.4.1	Design of the Tapers	199
7.4.2	Discrete Line Component Processing (Harmonic Analysis)	200
7.4.3	Background / Continuous Spectrum	201
7.4.4	Estimate Sensor Noise in Virtual Region	202
7.4.5	Covariance Matrix Estimate	202
7.5	Performance Simulation	203
7.5.1	$N = 50$ Element Uniform Circular Array, $R_\lambda = 5.0$	204
7.5.2	$N = 50$ Element Uniform Circular Array, $R_\lambda = 2.5$	209
7.5.3	Importance of $\hat{\sigma}_w^2 \mathbf{P}_{\text{vr}}$	214
7.6	Summary	214
8	Summary and Future Work	216
A	Appendix - Circular and Partial Circular Array Bending	222
A.1	Introduction	222
A.2	Circular Bow	222
A.3	Partial Circular Bow	223
B	Appendix - Detail for Sensitivity to Model Estimation Errors	226
B.1	Introduction	226
B.1.1	Interferer to Noise Ratio	226
B.1.2	Over/Under-estimate INR, $\Delta \text{INR} \neq 0$	226
B.1.3	Spatial Frequency Offset, $\Delta k \neq 0$	228
C	Appendix - Table of Variables	233
	Bibliography	237

List of Tables

Table	Page
1.1 Snapshot deficient / reduced rank adaptive algorithms	5
1.2 Correlated signal and interference algorithms	7
3.1 INR estimation error cases, single plane wave interferer	56
5.1 Comparison of CSS and related techniques	144
6.1 Random error model parameters for comparable distortion	150
7.1 Environment parameters, uniform circular array example	204
7.2 Array and CSS parameters, uniform circular array example	204
C.1 Table of Variables - Scalars	234
C.3 Table of Variables - Scalar functions	235
C.5 Table of Variables - Vectors and Matrices	236

List of Figures

Figure	Page
1.1 The array processing problem	2
2.1 Plane wave impinging on an arbitrary array	18
2.2 Spherical coordinate system	24
2.3 Comparison of resolution for multitaper spectral estimation	45
2.4 Comparison of multiple tapers	47
2.5 Example of MTSE with harmonic analysis	51
3.1 $\xi_{dB}(INR, [k_s - k_o])$, ΔINR Case 1 - single plane wave interferer	57
3.2 $\xi_{dB}(INR, [k_s - k_o])$, ΔINR Case 2 - single plane wave interferer	58
3.3 Bounds for Δkd for a specified ξ , single plane wave interferer	60
3.4 AOA accuracy requirements for specified ξ , $N = 32$ ULA, single interferer	62
3.5 AOA accuracy requirements for specified ξ , $N = 16$ ULA, single interferer	63
3.6 Impact of covariance estimated from visible space only	69
3.7 $N = 32$, Normalized SINR loss (dB) for $A_{bb} = -40$ dB	87
3.8 $N = 32$, Normalized SINR loss (dB) for $A_{bb} = -60$ dB	88
3.9 $N = 64$, Normalized SINR loss (dB) for $A_{bb} = -40$ dB	89
3.10 Classical PSD, mainlobe width impacts to performance	90
4.1 ABF performance, fixed INR , $N = 32$	104
4.2 ABF performance, fixed INR , $N = 16$	105
4.3 ABF performance, mixed INR , $N = 32$	107
4.4 Combined surface and shipping noise model characteristics, VLA	110
4.5 $\xi_{dB}(\theta)$, combined noise model, $M = 1, 4, 16$, VLA	111
4.6 $\xi_{dB}(\theta)$, combined noise model, $M = 64, 256, 1024$, VLA	112
4.7 3D isotropic noise	113
4.8 Distant shipping noise model, VLA	114
4.9 Surface noise model, VLA	115
4.10 Mixed spectra performance, weak strength line component	118
4.11 Mixed spectra performance, medium strength line component	119

4.12	Impact of estimation accuracy for harmonic analysis.	121
5.1	Example beampattern illustrating the signal cancellation effect	130
5.2	Analysis of impact of bias for correlated signal and interference using $\ \cdot \ _F^2$	135
5.3	Performance assessment for correlated signal and interference	137
5.4	Relative CSS performance for correlated and uncorrelated data	138
5.5	$SINR_e$ comparison of CSS and MVDR for correlated signal and interference	140
6.1	Circular bow and partial circle bow array deformation	149
6.2	Estimated wavenumber spectrum, impact of random errors	153
6.3	Estimated wavenumber spectrum, circular bow array bending	154
6.4	Estimated wavenumber spectrum, partial circular bow array bending	155
6.5	$N = 32$, $\sigma_g^2/c_h^2 = -30$ dB, constant $INR = 50$ dB	169
6.6	$N = 32$, $\sigma_g^2/c_h^2 = -10$ dB, constant $INR = 50$ dB	170
6.7	$N = 32$, $\sigma_g^2/c_h^2 = -10$ dB, variable $INR = [20, 50]$ dB, 2 passes	171
6.8	$N = 64$, below design frequency, random positional errors 10%	173
6.9	Circular bow in array shape, $H/L = 2.0\%$	175
6.10	Partial circular bow in array shape, $H/L = 4.0\%$, $L_2/L = 25\%$	177
6.11	Impact of error processing for ideal manifold response, fixed INR	180
6.12	Impact of two pass error processing for ideal manifold response, mixed INR	181
6.13	Impact of error processing for ideal manifold response, below design frequency	182
6.14	Performance comparison with/without non-ideal response processing	184
6.15	Comparison of final MTSE and MVDR spectra, fixed INR case	187
6.16	Comparison of final MTSE and MVDR spectra, mixed INR case	188
6.17	Comparison final MTSE and MVDR spectra, wide range INR case	189
6.18	Comparison of final MTSE and MVDR spectra, $\frac{1}{2}$ design frequency	190
7.1	Eigenvalues for \mathbf{R}_{iso} , various arrays	194
7.2	Partition of the visible region for multi-taper design, arbitrary array geometry	200
7.3	MVDR spectrum for ensemble covariance, $N = 50$, $R_\lambda = 5$ circular array	205
7.4	CSS performance, $N = 50$, $R_\lambda = 5$ circular array, $M = 5$ snapshots	206
7.5	CSS performance, $N = 50$, $R_\lambda = 5$ circular array, $M = 10$ snapshots	207
7.6	CSS performance, $N = 50$, $R_\lambda = 5$ circular array, $M = 20$ snapshots	208
7.7	MVDR spectrum for ensemble covariance, $N = 50$, $R_\lambda = 2.5$ circular array	210
7.8	CSS performance, $N = 50$, $R_\lambda = 2.5$ circular array, $M = 5$ snapshots	211
7.9	CSS performance, $N = 50$, $R_\lambda = 2.5$ circular array, $M = 10$ snapshots	212

7.10	CSS performance, $N = 50$, $R_\lambda = 2.5$ circular array, $M = 20$ snapshots . . .	213
7.11	Impact of covariance estimated from visible space only	215
A.1	Definition of a circular bow array deformity	223
A.2	Definition of a partial circular bow array deformity	225

Abstract

STRUCTURED COVARIANCE ESTIMATION FROM SPATIAL SPECTRA FOR ADAPTIVE BEAMFORMING

Joseph James Schwarzwald, PhD

George Mason University, 2010

Dissertation Director: Dr. Kathleen E. Wage

The covariance matrix for a sensor array observing a stationary space-time process is determined by the individual sensor element locations, the directional response and noise of those elements, and the spatial spectrum of the process. Under this model the covariance matrix has a particular structure that can be exploited, improving adaptive beamformer performance both in terms of the number of snapshots required for good performance and robustness against correlated signal and interference environments. These performance improvements are particularly beneficial for large aperture arrays with large numbers of sensor elements that are operating in non-stationary and multi-path environments. No closed form solution exists for estimating structured covariance for the general problem of an unknown number of signals in non-white noise. We look to exploit the naturally intuitive interpretation of the process in the azimuth-elevation or frequency-wavenumber domains to address the problem.

This dissertation develops a covariance from spatial spectrum (CSS) method by first estimating the spectrum of the process, and then applying standard spectral to covariance transforms. The initial characterization in the transform domain, either direction of arrival or wavenumber, provides a natural reinforcement of the underlying space-time process

model. Additionally, spectral estimation techniques take advantage of the number of spatial samples, in particular for arrays with many elements, in a manner simple snapshot averaging cannot. While ad-hoc, such a structured covariance technique can provide near optimal performance for passive signal detection or recovery with very few snapshots.

The first objective of this work is to understand the performance of minimum variance distortionless response adaptive beamforming when covariance is estimated from the spatial spectrum. Positive definiteness of the covariance matrix and estimation bias are investigated. Performance predictions are developed for the case of a uniform line array and classical power spectral estimation techniques. This analysis highlights the need to explicitly deal with mixed spectra that arise in environments containing both point source and spatially-spread signals. Thomson's multi-taper spectral estimation neatly combines both the convenience of the non-parametric spectral estimation algorithms and the required harmonic analysis to handle such mixed spectra. Adaptive beamformer performance is assessed for various interference and noise environments against existing snapshot deficient algorithms. Extensions to support arbitrary array geometry are considered.

A correlated signal and interference environment cannot be modeled as a stationary space-time process. A second objective of this work is to investigate how constraining the covariance to a stationary space-time process model mitigates signal cancellation due to correlation between the signal and interference. Reduction in correlation, and the resultant covariance bias are investigated. Adaptive beamformer performance in the presence of correlated signal and interference is assessed.

Structured covariance methods may suffer performance losses when real world conditions violate model assumptions. The final objective of this work is to understand the impacts of non-ideal array manifold response. The CSS techniques developed in the dissertation are extended to account for such non-ideal response. Adaptive beamformer performance is assessed for various interference and noise environments in the presence of random and deterministic array manifold response errors. Benefits to spectral estimation when using the non-ideal response processing are also seen.

Chapter 1: Introduction

1.1 Motivation

The deployment of long aperture arrays with large numbers of sensor elements has been enabled by the evolution of sensor, telemetry, and digital processing technology. Large arrays promise significant benefits in terms of theoretical processing gain and spatial resolution and are, for instance, employed regularly across a range of undersea acoustic applications. Adaptive beamforming algorithms have been successfully applied to these arrays to maximize a system's ability to perform well in complicated signal and interference environments. Beyond the theoretical gain, the ability of an algorithm to converge quickly provides many benefits, including minimizing data collection requirements, allowing the processor to adapt quickly to non-stationary environments, or providing better and more timely outputs to follow on processors such as target trackers. For many algorithms, increasing the number of sensor elements works against the desire to adapt quickly. Additionally, multipath environments introduce unique challenges that may cause substantial performance loss for algorithms not designed to handle them.

Figure 1.1 illustrates the general array processing problem. An array of sensors, shown in a linear arrangement, spatially samples the environment and provides the time varying outputs to an array processor that operates on the data. Signals or interference and noise may be originating from discrete point sources (arrows) or spatially spread fields (shown as distributed across space). There are several standard operations for the array processor. For a particular range and or direction of arrival, the processor may decide if a signal is present or not, the detection problem, or attempt to reconstruct the time domain waveform, the beamforming problem. Knowledge of the temporal characteristics of the signal may be exploited, such as in communications or active radar or sonar processing, or the signal may

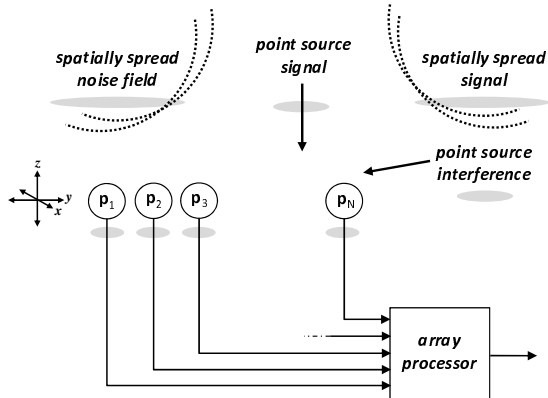


Figure 1.1: **The array processing problem:** The array of sensors spatially sample the environment, and provide the time varying outputs to an array processor. Standard functions for the array processor are detection or signal reconstruction.

be unknown. This work focuses on the unknown signal problem, where the processor is guided only by what it is able to estimate of the environment and a desired direction of arrival, i.e., the look direction.

The objective of an adaptive array processing algorithm is to suppress the noise-plus-interference components of the environment, while enhancing the response to the desired signal spatial signature, \mathbf{s} . For narrowband linear processors, this is accomplished by means of a weighting vector, \mathbf{w} , that is used to combine the N sensor array outputs, \mathbf{x}_m , at time index m to produce a scalar output, $y_m = \mathbf{w}^H \mathbf{x}_m$. Given the covariance matrix for the array outputs, $\mathbf{R} = E \{ \mathbf{x}_m \mathbf{x}_m^H \}$, several different formulations for determining an optimal set of weights lead to a solution of the form [1]

$$\mathbf{w}_{opt} = \gamma \mathbf{R}^{-1} \mathbf{s} \quad (1.1)$$

where \mathbf{s} is referred to as the steering vector, and γ is a normalization factor determined by the optimization. In practice, the covariance matrix \mathbf{R} is not known a priori, and must be estimated. When the noise and interference are Gaussian, the unconstrained maximum likelihood (ML) estimate of \mathbf{R} is the sample covariance matrix, $\hat{\mathbf{R}}_{SCM}$, [2]

$$\hat{\mathbf{R}}_{SCM} = \frac{1}{M} \sum_{m=1}^M \mathbf{x}_m \mathbf{x}_m^H \quad (1.2)$$

In practice, (1.2) is only valid over the duration that the environment can be considered stationary. Nonstationarity in the environment itself is a common condition that arises in both sonar and radar applications, and becomes a limiting factor in the ability to estimate \mathbf{R} from the data. In the case of sonar, the combination of the continuous motion of sound sources relative to the array at short ranges and the corresponding small resolution cells of the array ultimately set the time scale wherein short-term stationarity assumptions are valid [3]. In space-time adaptive processing (STAP) for radar, the resolution of range-Doppler cells is susceptible to nonstationarity in the form of heterogeneous clutter, caused by ground clutter varying over the surface of the earth [4]. These non-stationary conditions result in a limited amount of snapshot data available for processing that may be insufficient for an algorithm to converge, a condition referred to as snapshot deficient operation. Adaptive array processing algorithms that converge rapidly are important for achieving near the theoretical performance for larger arrays in nonstationary environments.

In addition to concerns caused by snapshot deficient operation due to nonstationarity, the problem of correlated signal and interference also arises in adaptive beamforming. Correlated interference arises in multipath or smart jamming scenarios, resulting in the signal cancellation effect [5]. Applications that have no a priori knowledge of the inbound signal at the desired direction of arrival, such as passive sonar, are subject to this effect. Algorithms based on the minimum variance distortionless response (MVDR) criteria [1, 6] pass the desired direction of arrival undistorted, but subsequently align the correlated interference component for maximum destructive interference, e.g., summing sinusoids 180° out of phase, to minimize the total output power. This results in an overall loss in output signal to interference and noise ratio (SINR). The signal cancellation effect can dominate performance, and occurs regardless of snapshot limitations. Adaptive array processing algorithms that mitigate the signal cancellation effect without a priori knowledge of the incoming signal

at the desired direction of arrival are also of great interest.

1.2 Adaptive Beamforming Algorithms

Adaptive beamforming algorithms have been actively researched over the past five decades. Many approaches for covariance estimation have been proposed, implemented and analyzed and work well within their design assumptions. Snapshot deficient operation and correlated signal and interference are the two main areas addressed by this thesis. We begin with a review of previous work in these areas, followed by a discussion of the techniques developed in the thesis.

Table 1.1 provides a listing of algorithms, developed specifically to address the snapshot deficient condition that occurs when the number of available snapshots is too small to obtain good covariance estimates using (1.2). Reduced rank algorithms reduce the dimensionality of the problem from the full rank, which is the number of array elements N , to a lower rank, $r < N$, such that the available snapshots, M , are no longer deficient with respect to the reduced dimension. Subspace, eigenspace, and reduced rank methods are similar in this regard, although the algorithms vary in how they are implemented. Table 1.2 lists some techniques that have been developed to address the correlated signal and interference problem.

1.2.1 Snapshot Deficient Algorithms

The very first adaptive beamforming techniques relied on adaptation of the weight vector using a feedback loop, such as the maximized signal to noise algorithm (MSN) of Howells [25] and Applebaum [26] or the classic least mean squares processor (LMS) developed by Widrow [27]. Frost extended these approaches to be space-time in nature by introducing an adaptive filter behind each array sensor [28]. Convergence rates, and therefore the snapshot data requirements of these techniques, were dominated by the adaptation constant and the eigenvalue spread of the underlying covariance. Sample matrix inversion (SMI) dramatically

Table 1.1: Snapshot deficient / reduced rank adaptive algorithms

YEAR	METHOD	AUTHOR	AREA
1973	diagonal loading	Cox [7]	mismatch
1977	Toeplitz constrained	Morgera [8]	structured covariance
1981	diagonal loading	Abramovich [9, 10]	snapshot deficient
1983	Hung-Turner projection (HTP)	Hung, Turner [11]	projection method
1988	Expectation Maximization (EM)	Fuhrmann, Barton, Robey [12–17]	structured covariance
1994	principal components inverse (PCI)	Kirsteins, Tufts [18]	reduced rank
1997	cross spectral metric (CSM)	Goldstein, Reed [19]	reduced rank
1998	multistage Wiener filter (MWF)	Goldstein, Reed, Scharf [20]	reduced rank
2004	indirect dominant mode rejection (IDMR)	Santos, Zoltowski [21–23]	snapshot deficient
2007	physically constrained ML (PCML)	Kraay, Baggeroer [24]	structured covariance

improved convergence times by inverting the estimated covariance matrix found using (1.2) directly [6]. Reed, Brennan, and Mallett [29] analyzed the performance of SMI as a function of the number of available snapshots, showing that for Gaussian interference and noise processes SMI achieves SINR within 3 dB of optimal on average, using $M = 2N$ snapshots. This represented an appreciably faster convergence than previously accomplished using LMS type methods. This result was also significant for showing that performance for SMI, under the stated Gaussian assumptions, was a function of the number of snapshots only. This is not the case when the desired signal was also present within the snapshot data used to estimate the covariance. For this situation, Miller showed that the convergence rate of the output SINR was severely degraded [30], and in addition, the required number of snapshots was also a function of the signal to noise ratio (SNR).

Signal mismatch occurs when the assumed steering vector, \mathbf{s} , is perturbed from the true steering vector. This can occur as a result of random perturbations of the array element positions, or variations in individual sensor amplitude or phase characteristics, or a combination of both. It may also occur due to inexact knowledge of the steering direction. The result is a degradation in adaptive beamformer performance. Krolik and Swingler [31] showed that errors in $\hat{\mathbf{R}}_{SCM}$ due to limited snapshot support can also cause unintentional signal mismatch as a result of improper estimation of the noise subspace. Carlson showed that another symptom of this improper estimation was poor sidelobe performance [32].

Diagonal loading was developed as a simple method to address some of these performance-related issues. Diagonal loading adds an additional constant diagonal term to the sample covariance matrix, i.e.,

$$\hat{\mathbf{R}}_{DL} = \hat{\mathbf{R}}_{SCM} + \sigma_{DL}^2 \mathbf{I} \quad (1.3)$$

Cox used diagonal loading to help with the signal mismatch problem, due to either array manifold errors or snapshot deficient processing [7]. Abramovich analyzed the impact of doing this, which he referred to as regularization for dealing with finite M [9]. He showed that when there were K interferers, diagonal loading could be used to reduce the number of required snapshots to be proportional to K , with as little as $M = K$ to achieve good results. His analysis went on to show that when $M < K$, no important interference suppression could be expected from diagonally-loaded sample covariance matrix inverse techniques [10]. This result was significant, in that it quantified the minimum snapshot support required for algorithms using the sample covariance matrix. Determination of an optimal value for the diagonal load factor, σ_{DL}^2 , has been of considerable interest with many published results [9, 32–35].

Chang and Yeh [36], and Yu and Lee [37] performed similar types of analysis for eigenspace adaptive beamformers, processors based on subsets of the eigenvectors of the covariance matrix. They showed that within \mathbf{R} , the signal and interference subspace is orthogonal to the noise subspace. These authors also indicated that SMI is degraded mostly by perturbed estimates of the noise subspace. Generally, for this class of subspace processors the number of required snapshots, M , is a function of the number of interferers, K , the desired signal SNR, and sometimes the number of array elements, N . As a rule of thumb, $M \geq K \cdot SNR_i$ achieves within 3 dB of the optimal SINR, where SNR_i is the input signal to noise ratio. In terms of convergence, this result for subspace methods is comparable to the result of Abramovich for diagonal loading.

Hung and Turner [11] introduced a method that used Gram-Schmidt orthogonalization

Table 1.2: Correlated signal and interference algorithms

YEAR	METHOD	AUTHOR	AREA
1982	spatial dither	Widrow, et al. [39]	spatial smoothing
1985	spatial smoothing (SS)	Shan [40]	sub array processing
1989	forward / backward avg. (FB/SS)	Pillai [41]	sub array processing
1990	redundancy averaging (RA)	Linebarger [42]	structured covariance
2004	indirect dominant mode rejection (IDMR)	Santos, Zoltowski [21–23]	structured covariance

to determine a set of basis vectors for the observed interference and noise. The steering vector, \mathbf{s} , was then projected onto the corresponding interference and noise null space. This method is efficient and can operate with fewer snapshots than interferers, at the expense of some of the interferers remaining completely unsuppressed. KIRSTEINS and TUFTS considered processing with the subspace defined by the dominant eigenvalue / eigenvector pairs in the sample covariance matrix with the principal components inverse (PCI) method [18]. Goldstein and Reed adapted this approach by using a metric to determine the relevance of the eigenvectors not by their eigenvalue magnitude alone but also incorporating a correlation with the steering vector, \mathbf{s} [19]. This method was labeled the cross spectral metric (CSM). Goldstein further extended the approach to efficiently form the weight vector, \mathbf{w} , directly from the snapshots, \mathbf{x}_m , without the need to explicitly form the sample covariance matrix or invert it. This multi-stage Wiener filter (MWF) [20] was demonstrated to outperform PCI and CSM as a function of reduced rank, r , and number of available snapshots, M [38].

1.2.2 Correlated Signal and Interference Algorithms

Table 1.2 lists techniques that have been developed to address the correlated signal and interference problem. Widrow, et al. [39] studied this problem and presented solutions to address it. One of them, called “spatial dither”, is to move the array spatially (or electronically) to modulate emissions received away from the look direction without distorting the desired signal. This technique evolves naturally into the concept of spatial smoothing, introduced by Shan and Kailath [40, 43]. Their approach partitions the overall array into subarrays, and combines the individual subarray sample covariance matrices to arrive at a

smoothed sample covariance matrix for the array. The spatial smoothing asymptotically decreases the effective correlation between the desired direction signal and the interfering signals with progressive smoothing, thereby reducing the effects of correlation and signal cancellation. The drawback for this type of approach is a decrease in effective array aperture due to the partitioning into subarrays. Pillai and Kwon [41] extended the spatial smoothing technique for arrays with conjugate symmetric array manifold response by including a forward and backward spatial smoothing component. They showed that for K interferers an array of length $3K/2$ was required, better than the $2K$ necessary using the original spatial smoothing algorithm.

Ragnunath and Reddy [44] summarized several key points with respect to correlated interference and spatial smoothing. First, more snapshots do not improve interferer suppression when interference is correlated with the desired signal, nor does diagonal loading. When sources are uncorrelated performance does improve with more data. Correlated signal and interference situations are dominated by the signal cancellation effect. This can be addressed with spatial smoothing, which is also helpful in dealing with finite data, but effectively decreases the array aperture due to the subarray processing.

1.2.3 Structured Covariance Algorithms

Structured covariance methods incorporate some a priori knowledge of the problem space to add additional constraints to the problem. These constraints may be, for instance, Toeplitz or block Toeplitz structure within the covariance matrix. The a priori knowledge may be based on established models, such as the space-time process observed being stationary, or the geometry of the array elements. In essence these constraints reduce the number of unknown quantities to estimate, or the size of the allowable solution space, and have been demonstrated to show convergence to the final solution with very little data in some scenarios. Thus, they offer the potential for meaningful adaptive processor performance with lower snapshot requirements than sample covariance methods and its reduced rank derivatives. Structured covariance algorithms have been applied to both the snapshot deficient

and correlated signal and interference problems, as indicated in Tables 1.1 and 1.2.

Morgera used knowledge that the covariance matrix has Toeplitz structure in many problems to increase the effective sample size of the available data by averaging down the diagonals of the sample covariance matrix [8]. Simplified performance expressions similar to the results for sample covariance methods could not be obtained, instead he observed that the performance of each instance maintained a dependence on the underlying covariance of the data. This implies that each situation encountered is its own problem in terms of performance.

Miller and Snyder [45] established a framework for using the expectation maximization (EM) algorithm to determine the ML estimate of a Toeplitz covariance matrix. Fuhrmann, and his students Robey and Barton continued development of this EM approach and further defined the Toeplitz or block-Toeplitz structure inherent in many array processing problems [12–17]. An important theoretical issue was to demonstrate that EM would converge to a positive definite solution given the data constraints. With this established, the technique was demonstrated to have good performance with limited snapshot data. For some problems it is necessary to embed the solution desired, a $N \times N$ matrix, into a larger circulant matrix problem, $N_{EM} \times N_{EM}$, to allow EM to operate properly in an efficient form, a technique known as a circulant matrix extension. Dembo determined a bound for the optimal value for N_{EM} [46] in terms of the eigendecomposition of the sample covariance matrix and the initial estimate of the covariance, with a value no less than $2N$. For larger values of N and high dynamic range spectra the resultant computational order becomes very large.

Linebarger [42] introduced redundancy averaging (RA), similar in form to Morgera’s algorithm, as a method to enforce a Toeplitz structure on the covariance matrix for uniform linear arrays. Correlated signal and interference perturb this structure in the sample covariance matrix. Redundancy averaging forms a new covariance matrix estimate by replacing the diagonals of the sample covariance matrix with their averaged values. This operation helps mitigate the influence of the signal cancellation effect, but has the potential to produce an indefinite covariance matrix estimate. Discussion of the existence and significance

of the residual covariance matrix bias can be found in [47, 48].

Indirect dominant mode rejection (IDMR) was developed to address both snapshot deficient processing and the residual correlated signal and interference in the covariance due to the limited snapshot support [21–23]. This technique forms the sample covariance matrix, then estimates the number of interferers and their respective directions of arrival via conventional beamforming or high resolution spectral analysis, e.g. MUSIC, in addition to estimating the spatially white noise variance. The algorithm then uses these estimates to formulate the covariance following the stationary process plane waves in white noise model. IDMR relies on MUSIC for best performance, and therefore requires an eigendecomposition of the sample covariance matrix. Because of this it also exhibits the $M > K$ limitation. Nor does IDMR present a way to neatly handle spatially spread interference, i.e., non-spatially white noise.

Kraay and Baggeroer [24] developed a computationally-intensive iterative technique, physically constrained maximum likelihood (PCML), that relied on further restricting the structure of the covariance by requiring that it correspond to physically propagating plane waves arriving at the array with valid elevation and azimuth. This technique has also been applied to shallow water mode filtering, with appropriate modification of the physical constraint to reflect the propagating mode structure in the water column [49]. For adaptive beamforming, the likelihood function was believed to be highly multimodal with respect to the estimate of the sensor noise, and determining the best choice of multiplicative updates, additive updates or more sophisticated minimization techniques, such as simulated annealing, remains an open issue.

1.2.4 Summary

In summary, snapshot deficient processing, signal mismatch, and correlated signal and interference are practical problems that need to be addressed by adaptive beamforming algorithms. Sample covariance matrix techniques have dominated the research space and

worked to address these issues but appear to be limited at the lower end of snapshot support by requiring the number of snapshots to be greater than or equal to the number of interferers, $M \geq K$, the performance bound indicated by Abramovich [9]. Structured covariance techniques offer a way to break through this barrier by incorporating additional knowledge of the problem into the algorithm. These techniques have been demonstrated to converge with very little snapshot data and provide near theoretically optimal performance. Several open issues exist with these methods, including computational intensity, structured model specification and parameter estimation, proof of convergence, positive definiteness of covariance, and performance in the presence of model errors.

1.3 Structured Covariance Based on Spatial Spectrum

The spatially and temporally stationary space-time random process is a common model for the observed environment in many applications in array signal processing. This model of the space-time process can be described using the Cramér spectral representation theorem [50]. This theorem provides a description of the random process as the sum of uncorrelated plane waves, distributed across the visible region of the array as a function of azimuth and elevation or across the visible region in the frequency-wavenumber domain. These domains are related to each other, and each properly describes the space-time process observed. The theory of second order characterizations of space-time random processes shows how either of these descriptions can be related to the space-time covariance of the process at the output of the observing array. This is directly analogous to the relationship between power spectral density and auto-correlation in the case of time series analysis.

Because the space-time covariance can be related to either of these representations, this dissertation considers estimating these spectral quantities first in order to compute the covariance at the output of the array. We refer to this as covariance from spatial spectrum (CSS). Several factors motivate this approach. First is the wealth of available research in the area of spectral estimation techniques, in particular those techniques that do not require a covariance matrix estimate a priori, and that are designed to operate on as little data

as possible. Second, the spectral representation model consists of uncorrelated plane wave components. When encountering correlated signal and interference scenarios, processors typically degrade in performance due to the signal cancellation effect. Constraining the estimated covariance to the stationary model significantly reduces the contribution of the correlation within the matrix, mitigating signal cancellation. Third, the stationary model imparts a structure to the covariance. As noted in Section 1.2.3, structured covariance matrix techniques have been demonstrated to converge much more rapidly than traditional sample covariance matrix techniques. While it is known that there is no simple closed form solution for the ML estimate for a structured covariance for the general problem of unknown number of signals in non-white noise [51], this thesis looks to exploit the naturally intuitive interpretation of the process in the azimuth-elevation or frequency-wavenumber domains to address the problem.

The space-time process may be modeled, via the spectral representation theorem, in the context of angle of arrival to the array. Sensor noise, typically modeled as an uncorrelated noise component within each sensor, is also a necessary part of the covariance observed by the adaptive processor. CSS processing for uniform linear and regularly-spaced array geometries is shown to be straightforward using standard power spectral estimation techniques and FFT processing. The expected value of the covariance estimate is investigated for the case of a uniform linear array using classical windowed averaged periodogram techniques since they are straightforward to analyze. The covariance estimate is shown to be biased. Adaptive beamformer performance is evaluated using the normalized SINR loss metric [29]. The impact of discrete, or point source interference may degrade performance significantly when the spatial separation from the steering vector, \mathbf{s} , is small. This motivates an additional step in the algorithm to detect, estimate, and subtract this type of discrete component from the available snapshot data to iteratively develop an estimate of the smooth continuous background noise covariance. The detected discrete components are then reintroduced to form the final covariance estimation. This allows operation with negligible normalized SINR loss under a large range of conditions. Thomson's multi-taper spectral estimation [52]

is a technique that neatly combines both the convenience of the non-parametric spectral estimation algorithms and the required harmonic analysis techniques that works well in this application. A processing flow incorporating Thomson's method is developed. Performance assessment of the final technique is carried out through simulation of various interference and noise environments, with excellent normalized SINR loss performance obtained below the $M = 2K$ requirement necessary for sample covariance type algorithms. Extensions to support arbitrary array geometry are developed.

A correlated signal and interference environment cannot be modeled as a stationary space-time process. The correlated component perturbs the Toeplitz structure of the covariance matrix in the uniform linear array case. The expected value of the estimated covariance for this problem, while constrained to the uncorrelated plane waves model, contains a bias term related to the original correlated data. Impact of this bias term is investigated, and it is seen that it is negligible as the array length increases. Adaptive beamformer performance is assessed through simulation, and compared to performance of the algorithm for the uncorrelated data case. Performance is seen to be practically identical between the two scenarios. Comparison to sample covariance based techniques, using the effective SINR metric, is also used to demonstrate successful mitigation of the signal cancellation effect. This is accomplished without loss in effective aperture, and provides the same low snapshot support requirements as the stationary space-time process case. The development of these results is used to show the relationship of the CSS approach to the techniques of covariance matrix tapers (CMT) [53] and the structured covariance algorithm of redundancy averaging. CSS is shown to provide an increase in effective sample size, similar to redundancy averaging, while maintaining a positive definite covariance matrix estimate, and differs from CMT in its ability to mitigate the effects of correlated signal and interference in the data.

This structured covariance approach relies on the assumption of an ideal array manifold response. A real-world array manifold response may be non-ideal due to random variation in gain, phase, and directionality in the sensors. Non-ideal response may also result from deterministic positional errors, e.g., the bending experienced by an underwater towed array.

Performance impact for both random and deterministic array manifold response errors is investigated, and the techniques developed earlier are extended to account for non-ideal response. Adaptive beamformer performance is assessed for various interference and noise environments in the presence of random and deterministic array manifold response errors, and improvements to spectral estimation when using this type of processing are seen.

The techniques developed in this dissertation provide the best benefit in situations with large aperture and large numbers of sensors, with ideal or partially perturbed array manifold response, and non-stationary environmental conditions. Underwater acoustic processing provides several application areas where these are the operational conditions of interest. This work reflects a desire to investigate areas of most interest to that processing space.

1.4 Dissertation Outline

The remainder of the dissertation is organized as follows. Chapter 2 defines the array processing models used in the work, and reviews the relevant background material in stochastic processes, spectral estimation, and optimal beamforming. Chapter 3 looks at the sensitivity of optimal beamforming algorithms to estimation errors, presents the algorithm for covariance estimation from spatial spectra, and investigates performance for the uniform line array case using classical spectral estimation techniques. Chapter 4 incorporates Thomson's multitaper spectral estimation with harmonic analysis into the approach, and assesses performance in relevant interference and noise environments. Chapter 5 considers the correlated signal and interference case, and the resultant covariance estimation bias and its impact in mitigating the signal cancellation effect. Chapter 6 analyzes the impact of non-ideal array manifold response, and extends the techniques developed to account for such conditions. Chapter 7 extends the techniques of Chapter 4 to non-uniformly spaced arrays. Chapter 8 summarizes the contributions of the work and discusses future research.

Chapter 2: Background

2.1 Introduction

In this chapter we review the theoretical material and concepts that are the foundation for the remainder of the work. Section 2.2 introduces the notations employed in the dissertation. Section 2.3 reviews the data models and assumptions used throughout, namely the narrowband process, independent snapshot model. This is also referred to as the frequency domain snapshot model. Section 2.4 reviews the wide sense stationary space-time random process and its representation via the Cramér spectral representation theorem. This representation of the process, as a sum of uncorrelated plane waves, is used to relate the familiar 2^{nd} order characterizations of space-time random processes, specifically the frequency-wavenumber spectrum and space-time covariance. Section 2.5 reviews optimal beamforming for the data models of interest, and the normalized signal to interference and noise ratio (SINR) performance measure. The chapter concludes with a review of relevant spectral estimation techniques in Section 2.6. The discussion centers on the relationships for the time series problem as it is usually the most familiar and may be directly applied to uniform linear array processing. Natural extensions to the larger dimension spatial problem are explained. Our particular focus is on non-parameteric techniques that do not require formation of a covariance matrix. Classical techniques such as the averaged windowed periodogram are such an approach. Thomson's multi-taper spectral estimation, a more powerful technique derived from the Cramér spectral representation, is also reviewed with a focus on its strengths in dealing with minimal data support and mixed power spectrum, i.e., those containing both smooth functions and line components.

2.2 Notation

The dissertation uses the following notational conventions. The italicized lower case, x , is a scalar variable, and x^* is the complex conjugate of x . A $P \times 1$ dimensional vector is represented as the bolded lowercase, $\mathbf{x} \in \mathbb{C}^P$, and is complex (or real-valued) as indicated. \mathbf{x}^T is the transpose of \mathbf{x} , and \mathbf{x}^H is the conjugate transpose of \mathbf{x} . The matrix of dimension $P \times Q$ is the bolded uppercase, $\mathbf{X} \in \mathbb{C}^{P \times Q}$, and is also complex (or real-valued) as indicated. In describing matrices, we may use the compact notation $\mathbf{X} = ((x_{rc}))_{rc}$ to indicate a matrix consisting of the elements (row, column) indicated by x_{rc} . This is sometimes useful in showing the values when they are a function of the position indices, e.g., $\mathbf{x} = ((\cos[\omega p]))_p \in \mathbb{R}^P$ is an P element vector containing the values $[\cos(\omega), \cos(2\omega), \cos(3\omega), \dots]^T$. Similar notation applies for vectors or higher dimensional matrices. The notation $\text{diag}(x_1, x_2, \dots)$ describes a diagonal matrix consisting of entries x_1, x_2, \dots on the main diagonal.

The expectation operator is given by $E\{x\}$. When describing random variables, $x \stackrel{d}{\rightarrow} f_x(x)$, indicates that the random variable, x , is distributed according to the probability density function, $f_x(x)$. Gaussian random variables are commonly encountered and have a specific notation for the appropriate density function. The P -variate Gaussian random variable, $\mathbf{x} \in \mathbb{R}^P$, with mean $\mathbf{m} = E\{\mathbf{x}\}$ and covariance $\mathbf{R}_x = E\{(\mathbf{x} - \mathbf{m})(\mathbf{x} - \mathbf{m})^T\}$ has the notation $\mathbf{x} \stackrel{d}{\rightarrow} RN_P(\mathbf{m}, \mathbf{R}_x)$. Similarly, the P -variate complex Gaussian random variable, $\mathbf{x} \in \mathbb{C}^P$, with mean $\mathbf{m} = E\{\mathbf{x}\}$ and covariance $\mathbf{R}_x = E\{(\mathbf{x} - \mathbf{m})(\mathbf{x} - \mathbf{m})^H\}$ has the notation $\mathbf{x} \stackrel{d}{\rightarrow} CN_P(\mathbf{m}, \mathbf{R}_x)$. We assume that all complex Gaussian random variables are circularly symmetric of the type described by Goodman [2]. The acronym *i.i.d.* stands for independent and identically distributed.

2.3 Data Models

2.3.1 Assumptions

Throughout the dissertation, we assume that the observed space-time process is narrowband and propagates in a homogeneous medium with velocity c and temporal frequency $f = c/\lambda$. The process consists of plane waves that are solutions to the homogeneous wave equation. This places a restriction on wavenumber, \mathbf{k} , such that $|\mathbf{k}| = 2\pi/\lambda$, or said another way, plane waves must correspond to physically propagating angles of arrival to the array. We typically assume that the process is spatially wide sense stationary (WSS) and zero mean. The spatially wide sense stationary property implies the spatial covariance is a function of difference in position only. Additional, WSS requires that the plane wave components making up the process are uncorrelated. This restriction is relaxed when dealing with the special condition of correlated signal and interference, as it violates the spatially stationary model. Snapshots are assumed independent over time index, m . Several formulations of narrowband bandwidth and sampling period may be used to reasonably support this assumption.

2.3.2 General Model

The general model of an N element array with arbitrary sensor positions subject to an incident plane wave is shown in Figure 2.1. The n^{th} element location, specified in Cartesian coordinates, is given as $\mathbf{p}_n = [x_n, y_n, z_n]^T$. The array element outputs resulting from this incident plane wave are described by the array manifold response vector, $\mathbf{v} = ((v_n(\vec{\mathbf{u}})))_n$. For an array of omni-directional sensors, under the narrowband assumption, the effect on the plane wave as it propagates across the array in space is approximated by a phase shift, and the array manifold response vector is $\mathbf{v} = ((\exp(-j\mathbf{k}^T \mathbf{p}_n)))_n = ((\exp(j\frac{2\pi}{\lambda} \vec{\mathbf{u}}^T \mathbf{p}_n)))_n$. Each array element is sampled simultaneously at time index m to produce a snapshot, $\mathbf{x}_m \in \mathbb{C}^N$, where the elements of the snapshot vector are the individual sensor outputs, $\mathbf{x}_m = ((x_n(m)))_n$. There are M snapshots available for processing.

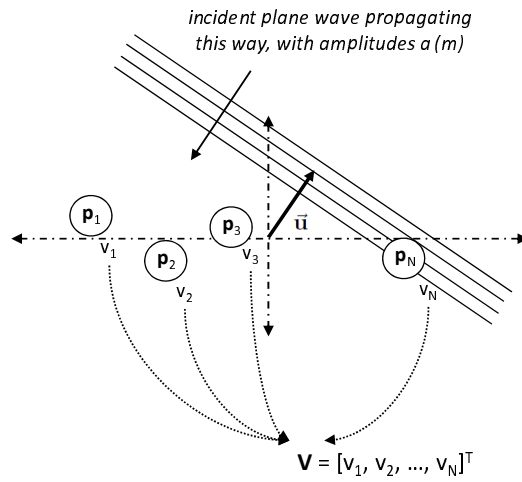


Figure 2.1: **Plane wave impinging on an arbitrary array:** The plane wave propagates with wavenumber, \mathbf{k} , opposite to unit directional vector, $\vec{\mathbf{u}}$, and impinges on an arbitrary array. Under the narrowband assumption, the effect on the plane wave as it propagates across the array in space is approximated by a phase shift. This is described by the array manifold response vector, $\mathbf{v} = ((\exp(j\frac{2\pi}{\lambda}\vec{\mathbf{u}}^T \mathbf{p}_n)))_n$.

We want to consider the output of the array observing a space-time process. The snapshot model consists of three terms and is given by

$$\mathbf{x}_m = \sum_{k=1}^K \mathbf{v}_k a_k(m) + \mathbf{n}_{b,m} + \mathbf{n}_{w,m} \quad (2.1)$$

Each of the individual terms are described as follows. The space-time process may consist of two types of sources. The first type corresponds to point sources in the environment. These arrival as discrete plane waves at the array. We assume K such sources exist. Each source has a given direction of arrival, $\vec{\mathbf{u}}_k$, with corresponding array manifold response vector, \mathbf{v}_k , as well as a source amplitude at each sampling instant, $a_k(m)$. Combining the array manifold responses, $\mathbf{V} = [\mathbf{v}_1, \mathbf{v}_2, \dots, \mathbf{v}_K]$, and point source amplitudes, $\mathbf{a}_m = ((a_k(m)))_k$, we can write (2.1) more succinctly as

$$\mathbf{x}_m = \mathbf{V}\mathbf{a}_m + \mathbf{n}_{b,m} + \mathbf{n}_{w,m} \quad (2.2)$$

Going forward we will assume that the discrete source amplitudes, \mathbf{a}_m , are *i.i.d.* $\mathbf{a}_m \xrightarrow{d} CN_K(\mathbf{0}, \mathbf{R}_a)$. This is standard model for passive sonar reception of far field discrete sources. The point sources may be correlated with each other or not. Specifying this attribute is a distinguishing feature between models. For a spatially stationary space-time process, the sources are uncorrelated by definition and $\mathbf{R}_a = \text{diag}(\sigma_1^2, \sigma_2^2, \dots, \sigma_K^2)$.

The second component of the space-time process is the background or environmental noise. This noise is spread spatially, and has a smooth, continuous distribution across some region of angle of arrival to the array. The background noise at each snapshot, $\mathbf{n}_{b,m}$, is *i.i.d.* $\mathbf{n}_{b,m} \xrightarrow{d} CN_N(\mathbf{0}, \mathbf{R}_b)$, and is uncorrelated with the discrete components of the process.

Each sensor also produces an internal noise, uncorrelated with the other sensors and also independent across snapshots. This noise is modeled as $\mathbf{n}_{w,m} \xrightarrow{d} CN_N(\mathbf{0}, \sigma_w^2 \mathbf{I})$. The sensor noise is uncorrelated with either component of the space-time process.

Because it is a linear combination of uncorrelated, zero mean, complex Gaussian random vectors, the snapshot \mathbf{x}_m is a zero mean complex Gaussian random vector. It is distributed as

$$\mathbf{x}_m \stackrel{d}{\rightarrow} CN_N(\mathbf{0}, \mathbf{R}_x), \quad \mathbf{R}_x = \mathbf{V}\mathbf{R}_a\mathbf{V}^H + \mathbf{R}_b + \sigma_w^2\mathbf{I} \quad (2.3)$$

Eqn. (2.3) is the general plane waves in non-white noise model, and can represent line component, continuous, or mixed spectra type of processes.

2.4 Space-Time Random Processes

This section begins with a review of the 2^{nd} order characterization of WSS space-time random processes. These characterizations are all that is necessary to develop minimum variance linear array processors, and additionally, for the class of Gaussian space-time processes provide complete specification the process. We review the relationships between covariance and frequency-wavenumber spectrum. Under the assumptions stated in Section 2.3.1, the process can additionally be described as the sum of uncorrelated plane waves allocated according to a distribution across all angles of arrival to the array. The relationship of the covariance to this model is also given.

This is followed with a review of the Cramér spectral representation, which provides a description of a stochastic process in terms of an orthogonal process in the transform domain. We review this concept for several reasons. First, the spectral representation can be used to develop the more familiar second order characterizations for the process and their relationships, rather than by stated definition. Second, from the spectral representation it becomes clear how a process may be characterized by one of the following: i) a smooth, continuous power spectral density, ii) a discrete (or line component) spectrum, or iii) a *mixed spectrum*, containing both smooth and line components. This formulation is fundamental to developing techniques to deal with mixed spectrum when they are encountered, which we will see in later chapters is essential for good adaptive beamformer performance.

Finally, while there are multiple methods for introducing the multitaper spectral estimator, Thomson's original formulation [52], reviewed in Section 2.6, is developed from the spectral representation.

2.4.1 2^{nd} Order Characterization of Space-Time Random Processes

The zero mean, WSS complex space-time process, $\{f(t, \mathbf{p})\}$, is defined for $-\infty < t < \infty$, and over some dimensionality of Cartesian space, \mathbb{R}^C , typically \mathbb{R}^3 so that $\mathbf{p} = [p_x, p_y, p_z]^T$. The following relationships define the important 2^{nd} order central moments of the process [1].

2^{nd} Order Characterizations

The space-time covariance between two points $\Delta\mathbf{p} = \mathbf{p}_1 - \mathbf{p}_2$ and times $\tau = t_1 - t_2$ is defined as

$$R_f(\tau, \Delta\mathbf{p}) = E \{ f(t, \mathbf{p}) f^*(t - \tau, \mathbf{p} - \Delta\mathbf{p}) \} \quad (2.4)$$

The temporal frequency spectrum-spatial correlation function, also referred to as the cross spectral density, is related to $R_f(\tau, \Delta\mathbf{p})$ by the Fourier transform of the time lag variable.

$$S_f(\omega, \Delta\mathbf{p}) = \int_{-\infty}^{\infty} R_f(\tau, \Delta\mathbf{p}) e^{-j\omega\tau} d\tau \quad (2.5)$$

The frequency-wavenumber spectrum is related to $S_f(\omega, \Delta\mathbf{p})$ by Fourier transform of the Cartesian spatial coordinate, $\Delta\mathbf{p}$, with note of the reverse sign convention of the complex exponential. The wavenumber vector, \mathbf{k} , has dimension C , similar to $\Delta\mathbf{p}$.

$$P_f(\omega, \mathbf{k}) = \int \cdots \int_{\mathbb{R}^C} S_f(\omega, \Delta\mathbf{p}) e^{j\mathbf{k}^T \Delta\mathbf{p}} d\Delta\mathbf{p} \quad (2.6)$$

Because of the Fourier transform pair relationships, the following inverse transforms may also be used.

$$R_f(\tau, \Delta \mathbf{p}) = (2\pi)^{-1} \int_{-\infty}^{\infty} S_f(\omega, \Delta \mathbf{p}) e^{j\omega\tau} d\omega \quad (2.7)$$

$$S_f(\omega, \Delta \mathbf{p}) = (2\pi)^{-C} \int \dots \int_{\mathbb{R}^C} P_f(\omega, \mathbf{k}) e^{-j\mathbf{k}^T \Delta \mathbf{p}} d\mathbf{k} \quad (2.8)$$

$$R_f(\tau, \Delta \mathbf{p}) = (2\pi)^{-1} (2\pi)^{-C} \int_{-\infty}^{\infty} e^{j\omega\tau} d\omega \int \dots \int_{\mathbb{R}^C} P_f(\omega, \mathbf{k}) e^{-j\mathbf{k}^T \Delta \mathbf{p}} d\mathbf{k} \quad (2.9)$$

We now look at specializing these results for the narrowband, independent snapshot model. For a narrowband, or monochromatic process at ω_o , we may write formally $P_f(\omega, \mathbf{k}) = P_f(\mathbf{k}) \cdot 2\pi\delta(\omega - \omega_o)$. This simplifies the relationship between the covariance and frequency-wavenumber spectrum.

$$R_f(\tau, \Delta \mathbf{p}) = (2\pi)^{-C} e^{j\omega_o\tau} \int \dots \int_{\mathbb{R}^C} P_f(\mathbf{k}) e^{-j\mathbf{k}^T \Delta \mathbf{p}} d\mathbf{k} \quad (2.10)$$

Further, under the assumption of independent snapshots the covariance is zero for $\tau \neq 0$, further simplifying the relationship to

$$R_f(\Delta \mathbf{p}) \equiv R_f(0, \Delta \mathbf{p}) = (2\pi)^{-C} \int \dots \int_{\mathbb{R}^C} P_f(\mathbf{k}) e^{-j\mathbf{k}^T \Delta \mathbf{p}} d\mathbf{k} \quad (2.11)$$

This shows that the narrowband, independent snapshot problem is principally a spatial problem, the temporal related aspects are not considered.

Matrix Representation

Consider an N element array of omni-directional sensors at locations \mathbf{p}_n , $n = 1, 2, \dots$, observing the process $\{f(t, \mathbf{p})\}$. The covariance matrix for the array outputs, ignoring any sensor noise component, is the matrix consisting of elements

$$\mathbf{R}_f = ((R_f(\mathbf{p}_r - \mathbf{p}_c)))_{r,c} \quad (2.12)$$

which can be expressed in matrix form succinctly using the frequency-wavenumber spectrum and array manifold response vector, $\mathbf{v}(\mathbf{k})$.

$$\mathbf{R}_f = (2\pi)^{-C} \int \dots \int_{\mathbb{R}^C} P_f(\mathbf{k}) \mathbf{v}(\mathbf{k}) \mathbf{v}^H(\mathbf{k}) d\mathbf{k} \quad (2.13)$$

Directional Distribution of Plane Waves

The space-time process may also be interpreted another way. The wavenumber restriction, $|\mathbf{k}| = 2\pi/\lambda$, implies that plane waves observed by the array must correspond to angles of arrival that may physically propagate to the array, i.e., $0 \leq \theta \leq \pi$ and $0 \leq \phi \leq 2\pi$ as shown in spherical coordinates in Figure 2.2 (following Van Trees [1], Figure 2.1). The stationary space-time process in this case may be modeled as the sum of uncorrelated plane waves, that are distributed according to a directional distribution, $G_f(\omega, \theta, \phi)$, across all angles of arrival to the array. $G_f(\omega, \theta, \phi)$ is similar to a probability density, and

$$\frac{1}{4\pi} \int_0^\pi \int_0^{2\pi} G_f(\omega, \theta, \phi) \sin \theta d\theta d\phi = 1 \quad (2.14)$$

Cox demonstrated the process for relating the covariance to the directional distribution [54]. Consider two sensors in the field at locations \mathbf{p}_1 , \mathbf{p}_2 . Each sensor has a respective frequency and directional response, $H_i(\omega, \theta, \phi)$, $i = 1, 2$. The difference in position, $\Delta\mathbf{p} = \mathbf{p}_1 - \mathbf{p}_2$, can be described in Cartesian or spherical coordinates.

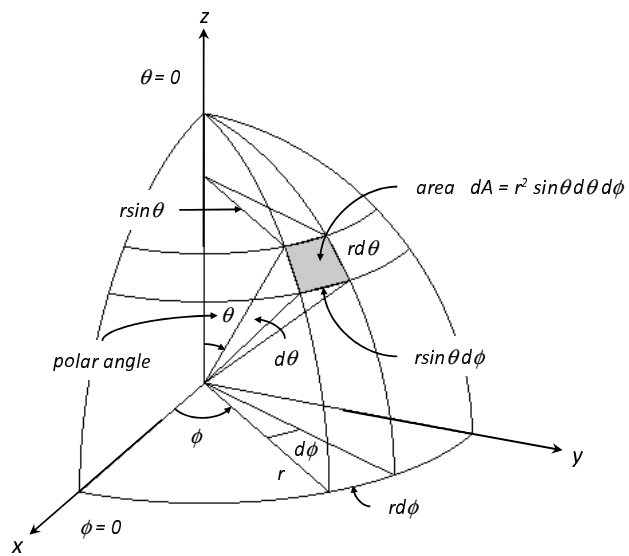


Figure 2.2: **Spherical coordinate system:** The spherical coordinate system is convenient for describing a space-time process by its directional distribution of uncorrelated plane wave components in azimuth and elevation [54].

$$\Delta \mathbf{p} = \mathbf{p}_1 - \mathbf{p}_2 = \begin{cases} [\Delta p_x, \Delta p_y, \Delta p_z]^T \\ [s \sin \gamma \cos \zeta, s \sin \gamma \sin \zeta, s \cos \gamma]^T \end{cases} \quad (2.15)$$

The cross-spectral density between the two sensors is expressed in spherical coordinates as

$$\begin{aligned} S_f(\omega, s, \gamma, \zeta) &= (4\pi)^{-1} S_f(\omega) \int_{-\pi}^{\pi} \int_0^{\pi} G_f(\omega, \theta, \phi) H_1(\omega, \theta, \phi) H_2^*(\omega, \theta, \phi) \\ &\times \exp\left(j \frac{\omega s}{c} [\sin \theta \sin \gamma \cos(\phi - \zeta) + \cos \theta \cos \gamma]\right) \sin(\theta) d\theta d\phi \end{aligned} \quad (2.16)$$

The function $S_f(\omega)$ in front of the integral translates the relative levels specified by the directional distribution, $G_f(\cdot)$, to the absolute levels observed at the array. The cross-spectral density and space-time covariance are a Fourier transform pair.

$$R_f(\tau, s, \gamma, \zeta) = \frac{1}{2\pi} \int_{-\infty}^{\infty} S_f(\omega, s, \gamma, \zeta) \exp(j\omega\tau) d\omega \quad (2.17)$$

For a narrowband process, we have $S_f(\omega, s, \gamma, \zeta) = S_f(s, \gamma, \zeta) \cdot 2\pi\delta(\omega - \omega_o)$. Computing the space-time covariance at $\tau = 0$, the covariance and cross spectral density are seen to be the same.

$$\begin{aligned} R_f(0, s, \gamma, \zeta) &= \frac{1}{2\pi} \int_{-\infty}^{\infty} S_f(s, \gamma, \zeta) \cdot 2\pi\delta(\omega - \omega_o) \exp(j\omega\tau) d\omega \\ &= S_f(s, \gamma, \zeta) \end{aligned} \quad (2.18)$$

Using (2.16), (2.18) with $H_i(\omega, \theta, \phi) = 1, i = 1, 2$, the covariance, $R_f(s, \gamma, \zeta)$, between two omnidirectional sensors in a given noise field, $G_f(\omega, \theta, \phi)$, can be found. This is particularly convenient if the noise field has a known form that can be conveniently represented in

spherical or cylindrical harmonics (see Cox [54]). The covariance matrix for an array of sensors is populated by values of this function, where $\Delta \mathbf{p} = \mathbf{p}_r - \mathbf{p}_c$.

$$\mathbf{R}_f = ((R_f(s, \gamma, \zeta))_{r,c}) \quad (2.19)$$

2.4.2 Cramér Spectral Representation

The spectral representation theorem for stationary random processes, due to Cramér [55], provides a mechanism for describing the properties of a WSS temporal or space-time random process in the respective transform domain, e.g., frequency or frequency-wavenumber. With this representation, the quantities of interest for a physically generated process have intuitive interpretation and representation, namely we can relate the distribution of power as a function of frequency (temporal or spatial) to the process. The following sections review the definition and properties of this representation, and show how it can be used to develop the relationships between the more common 2^{nd} order moment characterizations of random processes. We start with WSS temporal random process, as this is simpler notationally. The spectral representation and its properties for the continuous time random process is introduced, followed by the discrete time random process. The relationship between the two types when uniform sampling is applied to a continuous time random processes is presented. Extensions for WSS space-time random processes, in light of the model assumptions, follows. These sections make explicit use of Ω (radians/sec) as the continuous time frequency variable, and ω as the discrete time frequency variable (radians/sample). Further detail on the spectral representation theorem can be found in the references [50, 56–58].

Continuous Time

Let $\{f(t)\}$ be a zero mean, complex-valued stationary random process defined over time $-\infty < t < \infty$. Additionally, let $\{f(t)\}$ be stochastically continuous, a mild regularity condition that holds if and only if the autocorrelation function, $R(\tau)$, is continuous at the origin. Then by the Cramér spectral representation theorem there exists an orthogonal

process, $\{ Z(\Omega) \}$, such that for all t , a realization of the process, $f(t)$, can be expressed as

$$f(t) = \int_{-\infty}^{\infty} e^{j\Omega t} dZ(\Omega) \quad (2.20)$$

where equality is in the mean square sense and (2.20) is a Riemann-Stieljes integral. The orthogonal process is zero mean

$$E \{ dZ(\Omega) \} = 0 \quad (2.21)$$

and its corresponding covariance

$$E \{ dZ(\Omega_1) dZ^*(\Omega_2) \} = \begin{cases} 0 & \Omega_1 \neq \Omega_2 \\ dS^{(I)}(\Omega_1) & \Omega_1 = \Omega_2 \end{cases} \quad (2.22)$$

implies that disjoint frequencies are uncorrelated. The function $S^{(I)}(\Omega)$, known as the *integrated spectrum* of $\{ f(t) \}$, is a bounded, non-decreasing function. If $S^{(I)}(\Omega)$ is differentiable, then we may write

$$\frac{dS^{(I)}(\Omega)}{d\Omega} = S(\Omega) \quad (2.23)$$

and the covariance then becomes

$$E \{ dZ(\Omega) dZ^*(\Omega) \} = S(\Omega) d\Omega \quad (2.24)$$

The function $S(\Omega)$ is referred to as the power spectral density function. The integrated spectrum $S^{(I)}(\Omega)$ plays a role similar to a random variable cumulative distribution function, and many of the results for distribution functions may be applied to it. In analog to the *Lebesgue decomposition theorem* for distribution functions, the integrated spectrum can be

written as consisting of three components

$$S^{(I)}(\Omega) = S_1^{(I)}(\Omega) + S_2^{(I)}(\Omega) + S_3^{(I)}(\Omega) \quad (2.25)$$

- $S_1^{(I)}(\Omega)$ is absolutely continuous, meaning its derivative exists for almost all Ω such that $S^{(I)}(\Omega) = \int_{-\infty}^{\Omega} S(\Omega') d\Omega'$. A process with an integrated spectrum consisting of only this term, $S^{(I)}(\Omega) = S_1^{(I)}(\Omega)$, has a smooth background spectral component. White or colored noise processes (AR, MA, ARMA) are of this type. We refer to this as a process with *purely continuous spectrum*.
- $S_2^{(I)}(\Omega)$ is a step function with jumps of size p_l at frequencies Ω_l , $l = 1, 2, \dots$. A process with an integrated spectrum consisting of only this term, $S^{(I)}(\Omega) = S_2^{(I)}(\Omega)$, has a *purely discrete spectrum* or *line spectrum*. The harmonic random process, $\{f(t)\} = \sum_{l=1}^K A_l e^{j\Theta_l} e^{j\Omega_l t}$, where Θ_l is uniform $[-\pi, \pi]$ and A_l is a real-valued random variable, has this type of spectrum.
- $S_3^{(I)}(\Omega)$ is a continuous singular function. This type of pathologic function is not of practical use for spectral estimation, and we will assume that it is identically equal to 0 from now on.

From this classification of spectra, and the decomposition described by (2.25), we may encounter three types of stationary random processes. First, those with purely continuous spectrum. Second those with purely discrete spectrum. And last, those which are a combination of both types that we will call mixed spectrum processes.

The autocorrelation function, $R(\tau)$, and power spectral density, $S(\Omega)$, of the process can be related through the spectral representation and the properties of the orthogonal process. Starting with the definition of the autocorrelation function

$$R(\tau) = E\{f(t)f^*(t-\tau)\} \quad (2.26)$$

and replace $f(t)$ with its spectral representation (2.20)

$$R(\tau) = \int_{-\infty}^{\infty} e^{j\Omega_1 t} \int_{-\infty}^{\infty} e^{j\Omega_2(\tau-t)t} E \{ dZ(\Omega_1) dZ^*(\Omega_2) \} \quad (2.27)$$

Using the uncorrelated property of the covariance at disjoint frequencies, (2.22), this simplifies to

$$R(\tau) = \int_{-\infty}^{\infty} e^{j\Omega\tau} dS^{(I)}(\Omega) = \int_{-\infty}^{\infty} S(\Omega) e^{j\Omega\tau} d\Omega \quad (2.28)$$

where the well known result of the last integral assumes $S^{(I)}(\Omega)$ is differentiable. Because $R(\tau)$ is an absolutely integrable, deterministic function, (2.28) indicates that $R(\tau)$ and $S(\Omega)$ form a Fourier transform pair, such that

$$S(\Omega) = \frac{1}{2\pi} \int_{-\infty}^{\infty} R(\tau) e^{-j\Omega\tau} d\tau \quad (2.29)$$

Discrete Time

The spectral representation also applies to discrete time random processes, $\{f[n]\}$, with only slight modifications as outlined here. Given a stationary, discrete time random process, $\{f[n]\} - \infty < n < \infty$, a realization the process, $f[n]$, has spectral representation using the orthogonal process, $\{Z(\omega)\}$, given by

$$f[n] = \int_{-\pi}^{\pi} e^{j\omega n} dZ(\omega) \quad (2.30)$$

where equality is in the mean square sense. The limits of integration are restricted to $\pm\pi$ to reflect the unambiguous range of the discrete time frequency. The orthogonal process is zero mean, $E\{dZ(\omega)\} = 0$, with covariance

$$E \{ dZ(\omega_1) dZ^*(\omega_2) \} = \begin{cases} 0 & \omega_1 \neq \omega_2 \\ dS^{(I)}(\omega) & \omega_1 = \omega_2 \end{cases} \quad (2.31)$$

where the bounded, non-decreasing function $S^{(I)}(\omega)$ is the integrated spectrum of $\{f[n]\}$. The covariance implies disjoint frequencies are uncorrelated. If $S^{(I)}(\omega)$ is differentiable, then we may write

$$\frac{dS^{(I)}(\omega)}{d\omega} = S(\omega) \quad (2.32)$$

and the covariance of the increments becomes

$$E \{ dZ(\omega) dZ^*(\omega) \} = S(\omega) d\omega \quad (2.33)$$

The function $S(\omega)$ is referred to as the power spectral density function. Following the same procedure as in the continuous time case, the autocorrelation, $R[l] = E \{ x(n) x^*(n-l) \}$ and integrated spectrum are related via the spectral representation by

$$R[l] = \int_{-\pi}^{\pi} e^{j\omega l} dS^{(I)}(\omega) = \int_{-\pi}^{\pi} S(\omega) e^{j\omega l} d\omega \quad (2.34)$$

where the final familiar expression assumes $S^{(I)}(\omega)$ is differentiable. The power spectral density and autocorrelation form a Fourier transform pair such that

$$S(\omega) = \frac{1}{2\pi} \sum_{l=-\infty}^{\infty} R[l] e^{-j\omega l} \quad (2.35)$$

where equality is in the mean square sense.

Sampling and Aliasing

A sampled WSS continuous time random process $\{f_c(t)\}$, $-\infty < t < \infty$, with uniform sampling period T , produces a WSS discrete random process $\{f_d[n]\}$, $-\infty < n < \infty$. The subscripts c and d are used to reinforce the distinction between the continuous and discrete time domains. As a stationary discrete time random process, $f_d[n] = f_c(t_o + nT)$ has a spectral representation

$$f_d[n] = \frac{1}{2\pi} \int_{-\pi}^{\pi} e^{j\omega n} dZ_d(\omega) \quad (2.36)$$

where the orthogonal process $\{Z_d(\omega)\}$ has the properties outlined in Section 2.4.2. Following Section 2.4.2, the autocorrelation and power spectral density form a Fourier transform pair.

$$R_d[l] = \int_{-\pi}^{\pi} S_d(\omega) e^{j\omega l} d\omega, \quad S_d(\omega) = \frac{1}{2\pi} \sum_{l=-\infty}^{\infty} R_d[l] e^{-j\omega l} \quad (2.37)$$

Now we are interested to relate the discrete time process 2^{nd} order characterizations, $R_d[l]$ and $S_d(\omega)$, to the original continuous time counterparts, $R_c(\tau)$ and $S_c(\Omega)$. The discrete time autocorrelation function samples its continuous time counterpart. This follows directly from its definition

$$\begin{aligned} R_d[l] &= E\{x_d[n]x_d^*[n-l]\} \\ &= E\{x_c(t_o + nT)x_c^*(t_o + nT - lT)\} \\ &= R_c(lT) \end{aligned} \quad (2.38)$$

Two approaches may be taken to determine the form of the discrete time process power spectral density. The first considers both $R_c(\tau)$ and $S_c(\Omega)$ as deterministic functions, and utilizes the properties of the Fourier transform and the continuous time sampling indicated in (2.38) to arrive at

$$S_d(\omega) = \frac{1}{T} \sum_{\beta=-\infty}^{\infty} S_c\left(\frac{\omega - 2\pi\beta}{T}\right), \quad |\omega| \leq \pi \quad (2.39)$$

Details can be found in Oppenheim and Schaffer, problem 11.8 [59]. The second approach utilizes the spectral representation directly to arrive at the same result. Details can be found in Percival and Walden [56].

The relationship in (2.39) can be used to determine requirements on the sampling period, T , such that the resultant discrete spectrum is an accurate representation of the underlying continuous spectrum, i.e., the Nyquist sampling criteria. However, consider an alternate interpretation of (2.39). Even if the Nyquist sampling criteria is not met, using an estimate of the discrete spectrum, although it is an aliased version of the true spectrum, it is possible to determine the correct values for the covariance at the sample points indicated by (2.38). This is clearly insufficient to completely reconstruct the underlying spectrum, but still allows estimation of covariance matrix values necessary for adaptive processing.

In practice only a finite number of samples are available for processing. This is the effect of a finite duration observation window, and has a direct impact on the ability to estimate the discrete spectrum. Thomson dealt with this problem directly in formulation of the multitaper spectral estimator, which is reviewed in Section 2.6.

These concepts may be applied directly to uniform linear array processing problems. For regular arrays, those based on a multiple of a fixed spacing such as minimum redundancy arrays, additional complexity is introduced due to the impact of the equivalent *windowing* function, and its influence in the frequency domain, on the ability to estimate the discrete spectrum. Arbitrary array design also has this issue, and adds potentially unusual spectral combinations due to the non-uniform spacing compared to the uniform structure described

by (2.39).

Continuous Space-Time

The spectral representation extends to the case of a spatially and temporally stationary multidimensional random process, $\{f(t, \mathbf{p})\}$. Given a realization of the process, $f(t, \mathbf{p})$, there exists an orthogonal process, $\{Z(\omega, \mathbf{k})\}$, such that for all t, \mathbf{p}

$$f(t, \mathbf{p}) = \int_{-\infty}^{\infty} \dots \int_{-\infty}^{\infty} e^{j(\omega t - \mathbf{k}^T \mathbf{p})} dZ(\omega, \mathbf{k}) \quad (2.40)$$

The orthogonal process, $\{Z(\omega, \mathbf{k})\}$, is zero mean $E\{dZ(\omega, \mathbf{k})\} = 0$, and uncorrelated across disjoint frequency-wavenumber bands.

$$E\{dZ(\omega_1, \mathbf{k}_2)dZ^*(\omega_3, \mathbf{k}_4)\} = \begin{cases} 0 & (\omega_1, \mathbf{k}_2) \cap (\omega_3, \mathbf{k}_4) = 0 \\ P(\omega, \mathbf{k}) d\omega d\mathbf{k} & \omega_1 = \omega_2, \mathbf{k}_2 = \mathbf{k}_4 \end{cases} \quad (2.41)$$

where we have assumed that the integrated frequency-wavenumber spectrum, $P_x^{(I)}(\omega, \mathbf{k})$, is differentiable.

The relationships between covariance, cross spectral density, and frequency-wavenumber spectrum, stated earlier in Section 2.4.1, may be derived from the multidimensional spectral representation in (2.40).

Directional Distribution of Plane Waves

As an alternative to the frequency-wavenumber domain in (2.40), one may define the orthogonal process across all angles of arrival on a sphere [1, 50, 54].

$$dZ(\omega_o, \mathbf{p}) = \frac{1}{4\pi} \int_0^\pi \sin \theta d\theta \int_0^{2\pi} e^{-jk_o \mathbf{a}_r^T(\theta, \phi) \mathbf{p}} dZ(\omega_o, \theta, \phi) \quad (2.42)$$

where

$$f(t, \mathbf{p}) = \int_{-\infty}^{\infty} e^{j\omega t} dZ(\omega_o, \mathbf{p}) \quad (2.43)$$

with $k_o = 2\pi/\lambda$, and $\mathbf{a}_r(\theta, \phi)$ is a unit vector in the radial direction. The orthogonal process, $\{dZ(\omega_o, \theta, \phi)\}$, defines an integrated spectrum, $S(\omega)G^{(I)}(\omega, \theta, \phi)$, where we have used $G(\cdot)$ to be consistent with Section 2.4.1 and the function $S(\omega)$ scales the relative levels defined in $G(\cdot)$ to the absolute levels seen at the array. Assuming $G^{(I)}(\omega, \theta, \phi)$ is differentiable

$$E\{dZ(\omega_1, \theta_1, \phi_1)dZ^*(\omega_2, \theta_2, \phi_2)\} = \begin{cases} 0 & \theta_1 \neq \theta_2 \\ 0 & \phi_1 \neq \phi_2 \\ 0 & \omega_1 \neq \omega_2 \\ S(\omega)G(\omega, \theta, \phi)\frac{2\pi}{\sin\theta}d\omega & \theta_1 = \theta_2 \\ & \phi_1 = \phi_2 \\ & \omega_1 = \omega_2 \end{cases} \quad (2.44)$$

The cross spectral density is defined by

$$E\{dZ(\omega_o, \mathbf{p})dZ^*(\omega_o, \mathbf{p} - \Delta\mathbf{p})\} = S_f(\omega_o, \Delta\mathbf{p})\frac{d\omega}{2\pi} \quad (2.45)$$

Relating (2.45) to (2.42), and using (2.44) we have

$$S_f(\omega_o, \Delta\mathbf{p}) = \frac{1}{4\pi}S(\omega) \int_{-\pi}^{\pi} \int_0^{\pi} G_f(\omega, \theta, \phi) e^{-jk_o\mathbf{a}_r^T(\theta, \phi)\Delta\mathbf{p}} \sin(\theta)d\theta d\phi \quad (2.46)$$

One may compare this to the earlier expression (2.16), which also included directional response of the individual sensor elements and expanded the $\mathbf{a}_r^T \Delta \mathbf{p}$ terms in spherical coordinates. By defining the directional distribution, $G_f(\omega, \theta, \phi)$, and requiring disjoint regions in angle space to be uncorrelated (2.44) this shows how the spectral representation underlies the model of the stationary space-time process as the sum of uncorrelated plane waves distributed over all directions of arrival to the array.

2.5 Optimal Beamforming

This section reviews optimal beamforming techniques given observation of the interference and noise environment, and the related problem when the desired signal is also present in the data. The normalized SINR loss metric is a measure of the decrease in output SINR of an implemented beamformer compared to an optimal processor. The metric is frequently used to assess the performance of a given adaptive beamforming algorithm. This metric and its general application are reviewed.

2.5.1 Minimum Variance Distortionless Response (MVDR)

Given the series of snapshots, $\mathbf{x}_m \in \mathbb{C}^N$ with $E\{\mathbf{x}_m \mathbf{x}_m^H\} = \mathbf{R}_x$, the adaptive processor uses a weighted linear combination of the sensor outputs to produce the scalar output signal

$$y_m = \mathbf{w}^H \mathbf{x}_m \quad (2.47)$$

The processor should pass the desired direction of arrival, specified with steering vector \mathbf{s} , undistorted. This constraint is expressed

$$\mathbf{w}^H \mathbf{s} = 1 \quad (2.48)$$

The expected output power of the processor is

$$E \left\{ |y_m|^2 \right\} = E \left\{ | \mathbf{w}^H \mathbf{x}_m |^2 \right\} = \mathbf{w}^H \mathbf{R}_x \mathbf{w} \quad (2.49)$$

The design criteria is to minimize the expected output power, subject to the distortionless constraint. It can be shown that this design criteria is the same as maximizing the output SINR [1]. The optimization problem is then

$$\arg \min_{\mathbf{w}} \mathbf{w}^H \mathbf{R}_x \mathbf{w} \quad \text{s.t.} \quad \mathbf{w}^H \mathbf{s} = 1 \quad (2.50)$$

Using the method of Lagrange multipliers [60], the constrained cost function to be minimized is then

$$J(\mathbf{w}) = \mathbf{w}^H \mathbf{R}_x \mathbf{w} + \lambda (\mathbf{w}^H \mathbf{s} - 1) + \lambda^* (\mathbf{s}^H \mathbf{w} - 1) \quad (2.51)$$

The cost function is quadratic in \mathbf{w} . Taking the complex gradient with respect to \mathbf{w} , and setting to zero

$$\left. \frac{\partial J(\mathbf{w})}{\partial \mathbf{w}^*} = \mathbf{R}_x \mathbf{w} + \lambda \mathbf{s} = 0 \right|_{\mathbf{w}=\mathbf{w}_{opt}} \quad (2.52)$$

the optimal set of weights is

$$\mathbf{w}_{opt} = -\lambda \mathbf{R}_x^{-1} \mathbf{s} \quad (2.53)$$

Using (2.53) in (2.48) to solve for the Lagrange multiplier, we have $\lambda = -(\mathbf{s}^H \mathbf{R}_x \mathbf{s})^{-1}$, and combining the two produces the final weight vector

$$\mathbf{w}_{opt} = \frac{\mathbf{R}_x^{-1} \mathbf{s}}{\mathbf{s}^H \mathbf{R}_x^{-1} \mathbf{s}} \quad (2.54)$$

When the snapshot data used to estimate \mathbf{R}_x contains only the noise and interference environment, this processor is referred to as minimum variance distortionless response (MVDR). In the event the desired signal is also present in the snapshot data, the same solution for the weight vector results, but is sometimes referred to as minimum power distortionless response (MPDR) to indicate the difference in the observed data [1]. In practice, the distinction makes a significant difference in terms of the required snapshot support to achieve good performance [30].

2.5.2 Normalized SINR Loss

For cases involving uncorrelated signal and interference, the standard metric for performance of an adaptive beamformer is degradation in the output signal to interferer and noise ratio (SINR) compared to that obtainable with an optimal processor [29]. The normalized SINR loss, ξ , is defined as

$$\xi = \frac{SINR_a}{SINR_o} \quad (2.55)$$

The subscript o represents true quantities or optimal values, while the subscript a represents the actual or estimated values. For convenience, normalized SINR loss can be expressed on a dB scale, as $\xi_{dB} = -10 \log_{10}(\xi)$. In this way, $\xi_{dB} = 1$ implies an output SINR that is 1 dB lower than obtainable by an optimal processor. For the optimal processor, SINR is computed as

$$SINR_o = \frac{|\mathbf{w}_o^H \mathbf{s}|^2}{\mathbf{w}_o^H \mathbf{R}_o \mathbf{w}_o} \quad (2.56)$$

while for an implemented processor, SINR is computed as

$$SINR_a = \frac{|\mathbf{w}_a^H \mathbf{s}|^2}{\mathbf{w}_a^H \mathbf{R}_o \mathbf{w}_a} \quad (2.57)$$

The general expression for ξ , not assuming a particular form for the weights, is therefore

$$\xi = \frac{|\mathbf{w}_a^H \mathbf{s}|^2}{\mathbf{w}_a^H \mathbf{R}_o \mathbf{w}_a} \cdot \frac{\mathbf{w}_o^H \mathbf{R}_o \mathbf{w}_o}{|\mathbf{w}_o^H \mathbf{s}|^2} \quad (2.58)$$

We consider adaptive beamformers with weights designed using the minimum variance distortionless response (MVDR) criteria. Using (2.54) in (2.56), the SINR for the optimal processor is

$$SINR_o = \mathbf{s}^H \mathbf{R}_o^{-1} \mathbf{s} \quad (2.59)$$

while using (2.54) in (2.57) yields the SINR for an implemented processor

$$SINR_a = \frac{(\mathbf{s}^H \mathbf{R}_a^{-1} \mathbf{s}) (\mathbf{s}^H \mathbf{R}_a^{-1} \mathbf{s})}{\mathbf{s}^H \mathbf{R}_a^{-1} \mathbf{R}_o \mathbf{R}_a^{-1} \mathbf{s}} \quad (2.60)$$

Using (2.59) and (2.60) in (2.55), the expression for ξ becomes

$$\xi = \frac{\mathbf{s}^H \mathbf{R}_a^{-1} \mathbf{s}}{\mathbf{s}^H \mathbf{R}_o^{-1} \mathbf{s}} \cdot \frac{\mathbf{s}^H \mathbf{R}_a^{-1} \mathbf{s}}{\mathbf{s}^H \mathbf{R}_a^{-1} \mathbf{R}_o \mathbf{R}_a^{-1} \mathbf{s}} \quad (2.61)$$

This is a general expression for ξ when the beamformer weights are found via MVDR, but doesn't give any insight into performance as it relates to the quantities estimated for the underlying model. The matrix inverse operations also make it difficult to follow directly how model parameters influence the performance, except under some simplifying assumptions.

2.6 Spectral Estimation Techniques

This thesis investigates estimation of covariance for adaptive beamforming by first estimating the spatial or wavenumber spectrum. Clearly, techniques that require an estimate of the covariance a priori, such as Capon's MVDR [6] or MUSIC [61], are not usable for this

purpose. Two main techniques for spectral estimation based upon the data are reviewed briefly in this section. First, the classical windowed, averaged periodogram is a standard non-parametric technique that has efficient computation and ease of analysis related to the adaptive processor performance that will be carried out in Chapter 3. This is preferable to other parametric methods, or model based techniques, even though they may perform better in some scenarios. The section concludes with a review of Thomson's multitaper spectral estimation, in some ways a generalization of the classical windowed techniques. This algorithm provides benefits in terms of minimal data support, incorporation of harmonic analysis to deal with mixed spectrum processes, and can be extended to work with irregular sampled data.

2.6.1 Classical (nonparametric) Spectral Estimation

The windowed, averaged periodogram [59,62] is a standard technique for spectral estimation for uniform sampled data series. By applying a predetermined fixed window function or *taper*, $\mathbf{w} = ((w[n]))_n$, to the data the behavior of the spectral estimate can be controlled with regard to frequency resolution and spectral leakage, e.g., sidelobe suppression. These quantities must be traded off against each other. Performance aspects of well known window functions has been long established [63].

For simplicity, we assume a single dimension time series or uniform linear array processing. For either the time series or array processing problem the procedure is identical once the snapshots have been established. Time series processing typically considers a contiguous collection of N_{TOTAL} samples. This collection is then subdivided into M snapshots of N samples each. Within the time series the snapshots may be specified such that there is overlap of samples between adjacent snapshots. For the array processing application, each snapshot represents the simultaneous sampling of each of the N array elements. In either application, once obtained, each snapshot, \mathbf{x}_m , is multiplied element by element with the windowing function, $w[n]$.

$$\mathbf{y}_m = ((x_m[n]w[n]))_n = \mathbf{x}_m \odot \mathbf{w} \quad (2.62)$$

where \odot is the element by element, or Hadamard product. This windowed snapshot data is then Fourier transformed, typically using efficient FFT algorithms

$$Y_m[l] = \sum_{n=0}^{N-1} y_m[n] \exp\left(-j \frac{2\pi ln}{N_{FFT}}\right), \quad l = 0, 1, \dots, L-1 \quad (2.63)$$

The value of N_{FFT} may be selected to more finely sample the underlying spectrum, e.g., zero-padding, but the fundamental “resolution” of the transform is constant based on the amount of available samples, N . The final estimated spectrum is the averaged, magnitude squared of the outputs of (2.63)

$$\hat{P}[l] = \frac{1}{M} \sum_{m=1}^M |Y_m[l]|^2 \quad (2.64)$$

We reference the frequency domain as the transform domain of the time series, although for array processing the wavenumber is the spatial frequency, and once normalized by their respective sample period or sensor separation the two are equivalent. The averaged, modified periodogram processing shown here using the FFT provides a fixed resolution and sidelobe (leakage) performance across the frequency domain, based on the characteristics of the selected window. The array problem encounters the non-linear mapping between physical angle of arrival and wavenumber. If a fixed response across angle space is desired, the window function will necessarily become a function of angle of arrival, or $\mathbf{w}_l = ((w_l[n]))_n$, such that (2.63) becomes

$$Y_m[l] = \sum_{n=0}^{N-1} w_l[n] x_m[n] \exp\left(-j \frac{2\pi ln}{N_{FFT}}\right), \quad l = 0, 1, \dots, N_{FFT}-1 \quad (2.65)$$

2.6.2 Multitaper Spectral Estimation (MTSE)

The multitaper algorithm, originally developed by Thomson [52], formulates the spectral estimation problem as one of estimating the second order moments of the spectral representation of the process. This section reviews the important concepts for MTSE, and some of the details in its implementation for this dissertation. More thorough treatment can be found in the seminal work [52], as well as [56]. Development of spectral estimation as an averaged power measurement behind a filter bank has a good engineering intuition to it, and consideration of MTSE as a multi-rank estimator of this type can be found in [64, 65]. While intuitive, this approach loses some of the depth of Thomson’s work in terms of the underlying spectral representation, harmonic analysis, and the ability to adaptively combine the multiple spectral estimates to minimize local and broadband bias. The original work was in consideration of uniform sampled time series, which we follow here. Application of the method to uniform linear array processing in wavenumber space is immediate. For arbitrary array geometries, or operation in angle space, the concepts are the same and require only a specialized multitaper design [66], and more computationally intensive processing.

Fundamental Problem of Spectral Estimation

This review follows [52], where for clarity the temporal “centering” term, $e^{j(N-1)/2}$, has been omitted, and the relationships are shown for $M > 1$ available snapshots. Given the stationary discrete random process, $\{x[n]\}$, $-\infty < n < \infty$, we know from Section 2.4.2 that a realization of the process, $x[n]$, has spectral representation

$$x[n] = \int_{-1/2}^{1/2} e^{j2\pi fn} dZ(f) \quad (2.66)$$

where the covariance of the orthogonal increment process defines the power spectral density.

$$E\{dZ(f)dZ^*(f)\} = S(f)df \quad (2.67)$$

The problem of spectral estimation is to estimate the covariance of this process. However, $dZ(f)$ is not observable directly from the available, limited samples $x[n]$, $0 \leq n < N$. While the impact of this data limiting operation, or projection onto a finite number of samples, is obvious in the time domain its effect on the spectral representation of the process is less immediate. Taking the Fourier transform of the samples

$$y(f) = \sum_{n=0}^{N-1} x[n] e^{-j2\pi fn} \quad (2.68)$$

and inserting (2.66) into (2.68) gives what Thomson refers to as the fundamental equation of spectral estimation

$$y(f) = \int_{-1/2}^{1/2} \frac{\sin N\pi(f-v)}{\sin \pi(f-v)} dZ(v) \quad (2.69)$$

This result is a linear Fredholm integral equation of the 1st kind, and cannot be solved explicitly for $dZ(v)$. This is inline with our inability to reconstruct the entire realization of the process, $x[n]$, $-\infty < n < \infty$, from the limited sample observation. Eqn. (2.69) can be solved approximately, for a local region $(f_o - W, f_o + W)$ using an eigenfunction expansion of the kernel $\frac{\sin N\pi(v)}{\sin \pi(v)}$ and a local least squares error criterion. The eigenfunction equation is given by

$$\lambda_d(N, W) Q_d(N, W, f) = \int_{-W}^W \frac{\sin N\pi(v)}{\sin \pi(v)} Q_d(N, W, v) \quad (2.70)$$

where $0 < W < 1/2$ is a design choice and N is the number of available samples. There are N solutions to (2.70), indexed by the subscript d . The eigenvalues, $0 < \lambda_d(N, W) < 1$, give a measure of the concentration of the eigenfunction $Q_d(N, W, f)$ within the desired region, $[-W, W]$. For this particular problem, the solutions to (2.70) are known. The

$Q_d(N, W, f)$ are the discrete prolate spheroidal wave functions (DPSWF), which are related to $q_d(N, W, n)$, the discrete prolate spheroidal sequences (DPSS) by the Fourier transform

$$Q_d(N, W, f) = \epsilon_d \sum_{n=0}^{N-1} q_d(N, W, n) e^{-j2\pi fn} \quad (2.71)$$

where $\epsilon_d = 1$ for d even, j for d odd. These sequences are also known as the Slepian sequences. From Slepian [67], there are approximately $2NW$ significant eigenvalues for these functions. Defining the Fourier transform of the windowed samples, $y_m^{(d)}(f)$, as the d^{th} eigencoefficients of the data

$$y_m^{(d)}(f) = \sum_{n=0}^{N-1} \frac{1}{\epsilon_d} q_d(N, W, n) x_m[n] e^{-j2\pi fn} \quad (2.72)$$

The d^{th} eigenspectra, $\hat{S}_d(f)$, is computed by averaging the magnitude squared of $y_m^{(d)}(f)$ over all snapshots

$$\hat{S}_d(f) = \frac{1}{M} \sum_{m=1}^M \left| y_m^{(d)}(f) \right|^2 \quad (2.73)$$

Due to the orthogonality of $Q_d(N, W, f)$ over the interval $[-W, W]$, for locally near flat spectra the eigenspectra are approximately uncorrelated. By averaging them the overall variance of the final estimate is improved. Before considering the best method for combining the eigenspectra, one might be interested to use all N available eigenfunctions to improve the variance by increased averaging. The next section looks at why this is not recommended.

Looking at Multiple Tapers

To develop a better understanding of the difference between using a multitaper technique and a single taper classical technique consider a simple example illustrated in Figure 2.3. For a single snapshot of $N = 64$ samples, the example considers three approaches to estimating the spectrum using a windowed technique. Averaging multiple, uncorrelated estimates improves estimation accuracy. This can be accomplished using 4 non-overlapping Hann windows as illustrated in the top left in the Figure. Alternatively, a multitaper design also develops 4 overlapping, but orthogonal windows as shown on the top right. Both achieve the same improvement due to averaging uncorrelated estimates, but visually one would expect the multitaper design to perform better overall as it incorporates more of the sample data in each estimate. Looking at the lower plot in the Figure showing the magnitude squared of the equivalent window transfer function, the multitaper approach (shown in blue) has better frequency resolution than the non-overlapped Hann design (shown in red). In order to improve the resolution using the Hann window one may increase the length of the window, at the expense of providing fewer uncorrelated estimates. In the extreme, a single Hann window (shown in magenta) has better resolution than the multitaper but achieves no improvement due to averaging. Alternate formulations of the Hann based approach exist, such as 50% overlap, etc., but in general the multitaper has the best performance in terms of frequency resolution and overall improvement in variance due to averaging [68].

There is a limit to the number of tapers that may be applied meaningfully, based on N and the W selected. The rule of thumb established is that there are $2NW$ significant eigenvalues (sometimes more conservatively estimated as $2NW - 1$), indicating $2NW$ tapers are highly concentrated in the region $[-W, W]$. Continuing the example of Figure 2.3, Figure 2.4 shows the magnitude squared of the DPSWF for the six largest eigenvalues. In this example, W (shown as the red dash-dot line) is selected so that $2NW = 4$. The first four eigenfunctions have a mainlobe concentrated largely within $[-W, W]$, but for higher numbered windows the main lobe is mostly outside the desired region, and the sidelobe level has increased substantially. What this implies is that power estimates based

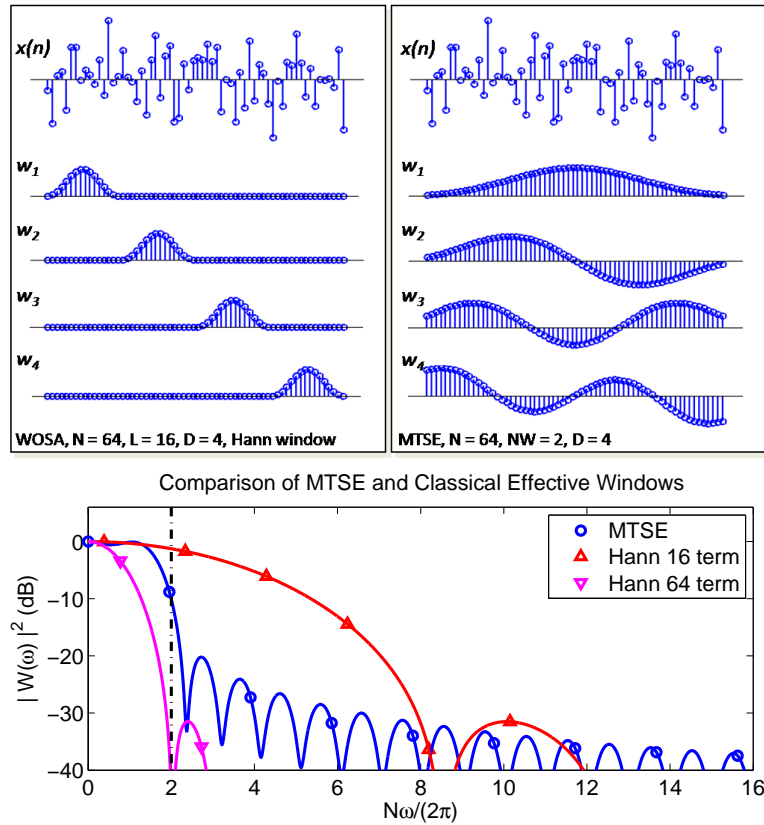


Figure 2.3: **Comparison of resolution for multitaper spectral estimation:** The general form of multi-taper spectral estimation also encompasses traditional weighted overlapped, segment averaged (WOSA) techniques. The upper left plot shows a time series divided into four nonoverlapping segments using a Hann window. The upper right shows the same time series with four orthogonal multitaper windows. Both provide an improvement in estimate variance via averaging by a factor of 4, but the windows on the right use all the sample data in each estimate. Also, as seen in the lower plot, the frequency resolution is improved compared to the four Hann window approach. A single Hann window has better resolution, but does not achieve any averaging.

on these windows are heavily influenced by frequency content outside the area of interest. Thomson referred to this type of effect as the broad band bias. This type of influence is undesirable, in particular for high dynamic range non-flat spectra. Limiting the number of employed windows such that $D \leq 2NW$ provides some robustness against broad band bias automatically. This can also be improved by appropriate combining of the individual eigenspectra as discussed in the next section.

Combining Eigenspectra

With N given, and W and D specified, the multitaper method computes the individual eigenspectra, $\hat{S}_d(f)$, using (2.73). For an assumed flat spectrum there is a fixed optimal weighting scheme for combining the individual $\hat{S}_d(f)$, however, this is of limited use. If one had a priori knowledge that the spectrum was white, altogether different estimation techniques could be applied [51]. For non-flat spectrum, adaptive weighting schemes have been developed to minimize the contribution of broadband bias while maintaining estimation accuracy. Defining the eigenspectra weighting function as $h_d(f)$, an iterative method for determining $h_d(f)$ for non-white noise that is optimal in mean-squared error sense is given by Percival and Walden [56]. Begin with an initial estimate of the spectrum, $\hat{S}_f^{(0)}(f)$, using the flat spectrum fixed weighting

$$\hat{S}_f^{(0)}(f) = \frac{\sum_{d=1}^D \lambda_d \hat{S}_d(f)}{\sum_{d=1}^D \lambda_d} \quad (2.74)$$

where the superscript indexing is introduced to indicate the appropriate iteration. Estimating the variance of the process as $\sigma^2 = \int_{-1/2}^{1/2} \hat{S}_f^{(0)}(f) df$, the following iterative procedure is carried out.

$$h_d^{(n)}(f) = \frac{\hat{S}_f^{(n-1)}(f)}{\lambda_d \hat{S}_f^{(n-1)}(f) - (1 - \lambda_d) \sigma^2} \quad (2.75)$$

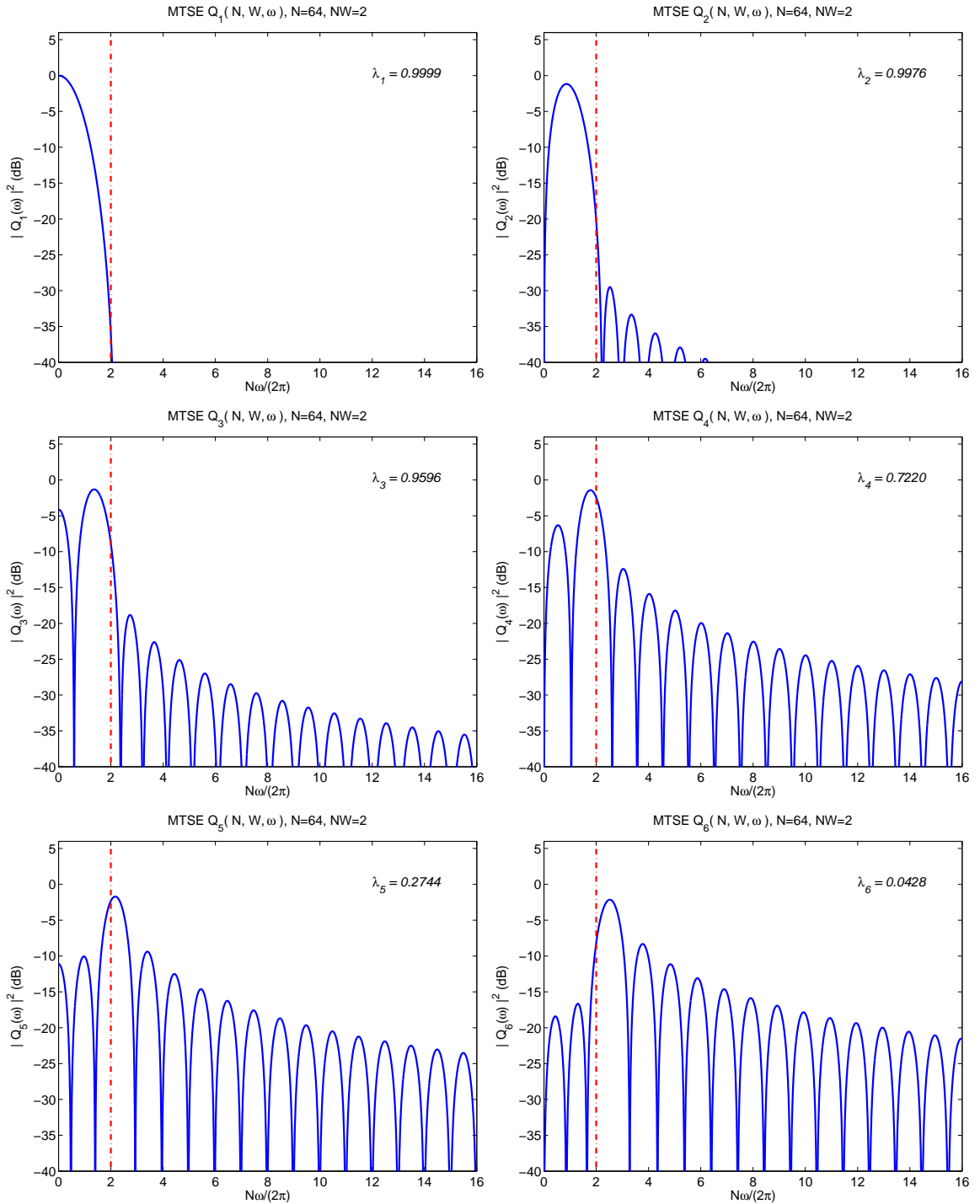


Figure 2.4: **Comparison of multiple tapers:** There are generally $2NW$ significant tapers that provide frequency content largely concentrated in the desired region. Additional tapers have significantly higher sidelobes and introduce the potential for broad band bias in the spectral estimate.

$$\hat{S}_f^{(n)}(f) = \frac{\sum_{d=1}^D |h_d(f)|^2 \hat{S}_d(f)}{\sum_{d=1}^D |h_d(f)|^2} \quad (2.76)$$

Typically, only 3 iterations of (2.75) followed by (2.76) are necessary for convergence.

Free Parameter Expansion

The formulation for multitaper spectral estimation develops an estimate of the power spectral density at f_o by considering the region $[f_o - W, f_o + W]$. This estimate is valid for any f in this region. For this reason, for a specific $\hat{S}_f(f'_o)$, there remains a question of which f_o in the range $f'_o - W \leq f_o \leq f'_o + W$ is most appropriate as all are valid. Thomson refers to this choice as the free parameter expansion of f_o . The final $\hat{S}_f(f'_o)$ should be a weighted average of these estimates, typically over the range $|f'_o - f_o| \leq 0.8W$. In practice, the eigencoefficients in (2.72) are computed using FFT techniques for efficiency. The most direct method of generating the additional eigencoefficients necessary for free parameter expansion is to continue to use the FFT with additional zero-padding. Throughout the dissertation, we refer to the scalar multiplier N_{FPE} as the value such that the full zero-padded FFT size is $N_{FFT} = N \times N_{FPE}$. Thus, N_{FPE} indicates the number of sampled “between points” available for free parameter expansion averaging.

Harmonic Analysis

As discussed in Section 2.4.2, the discrete random process may have a mixed spectrum, such that it consists of two independent processes - one with continuous spectrum and one with discrete spectrum. In terms of its spectral representation, a realization of a mixed spectrum stationary discrete random process $\{x[n]\}$ has spectral representation

$$x[n] = \int_{-1/2}^{1/2} e^{j2\pi fn} [dZ_1(f) + dZ_2(f)] \quad (2.77)$$

where $dZ_1(f)$ corresponds to the continuous spectrum process and has increments in continuum from $-1/2 \leq f \leq 1/2$, while $dZ_2(f)$ corresponds to the line spectrum process and has increments only at the discrete locations of the frequencies in the harmonic process, f_k for $k = 1, 2, \dots, K$. The line components (impulses) in the spectrum, caused by a portion of the process being a harmonic random process, cause difficulties with both classical and multitaper techniques. This is a result of the familiar modulation property of the Fourier transform. Windowing of the data in the time domain results in convolution in the frequency domain. If a line component has large SNR, the result is unintended spectral leakage across frequency, even for the multitaper algorithm. Thomson applied a harmonic analysis approach for dealing with this phenomenon.

At each frequency f_o , the multiple tapers define a region in the frequency domain, $[f_o - W, f_o + W]$. The continuous spectrum portion of the process, $\{dZ_1(f)\}$, is non-zero throughout the region $[f_o - W, f_o + W]$. For now, assume only a single line component may exist in this region. If a line component exists at f_o , the increment process $\{dZ_2(f)\}$ is only non-zero at f_o within $[f_o - W, f_o + W]$. Each realization of the process, $dZ_2(f)$, provides a complex valued constant at f_o . This allows us to establish an analysis of variance (ANOVA) test to detect the presence of the potential line component. For a single snapshot, this detection problem is termed the constant false alarm rate (CFAR) matched subspace detector by Scharf [69]. The procedure of [70] is used to extend the detector to multiple snapshots. Within the region $[f_o - W, f_o + W]$, define the subspace located at f_o only. Define a vector, \mathbf{q}_o , that consists of the mean value of each of the tapers

$$\mathbf{q}_o = \left[\sum_{n=0}^{N-1} q_1(n), \sum_{n=0}^{N-1} q_2(n), \dots, \sum_{n=0}^{N-1} q_D(n) \right]^T \quad (2.78)$$

and use this to form a projection matrix, \mathbf{P}_q , for the subspace

$$\mathbf{P}_q = \mathbf{q}_o (\mathbf{q}_o^H \mathbf{q}_o)^{-1} \mathbf{q}_o^H \quad (2.79)$$

The null projector for the subspace, \mathbf{P}_q^\perp ,

$$\mathbf{P}_q^\perp = \mathbf{I} - \mathbf{P}_q \quad (2.80)$$

defines “everywhere else” in the region $[f_o - W, f_o + W]$. Forming a vector of the eigenco-
efficients, $\mathbf{y}_m(f_o)$

$$\mathbf{y}_m(f_o) = \left[y_m^{(1)}(f_o), y_m^{(2)}(f_o), \dots, y_m^{(D)}(f_o) \right]^T \quad (2.81)$$

the detection statistic is formed by taking the ratio of the power of the eigencoefficients
in the f_o subspace to the power of the eigencoefficients outside that subspace. Formally,
following [70], the detection statistic $F(f_o)$ is computed as

$$F(f_o) = \frac{\sum_{m=1}^M \mathbf{y}_m^H(f_o) \mathbf{P}_q \mathbf{y}_m(f_o)}{\sum_{m=1}^M \mathbf{y}_m^H(f_o) \mathbf{P}_q^\perp \mathbf{y}_m(f_o)} \underset{H_0}{\overset{H_1}{\geq}} \gamma_{TH} \quad (2.82)$$

and compared to an appropriate threshold, γ_{TH} .

The importance of the detection of the line components in the spectrum is that they
may be identified, and after estimation of their unknown parameters (amplitude, frequency,
and phase) subtracted from the original data. The residual sample data is then subject to
the spectral estimation algorithm, now with line components removed. The final spectral
estimate numerically “adds” the line components to the continuous spectrum, with appro-
priate scaling for SNR and estimation accuracy. Figure 2.5 illustrates this process. $M = 20$
snapshots of $N = 64$ samples are available for processing. The snapshots contain a white
noise process, with power spectrum indicated by the dash-dot black line at 0 dB. The snap-
shots also contain a harmonic process consisting of 3 sinusoids at the locations indicated by
the vertical dash black lines. In the upper subplot, MTSE is shown in blue for $NW = 3$.
The characteristic “brick” from the equivalent window function is evident around the line

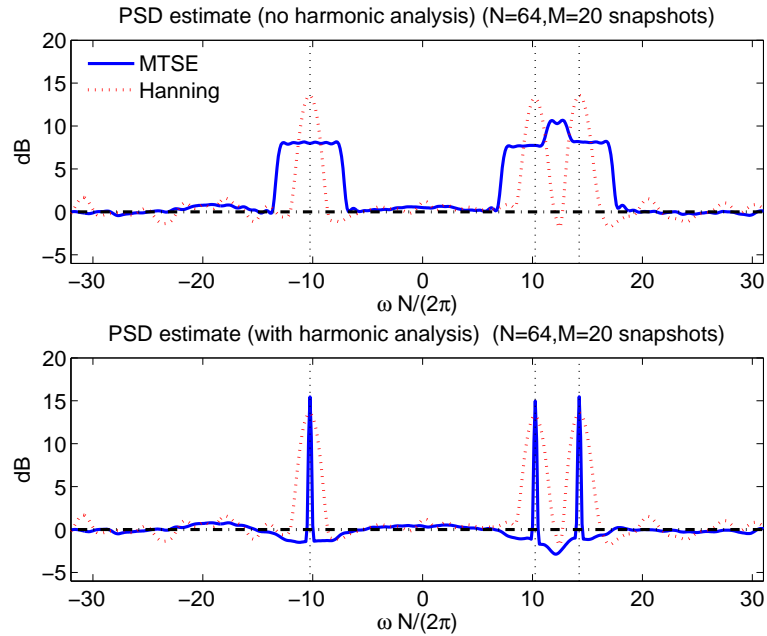


Figure 2.5: **Example of MTSE with harmonic analysis:** Prior to harmonic analysis, the standard MTSE algorithm shown in blue in the upper subplot, behaves similar to the classical Hann PSD shown in red. It provides lower variability in the spectrum, but its effective window width is much wider than the Hann window, evidenced as the line components are not resolved. With harmonic analysis, shown in the lower subplot, the spectral estimate clearly identifies the three line components and provides a smoother estimate of the background white spectrum.

component on the left. On the right, the two remaining line components are close enough so that the windows overlap. For comparison, a classical Hann window spectral estimate is shown in red. By itself, it has the resolution to identify all three peaks, but in general has more variability in the spectrum. The lower subplot shows the final MTSE product after harmonic analysis. The improvement from the incorporation of the harmonic analysis is evident.

Chapter 3: Structured Covariance Matrices Based On Frequency Wavenumber Spectral Estimation

3.1 Introduction

In this chapter we investigate how the frequency-wavenumber spectrum can be used as a basis for covariance matrix estimation for WSS space-time processes. We start by considering the sensitivity of a model based adaptive beamformer to errors in estimates of the model parameters. Performance of these processors with respect to the estimation of individual model parameters, such as interferer angle-of-arrival or interferer to noise ratio (INR), is investigated. The purpose is not to define a particular algorithm at this point, but to understand what features of the underlying problem are most significant in developing one. Where possible, estimation requirements are compared to Cramér Rao bounds as a method to confirm that we are not expecting too much in order to achieve a desired level of beamformer performance. Next, we review the relationships between the model for the array processing problem and the desired covariance. In addition to the contribution from physically propagating waves seen by the array, to maintain robustness it is necessary to also include contributions due to the sensor noise component. This requires defining a model that contains both of these elements, and that produces the proper covariance matrix estimate after transformation to the space-time domain. This leads to a straightforward approach for covariance estimation from spatial spectrum (CSS) for uniform arrays, and guides the development in Chapter 7 for arbitrary arrays. Concentrating on the uniform linear array case, the classical power spectral estimation techniques reviewed in Chapter 2 are applied to the problem. Expected values for the resulting covariance are developed and used to predict normalized SINR loss performance. These predictions show the need

to incorporate some form of harmonic analysis to mitigate the effects of line components in the spectrum. This allows the processor to maintain operation in the low normalized SINR loss region for a wide range of conditions.

3.2 Sensitivity of a Model Based Beamformer

This section assesses the performance of a model-based adaptive beamformer, based on the optimal beamformer, where the model parameters are estimated. Analysis is done to determine performance sensitivity to estimation errors for the individual model components. Without specifying the exact form of the processor, this analysis gives insight into what parameters within the model matter most in terms of impact to beamformer performance. Bounds are developed indicating the required estimation accuracy necessary to obtain an acceptable performance for an acceptable normalized SINR loss, ξ . The bounds are found to be well within accuracies obtainable for limited quantity data.

3.2.1 Single Plane Wave in Spatially White Noise

Consider the simple case of a single plane wave interferer in spatially white noise. This provides a basic understanding of sensitivity to error in estimation of the interferer *INR* or wavenumber, and develops a basis for more complicated models. The model for the covariance matrix for this problem is

$$\mathbf{R}_o = \sigma_n^2 \mathbf{v}_o \mathbf{v}_o^H + \sigma_w^2 \mathbf{I} \quad (3.1)$$

where $\mathbf{v}_o = ((e^{-j\mathbf{k}_o^T \mathbf{p}_n}))_n$ is the array manifold response for wavenumber \mathbf{k}_o . The unknown quantities are

- σ_w^2 , the variance of the uncorrelated sensor noise
- σ_n^2 , the variance of the plane wave interferer
- \mathbf{k}_o , the wavenumber of the plane wave interferer

The optimal beamformer weights for desired wavenumber, \mathbf{k}_s , specifying steering vector, \mathbf{s} , are given by (2.54). Given its simple structure, there is a closed form using the matrix inversion for \mathbf{R}_o^{-1} .

$$\mathbf{R}_o^{-1} = \sigma_w^{-2} \left[\mathbf{I} - \frac{\sigma_n^2/\sigma_w^2}{1 + \sigma_n^2/\sigma_w^2 \mathbf{v}_o^H \mathbf{v}_o} \mathbf{v}_o \mathbf{v}_o^H \right] \quad (3.2)$$

Recall that the projection matrix for the subspace spanned by a single vector, \mathbf{v} , is defined as $\mathbf{P}_v = \mathbf{v} (\mathbf{v}^H \mathbf{v})^{-1} \mathbf{v}^H$ which can be rearranged as $\mathbf{v}^H \mathbf{v} \mathbf{P}_v = \mathbf{v} \mathbf{v}^H$. Defining the quantity $\beta_o = \mathbf{v}_o^H \mathbf{v}_o (\sigma_w^2/\sigma_n^2 + \mathbf{v}_o^H \mathbf{v}_o)^{-1}$, the matrix inverse is represented as

$$\mathbf{R}_o^{-1} = \sigma_w^{-2} [\mathbf{I} - \beta_o \mathbf{P}_{\mathbf{v}_o}] \quad (3.3)$$

Eqn. (3.3) is similar to a projection matrix on the null space of \mathbf{v}_o . It is a weighted subtraction of the projection onto the range space of \mathbf{v}_o . As shown in Appendix B, β_o is a measure of the interferer to noise ratio, so the operation of the optimal beamformer can be interpreted as projecting out the interferer based on its relative strength against the spatially white noise. The complete expression for the weight vector is

$$\mathbf{w}_o = \frac{[\mathbf{I} - \beta_o \mathbf{P}_{\mathbf{v}_o}] \mathbf{s}}{\mathbf{s}^H [\mathbf{I} - \beta_o \mathbf{P}_{\mathbf{v}_o}] \mathbf{s}} \quad (3.4)$$

Note that the denominator is a scalar, and does not affect the shape of the beampattern other than as a gain.

We imagine a model based adaptive processor that knows the form of the covariance, estimates the unknown parameters, and uses the estimates to determine the adaptive weights using (3.4). We continue to use the convention of the subscript o to reflect the true or optimal quantity, while the subscript a reflects the estimated quantity. The estimated quantities reflect the true value and the estimation error, $\sigma_{w,a}^2 = \sigma_w^2 + \Delta\sigma_w^2$, $\sigma_{n,a}^2 = \sigma_n^2 + \Delta\sigma_n^2$, $k_a = k_o + \Delta k$. The estimated covariance matrix, \mathbf{R}_a , and the corresponding weight vector,

\mathbf{w}_a , are

$$\mathbf{R}_a = \sigma_{n,a}^2 \mathbf{v}_a \mathbf{v}_a^H + \sigma_{w,a}^2 \mathbf{I} \quad (3.5)$$

$$\mathbf{R}_a^{-1} = \sigma_{w,a}^{-2} [\mathbf{I} - \beta_a \mathbf{P}_{\mathbf{v}_a}] \quad (3.6)$$

$$\mathbf{w}_a = \frac{[\mathbf{I} - \beta_a \mathbf{P}_{\mathbf{v}_a}] \mathbf{s}}{\mathbf{s}^H [\mathbf{I} - \beta_a \mathbf{P}_{\mathbf{v}_a}] \mathbf{s}} \quad (3.7)$$

Because the weight vector does not depend on the absolute values of $\sigma_{w,a}^2$ and $\sigma_{n,a}^2$, only their ratio, we define the quantities

$$INR_o \equiv \frac{\sigma_n^2}{\sigma_w^2}, \quad INR_a \equiv \frac{\sigma_{n,a}^2}{\sigma_{w,a}^2} = INR_o \cdot \Delta INR \quad (3.8)$$

where $0 < \Delta INR < 1$ indicates an underestimate, and $\Delta INR > 1$ indicates an overestimate. We now investigate the sensitivity of ξ to under/over-estimation of INR , and if there is a range of Δk that is also tolerant such that ξ is near unity.

Over/Under-estimate of INR, $\Delta INR \neq 1$

For this analysis set $\Delta k = 0$, so that $\mathbf{P}_{\mathbf{v}_a} = \mathbf{P}_{\mathbf{v}_o}$, to concentrate on the behavior w.r.t. ΔINR . β_a may be expressed as

$$\beta_a = \frac{N}{(\sigma_n^2/\sigma_w^2)^{-1}(\Delta INR)^{-1} + N} \quad (3.9)$$

We'll consider the four scenarios given in Table 3.1 , which result in only two different approximations for performance. We have the additional condition on the upper right case that $(INR)^{-1}(\Delta INR)^{-1} \leq 1$, or $\Delta INR \geq (INR)^{-1}$. This puts a limit on the amount of underestimation considered, and eliminates the situation of gross underestimation of INR

Table 3.1: INR estimation error cases, single plane wave interferer:

	overestimate INR	underestimate INR
	$\Delta INR \geq 1$	$\Delta INR \leq 1$
$INR > 1$	$(INR)^{-1}(\Delta INR)^{-1} \ll 1, \beta_a \approx 1$	$(INR)^{-1}(\Delta INR)^{-1} \leq 1, \beta_a \approx 1$
$INR < 1$	$(INR)^{-1}(\Delta INR)^{-1} \leq 1, \beta_a \approx 1$	$(INR)^{-1}(\Delta INR)^{-1} \gg 1, \beta_a \approx 0$

when the interferer is strong. As seen in the Table, the two approximations to consider are Case 1. $\beta_a \approx 1$ and Case 2. $\beta_a \approx 0$.

Case 1. Overestimate or slightly underestimated INR, $\beta_a \approx 1$ As given in Appendix B, the general expression for the SINR loss is approximately

$$\xi \approx \frac{N - (1/N) |\mathbf{s}^H \mathbf{v}_o|^2}{N - (\beta_o/N) |\mathbf{s}^H \mathbf{v}_o|^2} \quad (3.10)$$

The performance depends on the number of elements, N , the INR , and the wavenumber separation. For a uniform linear array with element spacing d , with broadside as the desired steering vector, \mathbf{s} , (3.10) becomes

$$\xi \approx \frac{N - (1/N) \sin^2(k_o d N/2) / \sin^2(k_o d/2)}{N - (\sigma_w^2 / \sigma_n^2 + N)^{-1} \sin^2(k_o d N/2) / \sin^2(k_o d/2)} \quad (3.11)$$

Define the normalized frequency as the ratio of the operational frequency to the design frequency of the array, $f_{norm} = f/f_o, f \leq f_o$, the expression can be written in terms of the angle of incidence to the array, θ . Note the normalized wavenumber $k_o d = -\pi f_{norm} \cos \theta$.

$$\xi \approx \frac{N - (1/N) \sin^2(\pi f_{norm} \cos[\theta] N/2) / \sin^2(\pi f_{norm} \cos[\theta]/2)}{N - (\sigma_w^2 / \sigma_n^2 + N)^{-1} \sin^2(\pi f_{norm} \cos[\theta] N/2) / \sin^2(\pi f_{norm} \cos[\theta]/2)} \quad (3.12)$$

As θ moves away from the mainlobe at broadside this expression is ≈ 1 . Figure 3.1 on the left shows several curves for approximate SINR loss (in dB) for a 16 element ULA, each

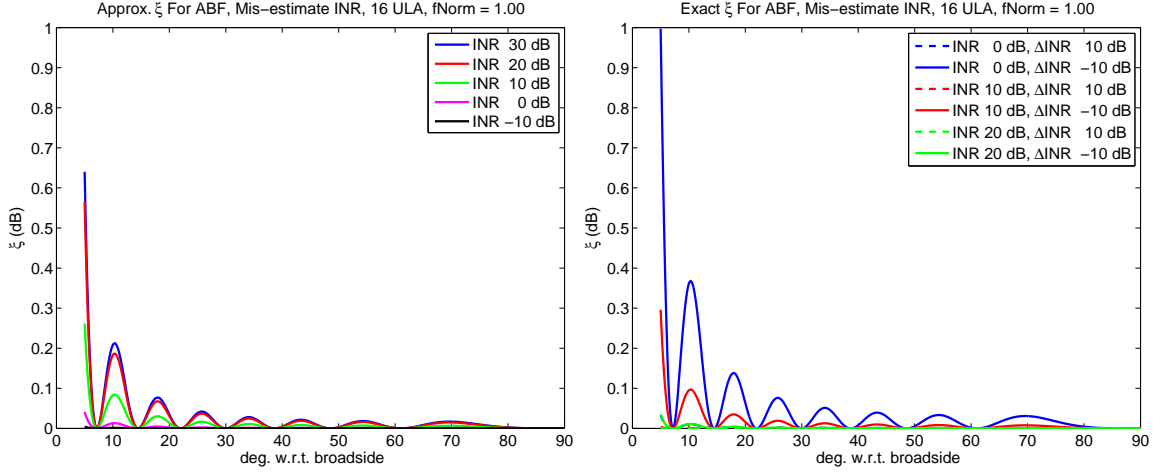


Figure 3.1: **Approx. and exact, $\xi_{dB}(INR, [k_s - k_o])$, ΔINR Case 1 - single plane wave interferer:** When INR is overestimated, or is strong and not substantially underestimated, the model based adaptive processor is fairly insensitive to INR estimation error. The plot on the left shows the approximate ξ_{dB} for several INR s, and is only a few tenths of a dB when the interferer is away from the mainlobe. The plot on the right shows the exact ξ_{dB} , which agrees closely except when the estimate of INR is grossly underestimated.

corresponding to different INR levels. This approximation is for cases of high INR , either overestimated or underestimated within a reasonable range, and low INR that is accurately or overestimated. Observe that outside the mainlobe, the loss is very low, a few tenths of a dB. In the Figure on right the exact expression for SINR loss is plotted for several test cases of INR , with $\Delta INR = \pm 10$ dB. All curves show low values in reasonable agreement with the approximation on the left when away from the main lobe. The exception is the blue trace for the case of 0 dB INR underestimated by 10 dB. This condition is outside the range restriction indicated earlier, $\Delta INR \geq (INR)^{-1}$, and represents a fairly large mis-estimation of the INR . In general, overestimating the INR is not a problem.

Case 2. Largely underestimated INR , $\beta_a \approx 0$ As given in Appendix B, the expression for the SINR loss for a uniform linear array in this case is approximately

$$\xi \approx \frac{N}{\mathbf{s}^H \mathbf{R}_o^{-1} \mathbf{s}} \cdot \frac{N}{\mathbf{s}^H \mathbf{R}_o \mathbf{s}} \quad (3.13)$$

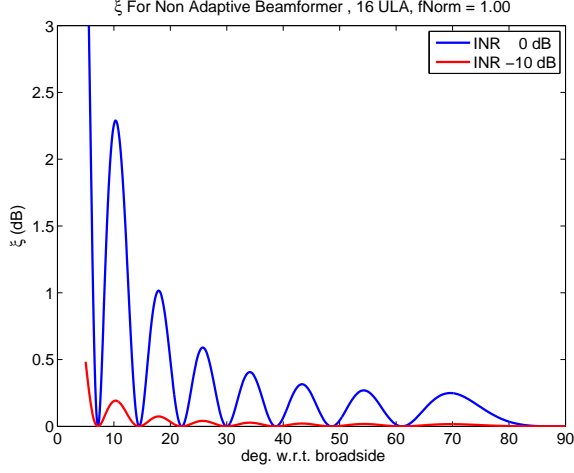


Figure 3.2: **Approx.** $\xi_{dB}(INR, [k_s - k_o])$, ΔINR **Case 2 - single plane wave interferer**: When INR is largely underestimated, the adaptive beamformer reduces to the conventional beamformer. Normalized SINR loss is highly dependent on INR , as the processor takes no action to specifically suppress the interferer.

This is the normalized SINR loss for the conventional (non-adaptive) beamformer.

$$\xi \approx \frac{N}{N - (\beta_o/N) |\mathbf{s}^H \mathbf{v}_o|^2} \cdot \frac{N}{N + \sigma_n^2/\sigma_w^2 |\mathbf{s}^H \mathbf{v}_o|^2} \quad (3.14)$$

Figure 3.2 shows the SINR performance for $INR = 0, -10$ dB. Large underestimation of the INR results in performance of the non-adaptive beamformer, effectively failing to take any corrective action in the weight determination to null the interference. The normalized SINR loss for this case shows the strong dependence between SINR loss and INR . This is expected for a non-adaptive processor, the larger the interferer the worse the performance. The zeros in the normalized SINR loss response occur due to the *fortunate* coincidence of the interferer and an existing null of the conventional beamformer beampattern.

Wavenumber Offset, $\Delta k \neq 0$

Now consider the impact of $\Delta k \neq 0$ on the performance. Assume that $\Delta INR = 1$, i.e., there is no error in estimating the INR , so that $\beta_a = \beta_o$. As given in Appendix B, the expression for the approximate SINR loss in this case is

$$\xi \approx \left[\sigma_n^2 / \sigma_w^2 \frac{|\mathbf{v}_o^H \mathbf{P}_{\mathbf{v}_a}^\perp \mathbf{s}|^2}{|\mathbf{P}_{\mathbf{v}_a}^\perp \mathbf{s}|^2} + 1 \right]^{-1} \quad (3.15)$$

We use this expression to determine a Δk that achieves an acceptable SINR loss, ξ_{OK} . This can then be compared to the Cramér Rao bound to see how reasonable it is in terms of our imagined model based processor. This results in the general expression for the single interferer in uncorrelated white noise case.

$$|\mathbf{v}_o^H \mathbf{P}_{\mathbf{v}_a}^\perp \mathbf{s}|^2 \leq |\mathbf{P}_{\mathbf{v}_o}^\perp \mathbf{s}|^2 \frac{1 - \xi_{OK}}{\xi_{OK} \sigma_n^2 / \sigma_w^2} \quad (3.16)$$

To simplify further requires some assumptions about the array geometry. We consider a ULA and analyze performance in terms of Δk , with an assumed desired steering vector corresponding to broadside, $k_s = 0$. Due to the choice of k_s , the interferer wavenumber k_o is the separation in wavenumber between the two. From Appendix B we have the following expression.

$$\Delta kd \leq \left(\frac{1}{\dot{D}^2(k_o d)} \cdot \left[N - \frac{1}{N} \frac{\sin^2(k_o d N / 2)}{\sin^2(k_o d / 2)} \right] \cdot \frac{1 - \xi_{OK}}{\xi_{OK} \sigma_n^2 / \sigma_w^2} \right)^{1/2} \quad (3.17)$$

$$\dot{D}(kd) = \frac{1}{2} \cdot \frac{N \sin(kd/2) \cos(kdN/2) - \sin(kdN/2) \cos(kd/2)}{\sin^2(kd/2)} \quad (3.18)$$

(3.17) contains oscillations that indicate there are areas in kd space that are more tolerant to the estimation error, Δk . These correspond to nulls in the conventional beam pattern that provide sufficient attenuation against the interference, simply by fortunate coincidence. We are interested in a smoother bound for the expression that eliminates oscillations and neatly spans the lower values. The final smoothed expression is

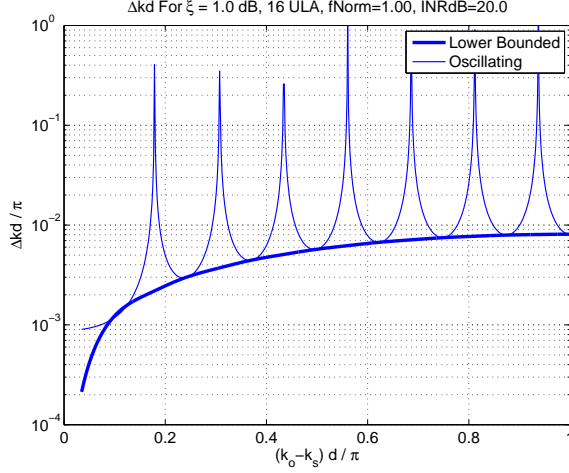


Figure 3.3: **Bounds for Δkd for a specified ξ , single plane wave interferer:** Eqn. (3.19), shown in the bolded blue, bounds the wavenumber estimation accuracy required to achieve a specified normalized SINR loss. This example shows the necessary accuracy to achieve $\xi_{OK,dB} = 1$ dB for an $N = 16$ element uniform linear array operated at design frequency, for an $INR = 20$ dB.

$$\Delta kd \leq \frac{2 |\sin(k_o d/2)|}{N} \left(\left[N - \frac{1}{N} \frac{\sin^2(k_o d N/2)}{\sin^2(k_o d/2)} \right] \frac{1 - \xi_{OK}}{\xi_{OK} \sigma_n^2 / \sigma_w^2} \right)^{1/2} \quad (3.19)$$

An example of the bounds produced for Δkd are shown in Figure 3.3. Eqn. (3.17) produces oscillations, shown as the thinner line in the Figure. Eqn. (3.19), shown as the thick line, smoothly bounds the bottom values. To be conservative, we use (3.19), although it is possibly too conservative as the separation between the interferer and the desired steering vector approaches zero. This corresponds to the interferer residing in the main lobe of the beamformer.

Comparison to the Cramér Rao Bound The spatial frequency / direction of arrival estimation accuracy specified by (3.19) results in a prescribed amount of normalized SINR loss, ξ_{OK} . This required accuracy can be compared to the Cramér Rao bound for the case of a single plane wave in noise. From [1], Eqn. (8.130) provides the CR bound for a given number of snapshots, M ,

$$C_{CR}(kd) = \frac{1}{M} \left[\frac{1}{N\sigma_n^2/\sigma_w^2} + \frac{1}{(N\sigma_n^2/\sigma_w^2)^2} \right] \frac{6}{(N^2 - 1)} \quad (3.20)$$

Figure 3.4 and Figure 3.5 show the comparison for the case of a $N = (32, 16)$ uniform linear array operating at the design frequency. In Figure 3.4, the left side graphs show the Δkd required to achieve a normalized SINR loss of $\xi_{OK} = (1, 2, 3)$ dB according to (3.19). The upper plot is for an INR of 50 dB, per element, while the lower plot is for INR of 20 dB. The change in required accuracy reflects the dependence on INR , strong interference must be nulled more accurately. The Cramér Rao bound is shown for $M = (1, 2, 10)$ snapshots. As can be seen in the Figure, the bound is significantly below the required accuracy, except very close to the desired signal AOA. On the right in the Figure, the plots show the exact SINR loss for the required Δkd , expressed in dB, found using (2.61). The peaks of the exact value, ξ , are in close agreement with the specified ξ_{OK} , showing the prediction for required direction of arrival accuracy is accurate. The exact ξ experiences periodic dips, corresponding to the nulls of the quiescent response of the beamformer. Figure 3.5 presents similar plots for the case of $N = 16$ elements.

3.2.2 Multiple Plane Waves in Spatially White Noise

Analysis was carried out to extend the results of Section 3.2.1 to the case of K plane wave interferers in spatially white noise. Due to the increased complexity of the problem the resulting expressions become tedious, and to produce results similar to that presented in Figure 3.4 and Figure 3.5 requires assumptions regarding the orthogonality, placement, and relative strength of the interferers. These assumptions make it difficult to draw conclusions about the general case. For large aperture arrays with many sensors, being able to resolve individual interferers results in performance that is dominated by the worst case single interferer as given in Section 3.2.1.

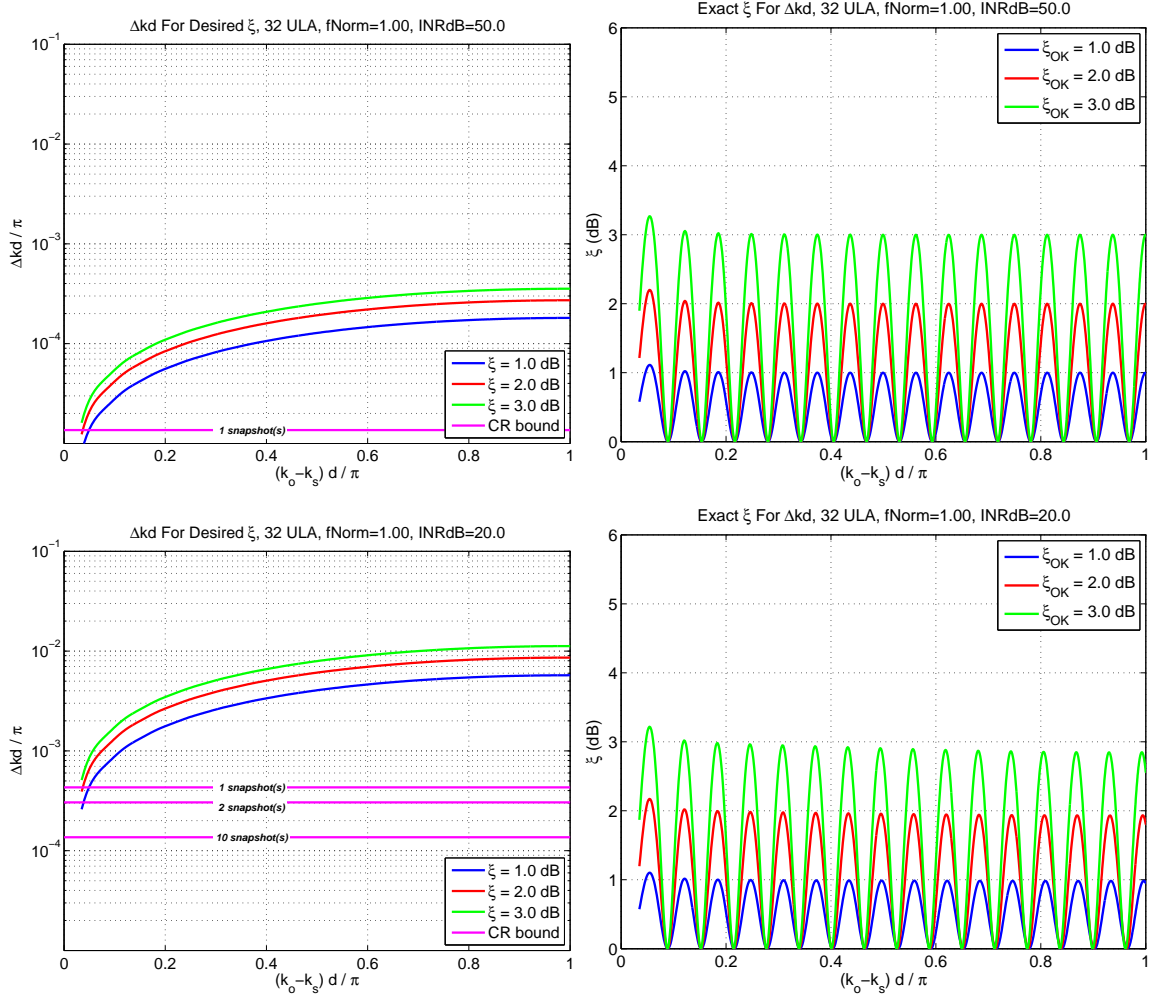


Figure 3.4: **AOA accuracy requirements for specified ξ , $N = 32$ ULA, single interferer:** The Cramér Rao bound is compared to bounds for required accuracy for an acceptable normalized SINR loss. This shows that even for a single snapshot, a model based adaptive processor can achieve within 1 dB of optimal. Estimation accuracy requirements and performance both increase with higher *INR*. Exact expressions for ξ for a given accuracy show good agreement with the requirement bound.

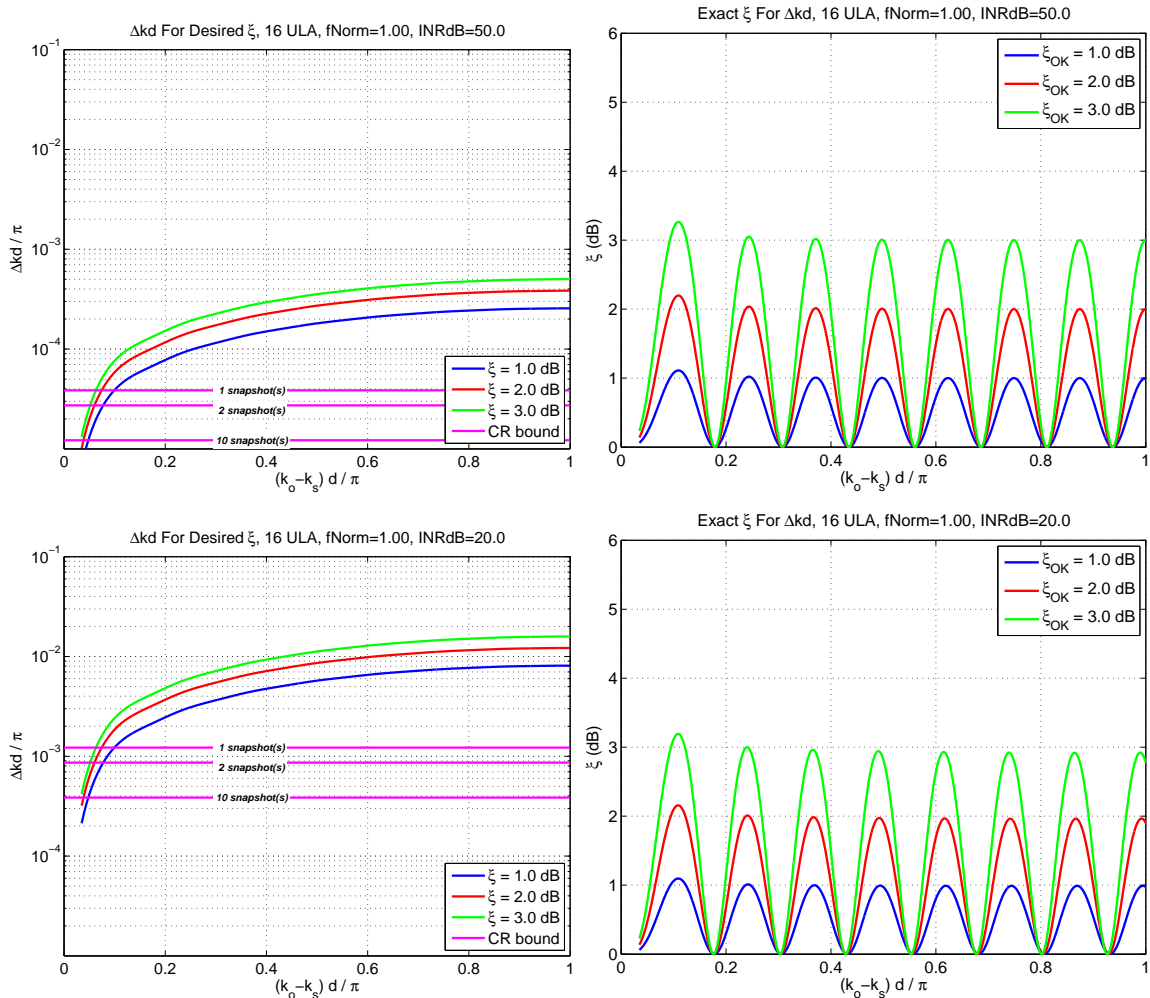


Figure 3.5: **AOA accuracy requirements for specified ξ , $N = 16$ ULA, single interferer**: Compared to the $N = 32$ case shown in Figure (3.4), more snapshots, M , are required for $N = 16$ to achieve the necessary wavenumber estimation accuracy close to the main lobe. This is a reflection of the CR bound (3.20) being proportional to M^{-1} compared to N^{-2} .

3.3 Model For Covariance

We start the development for estimating the covariance matrix by considering a model that incorporates the components that make up the covariance at the output of an N element array for the narrowband, stationary space-time process, $f(t, \Delta \mathbf{p})$. Using the spectral representation theorem, the space-time process can be represented as a sum of uncorrelated plane waves distributed as function of angle of arrival to the array, $G(\theta, \phi)$, or wavenumber, $G(\mathbf{k})$. The corresponding wavenumber spectrum for the process is proportional to this normalized distribution, $P_f(\mathbf{k}) = \alpha G(\mathbf{k})$, where α accounts for scaling the relative levels defined by $G(\mathbf{k})$ to the absolute power level seen at the array.

From the review in Chapter 2, a stationary random process may consist of two uncorrelated components, one corresponding to a continuous spectrum process, and another corresponding to a discrete spectrum, i.e., harmonic, process. The independent, white sensor noise adds a third component to the array output covariance. The m^{th} snapshot containing these components is

$$\begin{aligned} \mathbf{x}_m &= \sum_{k=1}^K \mathbf{v}_k a_k(m) + \mathbf{n}_{b,m} + \mathbf{n}_{w,m} \\ &= \mathbf{V} \mathbf{a}_m + \mathbf{n}_{b,m} + \mathbf{n}_{w,m} \end{aligned} \tag{3.21}$$

where \mathbf{v}_k is the array manifold response vector at spatial frequency \mathbf{k}_k . The covariance for this model consists of three uncorrelated parts based on these components

$$\mathbf{R}_x = \mathbf{V} \mathbf{R}_a \mathbf{V}^H + \mathbf{R}_b + \mathbf{R}_w \tag{3.22}$$

where $\mathbf{R}_a = E \{ \mathbf{a}_m \mathbf{a}_m^H \}$, $\mathbf{R}_b = E \{ \mathbf{n}_{b,m} \mathbf{n}_{b,m}^H \}$, $\mathbf{R}_w = E \{ \mathbf{n}_{w,m} \mathbf{n}_{w,m}^H \} = \sigma_w^2 \mathbf{I}$, and spatial stationarity requires the plane waves be uncorrelated, so that $\mathbf{R}_a = \text{diag}(\sigma_1^2, \sigma_2^2, \dots, \sigma_K^2)$.

We may then write

$$\mathbf{R}_x = \sum_{k=1}^K \sigma_k^2 \mathbf{v}_k \mathbf{v}_k^H + \mathbf{R}_b + \sigma_w^2 \mathbf{I} \quad (3.23)$$

Alternatively, grouping the terms for the space-time process, $\mathbf{R}_f = \mathbf{V} \mathbf{R}_a \mathbf{V}^H + \mathbf{R}_b$, separately from the sensor noise component we have

$$\mathbf{R}_x = \mathbf{R}_f + \mathbf{R}_w \quad (3.24)$$

The matrix \mathbf{R}_f includes all terms that correspond to physical propagating waves and can be decomposed via eigendecomposition

$$\begin{aligned} \mathbf{R}_f &= \mathbf{Q}_f \mathbf{\Lambda}_f \mathbf{Q}_f^H \\ &= \sum_{n=0}^{N_f-1} \lambda_{f,n} \mathbf{q}_{f,n} \mathbf{q}_{f,n}^H \end{aligned} \quad (3.25)$$

Depending on the particular form of the space-time process, $f(t, \Delta \mathbf{p})$, and the array geometry, \mathbf{R}_f may have rank $N_f < N$. In that event, some of the eigenvalues will be zero valued.

$$\mathbf{R}_f = \sum_{n=0}^{N_f-1} \lambda_{f,n} \mathbf{q}_{f,n} \mathbf{q}_{f,n}^H \quad (3.26)$$

Regardless of the rank of \mathbf{R}_f , the N eigenvectors \mathbf{Q}_f form a complete orthonormal set for the space $\mathbb{C}^{N \times N}$. Using (3.25) in (3.24), with $\mathbf{Q}_f \mathbf{Q}_f^H = \mathbf{I}$ the matrix \mathbf{R}_x can be expressed

$$\begin{aligned}
\mathbf{R}_x &= \mathbf{Q}_f \Lambda_f \mathbf{Q}_f^H + \sigma_w^2 \mathbf{Q}_f \mathbf{Q}_f^H \\
&= \sum_{n=0}^{N_f-1} (\lambda_{f,n} + \sigma_w^2) \mathbf{q}_{f,n} \mathbf{q}_{f,n}^H + \sum_{n=N_f}^{N-1} \sigma_w^2 \mathbf{q}_{f,n} \mathbf{q}_{f,n}^H \\
&= \mathbf{Q}_f \Lambda_x \mathbf{Q}_f^H
\end{aligned} \tag{3.27}$$

As evident in (3.27), the white noise contribution from \mathbf{R}_w guarantees that all the eigenvalues are non-zero, so that overall covariance, \mathbf{R}_x , is full rank.

3.3.1 Estimating Visible Space Covariance, $\hat{\mathbf{R}}_{vs}$

Consider the covariance associated with the space-time process only, \mathbf{R}_f . As reviewed in Chapter 2, the transform relationship between the frequency-wavenumber spectrum, $P_f(\mathbf{k})$, and the space-time covariance, \mathbf{R}_f , is

$$\mathbf{R}_f = (2\pi)^{-C} \int \dots \int_{vs} P_f(\mathbf{k}) \mathbf{v}(\mathbf{k}) \mathbf{v}^H(\mathbf{k}) d\mathbf{k} \tag{3.28}$$

where C in this expression is the dimension of the wavenumber used, $C = 1, 2$ or 3 . The range of integration is restricted to the visible region for the array, corresponding to physical propagating waves arriving at the array with some azimuth, $0 \leq \phi \leq 2\pi$, and elevation, $0 \leq \theta \leq \pi$. For a given estimate of the visible region frequency-wavenumber spectrum, $\hat{P}_{vs}(\mathbf{k})$, the corresponding covariance of the space-time process can be determined using (3.28)

$$\hat{\mathbf{R}}_{vs} = (2\pi)^{-C} \int \dots \int_{vs} \hat{P}_{vs}(\mathbf{k}) \mathbf{v}(\mathbf{k}) \mathbf{v}^H(\mathbf{k}) d\mathbf{k} \tag{3.29}$$

Spectral estimation techniques used to form the estimate $\hat{P}_{vs}(\mathbf{k})$ will not be able to distinguish between the contribution of the space-time process, $f(t, \Delta \mathbf{p})$, and the sensor noise

component apparent within the visible space. Any basis projection or steered beam power measurement technique will see both the content from $f(t, \Delta \mathbf{p})$ and the sensor noise.

$$\hat{P}_{\text{vs}}(\mathbf{k}) = \hat{P}_f(\mathbf{k}) + \hat{\sigma}_w^2 \quad (3.30)$$

$\hat{\mathbf{R}}_{\text{vs}}$ from (3.29) will contain the sum of both.

$$\hat{\mathbf{R}}_{\text{vs}} = \hat{\mathbf{R}}_f + \hat{\sigma}_w^2 (2\pi)^{-C} \int \int_{\text{vs}} \mathbf{v}(\mathbf{k}) \mathbf{v}^H(\mathbf{k}) d\mathbf{k} \quad (3.31)$$

Observe from (3.31) that the contribution due to the sensor noise component, when viewed only across the visible region, appears as an additional isotropic noise in the environment.

3.3.2 Visible and Virtual Space

For certain array geometries, or when operating below the design frequency, there may be a significant additional virtual space in addition to the visible space available to the array. Here we define what is meant by virtual space. Denote the subspace spanned by the columns of a matrix \mathbf{A} as $\text{span}(\mathbf{A}) \equiv \langle \mathbf{A} \rangle$. As shown earlier, with a sensor noise component present, $\mathbf{R}_x \in \mathbb{C}^{N \times N}$, and is full rank, thus $\langle \mathbf{R}_x \rangle = \langle \mathbb{C}^{N \times N} \rangle$. The visible space is defined by those plane waves that may physically propagate to the array with a given angle of arrival. For a particular geometry and operational frequency, the visible space may only occupy a subspace of $\mathbb{C}^{N \times N}$. $\langle \mathbf{R}_x \rangle$ then consists of two subspaces, one corresponding to the visible region, indicated with subscript vs, and one corresponding to the virtual region, indicated with subscript vr.

$$\langle \mathbf{R}_x \rangle = \langle \mathbf{R}_{\text{vs}} \rangle + \langle \mathbf{R}_{\text{vr}} \rangle \quad (3.32)$$

Wavenumbers in the virtual space do not correspond to physical propagating waves. Use of (3.29) directly as an estimate of covariance with failure to account for the sensor noise component within the virtual region subspace leads to poor sidelobe behavior within the

virtual region, and adaptive beamformers developed using this covariance alone suffer an overall loss in SINR.

This effect is illustrated in Figure 3.6. In this example, an $N = 8$ element uniform linear array has element spacing $d = \lambda/4$, essentially operating at half the design frequency for the array. Spectra are shown in normalized wavenumber space, $\psi' = \psi N/(2\pi)$, where $\psi = -k_z d$ (this makes the units directly comparable to FFT bin centers). Specifying power as per sensor element, there is an interferer at $\psi' = -1.5$ with power of 5 dB, indicated by the dash-dot arrow. There is a 3D isotropic noise component with power of -5 dB shown as the horizontal black line for $|\psi'| \leq 2$. Additionally, there is an uncorrelated sensor noise component with power of -15 dB, shown as the horizontal black line for $4 > |\psi'| > 2$. The effect of operation below design frequency is evident in the pedestal shape of the isotropic noise component, as it is spatially bandlimited. In this instance the visible region occupies the region $|\psi'| \leq 2$. The sensor noise component occupies the entire region $|\psi'| \leq 4$. In the upper subplot, the power pattern, shown in blue, is for an MVDR beamformer computed from $\hat{\mathbf{R}}_{\text{vs}}$ only (3.29). This processor has large sidelobe levels in the virtual region, $4 > |\psi'| > 2$, since it believes that subspace to be unoccupied. The lower subplot shows the power pattern for an MVDR beamformer using the ensemble covariance (both visible and virtual space), and properly accounts for the sensor noise in the virtual space. This processor is optimal for the problem and exhibits better sidelobe behavior. The sensor noise is, of course, present throughout the space and the beamformer based on the visible space alone suffers a normalized SINR loss of $\xi_{dB} = 8.4$ dB. The loss in performance is due to the noise amplification attributable to the sidelobes in the virtual region.

3.3.3 Regularly and Uniformly Spaced Array Geometry

A regularly spaced array geometry is described by an interelement spacing that is a multiple of a fixed quantity, d , in Cartesian coordinates. Uniform arrays are a special case of this with the interelement spacing simply the constant, d . The uniform linear array, in terms

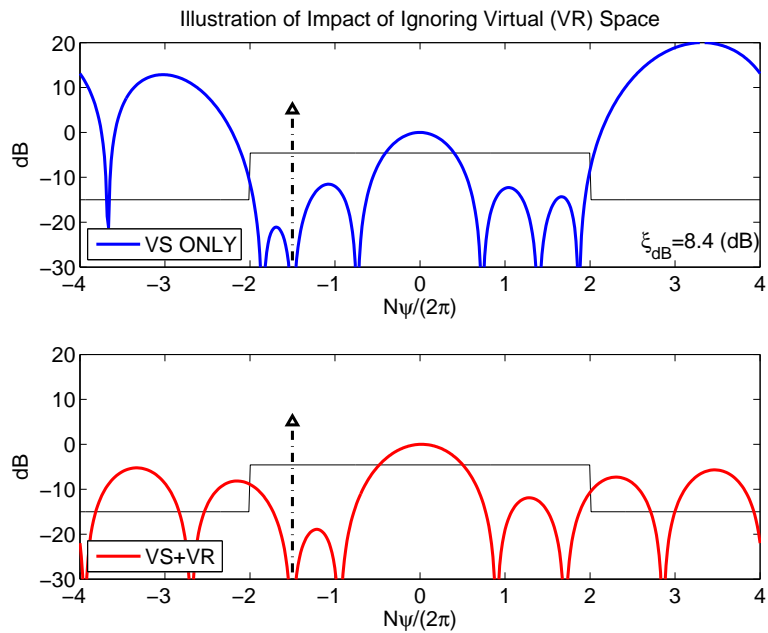


Figure 3.6: **Impact of covariance estimated from visible space only:** In this example a $N = 8$ ULA with spacing $d = \lambda/4$ observes a single point source in isotropic noise. In the upper subplot, the covariance matrix only accounts for the visible space and the resultant adaptive beamformer has poor sidelobe behavior in the virtual space, as it believes it is unconstrained in this area. In lower subplot, the covariance matrix is the ensemble covariance, accounting for the visible space and the sensor noise component in the virtual space. The visible space covariance results in a normalized SINR loss of 8.4 dB due to the unintended noise amplification cause by its elevated sidelobe levels.

of spatial sampling, is directly analogous to uniform sampled time series and the results of stationary processes and Fourier transform pairs and properties apply directly. This section concentrates on the uniform linear array, with some discussion of the implications of regularly spaced arrays at the conclusion. Extensions to higher dimension processing are straightforward.

The narrowband space-time process, $f(t, \Delta \mathbf{p})$, at frequency ω consists of plane waves propagating in a homogeneous medium with velocity c . These waves are solutions to the homogeneous wave equation, and are constrained in wavenumber such that $|\mathbf{k}| = \omega/c = 2\pi/\lambda$. This requires that the frequency-wavenumber spectrum, $P_f(\omega, \mathbf{k})$, for this process exist on the surface of a sphere in wavenumber space with radius $|\mathbf{k}|$.

Consider an N element uniform linear array with design frequency ω_o (spacing $d = \lambda_o/2$) and sensor elements at locations on the z axis, $p_n = (n - 1) d$ for $n = 0, \dots, N - 1$. With no ability to resolve spatial components in the k_x or k_y direction, the frequency-wavenumber spectrum, $P_f(\omega, \mathbf{k})$, may be projected down onto the k_z axis. After projection the spectrum maintains the strict bandlimiting to the range $|k_z| \leq 2\pi/\lambda$. From the review of sampling of random processes in Chapter 2 we have

$$R_f(\Delta p) = \frac{1}{2\pi} \int_{-2\pi/\lambda_o}^{2\pi/\lambda_o} P_f(k_z) e^{-j\Delta p k_z} dk_z \quad (3.33)$$

where $\Delta p = ld$ for integer l . For operation below the array design frequency, $\omega < \omega_o$, the wavenumber spectrum $P_f(k_z)$ is non-zero only over the range corresponding to the visible region of the array, $|k_z| \leq 2\pi/\lambda$, and the range of integration may be reduced to $\int_{-2\pi/\lambda}^{2\pi/\lambda}$.

Now consider the uncorrelated sensor noise component

$$R_w(\Delta p) = \sigma_w^2 \delta(\Delta p) \quad (3.34)$$

Even though it does not correspond to a component of a physically propagating space-time process, we can still define a wavenumber-spectrum and covariance Fourier transform pair

$$P_w(k_z) = \sum_{m=-\infty}^{\infty} R_w(\Delta p) e^{j\Delta p k_z} = \sigma_w^2 \quad (3.35)$$

$$R_w(\Delta p) = \frac{1}{2\pi} \int_{-2\pi/\lambda_o}^{2\pi/\lambda_o} P_w(k_z) e^{-j\Delta p k_z} dk_z \quad (3.36)$$

The difference between $P_f(k_z)$ and $P_w(k_z)$ is that $P_w(k_z)$ is non-zero over the entire interval, $|k_z| \leq 2\pi/\lambda_o$. The covariance for the output of the array that we are interested in is the sum of the two

$$R_x(\Delta p) = R_f(\Delta p) + R_w(\Delta p) \quad (3.37)$$

We can add the two wavenumber spectra, one for the space-time process and the other for the sensor noise component, to produce a composite spectrum

$$P_x(k_z) = P_f(k_z) + P_w(k_z), \quad |k_z| \leq 2\pi/\lambda_o \quad (3.38)$$

so that the covariance is related via

$$R_x(\Delta p) = \frac{1}{2\pi} \int_{-2\pi/\lambda_o}^{2\pi/\lambda_o} [P_f(k_z) + P_w(k_z)] e^{-j\Delta p k_z} dk_z \quad (3.39)$$

For convenience we can convert the expressions to normalized wavenumber, $\psi = -k_z d$ space. Defining the ψ spectrum as

$$P_{\psi,\alpha}(\psi) = \frac{1}{d} P_{\alpha}(k) \Big|_{k=-\psi/d}, \quad \alpha = x, f, w \quad (3.40)$$

the covariance sequence $R_{l,x}(l)$ and ψ spectrum are related

$$R_{l,x}(l) = R_x(ld) = \frac{1}{2\pi} \int_{-\pi}^{\pi} P_{\psi,x}(\psi) e^{j\psi l} d\psi \quad (3.41)$$

$P_{\psi,x}(\psi)$ is readily estimated over the entire range, $|\psi| \leq \pi$, from the snapshot data, \mathbf{x}_m , using classical power spectral estimation techniques. By accepting a fixed resolution in ψ space (which is non-uniform in angle space, θ) this can be done efficiently with FFT based processing. Using the estimate $\hat{P}_{\psi,x}(\psi)$ in (3.41)

$$\hat{R}_{l,x}(l) = \frac{1}{2\pi} \int_{-\pi}^{\pi} \hat{P}_{\psi,x}(\psi) e^{j\psi l} d\psi \quad (3.42)$$

As long as the limits of integration in (3.42) are over the entire range, $\int_{-\pi}^{\pi}$, the covariance estimate will contain the appropriate components for both the space-time process and the uncorrelated sensor noise.

One might arrive directly at (3.42) by inspection of the ULA problem, by observing that it is equivalent to the uniform sampled time series problem. We have followed this approach to be clear in how the space-time process and the sensor noise contribute to the overall covariance. The important concepts are that the process itself may be bandlimited, and that if the sensor noise component is estimated in the transform domain it must have the appropriate form such that it equates to $\hat{\sigma}_w^2 \mathbf{I}$ within the final covariance matrix estimate. This is straightforward for the ULA, but may be more involved in the case of arbitrary geometry arrays.

3.3.4 Positive Definiteness

In order for the estimated covariance to have value for adaptive beamforming, it is necessary to for it be Hermetian, $\hat{\mathbf{R}}_x = \hat{\mathbf{R}}_x^H$, and invertible. The Hermetian property and invertibility requirement implies the eigenvalues of $\hat{\mathbf{R}}_x$ are all real valued and greater than zero, or more simply that the matrix $\hat{\mathbf{R}}_x$ is positive definite. For arbitrary vector \mathbf{x} , not equal to the null

vector ($\mathbf{x}^H \mathbf{x} \neq 0$), the matrix \mathbf{A} is positive semi-definite if

$$\mathbf{x}^H \mathbf{A} \mathbf{x} \geq 0 \quad (3.43)$$

and is indicated notationally as $\mathbf{A} \geq 0$. The matrix \mathbf{A} is positive definite if

$$\mathbf{x}^H \mathbf{A} \mathbf{x} > 0 \quad (3.44)$$

and is indicated notationally as $\mathbf{A} > 0$.

Consider the regularly spaced linear array (higher dimension regular arrays follow naturally). From (3.42), the covariance matrix estimate is based on the estimate of the wavenumber spectrum, given in normalized wavenumber space, $\psi = -kd$

$$\hat{\mathbf{R}}_x = \frac{1}{2\pi} \int_{-\pi}^{\pi} \hat{P}_{\psi,x}(\psi) \mathbf{v}_{\psi}(\psi) \mathbf{v}_{\psi}^H(\psi) d\psi \quad (3.45)$$

We restrict the ψ -spectrum estimates, $\hat{P}_{\psi,x}(\psi)$, to be real-valued and greater than zero. This will have implications later in choice of algorithm but is a reasonable requirement for a power spectral estimator when the observed process has a white noise component. With this restriction we can express $\hat{P}_{\psi,x}(\psi)$ in the form

$$\hat{P}_{\psi,x}(\psi) = \hat{P}_{\psi,f}(\psi) + \hat{\sigma}_w^2 \quad (3.46)$$

where $\hat{P}_{\psi,f}(\psi)$ is the estimate of the space-time process spectrum, $\hat{P}_{\psi,f}(\psi) \geq 0$, and $\hat{\sigma}_w^2$ is the estimate of the sensor noise, $\hat{\sigma}_w^2 > 0$. Now

$$\begin{aligned} \mathbf{x}^H \hat{\mathbf{R}}_x \mathbf{x} &= \mathbf{x}^H \left(\frac{1}{2\pi} \int_{-\pi}^{\pi} \left[\hat{P}_{\psi,f}(\psi) + \hat{\sigma}_w^2 \right] \mathbf{v}_{\psi}(\psi) \mathbf{v}_{\psi}^H(\psi) d\psi \right) \mathbf{x} \\ &= \mathbf{x}^H \left(\hat{\mathbf{R}}_f + \hat{\mathbf{R}}_w \right) \mathbf{x} \end{aligned} \quad (3.47)$$

The first term is

$$\mathbf{x}^H \hat{\mathbf{R}}_f \mathbf{x} = \frac{1}{2\pi} \int_{-\pi}^{\pi} \hat{P}_{\psi,f}(\psi) |\mathbf{x}^H \mathbf{v}_{\psi}(\psi)|^2 d\psi \quad (3.48)$$

Both quantities in the integral in (3.48), $\hat{P}_{\psi,f}(\psi)$ and $|\mathbf{x}^H \mathbf{v}_{\psi}(\psi)|^2$, are real-valued and greater than or equal to zero, therefore $\hat{\mathbf{R}}_f \geq 0$. The second term is evaluated as

$$\mathbf{x}^H \hat{\mathbf{R}}_w \mathbf{x} = \hat{\sigma}_w^2 \mathbf{x}^H \left[\frac{1}{2\pi} \int_{-\pi}^{\pi} \mathbf{v}_{\psi}(\psi) \mathbf{v}_{\psi}^H(\psi) d\psi \right] \mathbf{x} \quad (3.49)$$

From Section (3.3.3) the integral reduces to

$$\frac{1}{2\pi} \int_{-\pi}^{\pi} \mathbf{v}_{\psi}(\psi) \mathbf{v}_{\psi}^H(\psi) d\psi = \mathbf{I} \quad (3.50)$$

so that

$$\mathbf{x}^H \hat{\mathbf{R}}_w \mathbf{x} = \hat{\sigma}_w^2 \mathbf{x}^H \mathbf{x} > 0 \quad (3.51)$$

and $\hat{\mathbf{R}}_w$ is positive definite. The sum of a positive semidefinite matrix and a positive definite matrix is positive definite, so we have $\hat{\mathbf{R}}_x > 0$ when $\hat{P}_{\psi,x}(\psi)$ is real-valued and greater than zero.

3.4 Performance When Using Classical PSD Techniques

3.4.1 Background

We begin the analysis of performance of estimating covariance from spatial spectrum (CSS) by considering estimates of the wavenumber spectrum found using classical spectral estimation techniques. We continue to focus on the uniform linear array with spacing $d = \lambda_o/2$. For a given fixed window function (or taper), $\mathbf{w} = ((w[n]))_n$, the windowed snapshot data

is

$$\mathbf{y}_m = ((x_m[n]w[n]))_n = \mathbf{x}_m \odot \mathbf{w} \quad (3.52)$$

The windowed data is used to form an averaged windowed periodogram estimate of the spectrum. Writing the array manifold response vector, $\mathbf{v}_\mathbf{k}(k_z) = ((e^{-jk_z dn}))_n$ in $\psi = -k_z d$ space, $\mathbf{v}_\psi(\psi) = ((e^{j\psi n}))_n$, the estimate is developed in two steps. First, compute the Fourier transform of the windowed data.

$$Y_m(\psi) = \sum_{n=0}^{N-1} y_m(n)e^{-j\psi n} = \mathbf{v}_\psi^H(\psi) \mathbf{y}_m \quad (3.53)$$

The final spectral estimated is the averaged, magnitude squared value of the Fourier transforms

$$\begin{aligned} \hat{P}_y(\psi) &= \frac{1}{M} \sum_{m=1}^M |Y_m(\psi)|^2 \\ &= \frac{1}{M} \sum_{m=1}^M \mathbf{v}_\psi^H(\psi) \mathbf{y}_m \mathbf{y}_m^H \mathbf{v}_\psi(\psi) \end{aligned} \quad (3.54)$$

$\hat{P}_y(\psi)$ is periodic in ψ with period 2π . We refer to the range $|\psi| \leq \pi$ as the region of support. The visible region of the array, when operating at frequency $f = c/\lambda$, ($f \leq f_o$), is restricted to the range $|\psi| \leq \pi(\lambda_o/\lambda)$. As discussed in Section 3.3.2, the remainder outside the visible region is referred to as the virtual region. The fixed window function, \mathbf{w} , provides a fixed resolution, i.e., “bin width”, across ψ space. This allows $\hat{P}_y(\psi)$ to be computed efficiently at several equal spaced locations throughout the supported region using FFT techniques.¹

¹It is possible to have the window function vary as a function of ψ , represented as \mathbf{w}_ψ . In this way one can design for a fixed resolution in angle space. This results in non-uniform “bin width” in ψ space. Multi-taper spectral estimation techniques lend themselves to this method of design. FFT techniques are not directly applicable, though, when the window function is not fixed so there a computational cost associated with the approach.

We can look at an alternate perspective on the estimated $\hat{P}_y(\psi)$ spectrum, in terms of an auto-correlation sequence $\hat{\rho}_y[n]$ defined by the windowed sensor outputs. Based on the Fourier transform property

$$|Y_m(\psi)|^2 = \mathcal{F} \left(\sum_{\beta=0}^{N-1} y_m[\beta] y_m^*[\beta - n] \right) \quad (3.55)$$

The sample autocorrelation per snapshot is

$$\hat{\rho}_{y,m}[n] = \sum_{\beta=0}^{N-1} y_m[\beta] y_m^*[\beta - n], \quad 0 \leq n < N, \quad \hat{\rho}_{y,m}[-n] = \hat{\rho}_{y,m}^*[n] \quad (3.56)$$

where the sequence $y_m[\beta]$ has value only in the range $[0, N - 1]$, and is zero elsewhere. As a convention, we use $\hat{\rho}[n]$ to represent a sample autocorrelation from the data itself, while reserving $R[n]$ to indicate an auto-correlation based on the ensemble, $E\{\cdot\}$. The overall sample autocorrelation is the average over all snapshots

$$\hat{\rho}_y[n] = \frac{1}{M} \sum_{m=1}^M \hat{\rho}_{y,m}[n] \quad (3.57)$$

Using (3.55), (3.56), and (3.57), in (3.54) we have

$$\hat{P}_y(\psi) = \sum_{n=-(N-1)}^{N-1} \hat{\rho}_y[n] e^{-j\psi n} \quad (3.58)$$

The estimated power spectrum and auto-correlation sequence are a familiar Fourier transform pair, with corresponding inverse transform relationship

$$\hat{\rho}_y[n] = (2\pi)^{-1} \int_{-\pi}^{\pi} \hat{P}_y(\psi) e^{j\psi n} d\psi \quad (3.59)$$

The covariance matrix for the array is formed from the $\hat{\rho}_y[n]$ values in a Toeplitz structure

$$\hat{\mathbf{R}}_y = ((\hat{\rho}_y[r - c]))_{r,c} \quad (3.60)$$

Expressed directly in matrix notation based on (3.59) this can be also be expressed as

$$\hat{\mathbf{R}}_y = (2\pi)^{-1} \int_{\pi}^{\pi} \hat{P}_y(\psi) \mathbf{v}_{\psi}(\psi) \mathbf{v}_{\psi}^H(\psi) d\psi \quad (3.61)$$

It is also useful when comparing related techniques to understand how the formation of $\hat{\mathbf{R}}_y$ relates to the operations used in the traditional sample covariance matrix. We start by examining (3.57), which is equivalent in result to (3.59) , but operates directly on the snapshot data in space-time domain. First, define a windowed sample covariance matrix

$$\mathbf{R}_{\mathbf{w},SCM} = \frac{1}{M} \sum_{m=1}^M (\mathbf{x}_m \odot \mathbf{w}) (\mathbf{x}_m \odot \mathbf{w})^H \quad (3.62)$$

The classical sample covariance matrix, $\mathbf{R}_{SCM} = \frac{1}{M} \sum_{m=1}^M \mathbf{x}_m \mathbf{x}_m^H$, uses (3.62) with $\mathbf{w} = \mathbf{1}$, the all one's vector. Showing the entries in the matrix in (3.62) explicitly

$$\mathbf{R}_{\mathbf{w},SCM} = \frac{1}{M} \sum_{m=1}^M \begin{bmatrix} x_{m,[0]} w_{[0]} x_{m,[0]}^* w_{[0]}^* & x_{m,[0]} w_{[0]} x_{m,[1]}^* w_{[1]}^* & \cdots & x_{m,[0]} w_{[0]} x_{m,[N-1]}^* w_{[N-1]}^* \\ x_{m,[1]} w_{[1]} x_{m,[0]}^* w_{[0]}^* & x_{m,[1]} w_{[1]} x_{m,[1]}^* w_{[1]}^* & & \\ x_{m,[2]} w_{[2]} x_{m,[0]}^* w_{[0]}^* & x_{m,[2]} w_{[2]} x_{m,[1]}^* w_{[1]}^* & & \\ \vdots & & \ddots & \\ x_{m,[N-1]} w_{[N-1]} x_{m,[0]}^* w_{[0]}^* & & & x_{m,[N-1]} w_{[N-1]} x_{m,[N-1]}^* w_{[N-1]}^* \end{bmatrix} \quad (3.63)$$

Comparing (3.56) to (3.63) we see that $\hat{\rho}_{y,m}[n]$ is the sum down each of the diagonals in the inner matrix in (3.63), where the diagonals correspond to the numbered index n as main, sub, or super diagonal according to

$$\begin{bmatrix} 0 & -1 & -2 & \cdots & -(N-1) \\ 1 & \searrow & \searrow & \searrow & \\ 2 & \searrow & & & \\ \vdots & \searrow & & & \\ N-1 & & & & \end{bmatrix} \quad (3.64)$$

By averaging over multiple snapshots, therefore, $\hat{\rho}_y[n]$ is the sum down the diagonals of $\mathbf{R}_{\mathbf{w},SCM}$. The covariance matrix $\hat{\mathbf{R}}_y$ is then populated with entries from $\hat{\rho}_y[n]$. Going forward as a convention, we will define this operation as diagonal-sum-replace (DSR), with a notation indicating the operation as

$$\hat{\mathbf{R}}_y = \text{DSR}(\mathbf{R}_{\mathbf{w},SCM}) \quad (3.65)$$

The DSR operation acts in a linear fashion for addition of matrices $\mathbf{A}, \mathbf{B} \in \mathbb{C}^{N \times N}$

$$\text{DSR}(\mathbf{A} + \mathbf{B}) = \text{DSR}(\mathbf{A}) + \text{DSR}(\mathbf{B}) \quad (3.66)$$

as well as in regards to the expectation operator

$$E\{\text{DSR}(\mathbf{A})\} = \text{DSR}(E\{\mathbf{A}\}) \quad (3.67)$$

3.4.2 Expected Value - Stationary Random Process

We now look at the expected value of the covariance, $\hat{\mathbf{R}}_y$, for the WSS space-time process. From (3.58), the expected value of $\hat{P}_y(\psi)$ is related to the sample autocorrelation, $\hat{\rho}_y[n]$,

$$E \left\{ \hat{P}_y(\psi) \right\} = \sum_{n=-(N-1)}^{N-1} e^{-j\psi n} E \left\{ \hat{\rho}_y[n] \right\} \quad (3.68)$$

The expected value of $E \left\{ \hat{\rho}_y \right\} = E \left\{ \hat{\rho}_{y,m} \right\}$.

$$E \left\{ \hat{\rho}_{y,m}[n] \right\} = R_x[n] \sum_{\beta=0}^{N-1} w[\beta] w^*[\beta - n] \quad (3.69)$$

where $R_x[n]$ is the ensemble covariance. The remaining summation term is the sample autocorrelation of the window, $\rho_{\mathbf{w}}[n] = \sum_{m=0}^{N-1} w[m] w^*[m - n]$. The final result for the expectation is then

$$E \left\{ \hat{\rho}_y[n] \right\} = R_x[n] \rho_{\mathbf{w}}[n] \quad (3.70)$$

From (3.70) directly, the expected value of the covariance matrix is

$$E \left\{ \hat{\mathbf{R}}_y \right\} = \mathbf{R}_x \odot \mathbf{R}_{\mathbf{w}} \quad (3.71)$$

where $\mathbf{R}_{\mathbf{w}} = \text{DSR}(\mathbf{w}\mathbf{w}^H) = ((\rho_{\mathbf{w}}[r - c]))_{r,c}$. Looking at the result in the frequency domain, using (3.70) in (3.68), we have

$$E \left\{ \hat{P}_y(\psi) \right\} = \sum_{n=-(N-1)}^{N-1} R_x[n] \rho_{\mathbf{w}}[n] e^{-j\psi n} \quad (3.72)$$

This can be expressed in the ψ domain as the convolution of the power pattern of the window, $C_{\mathbf{w}}(\psi) = |W(\psi)|^2 = \mathcal{F}(\rho_{\mathbf{w}}[n])$, with the underlying model spectrum, $P_{x,\psi}(\psi)$

$$\begin{aligned}
E \left\{ \hat{P}_y(\psi) \right\} &= C_{\mathbf{w}}(\psi) \circledast P_{x,\psi}(\beta) \\
&= \frac{1}{2\pi} \int_{-\pi}^{\pi} C_{\mathbf{w}}(\psi - \beta) P_{x,\psi}(\beta) d\beta
\end{aligned} \tag{3.73}$$

3.4.3 Performance Based On Expected Value

The result for the expected value of the covariance, (3.71), can be used to assess the performance of the algorithm. For a given window function (a.k.a. taper), \mathbf{w} , we first determine the matrix $\mathbf{R}_{\mathbf{w}} = \text{DSR}(\mathbf{w}\mathbf{w}^H)$. For each particular problem of interest, e.g., single plane wave in uncorrelated noise, from the known model ensemble covariance, \mathbf{R}_x . Using these in the normalized SINR loss expression (from Chapter 2) we can analyze adaptive beamformer performance using CSS.

$$\xi = \frac{\mathbf{s}^H (\mathbf{R}_x \circledast \mathbf{R}_{\mathbf{w}})^{-1} \mathbf{s}}{\mathbf{s}^H \mathbf{R}_x^{-1} \mathbf{s}} \cdot \frac{\mathbf{s}^H (\mathbf{R}_x \circledast \mathbf{R}_{\mathbf{w}})^{-1} \mathbf{s}}{\mathbf{s}^H (\mathbf{R}_x \circledast \mathbf{R}_{\mathbf{w}})^{-1} \mathbf{R}_x (\mathbf{R}_x \circledast \mathbf{R}_{\mathbf{w}})^{-1} \mathbf{s}} \tag{3.74}$$

Because of the Hadamard product nature of the relationship several things become apparent.

1. As the window function becomes ideal, the corresponding $\rho_{\mathbf{w}}[n] = 1$, and $\mathbf{R}_{\mathbf{w}} = \mathbf{1}$, the Hadamard product identity (the all 1's matrix). The estimated covariance goes to the ideal, $\hat{\mathbf{R}}_y \rightarrow \mathbf{R}_x$, and there is no performance loss. This corresponds to an idealized power pattern $C_{\mathbf{w}}(\psi) = 2\pi\delta(\psi)$. Such a power pattern requires an infinite number of elements in the array. For practical arrays there will be a bias to the resultant covariance matrix because of the non-zero width of $C_{\mathbf{w}}(\psi)$, indicating that, in general, this approach will not converge to the optimal solution. What we are interested in is the impact of the bias, and if there are conditions where the impact to performance is negligible.
2. It is difficult to simplify analysis because of the element-by-element nature of the

operation. There is no easy expression for the inverse of a Hadamard product, and other properties that are available are not helpful in the analysis of normalized SINR loss. This means we have to consider defined scenarios, and simulate over the range of parameters, such as $(\psi_s - \psi_o)$ and σ_n^2/σ_w^2 in the single plane wave interferer case.

3. The particular form of the classical window functions used for spectral estimation result in \mathbf{R}_w that is a normalized diagonally homogeneous correlation matrix, meaning it has a constant value on its main diagonal. From the eigenvalue majorization theorem [71], the eigenvalue spread of $\mathbf{R}_x \odot \mathbf{R}_w$ is less than or equal to the eigenvalue spread of \mathbf{R}_x . One can arrive at the same conclusion intuitively based on the following two points: 1) the eigenvalues are bounded by the min/max of the power spectrum [72] 2) the technique used here effectively convolves the underlying power spectrum with a smoothing window (the power pattern), which will decrease the resultant min/max of the smoothed spectrum compared to the original. Related details are available in the context of covariance matrix tapers in [53]. This property, while desirable because it lowers the condition number of the matrix, $\text{cond}(\mathbf{A}) = \frac{\lambda_{\max}(\mathbf{A})}{\lambda_{\min}(\mathbf{A})}$, does not give any further insight into performance, in particular since the matrix product, $\mathbf{R}_x \odot \mathbf{R}_w$, is biased compared to the ensemble covariance \mathbf{R}_x .
4. The analysis is for expected value, and assumes that the $\hat{P}_y(\psi)$ spectrum is the ideal $P_x(\psi)$ convolved with the function $C_w(\psi)$. In practice, classical PSD techniques will average over the M snapshots to reduce the variability in the estimate of the spectrum.

3.4.4 Prototype Power Pattern

To assist in the normalized SINR loss analysis we define a “prototype” window function. The idea here is that the power pattern, $C_w(\psi)$, is defined by an ideal bandlimited portion useful for identifying the impacts of mainlobe width, and a constant offset portion useful for identifying the impacts of sidelobes, or spectral leakage. Given definition for these

regions, the analysis is more straightforward and we can look at the two factors individually. Classically defined windows incorporate both features together, in some trade-off related to their design, making the analysis of individual window functions less insightful. We use subscripts in defining the prototype window as follows: lb stands for local bias and relates to the main lobe region, bb stands for broadband bias and corresponds to the sidelobe levels. $C_{\mathbf{w}}(\psi)$ is a periodic function with period 2π , and is defined explicitly over the region of support, $|\psi| \leq \pi$, as

$$C_{\mathbf{w}}(\psi) = C_{lb}(\psi) + C_{bb}(\psi) \quad (3.75)$$

The mainlobe is defined by an ideal bandlimited function

$$C_{lb}(\psi) = \begin{cases} A_{lb} & |\psi| \leq \psi_{lb} \\ 0 & |\psi| > \psi_{lb} \end{cases} \quad (3.76)$$

and the sidelobe level is defined by a constant

$$C_{bb}(\psi) = A_{bb} \quad |\psi| \leq \pi \quad (3.77)$$

The scale factors, A_{lb} and A_{bb} , are constrained according to the normalization

$$\frac{1}{2\pi} \int_{-\pi}^{\pi} C_{\mathbf{w}}(\psi) d\psi = 1 \quad (3.78)$$

By specifying two of the three parameters, $\{A_{lb}, A_{bb}, \psi_{lb}\}$, typically the latter two, and varying them separately, we can see their respective influence on performance. This provides a general feel for behavior of normalized SINR loss using classical PSD techniques. We have already shown that $E\{\hat{\mathbf{R}}_y\} = \mathbf{R}_x \odot \mathbf{R}_w$, so all that is necessary is to find \mathbf{R}_w for the prototype window. For the definition in (3.75), there is a closed form solution based on

the parameters, so it is straightfoward to find $\rho_{\mathbf{w}}[n]$. Starting with the Fourier transform relationship

$$\rho_w[n] = \frac{1}{2\pi} \int_{-\pi}^{\pi} C_w(\psi) e^{j\psi n} d\psi \quad (3.79)$$

we substitute in the definition for $C_{\mathbf{w}}(\psi)$ showing the explicit local and broadband bias terms

$$\rho_{\mathbf{w}}[n] = \frac{1}{2\pi} \int_{-\pi}^{\pi} [C_{lb}(\psi) + C_{bb}(\psi)] e^{j\psi n} d\psi \quad (3.80)$$

The solution consists of two terms, $\rho_{\mathbf{w}}[n] = \rho_{lb}[n] + \rho_{bb}[n]$. For the first term, $\rho_{lb}[n]$, we have

$$\rho_{lb}[n] = \frac{1}{2\pi} \int_{-\pi}^{\pi} C_{lb}(\psi) e^{j\psi n} d\psi = A_{lb}(\psi_{lb}/\pi) \text{sinc}([\psi_{lb}/\pi]n) \quad (3.81)$$

where $\text{sinc}(x) \equiv \sin(\pi x)/(\pi x)$. The second term, $\rho_{bb}[n]$, is

$$\rho_{bb}[n] = \frac{1}{2\pi} \int_{-\pi}^{\pi} C_{bb}(\psi) e^{j\psi n} d\psi = A_{bb}\delta[n] \quad (3.82)$$

The complete autocorrelation sequence, $\rho_{\mathbf{w}}[n]$, is the sum of the two

$$\rho_{\mathbf{w}}[n] = A_{lb}(\psi_{lb}/\pi) \text{sinc}([\psi_{lb}/\pi]n) + A_{bb}\delta[n] \quad (3.83)$$

Expressed in matrix form, where $\mathbf{R}_{lb,bb} = ((\rho_{lb,bb}[r-c]))_{r,c}$, we have

$$\mathbf{R}_{\mathbf{w}} = \mathbf{R}_{lb} + \mathbf{R}_{bb} \quad (3.84)$$

The resultant expected value of the estimated covariance matrix is then

$$E \left\{ \hat{\mathbf{R}}_y \right\} = \mathbf{R}_x \odot [\mathbf{R}_{lb} + \mathbf{R}_{bb}] \quad (3.85)$$

Observe in (3.85) that the broadband bias term, \mathbf{R}_{bb} , is a diagonal matrix with constant diagonal A_{bb} . The overall affect of the broadband bias term is the same as a diagonal loading in that it increases the main diagonal of the estimated covariance matrix. This is accomplished as a multiplicative, not additive, effect.

The prototype window described by (3.75) is not realizable with any array of finite length. So it is not possible to determine a set coefficients, \mathbf{w} , that would result in a power pattern of this type. This does not prevent our analysis, however, since we assume that the estimated spectra is available, $\hat{P}_y(\psi) = C_{\mathbf{w}}(\psi) \otimes P_{x,\psi}(\psi)$, and not how it was computed. The intent is to use the analysis to understand performance issues when using classical techniques. The conditions where the process works well and doesn't work well can be identified, and then used to guide development to extend the range of situations allowing useful operation.

3.4.5 Prototype Window Normalized SINR Loss

We now use (3.84) in the expression for SINR loss (3.74). The Hadamard product structure within the expression, (3.74) prevents a more compact form. Strictly speaking, the value of ξ found using (3.74) is not a random variable but a constant, since we are using the expected value of the estimated covariance, $E \left\{ \hat{\mathbf{R}}_y \right\}$. To understand the statistical behavior of ξ , we would need to insert the computational form of the estimated covariance given in (3.65) into (3.74). This is also not easily reducible to a more compact form. Morgera encountered similar difficulties for a Toeplitz structure constrained covariance estimator [8].

The conclusion is that for this type of structured covariance matrix estimation algorithm, the normalized SINR loss cannot be simplified into an expression that does not involve the particular covariance, \mathbf{R}_x , for the problem. This is unlike sample covariance matrix methods, where the performance can be derived in closed form as a random variable and

shown to be function of number of elements and snapshots only [29]. Performance of this structured covariance method depends on the problem. We can still use (3.74) to understand SINR loss performance, but have to be specific in defining the scenarios analyzed.

By specifying the parameters of our prototypical window function ($[A_{lb}$ or $A_{bb}]$, ψ_{lb}), for particular types of interference problems we will use the (3.74) to predict performance. We consider with the single plane wave interferer in uncorrelated noise case, signal of interest not present. This case, while simple, will highlight some of the features and weaknesses of the approach.

Single Plane Wave Interferer

Using (3.74) we analyze the impact of using CSS for the single plane wave in uncorrelated noise case. Normalized SINR loss is computed as a function of distance between the desired signal direction of arrival and the interferer location in ψ -space, $\Delta\psi = (\psi_s - \psi_o)$. For each $\Delta\psi$ we vary the difference between the per element INR and a fixed sidelobe level, A_{bb} . This is done for three values of ψ_{lb} , set to multiples of the mainlobe half width of the array, $(1, 2, 3)\frac{2\pi}{N}$. By increasing ψ_{lb} we get an indication of performance when using wider mainlobe windows, or operating below the design frequency.

Figures (3.7) - (3.8) show the results, plotting $\xi_{dB} = -10 \log_{10} \xi$. In each Figure there are four plots. In the upper left is an image showing the ξ_{dB} surface as a function of $\Delta\psi$ and $(INR_{PE} + A_{bb})$ in dB for the particular case of $\psi_{lb} = 2\pi/N$. This subplot provides some general behavior for the SINR loss surface. The values shown range from $[0, 1]$ dB, with $\xi_{dB} > 1$ being clipped at 1. This is to allow detailed visualization of the near optimal normalized SINR loss performance. For the purpose of analysis, we consider $\xi_{dB} < 1$ as good performance, and are not overly concerned with the behavior in higher normalized SINR loss regions. The upper right plot shows contour lines on the same $x - y$ plane, but for a fixed value of $\xi_{dB} = 0.2$ dB. Three curves are present, one for each of $\psi_{lb} = 2\pi/N \cdot \{1, 2, 3\}$ analyzed. The lower left and right plots show the same family of constant valued SINR loss contours, for values of $\xi_{dB} = 0.5, 1.0$ dB respectively. In Figure

3.7, the array has $N = 32$ elements, with $A_{bb} = -40$ dB. The same array is used in Figure 3.8, with an increased sibelobe suppression, $A_{bb} = -60$ dB. Figure 3.9 has increased array length $N = 64$ elements, with $A_{bb} = -40$ dB.

Several points become evident looking at the Figures. First, there is a large expanse in the $\Delta\psi - (INR_{PE} + A_{bb})$ plane where the normalized SINR loss performance is ≤ 0.5 dB. Clearly we would like to operate within this region. As $\Delta\psi$ approaches zero we begin to see real performance impacts. This effect gradually decreases as the $(INR_{PE} + A_{bb})$ value gets very small, indicating that if there were no interferer present performance would be nearly optimal.

As $(INR_{PE} + A_{bb})$ becomes large, > 10 dB, performance impacts are also observed. For sidelobe levels of most standard window functions, $A_{bb} > 30$ dB, so this occurs at INR greater than 40 dB per element. It is also interesting to note that it is not simply the spectral leakage due to the window that causes the performance loss. We can see this by comparing two cases with the same A_{bb} , the first with $\psi_{lb} = 2\pi/N$, and the second with $\psi_{lb} = 0$, an idealized window. The second case isolates the impact of the sidelobe level. Figure 3.10 shows the results for $N = 32$, $A_{bb} = -40$ dB, and $INR_{PE} = 40$ dB. The upper plot is the complete normalized SINR loss performance as a function of $\Delta\psi$. The blue trace is for non-zero mainlobe width, $\psi_{lb} = 2\pi/N$. Below $\Delta\psi = 0.20\pi$ the SINR loss is substantial. The same curve for the $\psi_{lb} = 0$ case, shown in red, is negligible. The lower plot is a zoomed area of the top plot, highlighting the loss range $[0,1]$ dB. Without mainlobe width, the sidelobe level has an equivalent impact to a diagonal load, which would cause the equivalent of underestimation of INR . As was seen earlier in Section 3.2, this particular interference and noise environment is relatively insensitive to errors in estimate of INR .

These results indicate that for CSS covariance matrix estimation based on classical power spectral based methods, near optimal SINR loss performance can be achieved when the interference has sufficient separation from the desired signal, or in the event the interferer is near the desired signal, its power per sensor element is substantially below the sidelobe level of the window used. In practical situations these conditions cannot be guaranteed. This

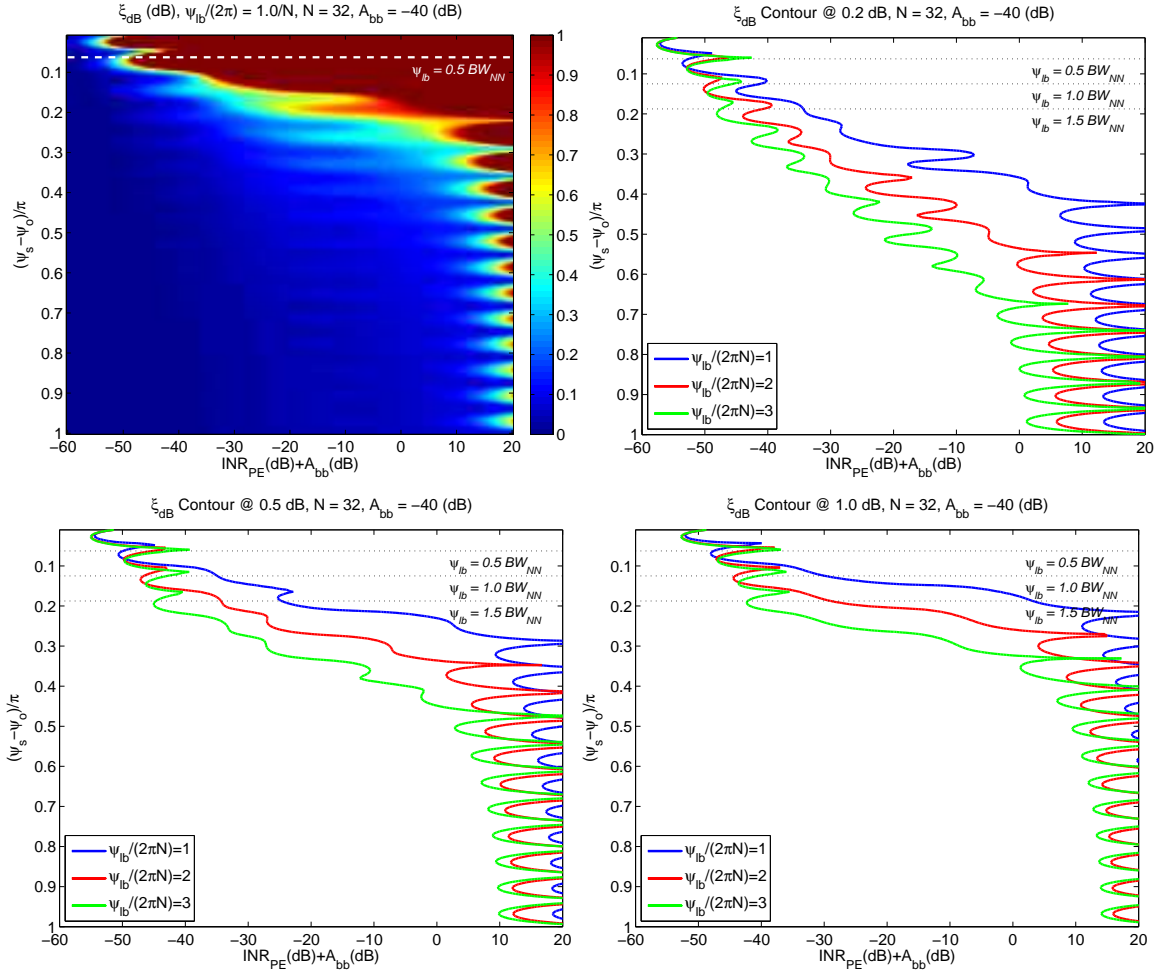


Figure 3.7: $N = 32$, **Normalized SINR loss (dB)** for $A_{bb} = -40$ dB: An analysis of normalized SINR loss shows near optimal performance when the interferer is far from the desired angle of arrival and sufficiently suppressed by the sidelobe of the window. Near the mainlobe, performance degrades quickly even as the INR is low.

leads us to consider methods to reduce the $(INR_{PE} + A_{bb})$ without modifying the window function used. One approach to address this is to detect that a discrete interferer is present, and subtract its influence from the data. The final covariance can then be computed using the parameters of the subtracted sources and the residual data covariance matrix. This type of process is similar to the harmonic analysis technique utilized by Thomson as part of his multi-taper spectral estimation [52], and we will refer to it as such going forward.

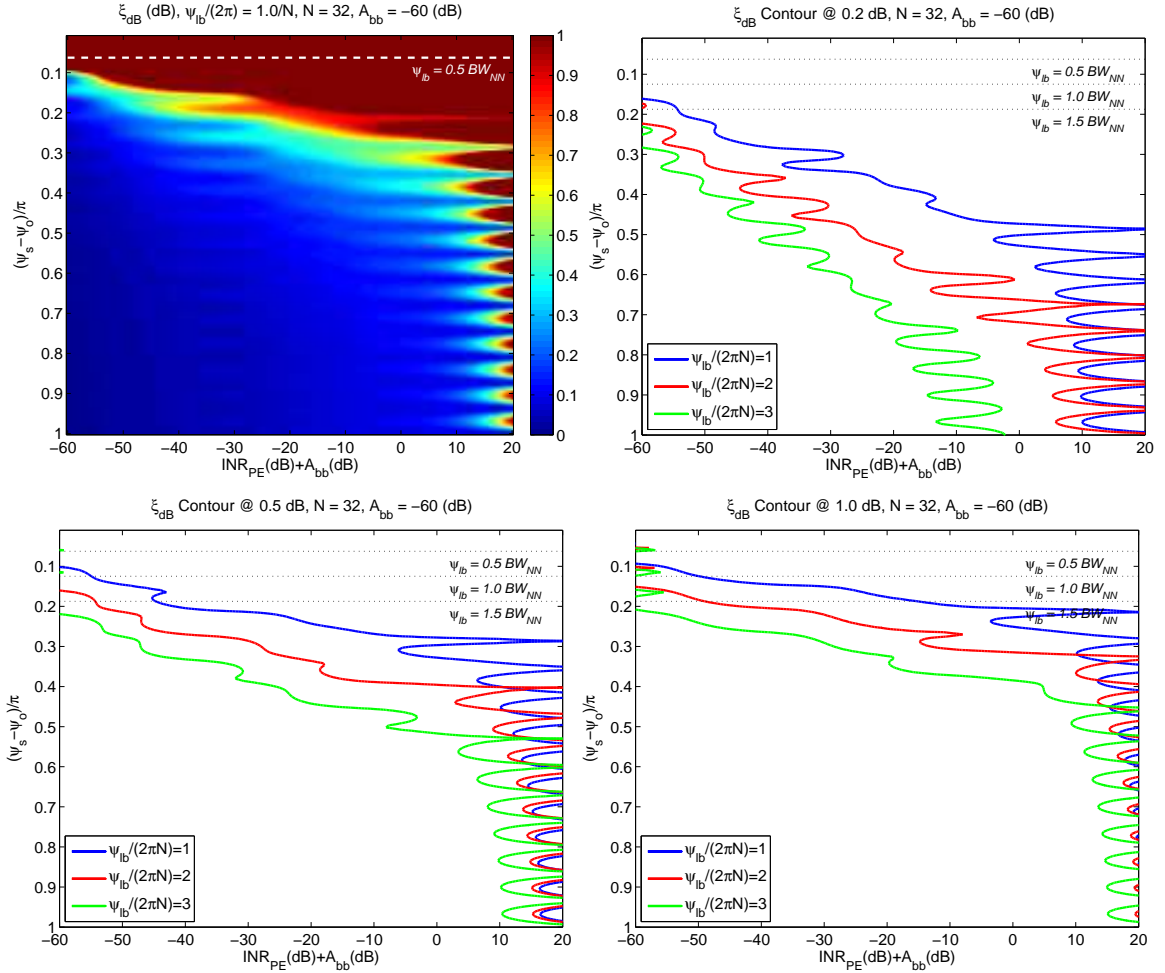


Figure 3.8: $N = 32$, **Normalized SINR loss (dB) for $A_{bb} = -60$ dB**: Increasing sidelobe suppression while maintaining a fixed width mainlobe improves tolerance to higher interferer INR , but at the expense of widening the area of degraded performance around the main lobe. Note that the x-axis units are $(INR + A_{bb})$ dB, so plots in this Figure represent INR that is 20 dB higher compared to Figure 3.7.

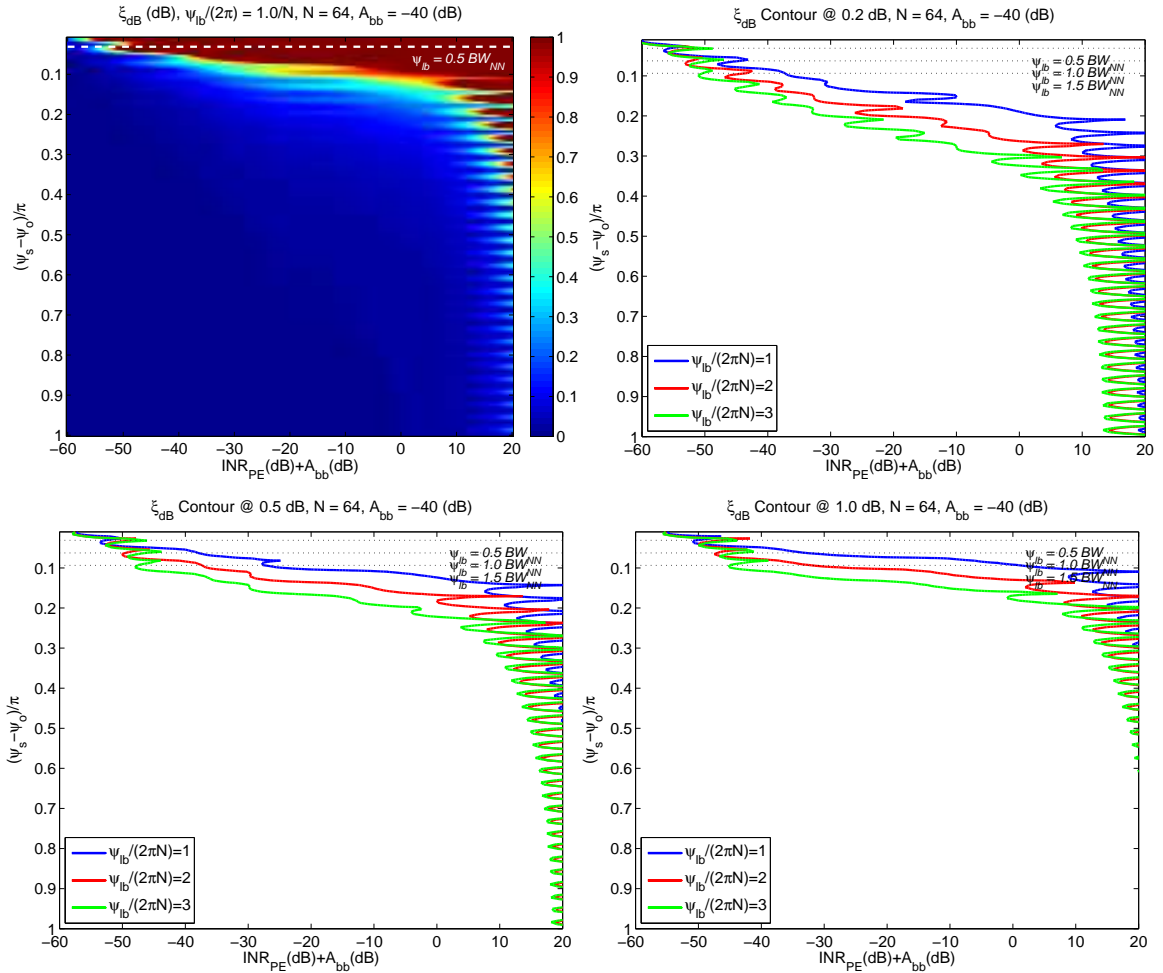


Figure 3.9: $N = 64$, **Normalized SINR loss (dB) for $A_{bb} = -40$ dB**: Increasing array aperture by a factor of 2 increases the region of good performance compared to Figure 3.7 in an absolute sense. When considered relative to the main lobe width they are comparable. This simply confirms that performance is driven by the array’s resolving capability, which improves with increased aperture.

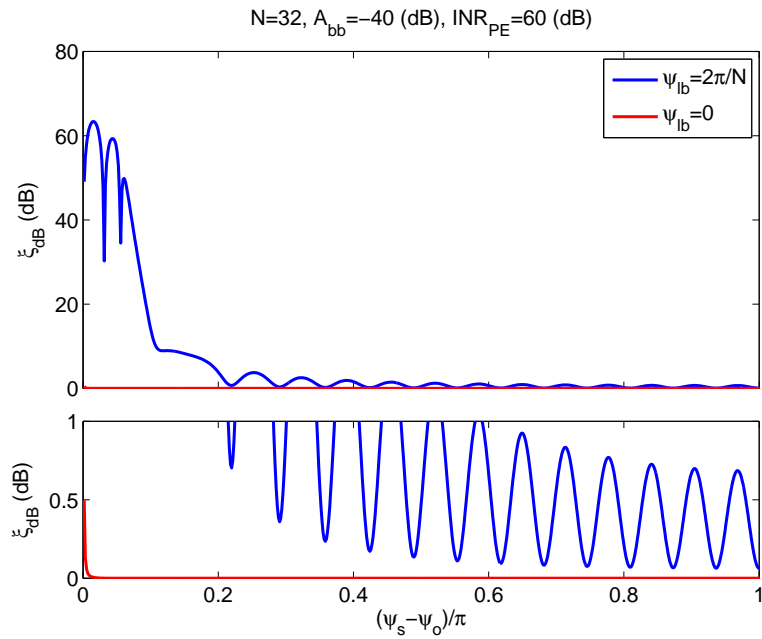


Figure 3.10: **Classical PSD, window main-lobe width impacts to performance:** A zero main lobe window (an ideal case shown in red) results in insignificant normalized SINR loss. A non-zero main lobe with the same sidelobe level (shown in blue) results in the normalized SINR loss seen in Figure 3.8. Non-zero main lobe width with no sidelobes (not shown) has the similar performance but lower ripple as $(\psi_s - \psi_o)/\pi$ increases.

3.5 Summary

This chapter investigated how to use the frequency-wavenumber spectrum as a basis for covariance matrix estimation. Analysis of a simple single plane wave interferer in white noise showed that the adaptive processor is relatively insensitive to estimation error of INR . Performance is more affected by wavenumber estimation accuracy in direct relation to the accurate placement of nulls, but the necessary performance is achievable in few or even one snapshot. The CR bound indicates estimation accuracy is inversely proportional to the number of snapshots, as M^{-1} , and number of sensors, as N^{-2} . This is in contrast to the closed form performance of sample covariance matrix techniques, where performance does not depend on the number of sensors, just the number interferers and snapshots (with use of diagonal loading). The model for the components in the desired covariance matrix was reviewed, as was the simple method for relating the covariance to the spatial spectrum using FFT techniques. Covariance matrix estimates developed in this manner, using classical power spectral estimation techniques, were seen to be biased. The normalized SINR loss performance indicated that to broaden the conditions under which useful performance can be achieved requires an additional step of harmonic analysis, the detection and subtraction of line components from the data.

Chapter 4: Structured Covariance Estimation with Thomson's MTSE

4.1 Introduction

Section 3.4 investigated performance of adaptive beamforming using covariance matrix estimates based on the wavenumber spectrum using classical spectral estimation techniques. The expected value of the estimated covariance is biased, $E\{\mathbf{R}_{PSD}\} = \mathbf{R}_x \odot \mathbf{R}_w$, so in general adaptive beamformers based on the CSS covariance do not converge to the optimal Wiener solution. However, analysis of the SINR loss performance for the uniform linear array case, as function of interferer to desired signal spacing, $\Delta\psi$, window characteristics, and INR showed that performance is within a few tenths of a dB from optimal under some conditions.

To maintain good normalized SINR loss performance, the interferer must have sufficient separation from the desired signal, in proportion to the window mainlobe width, $\Delta\psi \geq 2\psi_{lb} - 3\psi_{ub}$, with an interferer to noise ratio such that $(INR_{PE} + A_{bb}) \leq 10 \log_{10}(N)$ (dB). This was evident in Figures 3.7, 3.8, and 3.9. To continue to achieve good performance with smaller separation required the condition $(INR_{PE} + A_{bb}) \ll 0$ (dB). Neither of these conditions can be guaranteed in practice. These concerns motivate use of Thomson's multi-taper spectral estimation (MTSE) in forming the estimate of the frequency-wavenumber spectra instead of the classical techniques. This is for three reasons.

1. First, while the equivalent MTSE mainlobe width is larger than traditional window functions it provides two benefits: 1) averaging increased number of uncorrelated estimates of power within a particular band in wavenumber-space results in lower variance locally 2) estimates of the eigencoefficients within a particular band in wavenumber-space allow for direct formulation of a detection problem for line components based

on the underlying model for the stationary process and the Cramér spectral representation theorem. This eliminates the need to design new detection procedures based on estimated spectrum only, such as local noise floor averaging, etc., and can be done prior to forming the covariance matrix.

2. The parameters, amplitude, frequency and phase of the detected line components are used to coherently cancel (subtract) them from the data and the estimation process is repeated on the residual. This process is known as harmonic analysis and can be carried out iteratively [73] .
3. Combination of the various eigenspectra is accomplished via an adaptive weighting mechanism designed to minimize local and broadband bias [52, 56, 74], which often results in an equivalent window with very low sidelobe level, typically below -60 dB.

In this chapter we specify the details of incorporating Thomson’s MTSE, reviewed earlier in Chapter 2, into the covariance estimation procedure. The normalized SINR loss of this algorithm is then assessed via simulation with various signal and interference environments, and compared to other reduced rank algorithms as a function of available snapshots.

4.2 Covariance from Spatial Spectra (CSS) with MTSE

4.2.1 Introduction

This section provides the procedural outline for using Thomson’s MTSE with harmonic analysis as the method of choice for estimating the frequency-wavenumber spectra necessary to form an estimate of the covariance matrix at the output of the array. The development considers an N element uniform linear array, extension to more general geometries is considered in Chapter 7. The process has a mixed spectrum, with K point source signals having independent, random complex-valued amplitudes, $a_k(m) \stackrel{d}{\rightarrow} CN(0, \sigma_k^2)$. M snapshots are available for processing. The snapshot model is

$$\mathbf{x}_m = \sum_{k=1}^K \mathbf{v}_k a_k(m) + \mathbf{n}_{b,m} + \mathbf{n}_{w,m}, \quad \mathbf{x}_m \stackrel{d}{\rightarrow} CN_N \quad (4.1)$$

An estimate for the frequency-wavenumber spectra, for both process and sensor noise, $\hat{P}_x(\psi)$, is formed using MTSE, and used to compute an estimate of the covariance.

$$\hat{\mathbf{R}}_x = (2\pi)^{-1} \int_{\pi}^{\pi} \hat{P}_x(\psi) \mathbf{v}_{\psi}(\psi) \mathbf{v}_{\psi}^H(\psi) d\psi \quad (4.2)$$

The integral in (4.2) may be implemented using a numerical summation

$$\hat{\mathbf{R}}_x = \frac{\Delta k}{2\pi} \sum_{b=-L/2}^{L/2-1} \hat{P}_x(l\Delta k) \mathbf{v}(l\Delta k) \mathbf{v}^H(l\Delta k) \quad (4.3)$$

Alternatively, for the uniform linear array one can take advantage of the frequency-wavenumber spectrum and covariance being single dimension, and relate them by the 1-D inverse Fourier transform

$$\hat{R}_x[n] = \frac{1}{2\pi} \sum_{l=0}^{L-1} \hat{P}_x(l\Delta k) e^{jl\Delta kn} \quad (4.4)$$

and populate the covariance matrix as $\hat{\mathbf{R}}_x = ((\hat{R}_x[r-c]))_{r,c}$. If the value of L permits use of fast Fourier transform techniques, this is the most efficient implementation.

4.2.2 Number of Tapers, D

To exploit the efficiencies of FFT based processing when using MTSE to estimate the spectrum, $\hat{P}_x(\psi)$, we allow the spectral estimation to maintain a fixed resolution in normalized wavenumber space, $\psi = -k_z d$. This allows a single set of tapers to be used. A necessary design choice is the width of the analysis region, W , where typically choices are

$NW = 1.5, 2.0, 2.5$. The number of significant tapers supported by a particular width, W , is $D = 2NW - 1$. The case of $NW = 1$ results in a single usable taper and reverts to a standard classical PSD method. No harmonic analysis is possible in this scenario. As a practical matter we usually select $D = 2NW$. The last taper is not as concentrated in the analysis region but still provides useful information. This is done to increase the number of basis vectors used in the harmonic analysis detection statistic. The D tapers are designed according to the appropriate eigenvalue or generalized eigenvalue problem [52,66]. For the ULA case , the resultant tapers are the discrete prolate spheroidal sequences.

$$q_d(n) = \text{dpss} (N, NW) , d = 1, \dots , D \quad (4.5)$$

4.2.3 FFT and Zero-Padding

Snapshot data are windowed and FFT'd to produce the MTSE eigencoefficients

$$y_m^{(d)}(l) = \sum_{n=0}^{N-1} x_m(n) q_d(n) \exp(-j2\pi ln/N_{FFT}) \quad (4.6)$$

for the set of points $l = 0, \dots, N_{FFT} - 1$. We specify the FFT size, N_{FFT} , in (4.6) independently from the number of array elements, N . The nominal set of points would be $N_{FFT} = N$, with a greater number of points, $N_{FFT} > N$, generated using the zero-padding technique [59] ($N_{FFT} < N$ is possible using polyphase techniques [75] but not likely a case of interest as typically applications scan through more points in wavenumber space, or direction of arrival, than N and not less). The zero-pad operation is important for several reasons. First, and most importantly, the detection process within harmonic analysis performs a subtraction of discrete harmonic (point source) components in the data. This is done by estimating the unknown line component parameters: wavenumber, amplitude, and phase. Many algorithms exist for estimating parameters of sinusoids in noise. Assuming that multiple interferers are sufficiently separated, these parameters are conveniently estimated optimally using FFT techniques [76]. The precision to which this

can be accomplished, without additional techniques such as curve fitting between FFT bins, is directly proportional to the fineness of the FFT spacing in wavenumber space. The zero-padding operation is an efficient method for increasing this fineness. The zero-padding is also useful in the smoothing operation Thomson refers to as free parameter expansion, FPE [52]. The zero-padded bins are effectively the values required to perform the operation.

4.2.4 Discrete Line Component Processing (Harmonic Analysis)

The harmonic analysis algorithm operates on the eigencoefficients, $Y_{m,d}(l)$, to determine the presence of discrete line components as presented in Section 2.6.2. The detection statistic is computed as the ratio of the power in the line component subspace to the power outside that subspace in the region $[f_o - W < f \leq f_o + W]$.

$$F(f_o) = \frac{\sum_{m=1}^M \mathbf{y}_m^H(f_o) \mathbf{P}_q \mathbf{y}_m(f_o)}{\sum_{m=1}^M \mathbf{y}_m^H(f_o) \mathbf{P}_q^\perp \mathbf{y}_m(f_o)} \underset{H_0}{\overset{H_1}{\gtrless}} \gamma_{TH} \quad (4.7)$$

The choice of threshold, γ_{TH} , can be determined using a Neyman-Pearson criteria assuming Gaussian noise statistics. Practically, it is also useful to define a minimum limit allowable for detection, e.g., $\gamma_{min}^{(dB)} = 10 \log_{10}(\gamma_{min})$, such that

$$\gamma_{TH} = \max(\gamma_{NP}, \gamma_{min}) \quad (4.8)$$

with $\gamma_{min}^{(dB)} = 3$ dB typically. This non-optimal lower limit is a simple mechanism to prevent excessive false detections due to non-Gaussian noise or numerical issues associated with iterative line component subtraction (below). This has a minimal impact on overall performance, as the main purpose of the harmonic analysis step is to eliminate high powered, not low powered, discrete interference. This test is valid for a single line component present within the analysis region, $[f_o - W < f \leq f_o + W]$. If the interference environment is dense with respect to the array resolution, additional tests such as the double F line test in [74] may be appropriate.

For a detected line component, it is assumed that the wavenumber remains constant across all snapshots. For the k^{th} line component the wavenumber, ψ_k , is required to estimate the remaining parameters per snapshot and form the overall covariance matrix. With sufficient zero-padding, ψ_k , can be estimated as

$$\hat{\psi}_k = \arg \max_{\psi} F(\psi) > \gamma_{TH} \quad (4.9)$$

The remaining parameters are estimated per snapshot using matched filter techniques. Defining the reference sinusoid waveform

$$\mathbf{s}_{ref,k} = ((e^{j\psi_k n}))_n \quad (4.10)$$

the complex-amplitude and interferer power are estimated as

$$\hat{a}_k(m) = \frac{1}{N} \mathbf{s}_{ref,k}^H \mathbf{x}_m, \quad \hat{\sigma}_k^2 = \frac{1}{M} \sum_{m=1}^M |\hat{a}_k(m)|^2 \quad (4.11)$$

While not required strictly for the processing, the interferer to noise ratio for each detected discrete component may be estimated. This is useful when generating a composite spectrum for visualization. A composite spectrum is generated based on the estimated continuous background spectrum of the residual snapshot data (post harmonic analysis), with numerical insertion of the discrete components. The insertion technique requires knowledge of the INR to properly represent the uncertainty of a particular estimate.

$$INR_k = \frac{\sum_{m=1}^M |\hat{a}_k(m)|^2}{(D-1)^{-1} \sum_{m=1}^M \mathbf{y}_m^H \left(\hat{\psi}_k \right) \mathbf{P}_{\mathbf{q}}^{\perp} \mathbf{y}_m \left(\hat{\psi}_k \right)} \quad (4.12)$$

Influence of the K detected components is removed from the snapshot data to produce the residual data snapshots, $\mathbf{x}_{b,m}$. This can be accomplished with one of two methods.

Method 1. Coherent Subtraction

$$\mathbf{x}_{b,m} = \mathbf{x}_m - \sum_{k=1}^K \hat{a}_k(m) \mathbf{s}_{ref,k} \quad (4.13)$$

Method 2. Null Projection

$$\mathbf{P}_k^\perp = \mathbf{I} - \mathbf{s}_{ref,k} (\mathbf{s}_{ref,k}^H \mathbf{s}_{ref,k})^{-1} \mathbf{s}_{ref,k}^H \quad (4.14)$$

$$\mathbf{P}_K^\perp = \prod_{k=1}^K \mathbf{P}_k^\perp \quad (4.15)$$

$$\mathbf{x}_{b,m} = \mathbf{P}_K^\perp \mathbf{x}_m \quad (4.16)$$

Method 2 is more computationally intensive, but is not sensitive estimation accuracy of the amplitude coefficients, $\hat{a}_k(m)$.

4.2.5 Background / Continuous Spectrum

Once harmonic analysis is complete the residual snapshot data is used to compute the final smooth, continuous background spectrum. The snapshot data are windowed and FFT'd to produce the eigencoefficients

$$y_{b,m}^{(d)}(l) = \sum_{n=0}^{N-1} x_{b,m}(n) q_d(n) \exp(-j2\pi ln/N_{FFT}) \quad (4.17)$$

The eigencoefficients are used to produce the individual eigenspectra.

$$\hat{P}_b^{(d)}(l) = \frac{1}{M} \sum_{m=1}^M \left| y_{b,m}^{(d)}(l) \right|^2 \quad (4.18)$$

The individual eigenspectra are then linearly combined according to a set of weights

$$\hat{P}_{x,b}(l) = \sum_{d=1}^D h_d(l) \hat{P}_b^{(d)}(l) \quad (4.19)$$

The weights, $h_d(k)$, may be fixed, which is optimal for an underlying white spectrum, or determined adaptively. We use the algorithm in Section 2.6.2, detailed in [56], as it provides the benefits of adaptivity with less complexity than the approach original presented by Thomson [52].

4.2.6 Covariance Matrix Computation

The final estimate of the covariance matrix is the formed using line component and continuous background spectrum products.

$$\hat{\mathbf{R}}_a = \text{diag}(\hat{\sigma}_1^2, \hat{\sigma}_2^2, \dots, \hat{\sigma}_K^2) \quad (4.20)$$

$$\hat{\mathbf{V}} = [\mathbf{s}_{ref,1}, \mathbf{s}_{ref,2}, \dots, \mathbf{s}_{ref,K}] \quad (4.21)$$

$$\hat{\mathbf{R}}_{MTSE} = \hat{\mathbf{V}} \hat{\mathbf{R}}_a \hat{\mathbf{V}}^H + (2\pi)^{-1} \int_{-\pi}^{\pi} \hat{P}_{x,b}(\psi) \mathbf{v}_\psi(\psi) \mathbf{v}_\psi^H(\psi) d\psi \quad (4.22)$$

4.2.7 Composite Spectrum Generation

Because we develop the estimate of the line and continuous components of the wavenumber spectrum, $\hat{P}_x(\psi)$, we may also be interested in visualizing this spectrum directly in addition to forming the covariance matrix. This is, of course, the original purpose of the power spectral density techniques we have used. The smooth continuous component is the direct output from the MTSE processing of the residual snapshot data, $\mathbf{x}_{b,m}$, yielding $\hat{P}_{x,b}(\psi)$. The discrete components previously estimated and subtracted are then added back into the numerical spectrum. To avoid implying better resolution than is available with the data,

peak width is set proportional to estimation accuracy given the estimated SNR of the line component.

Unbiased Spectral Estimate In White Noise

In this type of spectral estimation, each point in the spectral estimate is scaled such that it is an unbiased estimate of the noise power for a white noise input. In terms of classical PSD techniques, this implies that the window function has been scaled such that $\mathbf{w}^H \mathbf{w} = 1.0$. MTSE tapers are scaled in accordance with this approach. Plane wave, or discrete sinusoidal components experience a processing gain due to the coherent gain of the window function. The maximum gain achieved is obtained using $\mathbf{w} = \frac{1}{\sqrt{N}} \mathbf{1}$, and equates to $10 \log_{10}(N)$ dB. What this is saying is that a snapshot, $\mathbf{x}_m \stackrel{d}{\rightarrow} CN_N(0, \sigma^2 \mathbf{I})$, will produce an expected value at any power spectral estimate, $E \left\{ \hat{P}(\psi) \right\} = \sigma^2$, while a snapshot corresponding to a plane wave component, $\mathbf{x}_m = A_o \mathbf{v}_\psi(\psi_o)$ will produce a value of $E \left\{ \hat{P}(\psi_o) \right\} \leq N A_o^2$. Detailed discussion of the incoherent and coherent gain of the classical window functions is found in [63]. The coherent gain of the MTSE tapers can be found by computing

$$CG_{MTSE} = \frac{1}{D} \sum_{d=1}^D \left| \sum_{n=0}^{N-1} q_d(n) \right|^2 \quad (4.23)$$

Because the choice of coherent gain is somewhat arbitrary for the re-inserted spectral component, it is also sometimes convenient to use the maximum theoretical processing gain, $CG = 10 \log_{10}(N)$, such that the composite spectrum looks similar, on a relative scale, to that obtained using MVDR techniques.

$$\hat{P}_{dB}(\psi_k) = 10 \log_{10} \left(\frac{1}{M} \sum_{m=1}^M |A_k(m)|^2 \right) + 10 \log_{10}(N) \quad (4.24)$$

Refer to the earlier Figure 2.5 for a visualization of the effectiveness of harmonic analysis.

4.3 Performance Simulation

We now look at performance of the covariance from spatial spectrum (CSS) approach using Thomson's MTSE as presented in Section 4.2. Chapter 3 analyzed CSS performance using classical power spectral estimation techniques, and performance predictions highlighted the need to incorporate harmonic analysis to make the approach effective. Because the normalized SINR loss cannot be simplified to remove the underlying covariance from the expression, each type of noise and interference environment encountered may perform differently. The following sections look at several common scenarios to assess CSS with MTSE effectiveness under meaningful conditions.

4.3.1 Discrete Interference

The discrete interference test cases investigate CSS performance when the noise and interference environment consists of line components in spatially white noise for an N element uniform linear array. Monte Carlo simulation measures the normalized SINR loss performance as a function of the number of available snapshots, M , for the given test configuration. Four algorithms are run in each test case.

1. CSS using Thomson's MTSE as the spectral estimation algorithm. The parameters $NFPE$, NW , D , γ_{TH} are specified.
2. CSS using classical spectral estimation with a Hann window.
3. Sample covariance matrix with optimal diagonal loading. The loading factor is found via exhaustive search for the level providing the best normalized SINR loss performance at each test point.
4. Multistage Wiener Filter (MWF). The MWF rank, r , is set to $\min(r_{opt}, M)$, where the optimal reduced rank, r_{opt} , depends on the interference.

Fixed INR

The fixed *INR* test case has six high *INR* point sources located at $(-65^\circ, -40^\circ, -25^\circ, 30^\circ, 45^\circ, 60^\circ)$ with respect to broadside. All interferers have a per element *INR* of 50 dB. The steering vector, \mathbf{s} , corresponds to broadside. The optimal MWF rank is $r_{opt} = 6$, corresponding to the $K = 6$ strong interferers in the environment.

$N = 32$ Element Uniform Linear Array: For an $N = 32$ element ULA test case, the MTSE parameters are $NFPE = 64$, $NW = 2$, $D = 4$ and $\gamma_{TH} = 4$ dB. Figure 4.1 shows the results. In the top left of the Figure, various wavenumber spectral estimates are shown for $M = 10$ snapshots. The true locations of the interferers are indicated by the vertical black dotted lines, and the spatially white noise floor is indicated by the line at 0 dB. For MTSE with harmonic analysis all six interferers are clearly indicated. Due to estimation accuracies, there is residual energy in the interferer line components after subtraction. This shows in the final spectrum as the sidebands around the discrete lines, noticeable in this case due to the strong line component power. The lower left plot in the Figure shows the an example of the adaptive beamformer power pattern for CSS with MTSE in blue. All discrete interferers are properly nulled and the pattern shape near the mainlobe is in close agreement with the optimal MVDR pattern.

The normalized SINR loss performance in dB is shown on the right. The upper right shows the performance for $M = 1$ to 32, with the lower right showing a zoomed inset. For each algorithm tested there are two curves provided, one for both the 50th and 90th percentiles of performance (with the 90th percentile curve at or above the 50th). From the curves, the CSS with MTSE adaptive beamformer achieves within 1.5 dB from optimal in 90% of trials with two or more snapshots. Covariance estimated via a classical Hann windowed PSD is within 2 dB in 90% of trials. Optimal diagonal load and MWF perform identically, and follow the expected 3 dB in 50% of trials at $2K = 12$ snapshots. The CSS techniques show much faster convergence than the sample covariance based techniques, and operates with less snapshots than interferers, $M < K$.

$N = 16$ Element Uniform Linear Array: For an $N = 16$ element ULA test case, the MTSE parameters are $NFPE = 64$, $NW = 1.5$, $D = 3$ and $\gamma_{TH} = 4$ dB. Figure 4.2 shows the results in similar format to Figure 4.1. What is clear from the figure is that with the lower resolving capability of the array, due to its shorter length, the harmonic analysis is ineffective and the resulting normalized SINR loss is poor. Optimal diagonal loading and MWF perform identically to the $N = 32$ test case. This is because their performance is dictated by the number of interferers, K , and snapshots, M , and not the number of sensor elements, N . Approaches such as the double line test used by Haykin [74] could be applied to improve line component detection for closely spaced interferers. Results for $N = 24$ (not shown), show harmonic analysis to be partially effective, with normalized SINR loss slightly higher than the $N = 32$ case but still better than the comparative techniques.

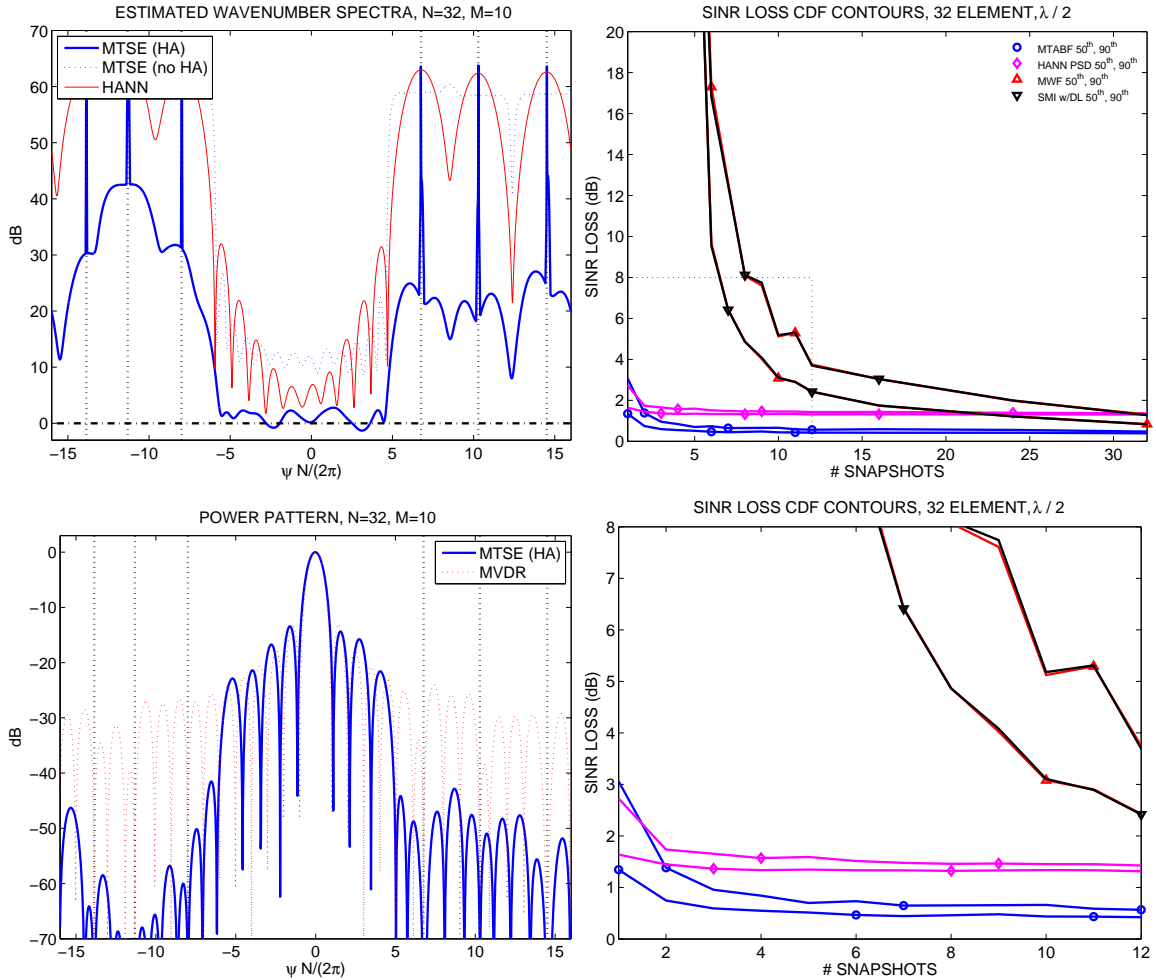


Figure 4.1: **ABF performance, fixed INR , $N = 32$** : Normalized SINR loss as a function of number of available snapshots, M , is shown on the right for a test case using an $N = 32$ uniform linear array observing $K = 6$ high INR interferers in spatially white noise. Both the 50th and 90th percentile performance are shown for each algorithm. This test case shows an adaptive beamformer derived using CSS with MTSE achieves within 1.5 dB from optimal in 90% of trials with two or more snapshots (blue trace). Covariance estimated via a classical Hann windowed PSD is within 2 dB (magenta trace). Optimal diagonal load (SMI w/DL, black trace) and multi-stage Wiener filter (MWF, red trace) perform identically, and follow the expected 3 dB in 50% of trials at $2K = 12$ snapshots.

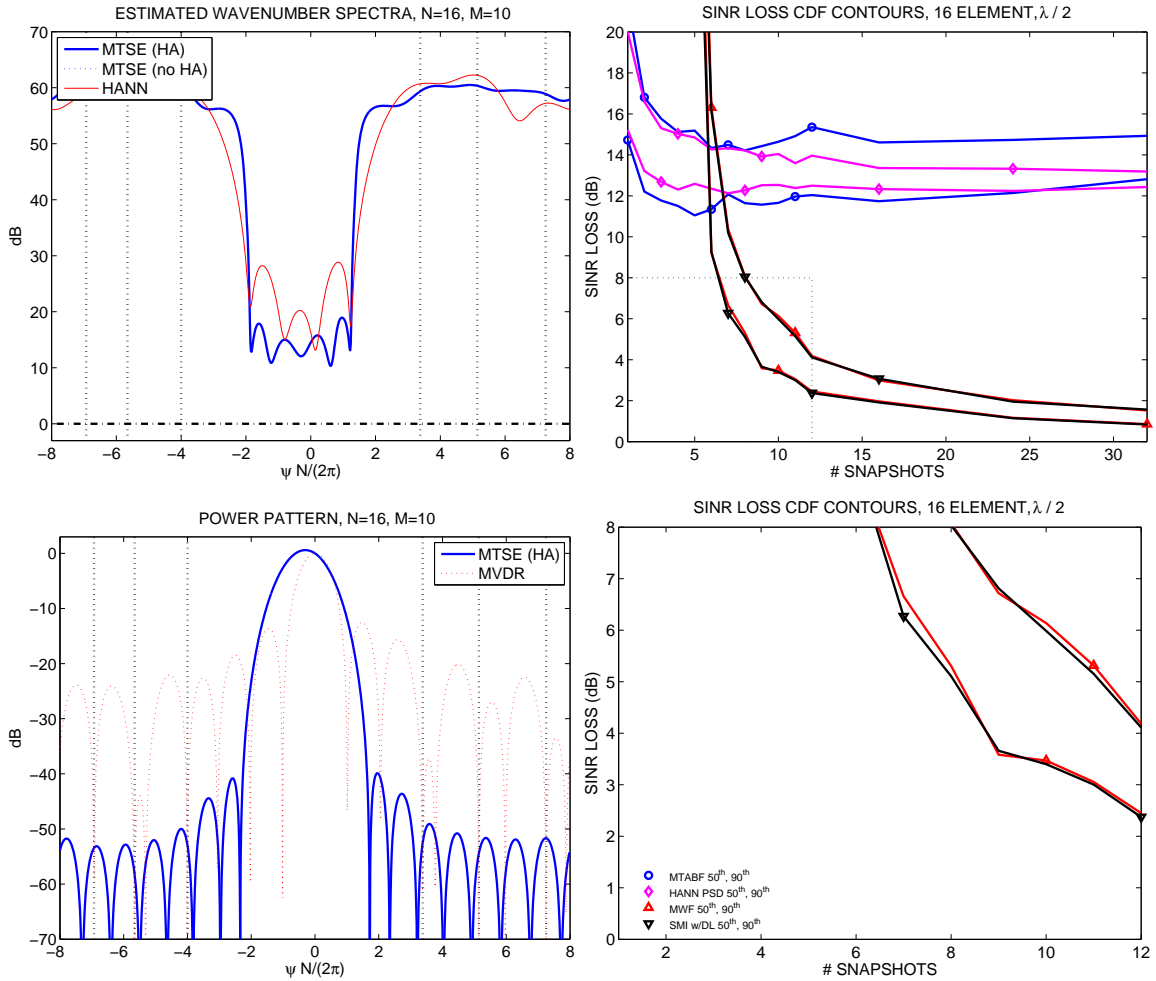


Figure 4.2: **ABF performance, fixed INR , $N = 16$** : The performance for the $N = 16$ test case follows the same layout as Figure 4.1. With only $N = 16$ elements, the harmonic analysis is ineffective as seen in the estimated spectra in the upper left. Correspondingly, the normalized SINR loss is worse in this case. Optimal diagonal loading and MWF perform the same as the $N = 32$ case, because their performance is dictated by K and M which remain the same. These results indicate that for CSS with MTSE to be effective, the array must have enough resolution for harmonic analysis to be successful.

Mixed INR

The mixed *INR* test case has six *INR* point sources located at $(-65^\circ, -40^\circ, -25^\circ, 30^\circ, 45^\circ, 60^\circ)$ with respect to broadside. The per element *INR* is $(-2, -2, -2, -2, 50, 50)$ dB. The steering vector, \mathbf{s} , corresponds to broadside. The optimal MWF rank is $r_{opt} = 2$, corresponding to the two strong interferers in the environment. The MTSE parameters are identical to the fixed *INR*, $N = 32$ test case. Figure 4.3 shows the results. The harmonic analysis is successful at identifying 5 of the 6 line components, although this varies with 6 of 6 depending on the trial. The strong *INR* components have much lower residuals than before, indicating better estimation accuracy due to fewer strong components in the data as one would expect. Optimal diagonal loading and MWF perform identically, and converge quicker than the prior test case as the number of strong interferers is only two, within 3 dB at $M = 4$ snapshots in 50% of trials. Normalized SINR loss performance for the CSS techniques is comparable to that seen earlier at $N = 32$. For CSS with MTSE, performance is within 1 dB of optimal in 90% of trials at $M = 2$ snapshots.

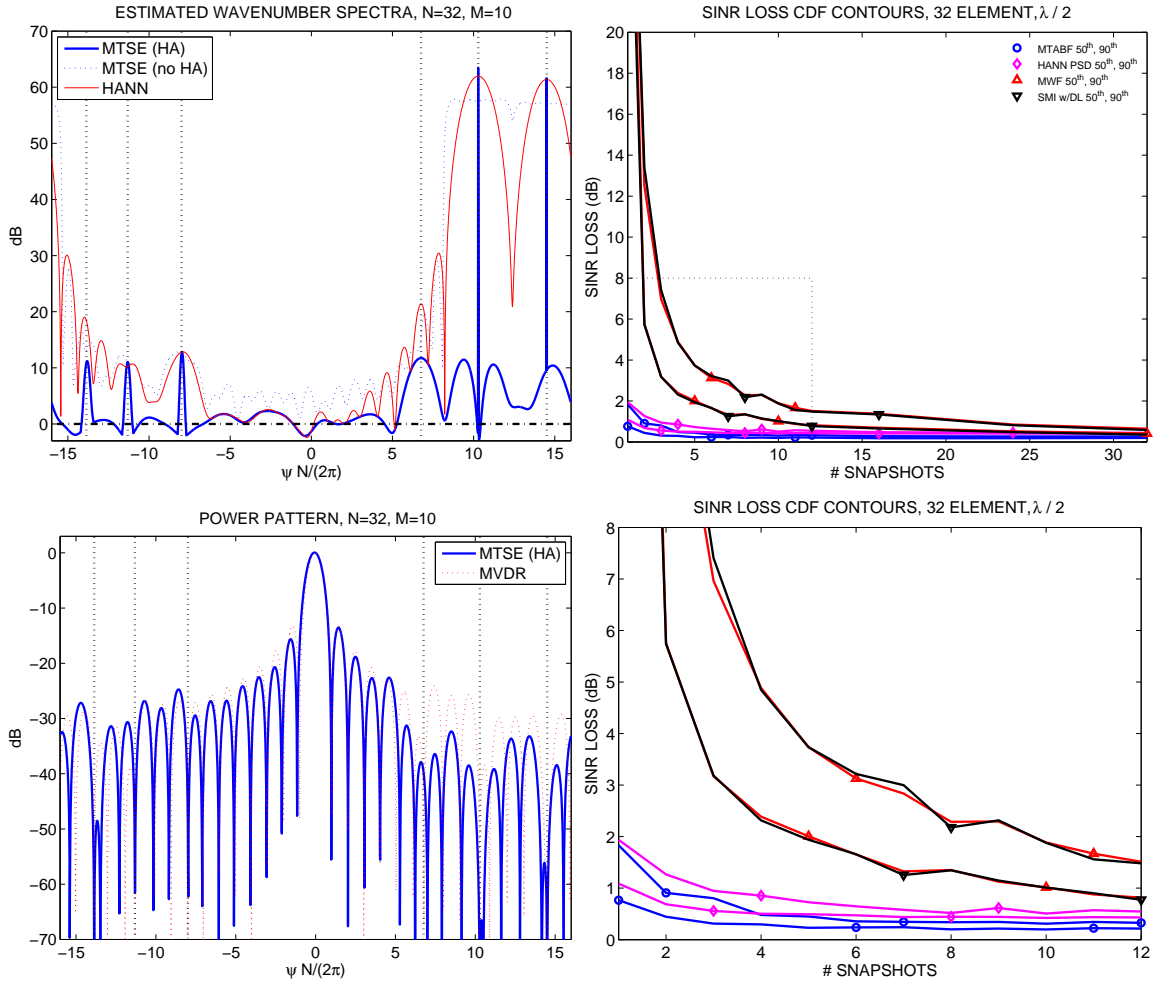


Figure 4.3: **ABF performance, mixed INR , $N = 32$** : CSS techniques show consistent performance between the mixed INR and fixed INR test cases, operating within 1 dB of optimal with $M = 2$ snapshots in 90% of trials when using MTSE. The performance of optimal diagonal loading and MWF improves in this test case, as the number of strong interferers has been reduced, but does not converge as quickly as the CSS methods.

4.3.2 Spatially Spread Interference

The spatially spread interference test cases assess CSS with MTSE performance when the interference and noise is a continuous spectrum process only. An $N = 32$ element uniform linear array is considered, with possible orientation either in the horizontal or vertical direction. Additionally, we investigate operation at $1, \frac{1}{2}, \frac{1}{4}$ of the design frequency for the array. The normalized SINR loss is computed as a function of the steering vector angle of arrival, $90^\circ \leq \theta_s \leq 180^\circ$, with respect to endfire, and as a function of the number of available snapshots. A total of eight different scenarios are investigated. Results presented here are not comprehensive for every scenario, but representative of the results in each environment. Optimal diagonal loading is used as a comparative algorithm, where the optimal loading factor is found via exhaustive search at each test point. The MTSE algorithm is configured with $NFPE = 32$, $NW = 2$, $D = 4$, and $\gamma_{TH} = 8$ dB.

Figure 4.4 shows the directional distribution in elevation for the combined distant shipping and surface noise model [54]. The distribution is symmetric in azimuth. The array is oriented vertically (VLA), and the corresponding MVDR wavenumber spectrum for operation at $1, \frac{1}{2}, \frac{1}{4}$ of the design frequency is shown on the right. Note the asymmetry in the spectrum due to the higher noise power at the surface. Simulations for $M = 1, 4, 16, 64, 256$, and 1024 snapshots were performed. Figures 4.5 and 4.6 show the results. In each set of figures, the average normalized SINR loss performance is shown for each of the three operational frequencies as a function of angle. Because harmonic analysis is not expected to play a factor, we use the expected performance for CSS with classical spectral estimation techniques using a Blackman window as the expected result for CSS with MTSE, since the Blackman window and the equivalent multitapered window are similar. The fixed widths, i.e., FFT bins, in wavenumber space are shown as gray dashed lines in each plot. The spacing is non-uniform when converted to angle-space, and operation below design frequency reflects the lowered resolving power of the array as indicated by fewer “bins”. Looking at the performance, CSS with MTSE converges almost instantly, and outperforms optimal

diagonal loading across the entire range for $M < 64$. Performance up to $M = 1024$ is included to demonstrate that optimal diagonal loading does approach optimal performance, $\xi_{dB} = 0$, as M becomes very large. CSS with MTSE in this case behaves like CSS with classical spectral techniques, and is biased due to the finite N regardless of M , particularly in the endfire region in this case. This represents a fundamental contrast between the two approaches.

All noise models tested behave in a similar fashion. For the remainder of the included cases only the $M = 4$ results are shown. Figure 4.7 shows the results for 3D isotropic noise. In the case of operation at the design frequency, the spectrum is white and both algorithms perform identically. Below design frequency CSS with MTSE outperforms optimal diagonal loading by 0.25 to 1.00 dB, depending on desired angle of arrival in the $M = 4$ snapshot case. It is interesting to note that the diagonal loading follows a similar performance curve as CSS in the endfire region for the limited amount of snapshot data. Figure 4.8 shows the results for the distant shipping noise model, vertically oriented array. This is a significantly non-flat spectrum, and CSS with MTSE clearly outperforms diagonal loading. Figure 4.9 shows the results for the surface noise model, vertically oriented array. Performance is comparable to that seen for the combined noise model.

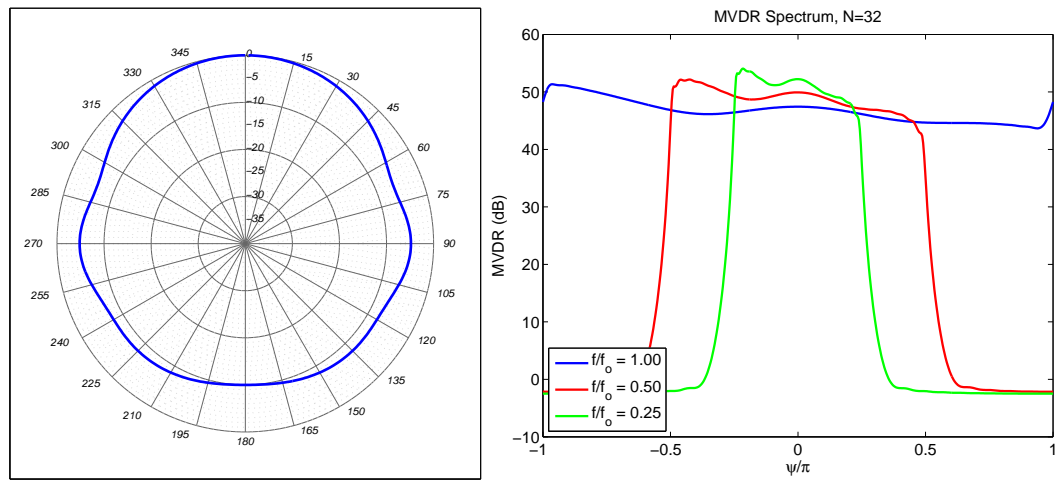


Figure 4.4: **Combined surface and shipping noise model characteristics, VLA:** The combined surface and shipping noise model from [54] is appropriate for (100-500) Hz underwater acoustic processing, and is similar to Urick [77] for moderate shipping. The distribution in elevation is shown on the left, with 0° pointing towards the surface. The MVDR spectra for a vertically oriented uniform linear (VLA) is shown on the right, operating at $1, \frac{1}{2}, \frac{1}{4}$ of the design frequency for the array.

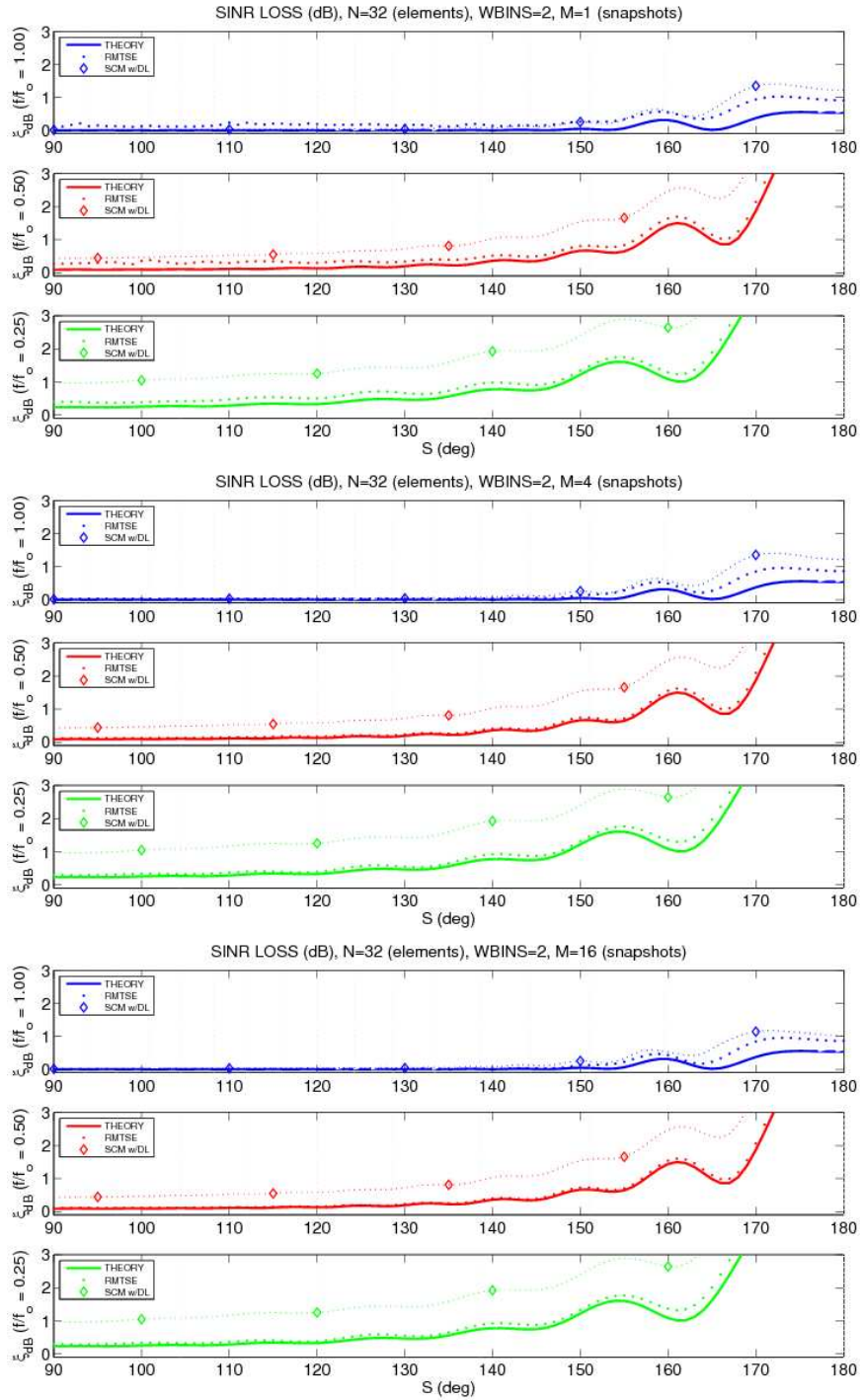


Figure 4.5: $\xi_{dB}(\theta)$, combined surface and shipping noise model, $M = 1, 4, 16$, VLA:

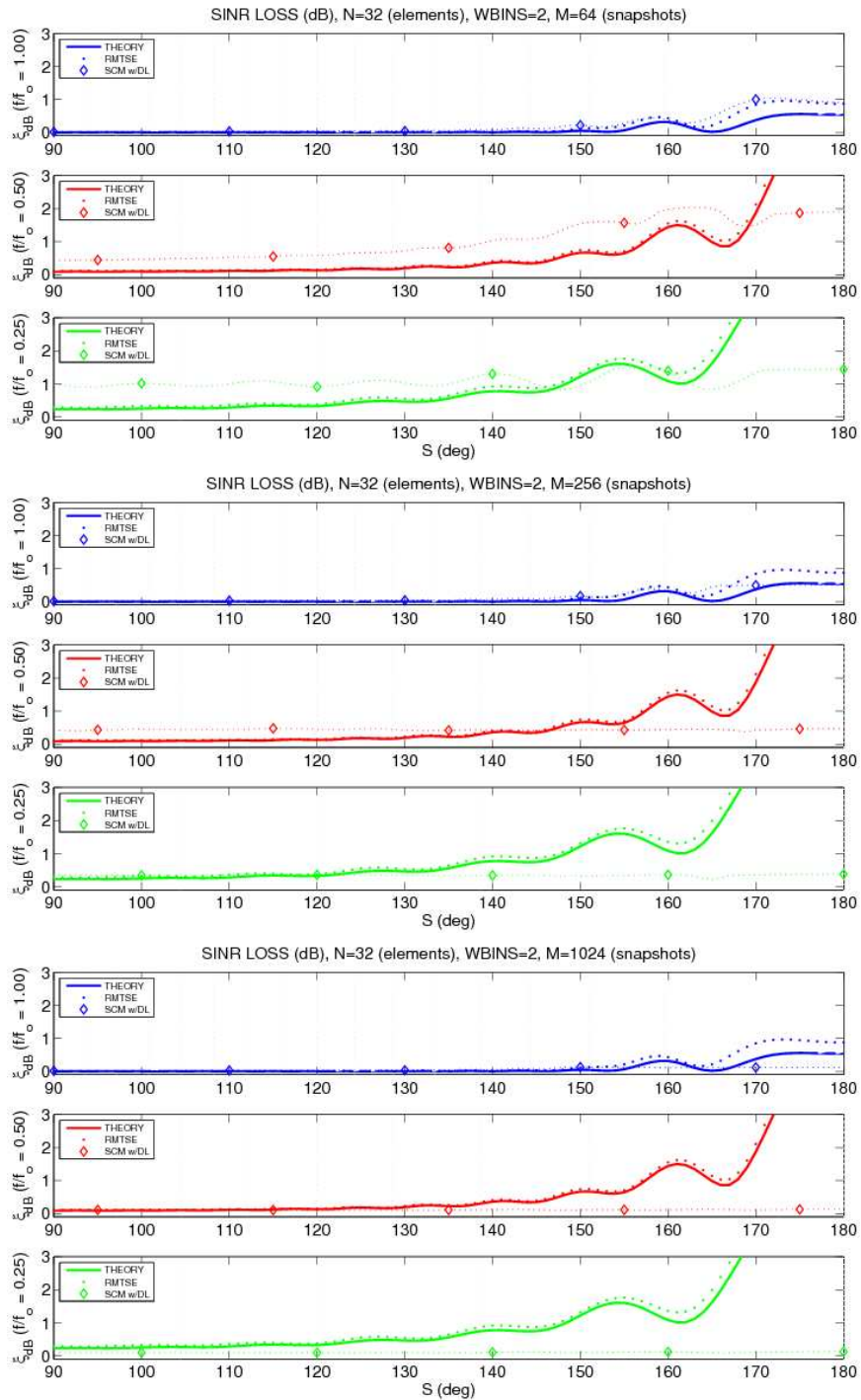


Figure 4.6: $\xi_{dB}(\theta)$, combined surface and shipping noise model, $M = 64, 256, 1024, \text{VLA}$:

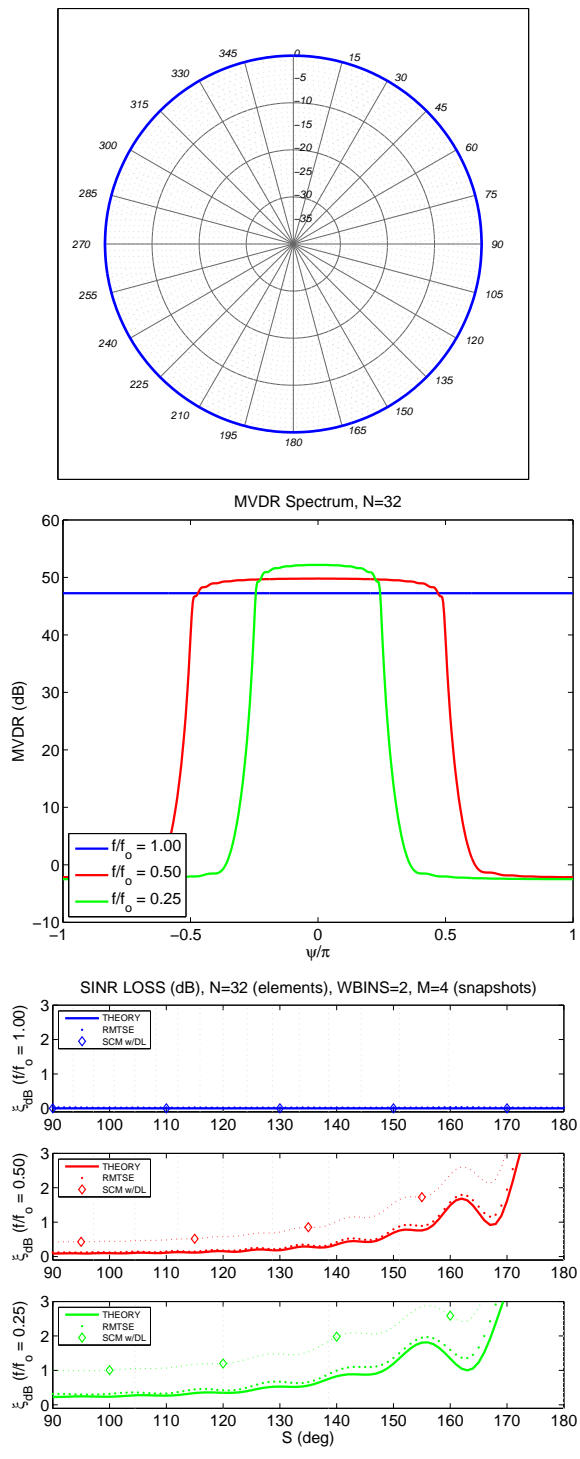


Figure 4.7: 3D isotropic noise:

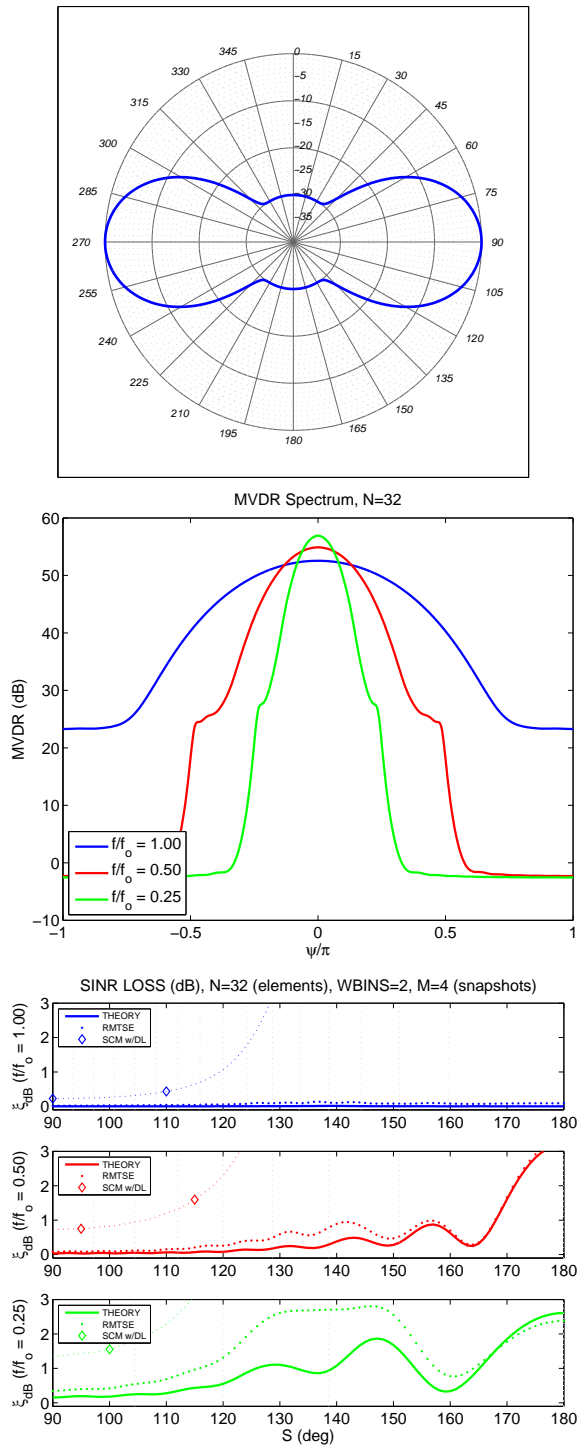


Figure 4.8: Distant shipping noise model, VLA:

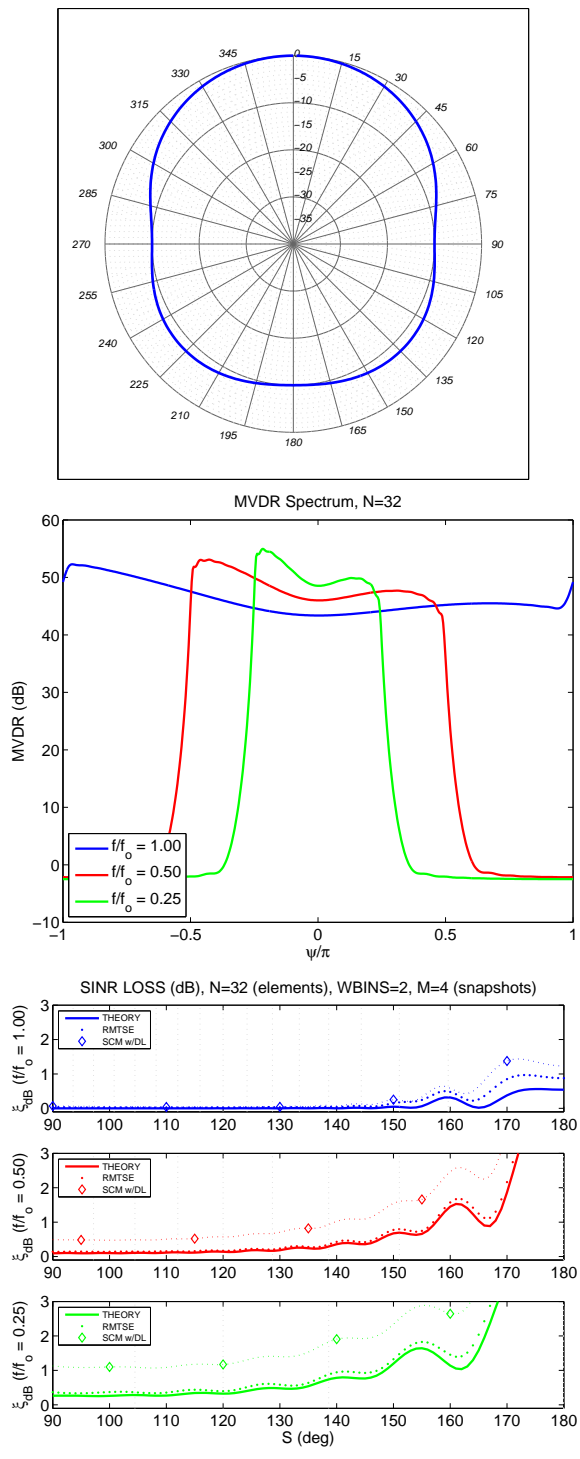


Figure 4.9: Surface noise model, VLA:

4.3.3 Mixed Spectra

The mixed spectra test case contains both discrete and spatially spread components in the interference and noise environment. For this test case we use the distant shipping noise model and include a single discrete component. Two test cases are presented, the first where the point source has low SNR , and a second where the point source has medium SNR . Other test cases were investigated and are comparable in performance to those presented here, but are not shown. For these scenarios we use an $N = 64$ uniform line array. CSS with MTSE is configured with $NFPE = 64$, $NW = 2$, $D = 4$, and $\gamma_{TH} = 6$ dB. Optimal diagonal loading is used for comparison, with optimal loading factor determined by exhaustive search. Three levels of snapshot support are tested, $M = 4, 16$, and 64 , with the steering vector angle of arrival swept across the full visible range $0^\circ \leq \theta_s \leq 180^\circ$ with respect to endfire. Operation at full and half of the design frequency for the uniform linear array is investigated.

There is no assignment of signal or interferer designation to the sources in the environment. The average normalized SINR loss, ξ_{dB} , is computed as a function of θ_s and M . If the discrete component is a signal of interest, ξ_{dB} at or near its location gives an indication of detector or beamformer performance when the signal is present in the data. This is the case discussed earlier in Section 2.5.1 in the context of the MPDR beamformer. If it is an interferer, then ξ_{dB} away from its location gives an indication of detector or beamformer performance in an MVDR context.

Figure 4.10 shows the performance for the weak discrete component case. The MVDR spectra is shown in the upper left, with the final MTSE spectra shown in the bottom left for $M = 64$. The harmonic analysis is unsuccessful in detecting the line component explicitly, but because of its relatively low SNR we must look at the normalized SINR loss curves to understand the impact. The upper right plots reflect operation at the design frequency. The upper right, top subplot, shows ξ_{dB} for CSS with MTSE for the three different amounts of snapshot data. Performance is essentially the same in all cases. There is some mismatch in the immediate vicinity of the discrete component, and nearly optimal

performance everywhere else. The upper right, bottom subplot, shows ξ_{dB} for optimal diagonal loading. Here the influence of more available snapshots is visible, as three curves can be seen. More snapshots provides better performance and a lower ξ_{dB} . Comparing the two, CSS with MTSE outperforms the diagonally loaded sample covariance matrix across large portions of the visible space by several dB. The lower right plot shows the performance at $\frac{1}{2}$ the design frequency. Performance is comparable to operation at the design frequency for CSS with MTSE, only slightly worse near endfire. Diagonal loading has a higher variability in performance than previously, both better and worse performing depending on the number of available snapshots, however CSS with MTSE is clearly better across a broad range of the visible space.

Figure 4.11 shows the results for the case where the discrete component is a “medium” SNR . Both techniques suffer larger normalized SINR loss degradation nearby to the location of the discrete component, presumably in response to its higher SNR . Away from the discrete component ξ_{dB} is comparable to the weak discrete case of Figure 4.10.

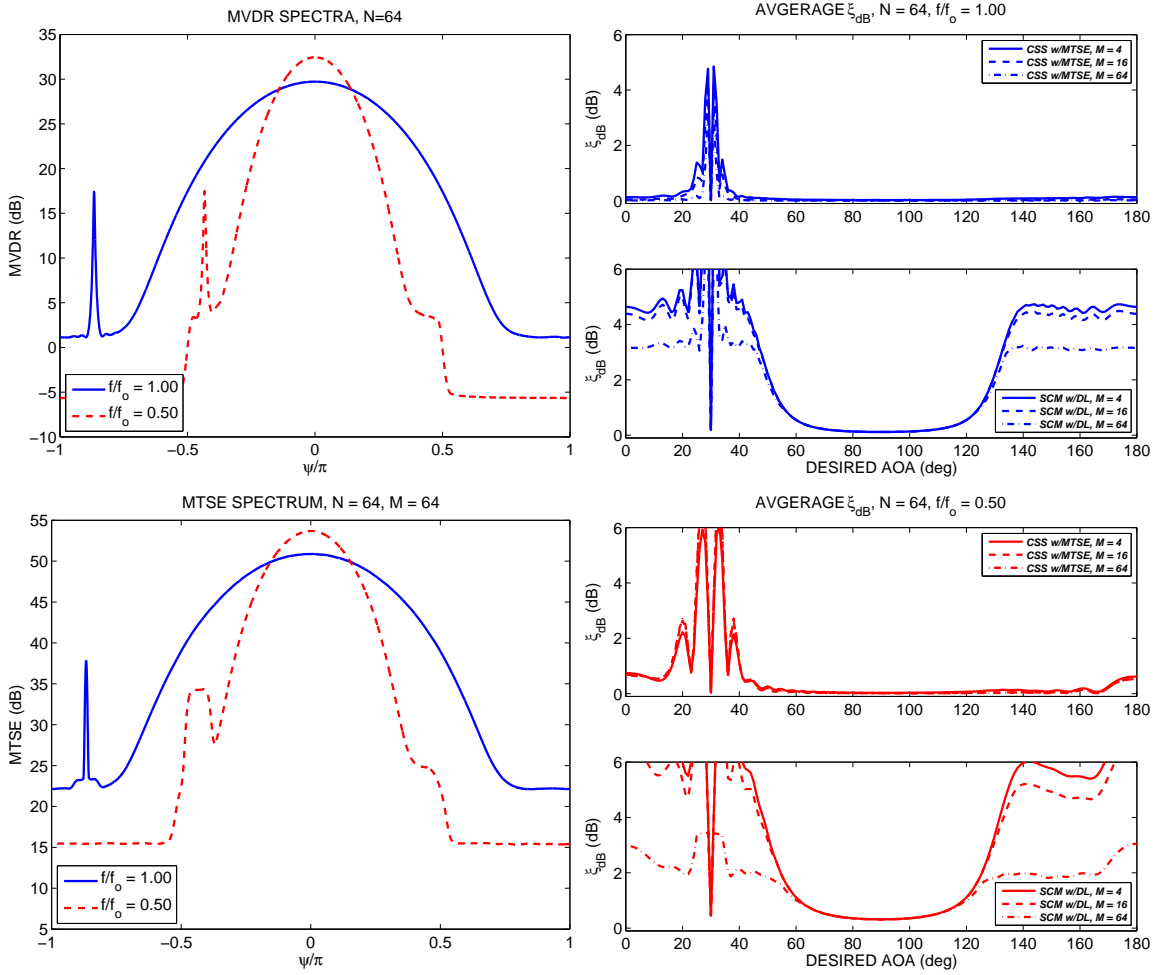


Figure 4.11: **Mixed spectra performance, medium strength line component:** Both CSS with MTSE and optimal diagonal loading experience greater normalized SINR loss nearby to the line component when its strength is increased. CSS with MTSE still outperforms optimal diagonal load across a large portion of the visible region with lower number of available snapshots.

4.3.4 Impact of Harmonic Analysis

Performance of the CSS with MTSE algorithm was assessed via simulation for a single interferer in spatially white noise test case. This is the same type of analysis done for classical PSD techniques in Chapter 3. As a relative comparison, classical PSD using a Blackman window is shown also. The purpose of the simulation was to determine the effect of increased zero-padding for harmonic analysis, and overall impact to adaptive beamformer performance as a result. Simulations are run for an $N = 16$ element uniform linear array, with a single interferer in spatially white noise and $M = 4$ available snapshots. The per element INR of the interferer is varied as $[20, 30, 40]$ dB and the separation between the desired angle of arrival and the interferer is swept through $[0^\circ, 90^\circ]$. The normalized SINR loss curves are shown in Figure 4.12. Also shown in gray dash is half the main lobe null to null bandwidth for the array, $0.5BW_{NN}$. The CSS with classical estimation, indicated as BLACKMAN, follows the expected performance from Chapter 3, and is proportional to the INR when the separation is on the order of 1 to $1.5 BW_{NN}$. In the upper set of plots, the CSS with MTSE algorithm uses $NFPE = 256$ (or $N_{FFT} = 16 \times 256$). The performance of the CSS with MTSE based adaptive beamformer is substantially better than the classical PSD approach, within 1 dB for all INR levels at $0.5BW_{NN}$. Performance is directly attributable to the ability to detect and subtract the interferer through the harmonic analysis process. The residual interferer post cancellation is substantially lower in power, which creates a much lower $(INR_{PE} - A_{bb})$. This moves performance into the large “blue” areas in Figures (3.7) - (3.9). Lowering the $NFPE$ results in less accurate parameter estimation, with a subsequent increase in normalized SINR loss. The lower set of plots show the result for $NFPE = 64$. The performance is worse as expected, but still better than the classical PSD approach. Other methods may be available to precisely determine the interferer parameters in the harmonic analysis process, as the performance is clearly better with improved estimates given the same snapshot sample data.

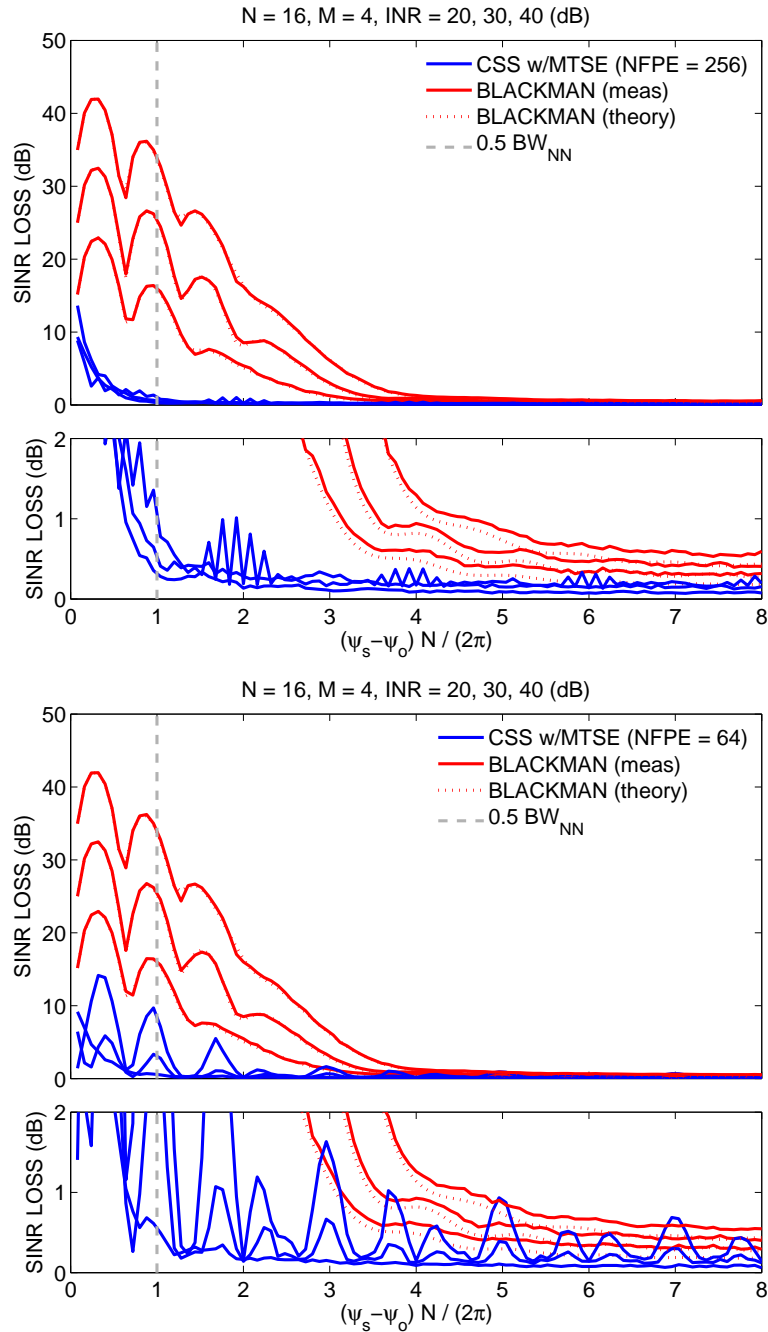


Figure 4.12: **Impact of estimation accuracy for harmonic analysis:** Improved line component parameter estimation improves overall adaptive beamformer performance. This test case measures normalized SINR for CSS with MTSE or classical PSD with Blackman window for an $N = 16$ element array and $M = 4$ snapshots. The top figure shows performance for $NFPE = 256$, while the bottom uses $NFPE = 64$. Interferer frequency/phase/amplitude estimation performance is directly related to the fineness of the search grid, and drives overall beamformer performance.

4.4 Summary

This chapter outlined the procedure for incorporating Thomson's multitaper spectral estimation as the spectral estimation engine used within CSS. Normalized SINR loss performance was assessed via simulation for a number of interference and noise scenarios. Performance was seen to converge with very few snapshots to near optimal, and in many cases with fewer snapshots than interferers. This is a key result, and is possible because the CSS technique estimates the interferers in the spatial domain. In this domain multiple interferers may be visible even in a single snapshot. This is significantly better than what is achievable using diagonal loading or comparable reduced rank sample covariance based techniques. These techniques require at least as many snapshots as interferers and typically more to achieve near optimal performance, an result of processing incorporating time averaging only. Line component, spatially spread, and mixed spectra conditions were considered. It was observed that performance could be improved by increasing the estimation accuracy of the harmonic analysis step, providing better cancellation of the line components within the data.

Chapter 5: Correlated Signal and Interference

5.1 Introduction

So far we have considered the case of a wide sense stationary narrowband space-time process. One of the properties of such a process is that it can be represented as a sum of uncorrelated plane waves, distributed across all directions of arrival to the array. This model does not describe every situation that may be encountered. An important case of interest is when there is correlation between two or more plane wave components observed by the array. This may occur in situations of multipath or smart jamming. Under these conditions the covariance is function of absolute position, not relative, and the process is not wide sense stationary. Failure to account for the correlation within the data can lead to signal cancellation [39], and an overall loss in output SNR.

This chapter considers the scenario where the snapshot data contains both the signal of interest and interference correlated with it. Wavenumber or spatial spectra provide no correlation information. Because of this, we intuitively expect that covariance from spatial spectrum (CSS) will provide a level of robustness against the effects of correlated signal and interference on performance [78]. In this chapter it is shown that CSS is biased in two ways. The first bias is in a manner similar to the bias seen in Chapter 3 for the wide sense stationary process case due to the method of spectral estimation. The second bias is specific to the correlation within the data. Performance is assessed in comparison to CSS operating on uncorrelated data, as well with the effective SINR metric [79], an appropriate measure of output SINR in the correlated signal and interference scenario. The bias attributable to the correlation component is found to have negligible impact on performance. The chapter concludes with a comparison of CSS and the related techniques of covariance matrix tapers [53] and redundancy averaging [42].

5.2 Covariance for Correlated Signals

In the case where the point source signals are correlated the space-time process is not spatially stationary. Referring back to the Cramér spectral representation of the stationary space-time process, the correlation violates the requirement that disjoint regions in wavenumber space be uncorrelated. In terms of the covariance, the effect is seen as a dependence on absolute as well as relative position. This is visible when examining the covariance matrix based on the model for the snapshot data, \mathbf{x}_m .

$$\mathbf{x}_m = \sum_{k=1}^K \mathbf{v}_k a_k(m) + \mathbf{n}_m = \mathbf{V} \mathbf{a}_m + \mathbf{n}_m \quad (5.1)$$

where we have combined the background noise component and sensor noise component together, $\mathbf{n}_m = \mathbf{n}_{b,m} + \mathbf{n}_{w,m}$, $\mathbf{n}_m \stackrel{d}{\rightarrow} CN_N(\mathbf{0}, \mathbf{R}_n)$. The covariance matrix is

$$E \{ \mathbf{x}_m \mathbf{x}_m^H \} = \mathbf{R}_x = \mathbf{V} \mathbf{R}_a \mathbf{V}^H + \mathbf{R}_n \quad (5.2)$$

where $\mathbf{R}_a = E \{ \mathbf{a}_m \mathbf{a}_m^H \}$. Now, specifically \mathbf{R}_a is not a diagonal matrix. The off diagonal terms represent the cross-correlation between the plane waves. \mathbf{R}_a can be expressed as a combination of a diagonal matrix and an off-diagonal matrix.

$$\mathbf{R}_a = \mathbf{R}_{a,U} + \mathbf{R}_{a,C} \quad (5.3)$$

The subscript U is used to reinforce that the diagonal matrix relates to uncorrelated plane waves, while the the subscript C is used to reinforce that the off-diagonal matrix corresponds to the terms representing the correlation. Now

$$\mathbf{R}_x = \mathbf{V} \mathbf{R}_{a,U} \mathbf{V}^H + \mathbf{R}_n + \mathbf{V} \mathbf{R}_{a,C} \mathbf{V}^H \quad (5.4)$$

We recognize the first two terms as the covariance for the stationary process model. We refer to this portion of the overall covariance as

$$\mathbf{R}_{x,U} = \mathbf{V}\mathbf{R}_{a,U}\mathbf{V}^H + \mathbf{R}_n \quad (5.5)$$

The remaining portion, due to the off-diagonal entries of the matrix \mathbf{R}_a , is referred to in a similar fashion.

$$\mathbf{R}_{x,C} = \mathbf{V}\mathbf{R}_{a,C}\mathbf{V}^H \quad (5.6)$$

To see the impact of the off-diagonal terms, consider the simple scenario of an $N = 2$ element array observing two correlated plane waves with no noise. The array manifold response vectors are $\mathbf{v}_1 = ((\exp[-j\mathbf{k}_1^T \mathbf{p}_n]))_n$ and $\mathbf{v}_2 = ((\exp[-j\mathbf{k}_2^T \mathbf{p}_n]))_n$, and the covariance matrix of the planes waves is

$$\mathbf{R}_a = \mathbf{R}_{a,U} + \mathbf{R}_{a,C} = \begin{bmatrix} \sigma_1^2 & \rho\sigma_1\sigma_2 \\ \rho^*\sigma_1\sigma_2 & \sigma_2^2 \end{bmatrix} \quad (5.7)$$

Expanding out the portion of the covariance related to $\mathbf{R}_{a,U}$, we have

$$\begin{aligned} \mathbf{R}_{x,U} &= \sum_{k=1}^2 \sigma_k^2 \mathbf{v}_k \mathbf{v}_k^H \\ &= \sum_{k=1}^2 \sigma_k^2 \begin{bmatrix} \exp(-j\mathbf{k}_k^T [\mathbf{p}_1 - \mathbf{p}_1]) & \exp(-j\mathbf{k}_k^T [\mathbf{p}_1 - \mathbf{p}_2]) \\ \exp(-j\mathbf{k}_k^T [\mathbf{p}_2 - \mathbf{p}_1]) & \exp(-j\mathbf{k}_k^T [\mathbf{p}_2 - \mathbf{p}_2]) \end{bmatrix} \end{aligned} \quad (5.8)$$

which is a function of the relative difference in position of the elements. For the portion of the covariance related to $\mathbf{R}_{a,C}$, we have

$$\mathbf{R}_{x,C} = \begin{bmatrix} & \\ \mathbf{v}_1 & \mathbf{v}_2 \end{bmatrix} \begin{bmatrix} 0 & \rho\sigma_1\sigma_2 \\ \rho^*\sigma_1\sigma_2 & 0 \end{bmatrix} \begin{bmatrix} & \\ \mathbf{v}_1 & \mathbf{v}_2 \end{bmatrix}^H \quad (5.9)$$

which is expanded out as

$$\begin{aligned} \mathbf{R}_{x,C} &= \rho\sigma_1\sigma_2\mathbf{v}_1\mathbf{v}_2^H + \rho^*\sigma_1\sigma_2\mathbf{v}_2\mathbf{v}_1^H \\ &= \rho\sigma_1\sigma_2 \begin{bmatrix} \exp(-j[\mathbf{k}_1^T\mathbf{p}_1 - \mathbf{k}_2^T\mathbf{p}_1]) & \exp(-j[\mathbf{k}_1^T\mathbf{p}_1 - \mathbf{k}_2^T\mathbf{p}_2]) \\ \exp(-j[\mathbf{k}_1^T\mathbf{p}_2 - \mathbf{k}_2^T\mathbf{p}_1]) & \exp(-j[\mathbf{k}_1^T\mathbf{p}_2 - \mathbf{k}_2^T\mathbf{p}_2]) \end{bmatrix} \\ &\quad + \rho^*\sigma_1\sigma_2 \begin{bmatrix} \exp(-j[\mathbf{k}_2^T\mathbf{p}_1 - \mathbf{k}_1^T\mathbf{p}_1]) & \exp(-j[\mathbf{k}_2^T\mathbf{p}_1 - \mathbf{k}_1^T\mathbf{p}_2]) \\ \exp(-j[\mathbf{k}_2^T\mathbf{p}_2 - \mathbf{k}_1^T\mathbf{p}_1]) & \exp(-j[\mathbf{k}_2^T\mathbf{p}_2 - \mathbf{k}_1^T\mathbf{p}_2]) \end{bmatrix} \end{aligned} \quad (5.10)$$

The off-diagonal terms in (5.10) contain mixed products of the wavenumber, \mathbf{k}_k , and the sensor positions, \mathbf{p}_n . This prevents the simplification possible in (5.8), with the result that $\mathbf{R}_{x,C}$ is not a function of the relative difference in position of the elements alone.

5.3 Expected Value

To proceed in analyzing the expected value of the covariance matrix estimate, we use CSS with classical power spectral estimation as was done in Chapter 3. Recall from Chapter 3 for a stationary process we have

$$\mathbf{x}_m = \sum_{k=1}^K \mathbf{v}_k a_k(m) + \mathbf{n}_m, \quad \mathbf{x}_m \stackrel{d}{\rightarrow} CN_N(\mathbf{0}, \mathbf{V}\mathbf{R}_{a,U}\mathbf{V}^H + \mathbf{R}_n) \quad (5.11)$$

where we have used the subscript U to re-inforce the process is stationary and that $\mathbf{R}_{a,U}$ is a diagonal matrix. The CSS covariance matrix estimate is found from the windowed (tapered) snapshots, $\mathbf{y}_m = \mathbf{x}_m \odot \mathbf{w}$, as

$$\hat{\mathbf{R}}_y = \text{DSR}(\mathbf{R}_{\mathbf{w},SCM}) = \text{DSR}\left(\frac{1}{M} \sum_{m=1}^M \mathbf{y}_m \mathbf{y}_m^H\right) \quad (5.12)$$

with expected value $E\{\hat{\mathbf{R}}_y\} = \mathbf{R}_{x,U} \odot \mathbf{R}_{\mathbf{w}}$. Alternatively, we may write out the windowed snapshot model for this case

$$\begin{aligned} \mathbf{y}_m &= \sum_{k=1}^K (\mathbf{v}_k \odot \mathbf{w}) a_k(m) + (\mathbf{n}_m \odot \mathbf{w}) \\ &= \sum_{k=1}^K \bar{\mathbf{v}}_k a_k(m) + \bar{\mathbf{n}}_m \\ &= \bar{\mathbf{V}} \mathbf{a}_m + \bar{\mathbf{n}}_m \end{aligned} \quad (5.13)$$

where the overbar notation, e.g., $\bar{\mathbf{v}}_k$, reflects a tapered quantity. The tapered snapshots are distributed as

$$\mathbf{y}_m \stackrel{d}{\rightarrow} CN_N\left(\mathbf{0}, \bar{\mathbf{V}} \mathbf{R}_{a,U} \bar{\mathbf{V}}^H + \bar{\mathbf{R}}_n\right) \quad (5.14)$$

From (5.12), the DSR linearity properties from Chapter 3, and (5.14) we have

$$E\{\hat{\mathbf{R}}_y\} = \text{DSR}(E\{\mathbf{y}_m \mathbf{y}_m^H\}) = \text{DSR}\left(\bar{\mathbf{V}} \mathbf{R}_{a,U} \bar{\mathbf{V}}^H + \bar{\mathbf{R}}_n\right)$$

The two expressions for the expectation are equivalent, so we have the relationship

$$\mathbf{R}_{x,U} \odot \mathbf{R}_{\mathbf{w}} = \text{DSR}\left(\bar{\mathbf{V}} \mathbf{R}_{a,U} \bar{\mathbf{V}}^H + \bar{\mathbf{R}}_n\right) \quad (5.15)$$

Now we consider that the plane wave components are correlated, so that

$$\mathbf{y}_m \stackrel{d}{\rightarrow} CN_N \left(\mathbf{0}, \bar{\mathbf{V}} [\mathbf{R}_{a,U} + \mathbf{R}_{a,C}] \bar{\mathbf{V}}^H + \bar{\mathbf{R}}_n \right) \quad (5.16)$$

We continue to use (5.12), so that the expected value of the estimated covariance is now

$$E \left\{ \hat{\mathbf{R}}_y \right\} = \text{DSR} \left(\bar{\mathbf{V}} [\mathbf{R}_{a,U} + \mathbf{R}_{a,C}] \bar{\mathbf{V}}^H + \bar{\mathbf{R}}_n \right) \quad (5.17)$$

Using the DSR properties, the expected value consists of two terms

$$E \left\{ \hat{\mathbf{R}}_y \right\} = \text{DSR} \left(\bar{\mathbf{V}} \mathbf{R}_{a,U} \bar{\mathbf{V}}^H + \bar{\mathbf{R}}_n \right) + \text{DSR} \left(\bar{\mathbf{V}} \mathbf{R}_{a,C} \bar{\mathbf{V}}^H \right) \quad (5.18)$$

From (5.15), the first term is the CSS with classical spectral estimation covariance as if the process were in fact stationary, so the final result is

$$E \left\{ \hat{\mathbf{R}}_y \right\} = \mathbf{R}_{x,U} \odot \mathbf{R}_w + \text{DSR} \left(\bar{\mathbf{V}} \mathbf{R}_{a,C} \bar{\mathbf{V}}^H \right) \quad (5.19)$$

Eqn. (5.19) implies that for a correlated signal and interference problem, the CSS with classical spectral estimation technique produces a covariance matrix estimate that is an estimate of the covariance as if the process were uncorrelated, $\mathbf{R}_{x,U} \odot \mathbf{R}_w$, with an additional bias term $\text{DSR} \left(\bar{\mathbf{V}} \mathbf{R}_{a,C} \bar{\mathbf{V}}^H \right)$. In terms of addressing signal cancellation, the first term has clearly eliminated the correlation in the estimated covariance and we would expect an adaptive beamformer based only on this part of the estimate to have a performance consistent with that seen in Chapters 3 and 4, even if the process itself has correlated components. In the next section we investigate the impact of the remaining bias term, $\text{DSR} \left(\bar{\mathbf{V}} \mathbf{R}_{a,C} \bar{\mathbf{V}}^H \right)$, on performance.

5.4 CSS Performance with Correlated Signal and Interference

5.4.1 Introduction

Correlated signal and interference introduces the potential for signal cancellation for some adaptive beamforming algorithms. The minimum variance distortionless response (MVDR) beamformer is derived to be optimal for a spatially stationary space-time process, i.e., uncorrelated noise and interference [6]. The MVDR approach can be extended when both the desired signal and interference are present in the snapshot data, the so called minimum power distortionless response (MPDR) beamformer. MPDR attempts to minimize output power while constrained to be distortionless in the direction of the desired signal, $\mathbf{w}_{\text{MPDR}} \propto \mathbf{R}^{-1}\mathbf{s}$ [1]. This allows the desired signal through due to the distortionless constraint, but in the event of correlated interference the processor uses the interferer to destructively cancel the desired signal in the overall attempt to minimize output power [5, 39].

Figure 5.1 shows an example illustrating the signal cancellation effect on the resultant power pattern. The desired signal is at broadside, with an interferer located at 45° w.r.t. broadside. In the upper subplot, the interferer is uncorrelated and is nulled appropriately. In the lower subplot, the interferer is correlated and the processor steers a beam toward it to use in cancelling the desired signal to lower total output power. Spatial smoothing techniques have been developed to deal with correlated signal and interference at the expense of reducing the effective aperture of the array [40, 41, 43]. The redundancy averaging approach also addresses the correlated interference problem without reduction in effective array aperture, but may result in an indefinite covariance matrix [42, 48].

MMSE beamformers, $\mathbf{w}_{\text{MMSE}} \propto \mathbf{R}^{-1}E\{\mathbf{x}_m a_m^*\}$, in fact use the correlation constructively to improve the output signal quality, therefore they do not suffer from signal cancellation. However, this approach is not applicable when the desired signal is unknown and is not pursued in the dissertation.

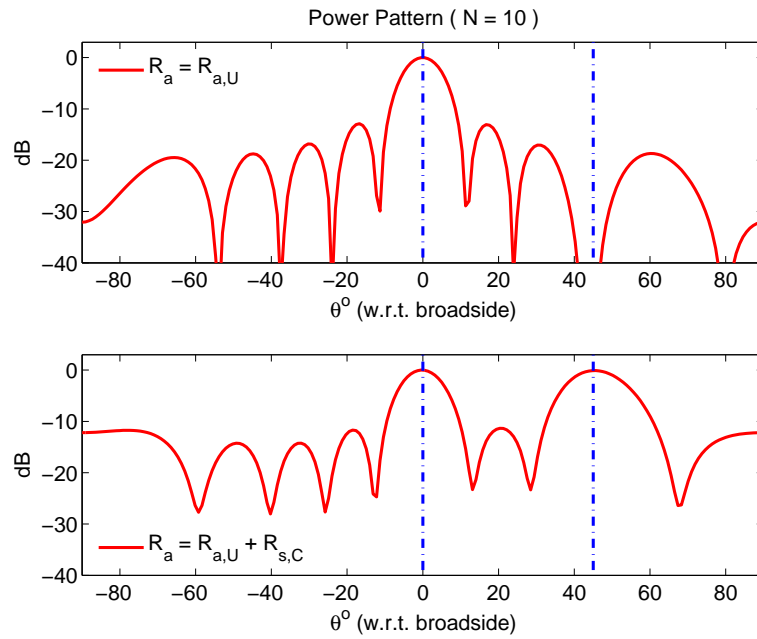


Figure 5.1: **Example beampattern illustrating the signal cancellation effect:** When the interferer at 45° w.r.t. broadside is uncorrelated with the signal at broadside, the MPDR adaptive beamformer nulls it as seen in the upper subplot. If the interferer is correlated with the signal at broadside, the MPDR beamformer steers an additional beam towards it as seen in the lower subplot. The processor uses the interferer to coherently subtract from the desired signal for an overall loss in output signal power and therefore a lower output SINR.

5.4.2 Relative Contribution of Correlated and Uncorrelated Components

There are two main questions of interest for adaptive beamformers based upon the covariance from spatial spectrum estimate, referred to as $\hat{\mathbf{R}}_{CSS}$. First, does $\hat{\mathbf{R}}_{CSS}$ convey any information regarding the correlation component in the data if it exists. Second, how well do beamformers based upon $\hat{\mathbf{R}}_{CSS}$ perform compared to an adaptive processor using a covariance for the data where there is no correlation present. We know from Section 5.3 that the expected value of $\hat{\mathbf{R}}_{CSS}$ contains the covariance if the data were uncorrelated plus an additional term.

$$\begin{aligned} E \left\{ \hat{\mathbf{R}}_{CSS} \right\} &= \mathbf{R}_{x,U} \odot \mathbf{R}_w + \text{DSR} \left(\overline{\mathbf{V}} \mathbf{R}_{a,C} \overline{\mathbf{V}}^H \right) \\ &= \mathbf{R}_{CSS,U} + \mathbf{R}_{CSS,C} \end{aligned} \tag{5.20}$$

The impact of the second term can be considered as a bias in $E \left\{ \hat{\mathbf{R}}_{CSS} \right\}$. Indukumar investigated this type of bias for the related technique of redundancy averaging [47]. By considering the case of two interferers with no noise component, explicit expressions for the bias term showed that for redundancy averaging the bias was not guaranteed to go to zero even if the array length was extended infinitely. Linebarger demonstrated for the same case, that the relative contribution of the non-zero bias component went to zero as the array length was extended to infinity. This was shown using the ratio of the Froebenius norm squared, $\| \cdot \|_F^2$, of the bias component to the unbiased component within the overall covariance. This implied that while the bias term existed, its impact as measured by the relative power indicated by $\| \cdot \|_F^2$ vanished as the array length increased.

We follow a similar line of analysis using a two tone scenario with no noise. The signals have angles of arrival given by ψ_1 and ψ_2 with corresponding array manifold response vectors, \mathbf{v}_1 and \mathbf{v}_2 , and respective variances σ_1^2 and σ_2^2 . The correlation between the two signals is described by a magnitude and phase as $\zeta = E \{ a_1(m) a_2^*(m) \} = A_\zeta e^{j\angle\zeta}$. The

ensemble covariance consists of correlated and uncorrelated terms.

$$\begin{aligned}
\mathbf{R} &= \mathbf{V}\mathbf{R}_{a,U}\mathbf{V}^H + \mathbf{V}\mathbf{R}_{a,C}\mathbf{V}^H \\
&= \mathbf{R}_U + \mathbf{R}_C
\end{aligned} \tag{5.21}$$

We are interested in determining where the relative ratio of $\|\cdot\|_F^2$ shows that the bias term is insignificant within $E\{\hat{\mathbf{R}}_{CSS}\}$, compared to the same ratio for the ensemble covariance, i.e.,

$$\frac{\|\hat{\mathbf{R}}_{CSS,C}\|_F^2}{\|\hat{\mathbf{R}}_{CSS,U}\|_F^2} \ll \frac{\|\mathbf{R}_C\|_F^2}{\|\mathbf{R}_U\|_F^2} \tag{5.22}$$

When (5.22) is valid it indicates that CSS has substantially diminished the contribution of the correlated component, as measured using $\|\cdot\|_F^2$. Consider the problem for an N -element uniform linear array. It can be shown that the uncorrelated and correlated components for the ensemble covariance are

$$\|\mathbf{R}_U\|_F^2 = N^2(\sigma_1^4 + \sigma_2^4) + 2\sigma_1^2\sigma_2^2|\mathbf{v}_1^H\mathbf{v}_2|^2 \tag{5.23}$$

$$\|\mathbf{R}_C\|_F^2 = 2\sigma_1^2\sigma_2^2A_\zeta^2 \left[N^2 + \cos(2\angle\zeta + \Delta\psi[N-1]) \frac{\sin^2(\Delta\psi N/2)}{\sin^2(\Delta\psi/2)} \right] \tag{5.24}$$

where $\Delta\psi = \psi_2 - \psi_1$. The expressions for the components of $E\{\hat{\mathbf{R}}_{CSS}\}$ use the following property. For a Hermitian, Toeplitz matrix, \mathbf{A} ,

$$\mathbf{A} = \begin{bmatrix} \rho[0] & \rho^*[1] & \rho^*[2] & \cdots \\ \rho[1] & \rho[0] & \rho^*[1] & \\ \rho[2] & \rho[1] & \rho[0] & \ddots \\ \vdots & & \ddots & \ddots \end{bmatrix} \quad (5.25)$$

the Froebenius norm squared of \mathbf{A} is

$$\|\mathbf{A}\|_F^2 = \sum_{n=-(N-1)}^{N-1} (N - |n|) |\rho[n]|^2 \quad (5.26)$$

This yields a simplified expression for the $\|\cdot\|_F^2$ of the uncorrelated component of $E \{ \hat{\mathbf{R}}_{CSS} \}$.

$$\|\hat{\mathbf{R}}_{CSS,U}\|_F^2 = \sum_{n=-(N-1)}^{(N-1)} (N - |n|) |\rho_{\mathbf{w}}[n]|^2 [(\sigma_1^4 + \sigma_2^4) + 2\sigma_1^2\sigma_2^2 \cos(\Delta\psi n)] \quad (5.27)$$

where $\rho_{\mathbf{w}}[n]$ is the sample autocorrelation of the taper used, \mathbf{w} . The correlated component cannot be similarly reduced because of the summation term in the sample autocorrelation, $\rho_{CSS,C}[n]$, with a simplest expression for arbitrary \mathbf{w} given as

$$\|\hat{\mathbf{R}}_{CSS,C}\|_F^2 = \sum_{n=-(N-1)}^{N-1} (N - |n|) |\rho_{CSS,C}[n]|^2 \quad (5.28)$$

where

$$\begin{aligned} \rho_{CSS,C}[n] &= \sum_{r=n}^{N-1} \sigma_1 \sigma_2 w(r) w^*(r-n) [\zeta e^{j\psi_2 r - \psi_1[r-n]} + \zeta^* e^{j\psi_1 r - \psi_2[r-n]}] \\ n &\geq 0, \rho_{CSS,C}[-n] = \rho_{CSS,C}^*[n] \end{aligned} \quad (5.29)$$

$$|\rho_{CSS,C}[n]|^2 = A_\zeta^2 \sigma_1^2 \sigma_2^2 \left| \sum_{r=n}^{N-1} w(r) w^*(r-n) \left[e^{j\psi_2 r - \psi_1[r-n] + \angle\zeta} + e^{j\psi_1 r - \psi_2[r-n] - \angle\zeta} \right] \right|^2 \quad (5.30)$$

Figure 5.2 shows the metric

$$M_{F2} = 10 \log_{10} \left(\frac{\|\mathbf{R}_{CSS,C}\|_F^2 / \|\mathbf{R}_{CSS,U}\|_F^2}{\|\mathbf{R}_C\|_F^2 / \|\mathbf{R}_U\|_F^2} \right) \quad (5.31)$$

for the case $N = 32$, across the range of $\Delta\psi$ and with correlation coefficient $\zeta = e^{j\theta_\zeta}$, $\theta_\zeta \in [-\pi, \pi]$. From the Figure, $M_{F2} \leq -10$ occurs for $|N\Delta\psi/(2\pi)| \geq 2.0$, with $M_{F2} \leq -20$ occurring for $|N\Delta\psi/(2\pi)| \geq 2.5$. As $N \rightarrow \infty$, this region becomes more concentrated around $\Delta\psi = 0$ in a similar fashion to that described by Linebarger.

5.4.3 Normalized SINR Loss w.r.t. Uncorrelated Ensemble Covariance

The type of analysis in (5.31) based on $\|\cdot\|_F^2$ gives a general idea about what is going on and may be useful in understanding the limiting behavior as $N \rightarrow \infty$. A more useful measure for practical array lengths remains the normalized SINR loss. Because MVDR is not designed for the correlated signal and interference case, normalized SINR loss calculations based on the ensemble covariance containing the correlation are inappropriate. They do not predict the detrimental affects of the signal cancellation described earlier. We continue to use the normalized SINR loss to understand performance, but for this reason use the ensemble covariance for the uncorrelated data scenario, $\mathbf{R}_{x,U}$, as the reference covariance. This effectively compares the performance of CSS with the optimal beamformer *as if there were no correlation contained in the data*. The subscript \mathbf{R}_C is used to indicate that this is the normalized SINR loss for correlated data case.

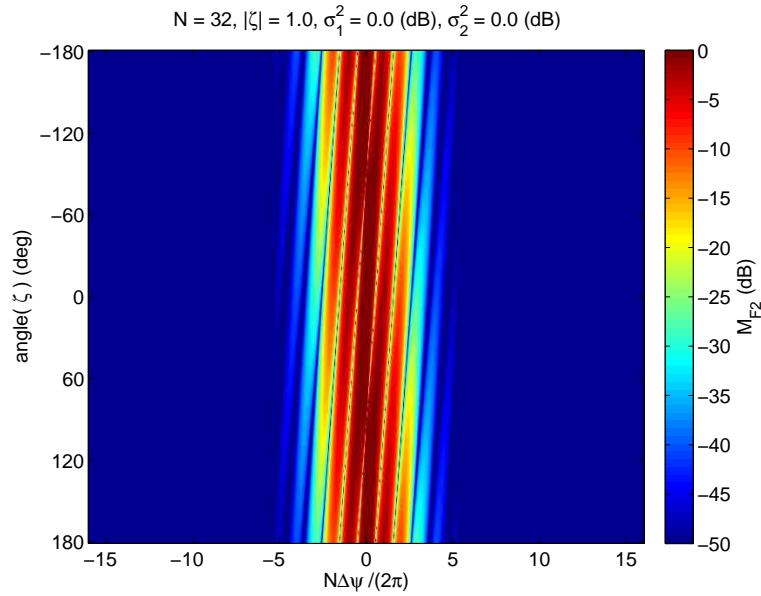


Figure 5.2: **Analysis of impact of bias for correlated signal and interference using $\| \cdot \|_F^2$:** For an $N = 32$ uniform linear array, this example shows the ratio specified by (5.31). This metric shows how much the correlated component is contributing to the estimate of the covariance, compared to its contribution in the ensemble covariance, as measured using $\| \cdot \|_F^2$ and expressed in dB. At a value of -10 dB, this implies the correlated component in the estimated covariance contributes 10% of the correlated component contribution in the ensemble. For mitigating signal cancellation we would like the value to be as small as possible. This metric tends to be too conservative as a measure of the region of good performance (although useful in a limiting sense as $N \rightarrow \infty$), since it is not a direct indicator of SINR loss.

$$\xi_{\mathbf{R}_C} = \frac{\mathbf{s}^H (\hat{\mathbf{R}}_{CSS,U} + \hat{\mathbf{R}}_{CSS,C})^{-1} \mathbf{s}}{\mathbf{s}^H \mathbf{R}_{x,U}^{-1} \mathbf{s}} \cdot \frac{\mathbf{s}^H (\hat{\mathbf{R}}_{CSS,U} + \hat{\mathbf{R}}_{CSS,C})^{-1} \mathbf{s}}{\mathbf{s}^H (\hat{\mathbf{R}}_{CSS,U} + \hat{\mathbf{R}}_{CSS,C})^{-1} \mathbf{R}_{x,U} (\hat{\mathbf{R}}_{CSS,U} + \hat{\mathbf{R}}_{CSS,C})^{-1} \mathbf{s}}. \quad (5.32)$$

As a second measure of performance in addition to $\xi_{\mathbf{R}_C}$, which is an absolute measure, we are interested in the relative performance compared to CSS when there is no correlation within the data. This was the case considered earlier in Section 3.4.5. This performance is referred to as

$$\xi_{\mathbf{R}_U} = \frac{\mathbf{s}^H (\hat{\mathbf{R}}_{CSS,U})^{-1} \mathbf{s}}{\mathbf{s}^H \mathbf{R}_{x,U}^{-1} \mathbf{s}} \cdot \frac{\mathbf{s}^H (\hat{\mathbf{R}}_{CSS,U})^{-1} \mathbf{s}}{\mathbf{s}^H (\hat{\mathbf{R}}_{CSS,U})^{-1} \mathbf{R}_{x,U} (\hat{\mathbf{R}}_{CSS,U})^{-1} \mathbf{s}} \quad (5.33)$$

We are interested in the difference between the two performance measures, (5.32), (5.33)

$$\Delta \xi_{dB} = \xi_{\mathbf{R}_C, dB} - \xi_{\mathbf{R}_U, dB} \quad (5.34)$$

where $\xi_{dB} = -10 \log_{10} \xi$.

Figure 5.3 shows $\Delta \xi_{dB}$ and $\xi_{\mathbf{R}_C, dB}$ for an $N = 32$ uniform linear array across the range of $\Delta \psi$ and $\angle \zeta$, $SNR = INR = 10$ dB. The Hann window function was selected for \mathbf{w} for CSS with classical spectral estimation. For this Figure, $|\zeta| = 1.0$, which is the most demanding case. The lower graph shows $\Delta \xi_{dB}$ is nearly zero except for a limited region with particular values of $\angle \zeta$.

Figure 5.4 shows the result when both the magnitude and angle of ζ are varied. The upper plot shows the average $\xi_{\mathbf{R}_C, dB}$ in red for all values of $\angle \zeta$ and $|\zeta| \in [0.0, 1.0]$. The blue trace represents $\xi_{\mathbf{R}_U, dB}$ as predicted from Chapter 3. The lower subplot shows averaged $\Delta \xi_{dB}$ specifically for values of $|\zeta| = \frac{l}{10}$, $l = 0, \dots, 10$ and random $\angle \zeta$. The simulation shows normalized SINR loss performance of CSS operating on data with correlated signal and interference is always less than 0.2 dB from CSS operating on uncorrelated data. In

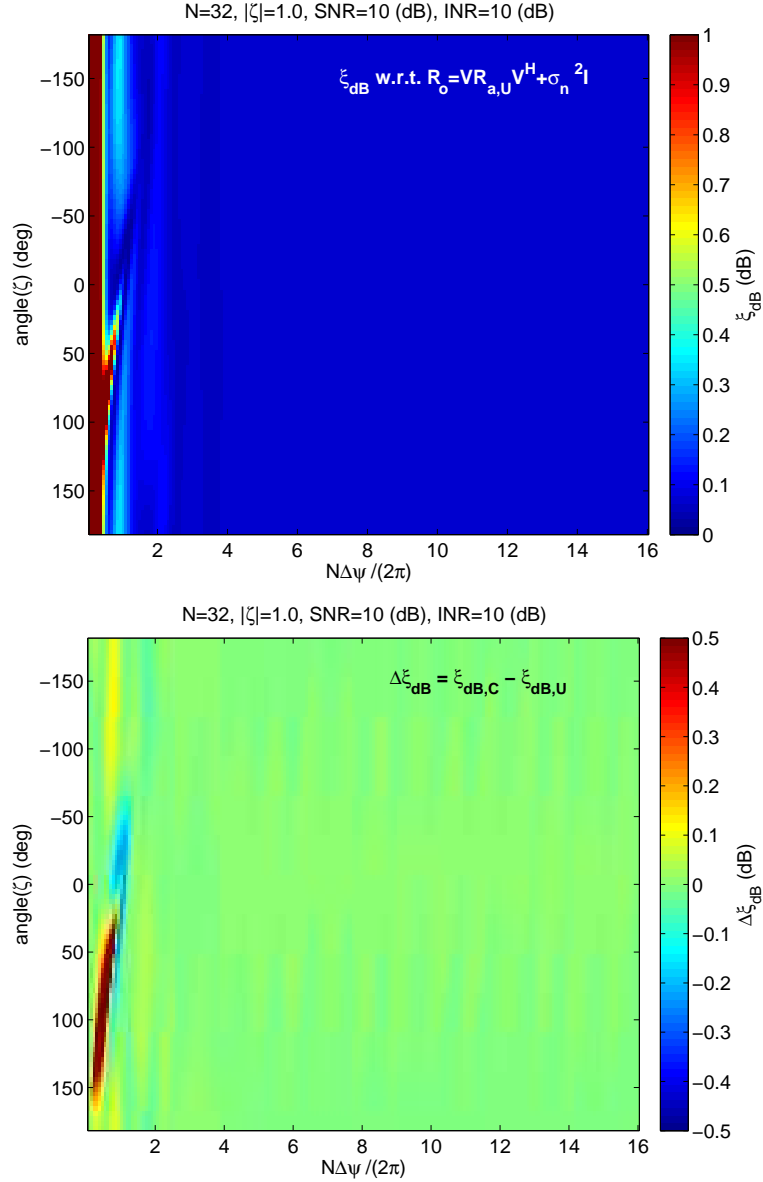


Figure 5.3: Performance assessment for correlated signal and interference: For the case of an $N = 32$ uniform linear observing correlated signal and interference, the upper plot shows the predicted normalized SINR loss (dB) of CSS with classical spectral estimation as a function of separation between the sources and the correlation angle (correlation magnitude is fixed at $|\zeta| = 1$). Performance is determined with respect to an optimal processor using an ensemble covariance where the signal and interference are uncorrelated - such a processor is the best possible since the goal is to reduce the impact of the correlation in the data. Performance is within 0.2 dB almost everywhere, except when the sources are very close. The lower plot compares the relative performance of the CSS with classical spectral estimation for uncorrelated and correlated signal and interference. This shows that CSS performs nearly identically whether or not the signal and interference are correlated.

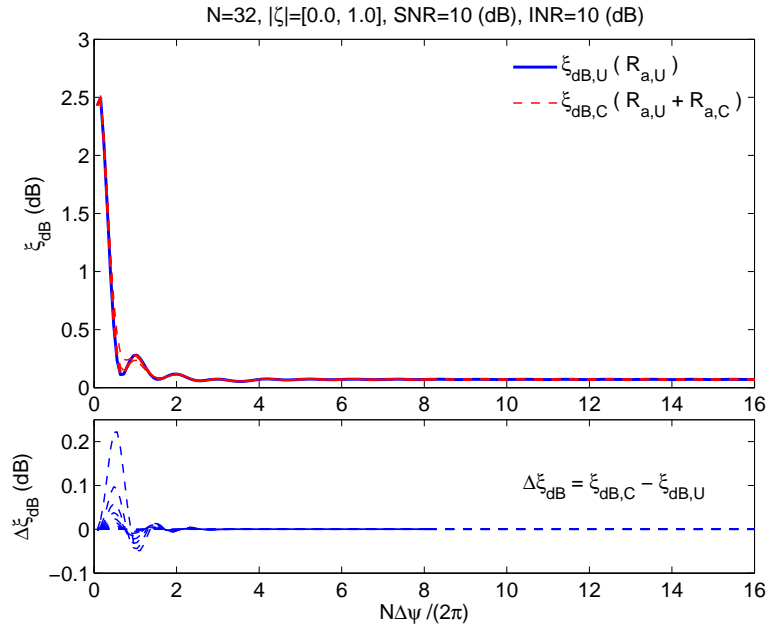


Figure 5.4: **Relative CSS performance for correlated and uncorrelated data:** Continuing the case of an $N = 32$ uniform linear array with two sources, the upper subplot shows the normalized SINR loss of CSS with classical spectral estimation for both uncorrelated and correlated sources. The close agreement between the results for uncorrelated data, shown in blue, and for correlated data, shown in red, indicate that CSS largely mitigates the potential signal cancellation due to correlation. The lower subplot shows the difference, $\Delta\xi_{dB}$, between the two averaged for all correlation coefficient magnitudes and angles. Performance when the interference is correlated is nearly identical to when it is not, with a worst case difference of 0.2 dB.

most cases its performance is effectively identical.

These results show that while $E \{ \hat{\mathbf{R}}_{CSS} \}$ has a bias component when correlated signal and interference are present, its impact is negligible as performance is nearly identical to the uncorrelated signal and interference case. Covariance estimates based on frequency wavenumber spectrum have a strong decorrelating effect when signal and interference are correlated, and dramatically reduce the potential for signal cancellation to negatively impact performance.

5.4.4 Effective SINR

The results from the previous sections indicate that CSS techniques should perform consistently in the presence of correlated signal and interference, regardless of correlation coefficient or angle. Also, the performance should be inline with CSS performance as if the data were uncorrelated. We illustrate this with an example and contrast the performance with MVDR, whose performance degrades due to correlation. To do this we use the effective signal to interference and noise ratio, $SINR_e$, of Tsai [79]. This metric measures the adaptive beamformer impact on the desired signal, the portion of the interference correlated with the desired signal, the portion of the interference uncorrelated with the desired signal, and the background noise. Closed form solutions predict $SINR_e$ for MVDR for the correlated signal and single interferer case.

The test case is from Example 6.12.1 [1], and has an $N = 10$ element uniform linear array with desired signal present and at broadside, and a single interferer at -17° w.r.t. broadside. For a specified (SNR, INR) pair simulations are run sweeping the magnitude of the correlation coefficient, $|\zeta|$, from 0 to 1 with random phase in $[0, 2\pi]$. CSS with MTSE is used with $NW = 1.5$, $D = 3$, $NFPE = 32$, and $\gamma_{TH} = 3$ dB. The simulation results are shown in Figure 5.5. CSS with MTSE maintains a consistent performance, regardless of correlation coefficient, with near optimal effective $SINR_e$.

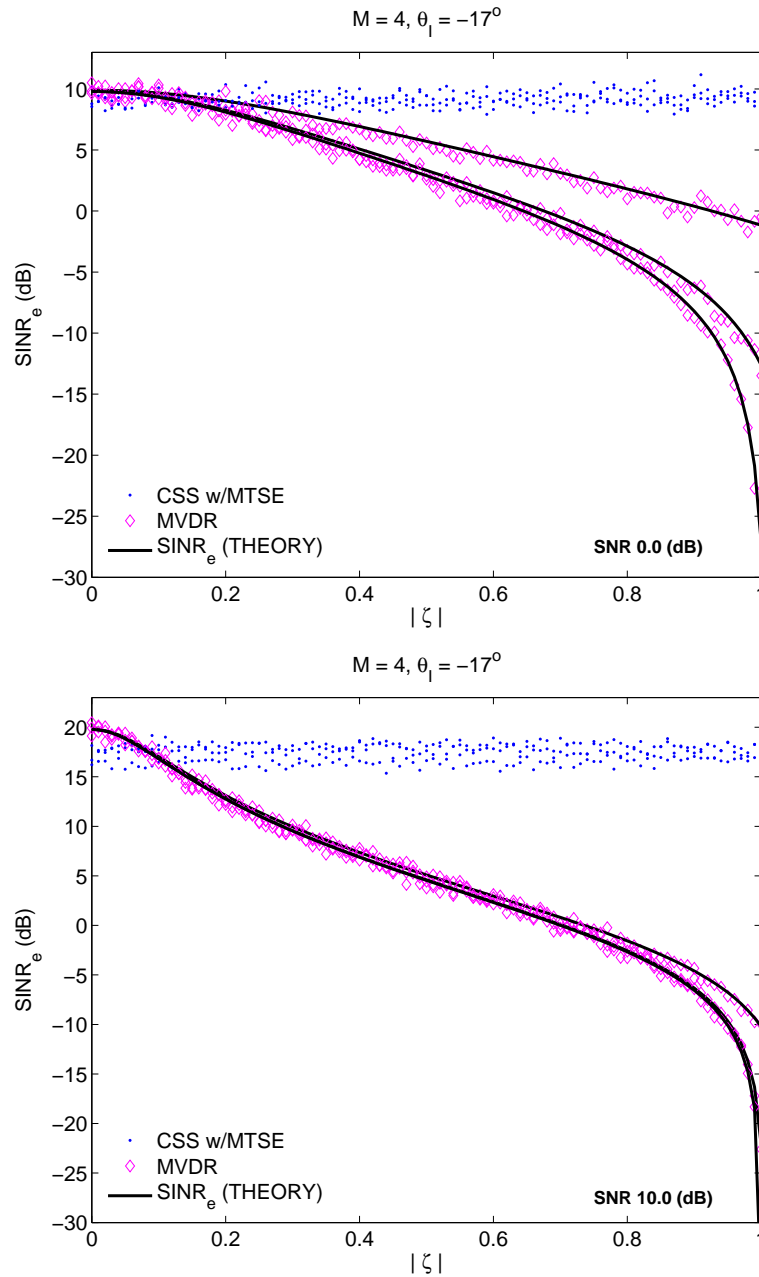


Figure 5.5: $SINR_e$ comparison of CSS and MVDR for correlated signal and interference: Following the test case of Example 6.12.1 [1], the effective SINR is shown for $SNR = 0$ dB, $INR = -10, 0, 10$ dB. The black curve shows the predicted $SINR_e$ for MVDR. Increasing INR allows greater signal cancellation and results in a progressively lower curve in the plot. Simulations for MVDR, show as the magenta diamond, match the theory. The performance for CSS with MTSE is consistent regardless of the magnitude of the correlation coefficient. Its value is near optimal (the same as MVDR for $|\zeta| = 0$) in all cases. The lower plot shows $SINR_e$ for $SNR = 10$ dB with $INR = -10, 0, 10$ dB. MVDR follows the theoretical curve. CSS with MTSE does not achieve the optimal $SINR_e$, but maintains a consistent performance for all $|\zeta|$.

5.5 Related Techniques

This section shows the relationship of covariance matrix estimates found using the CSS technique with the traditional sample covariance matrix and the techniques of redundancy averaging and covariance matrix tapers. We assume application to a uniform linear array, although CSS and CMT techniques are not restricted to only this type of array.

5.5.1 Redundancy Averaging

Redundancy averaging [42, 47, 48] was introduced to address the correlated signal and interference problem. It takes advantage of the multiple available estimates of the space-time correlation at a given spatial lag by averaging them, and then generates a covariance matrix using the averaged values. For the uniform line array, this amounts to replacing diagonals in the sample covariance matrix with the average diagonal values. This same concept has enjoyed repeated introduction, sometimes to address correlated signal and interference [80], sometimes to improve effective sample size [8]. Define an averaged diagonal value for the n^{th} diagonal for the m^{th} snapshot, $\mathbf{x}_m = ((x_m[n]))_n$

$$\rho_{RA,m}[n] = \frac{1}{N - |n|} \sum_{\beta=0}^{N-1} x_m[\beta] x_m^*[\beta - n] \quad (5.35)$$

where we assume the sequence $x_m[\beta] = 0$ for $\beta < 0$, $\beta \geq N$. The sample autocorrelation for the each snapshot, \mathbf{x}_m , is

$$\rho_{x,m}[n] = \sum_{\beta=0}^{N-1} x_m[\beta] x_m^*[\beta - n] \quad (5.36)$$

Observe that (5.35) applies a sample autocorrelation, $\rho_{\mathbf{w}}[n]$, to the data sample autocorrelation, where

$$\rho_{\mathbf{w}}[n] = \frac{1}{N - |n|} \quad (5.37)$$

With these, the redundancy averaged values (5.35) can be written as

$$\rho_{RA,m}[n] = \rho_{x,m}[n]\rho_{\mathbf{w}}[n] \quad (5.38)$$

The final values are then averaged over all snapshots, $\rho_{RA}[n] = \frac{1}{M} \sum_{m=1}^M \rho_{RA,m}[n]$. The covariance matrix for redundancy averaging is then formed from the sequence as

$$\mathbf{R}_{RA} = ((\rho_{RA}[r - c]))_{r,c} \quad (5.39)$$

In terms of the DSR operation,

$$\mathbf{R}_{RA} = \text{DSR}(\mathbf{R}_{SCM}) \odot \mathbf{T}_{RA} \quad (5.40)$$

where

$$\mathbf{T}_{RA} = ((\rho_{\mathbf{w}}[r - c]))_{r,c} \quad (5.41)$$

In comparison, CSS defined via the DSR operation in (5.12) replaces diagonals in the covariance with the sum of all the entries on the diagonal, and not their average value as is done for redundancy averaging. The particular window sample autocorrelation, $\rho_{\mathbf{w}}[n] = (N - |n|)^{-1}$, used for redundancy averaging results in an unbiased expected value, $E\{\rho_{RA}[n]\} = R_x[n]$ and $E\{\mathbf{R}_{RA}\} = \mathbf{R}_x$, if the data is uncorrelated. However, it also results in \mathbf{R}_{RA} being an indefinite matrix. This is a familiar result in the context of time series analysis, as (5.35) is the form of the unbiased estimator for the auto-correlation of a sequence. While unbiased, its form in (5.38) shows the sequence is a product of two functions. The Fourier transform of this product is the estimate of the power spectral density. It is the convolution

$$\hat{P}_{RA}(\psi) = \frac{1}{2\pi} \int_{-\pi}^{\pi} C_{\mathbf{w}}(\psi - \beta) \hat{P}_{\rho_x, \psi}(\beta) d\beta \quad (5.42)$$

where $\hat{P}_{\rho_x, \psi}(\psi) = \mathcal{F}(\rho_x[n])$ and $C_{\mathbf{w}}(\psi) = \mathcal{F}(\rho_{\mathbf{w}}[n])$. For the particular $\rho_{\mathbf{w}}[n]$ used in redundancy averaging, $C_{\mathbf{w}}(\psi)$ is not strictly greater than zero, and as a result portions of $\hat{P}_{RA}(\psi)$ may become negative valued. This is a clearly invalid condition for a power spectral density. In its matrix form, this condition presents itself by making the covariance \mathbf{R}_{RA} indefinite. This is undesirable, and is mentioned directly in [42] as a realistic concern for the redundancy averaging approach.

5.5.2 Covariance Matrix Tapers

The method of covariance matrix tapers [53, 81] provides a measure of robustness to sample covariance matrix processing by modifying the sample covariance matrix with a taper matrix, \mathbf{T}_{CMT} , according to

$$\mathbf{R}_{CMT} = \mathbf{R}_{SCM} \odot \mathbf{T}_{CMT} \quad (5.43)$$

The taper matrix, \mathbf{T}_{CMT} , is designed specifically to impart null widening properties, diagonal loading, or other desirable features. It is required that it be positive semidefinite, $\mathbf{T}_{CMT} \geq 0$, and Hermetian, $\mathbf{T}_{CMT} = \mathbf{T}_{CMT}^H$. An additional desirable feature is that \mathbf{T}_{CMT} is a normalized diagonally homogeneous (NDH) matrix, meaning it is a constant down its main diagonal. Because it is based on the sample covariance matrix, CMT does not attempt to address the correlated signal and interference condition directly. Additional processing, such as spatial smoothing is necessary to mitigate signal cancellation.

5.5.3 Comparison Summary

Table 5.1 summarizes some of the key comparisons between these techniques when applied to uniform linear arrays. CSS with classical power spectral density methods is indicated

Table 5.1: Comparison of CSS and related techniques

\mathbf{R}	form	$E\{ \}$	$\mathbf{x}^H \mathbf{R} \mathbf{x}$	conditions
$\hat{\mathbf{R}}_{CSS}$	$\text{DSR}(\mathbf{R}_{\mathbf{w},SCM})$	$\mathbf{R}_{x,U} \odot \mathbf{R}_{\mathbf{w}} + \text{DSR}(\overline{\mathbf{V}} \mathbf{R}_{a,C} \overline{\mathbf{V}}^H)$	> 0	$C_{\mathbf{w}}(\psi) > 0$ $\hat{P}_y(\psi) > 0$
$\hat{\mathbf{R}}_{RA}$	$\text{DSR}(\mathbf{R}_{SCM}) \odot \mathbf{T}_{RA}$	$\mathbf{R}_{x,U} + \text{DSR}(\mathbf{V} \mathbf{R}_{a,C} \mathbf{V}^H) \odot \mathbf{T}_{RA}$	indefinite	
$\hat{\mathbf{R}}_{CMT}$	$\mathbf{R}_{SCM} \odot \mathbf{T}_{CMT}$	$\mathbf{R}_x \odot \mathbf{T}_{CMT}$	> 0	$\mathbf{R}_{SCM} > 0$

as $\hat{\mathbf{R}}_{CSS}$. The general entry for $E\{ \hat{\mathbf{R}}_{CSS} \}$ developed in Section 5.3 is given, considering both uncorrelated and correlated point source signals. In the event the underlying process is stationary, $R_{a,C} = \mathbf{0}$, and the expression simplifies. The $\hat{\mathbf{R}}_{CSS}$ technique provides benefits found in both $\hat{\mathbf{R}}_{RA}$ and $\hat{\mathbf{R}}_{CMT}$. It uses the DSR operation which is beneficial for correlated signal and interference, similar to RA. It also provides the equivalent benefits, in expected value, of covariance matrix tapering. As additional positive attributes, $\hat{\mathbf{R}}_{CSS}$ maintains positive definiteness with reasonable restrictions on the choice of window function and resultant power spectral density estimate. The DSR processing provides additional data averaging, or alternatively an increase in effective sample size over $\hat{\mathbf{R}}_{CMT}$ which uses only the sample covariance matrix.

5.6 Summary

This chapter investigated application of CSS techniques to the problem of correlated signal and interference. It was shown that the correlation introduces an additional bias to the covariance matrix estimate. The influence of the bias on performance, however, was seen to be negligible. CSS operating on correlated signal and interference data performs nearly identically to operation on similar data without correlation. This was verified via simulation considering the effective SINR. While MVDR is known to degrade in performance as correlation increases, CSS maintains a consistent performance regardless of magnitude of correlation. The analysis performed provided an opportunity to related CSS to the techniques of redundancy averaging and covariance matrix tapers, and it was seen that CSS

provides benefits of both techniques with additional advantages of its own.

Chapter 6: Non-Ideal Array Manifold Response

6.1 Introduction

The CSS methods presented in Chapters 3 and 4 inherently assume an underlying structure based upon the observed narrowband space-time process consisting of sums of physically propagating plane waves. For an array of ideal omnidirectional sensors, the array manifold response takes on a form based on the complex-exponential, $\mathbf{v}(\mathbf{k}) = ((\exp[-j\mathbf{k}^T \mathbf{p}_n]))_n$. Real-world sensors and arrays may exhibit perturbations to this ideal response that alter the form of the encountered covariance from its assumed structure. For a uniform linear array, the ideal manifold response results in a Toeplitz covariance matrix. With any amount of array manifold response error, this Toeplitz structure no longer holds. This is similar to the effect encountered when investigating the correlated signal and interference scenario. The ML estimate of an unstructured covariance [2] is the sample covariance matrix, and the set of algorithms that build upon it are most applicable if the underlying problem is unstructured. We are interested in determining if there are conditions where there is partial structure, i.e., some of the underlying form exploited in Chapters 3 and 4 remains that can help the problem.

In this chapter we review types of non-ideal array manifold responses and their impact on structured covariance beamformer performance. We then develop a technique to mitigate the impact based on data already available via CSS with MTSE processing. This is done by estimating the array manifold response corresponding to detectable line components in the spectrum, since these typically dominate the overall performance, and incorporating this discrete set of non-ideal response vectors into the covariance. Performance is assessed through simulation for non-ideal array manifold response scenarios of interest.

This approach differs from techniques that concentrate on estimating the steering vector,

for example using the principal eigenvector of the clutter covariance matrix for radar [82], or via estimates of the actual sensor positions such as for towed arrays. Techniques applied to towed arrays have used GPS data for the tow vessel and a water pulley model for the array [83], algorithms to optimize the “focus” or sharpness of the wavenumber spectrum [84], or observations of broadband signals in the environment [85]. As a narrowband processing algorithm operating directly on the snapshot data, the technique developed here may be valuable in concert with these techniques as the array displacement becomes significant, in particular in light of the similarity between the circular bow array deformity in Section 6.2.2 and observed array behavior during turning maneuvers [83].

6.2 Types of Non-Ideal Array Manifold Responses

6.2.1 Random Errors

Random errors in array manifold response are considered as zero mean perturbations from the nominal array response values. These may arise from non-ideal sensor gain or phase, manufacturing precision, or other component tolerances. We use two approaches for describing these effects. The first, detailed in [1], provides a random error term for each physical quantity related to each sensor, namely, position, amplitude response, and phase response. Each error term, Δ_i , is specified as a Gaussian random variable, $\Delta_i \stackrel{d}{\rightarrow} N(0, \sigma_i^2)$. Indicating the “actual” value of a quantity, x , using the additional subscript a , e.g., x_a , the effective position of the n^{th} sensor element with nominal position \mathbf{p}_n is

$$\mathbf{p}_{n,a} = \mathbf{p}_n + [\Delta_x, \Delta_y, \Delta_z]^T \quad (6.1)$$

and the overall array manifold response is

$$\mathbf{v}_a = \left(\left([1 + \Delta_A] \exp [j\Delta_\theta] \exp [-j(\mathbf{k}^T \mathbf{p}_{n,a})] \right) \right)_n \quad (6.2)$$

This provides complete specification of the potential random errors, $(\Delta_x, \Delta_y, \Delta_z, \Delta_A, \Delta_\theta)$, and is useful for analysis of performance impacts in relation to each of the individual quantities. A simpler model reduces the random error contribution to a multiplicative effect on the amplitude and phase only. Define the vector

$$\mathbf{h} = c_h \mathbf{1} + \mathbf{g}, \quad \mathbf{g} \stackrel{d}{\rightarrow} CN_N(0, \sigma_g^2 \mathbf{I}) \quad (6.3)$$

where c_h is a constant. The non-ideal array manifold response is

$$\mathbf{v}_a = \mathbf{v} \odot \mathbf{h} = c_h \mathbf{v} + \mathbf{v}_g \quad (6.4)$$

The constant c_h is chosen such that

$$\mathbf{v}_a^H \mathbf{v}_a = \mathbf{v}^H \mathbf{v} \quad (6.5)$$

The ratio σ_g^2/c_h^2 is a single metric that provides a measure of the difference between between the ideal and actual array manifold responses. Expressed in dB as $10 \log_{10}(\sigma_g^2/c_h^2)$, this value gives some indication of how far down the perturbation components are from the nominal response.

The simpler model of (6.4) is useful for varying array response as a function of angle of arrival, while the more explicit model of (6.2) is more appropriate for analyzing operation below the design frequency where there is a non-zero virtual region and isotropic noise component. For reference, Table 6.1 lists the model parameters that produce average comparable distortion levels between the two models. For the explicit model, phase and amplitude variations are set at $\sigma_\theta = 15^\circ$, and $3\sigma_A$ corresponds to ± 3 dB. The positional variation is given in the table in units of percent with respect to array element spacing.

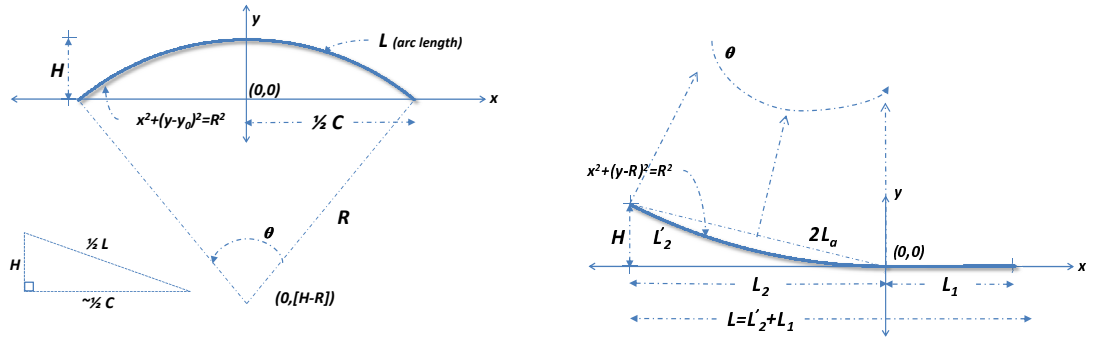


Figure 6.1: **Circular bow and partial circle bow array deformation:** The circular bow deformation, shown on the left, and the partial circular bow deformation, shown on the right, are models for the types of bending experienced by a towed array. The deterministic displacement from the nominal linear position cause the array manifold response to be altered from its assumed ideal form.

6.2.2 Deterministic Errors

In addition to random errors, arrays may also experience deterministic types of array manifold response perturbation. This results from deformation of the array which causes a non-zero mean, non-random disturbance in the positions of the elements. With underwater acoustic arrays, such deformation can occur due to hydrodynamics for towed arrays in motion [84]. Here we consider two types of positional errors for linear arrays, circular and partial circular bows. Figure 6.1 shows an illustration of these two types of conditions. Further details on the specific geometries can be found in Appendix A. Positional errors which simply rotate or translate the array in space are not considered.

Table 6.1: Random error model parameters for comparable distortion

$N = 32$ ULA, $d = \lambda_o/2$			
$f = f_o$		$f = f_o/2$	
$\sigma_{\Delta x,y,z}$ (% d)	$10 \log_{10} (\sigma_g^2/c_h^2)$	$\sigma_{\Delta x,y,z}$ (% d)	$10 \log_{10} (\sigma_g^2/c_h^2)$
1	-21	1	-27
2	-15	2	-21
4	-9	4	-15
8	-5	8	-9

6.3 Impact to Structured Covariance Matrix

ABF Performance

The technique of computing covariance based on estimates of the wavenumber spectrum is clearly influenced by factors that impact the ability to accurately estimate that spectrum, or how accurately that spectrum, based on complex exponentials, represents the true underlying situation. Using the simple model from Section 6.2.1, the actual array manifold response vector is $\mathbf{v}_a = c_h \mathbf{v} + \mathbf{v}_g$. The ideal array manifold response, \mathbf{v} , is scaled and the additional bias term is $\mathbf{v}_g = \mathbf{v} \odot \mathbf{g}$. The array manifold response $\mathbf{v}(\mathbf{k}) = ((e^{-j\mathbf{k}^T \mathbf{p}_n}))_n$. Multiplication of the individual complex Gaussian elements in \mathbf{g} by complex exponential scale factors does not change their statistics, so we have

$$\mathbf{g}, \mathbf{v}_g \stackrel{d}{\rightarrow} CN_N(0, \sigma_g^2 \mathbf{I}) \quad (6.6)$$

so that the bias in any given realization is a complex Gaussian random vector. Consider a single interferer in uncorrelated white noise.

$$\mathbf{x}_m = (c_h \mathbf{v} + \mathbf{v}_g) a(m) + \mathbf{n}_m \quad (6.7)$$

The covariance for this case for a given instance of \mathbf{v}_g is

$$E \{ \mathbf{x}_m \mathbf{x}_m^H | \mathbf{v}_g \} = \sigma^2 \left(|c_h|^2 \mathbf{v} \mathbf{v}^H + c_h \mathbf{v} \mathbf{v}_g^H + c_h^* \mathbf{v}_g \mathbf{v}^H + \mathbf{v}_g \mathbf{v}_g^H \right) + \mathbf{R}_n \quad (6.8)$$

In any given instance of this scenario, the error is unknown but non-random, and will produce a particular wavenumber spectrum. The covariance over the ensemble of error vectors, \mathbf{v}_g , is

$$E \{ \mathbf{x}_m \mathbf{x}_m^H \} = \sigma^2 |c_h|^2 \mathbf{v} \mathbf{v}^H + \mathbf{R}_n + \sigma^2 \sigma_g^2 \mathbf{I} \quad (6.9)$$

The ensemble power spectrum for this case appears as the original with the line component scaled $|c_h|^2$, with an elevated noise floor corresponding to the $\sigma^2\sigma_g^2\mathbf{I}$ term. In a given realization, though, it is a single vector, \mathbf{v}_g , causing the elevated sidelobes and not an ensemble of plane waves from all directions. This phenomena is illustrated in Figure 6.2. As the ratio σ_g^2/c_h^2 increases there is larger and larger array manifold error, and the rise in the perceived noise floor is clear.

Zatman, in considering the impact of random errors on structured covariance techniques [86], showed that the normalized SINR loss performance of such techniques would degrade and was proportional to the difference between the sidelobe levels due to the errors and the true noise floor. This is also highlighted in Figure 6.2, as the red patched area indicates this difference. Inset in each plot is the expected increase in normalized SINR loss, $\Delta\xi_{dB}$, which is equal to the rise in the noise floor.

$$\Delta\xi_{dB} \approx \max(0, INR_{dB} + (\sigma_g^2/c_h^2)_{dB}) \quad (6.10)$$

Deterministic array manifold response error also causes an impact to the estimated wavenumber spectrum. This impact is a function of both the positional displacement and the angle of arrival of the discrete point source. This phenomena is illustrated in Figure 6.3 for the circular bow array deformity. Due to the symmetry of the array bend, we expect that the sidelobe structure resulting from the circular bow is also symmetric in wavenumber space. In the upper left of Figure 6.3, a center displacement of $H/L = 0.002\%$ is shown, with no visual impact apparent in the estimated wavenumber spectrum. The percentage increases, left to right and top to bottom, as $H/L = [0.02, 0.2, 2.0]\%$ with the increasing sidelobe level a clear result. The circular bow distortion causes the single discrete source to appear as a symmetric, spatially spread interference.

Figure 6.4 shows similar effects in the estimated wavenumber spectrum for the partial circular bow case. For these plots, the length L_2 is chosen to be 25% of the overall array length, L . Because the deformity is not symmetric, the corresponding influence in

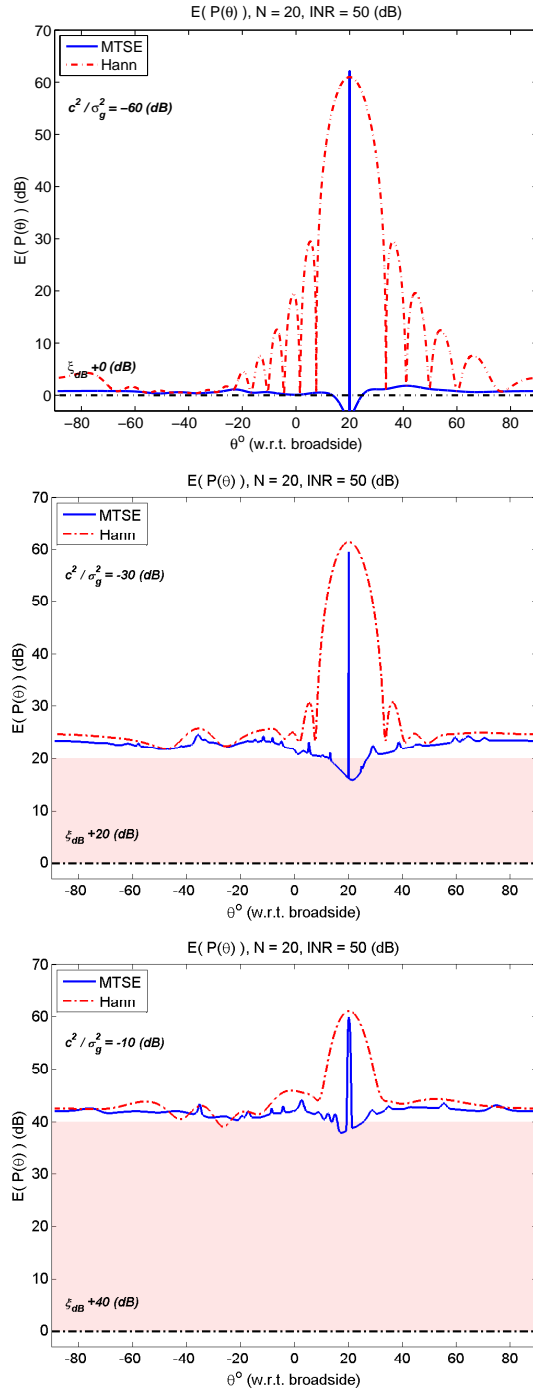


Figure 6.2: **Estimated wavenumber spectrum, impact of random errors:** Random errors in the array manifold response raise the perceived noise in the wavenumber spectrum, acting as sidebands around the line component in the spectrum. Structured covariance algorithms that assume ideal array manifold response degrade in performance in direct proportion to the amount the “raised” noise floor exceeds the true noise floor. The three plots show this elevated noise floor over the true noise floor, shown in black dash-dot at 0 dB, for increasing magnitude of random errors.

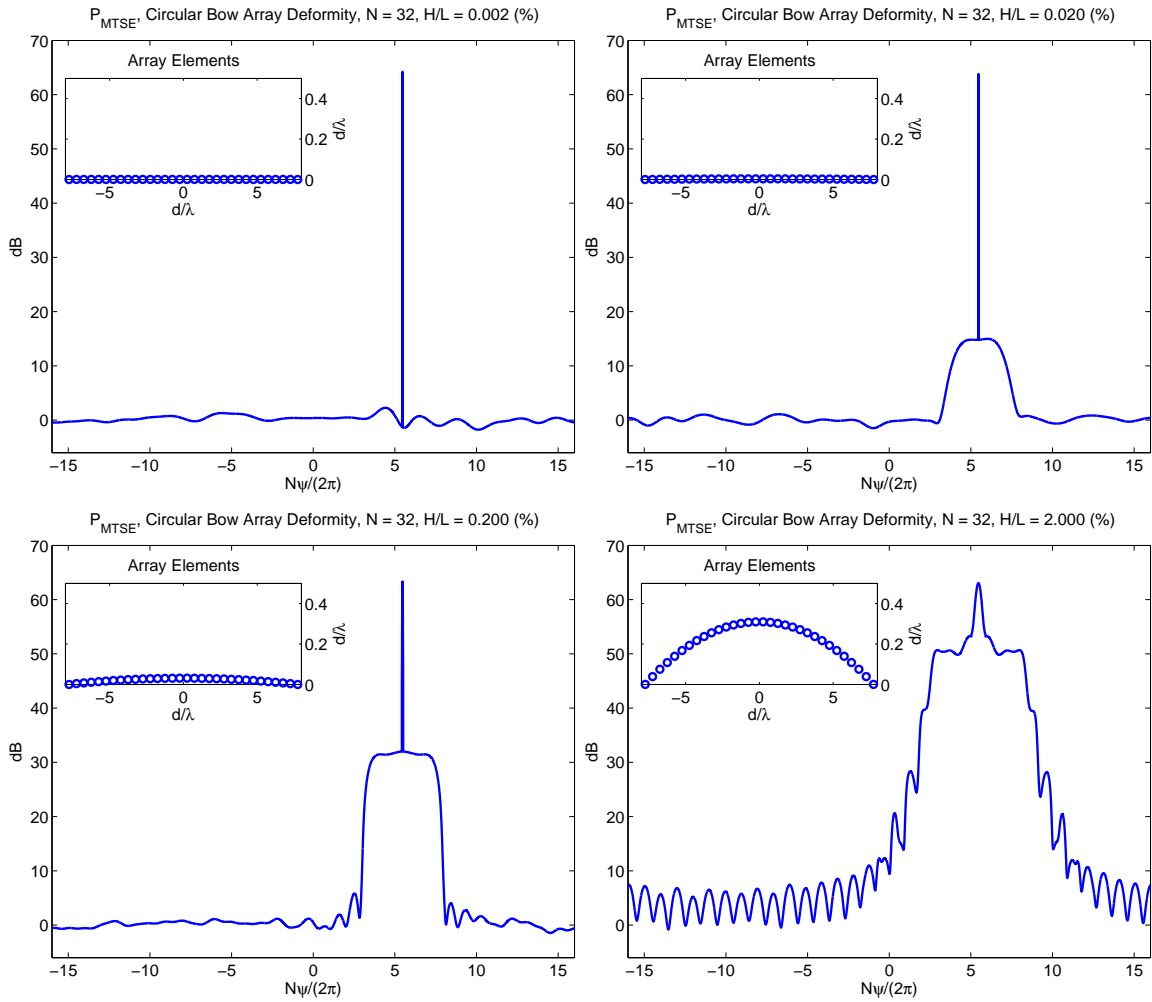


Figure 6.3: **Estimated wavenumber spectrum, circular bow array bending:** A linear array bent to a circular bow shape causes the appearance of increasingly higher sidebands around the line component as the severity of the bending increases.

wavenumber space is not expected to be symmetric. In the upper left in the Figure, an end displacement, H , is set such that $H/L = 0.002\%$. Again, there is no visible impact to the estimated wavenumber spectrum. The percentage increases, left to right and top to bottom, as $H/L = [0.02, 0.2, 2.0]\%$ with increasing and asymmetric sidelobe structure still clearly visible.

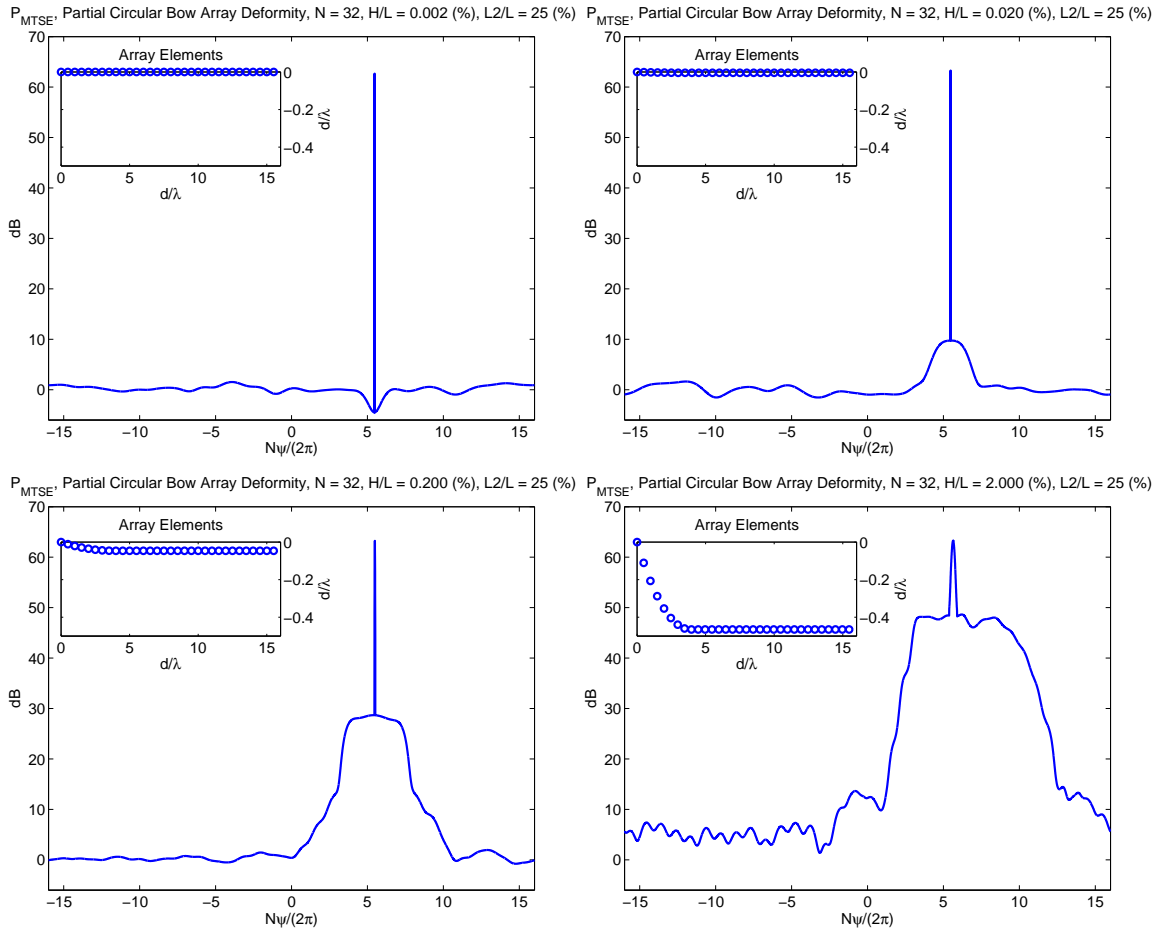


Figure 6.4: **Estimated wavenumber spectrum, partial circular bow array bending:** A linear array bent to a partial circular bow shape causes increasingly higher asymmetric sidebands around the line component as the severity of the bending increases.

6.4 Mitigation Techniques

6.4.1 Introduction

The non-ideal array manifold response can be expressed in the snapshot model by adding an error vector (or calibration error), \mathbf{u}_k , to the ideal response vector, \mathbf{v}_k , in building the snapshots.

$$\mathbf{x}_m = \sum_{k=1}^K (\mathbf{v}_k + \mathbf{u}_k) a_k(m) + \mathbf{n}_m \quad (6.11)$$

The background noise arrives as plane waves at the array and is also affected by the non-ideal array manifold response. However, we do not consider this impact under the assumption that the dominant source of performance degradation is caused by the interaction of the large *INR* line components and the non-ideal response. Because the error vectors are additive to the ideal response vector, we can see that the snapshots consist of a set of terms corresponding to the ideal array manifold response, and the additional error terms.

$$\mathbf{x}_m = \left[\sum_{k=1}^K \mathbf{v}_k a_k(m) + \mathbf{n}_m \right] + \sum_{k=1}^K \mathbf{u}_k a_k(m) \quad (6.12)$$

The ideal array manifold response is what drives the structure in the CSS algorithms. The case considered here is where the array manifold response errors exist, but are small in magnitude compared to the true array manifold response. We call this situation “partially structured”, to reflect that the ideal array manifold response is still somewhat discernible in the data. The MTSE harmonic analysis still provides the estimates of the observable plane wave components, provided they maintain a sufficient SNR over the apparent raised noise floor such that line component detection is possible. We would like to take advantage of this information to further estimate the array manifold response errors, \mathbf{u}_k , contributed by the large line components to improve performance and overcome the limitations outlined

by Zatman [86].

We consider the random error case as our starting point, and develop an algorithm to deal with random array manifold perturbation. This can be done in a straightforward manner. We do not develop a separate algorithm for deterministic array manifold errors. An optimal algorithm for such conditions could be envisioned that estimates the error model parameters, H for circular bow, and H and $L2$ for partial circular bow, or the parabolic parameters in [83], and uses that information to assist in estimating the array manifold errors. Here we simply take the technique developed for random errors, and see to what extent deterministic errors may be processed effectively for the two types of non-random errors considered.

6.4.2 MMSE Unbiased Linear Estimate of Calibration Errors

This section develops the minimum mean squared error, linear unbiased estimate of the calibration errors. Assume there are K line components, and $M \geq K$ snapshots observed. We start with the snapshot model containing non-ideal array manifold responses, $\mathbf{v}_{k,a} = \mathbf{v}_k + \mathbf{u}_k$. The collection of snapshots, $m = 1, \dots, M$ can be arranged as a matrix

$$\mathbf{X} = [\mathbf{x}_1, \mathbf{x}_2, \dots, \mathbf{x}_M] = (\mathbf{V} + \mathbf{U}) \mathbf{A} + \mathbf{N} \quad (6.13)$$

where the individual matrices similarly consist of the original vectors, $\mathbf{V} = [\mathbf{v}_1, \mathbf{v}_2, \dots, \mathbf{v}_K]$, $\mathbf{U} = [\mathbf{u}_1, \mathbf{u}_2, \dots, \mathbf{u}_K]$, $\mathbf{A} = [\mathbf{a}_1, \mathbf{a}_2, \dots, \mathbf{a}_M]$, and $\mathbf{N} = [\mathbf{n}_1, \mathbf{n}_2, \dots, \mathbf{n}_M]$. For now, assume that we have a priori knowledge of the ideal array manifold responses, \mathbf{V} , and signal amplitudes, \mathbf{A} . In practice we will use the estimates provided by the MTSE harmonic analysis processing for these values. We can also represent the matrix \mathbf{A} in an additional way, with each row representing the amplitude time series for the corresponding point source signal.

$$\boldsymbol{\alpha}_k^T = [a_k(1), a_k(2), \dots, a_k(M)] \quad (6.14)$$

$$\mathbf{A} = [\boldsymbol{\alpha}_1, \boldsymbol{\alpha}_2, \dots, \boldsymbol{\alpha}_K]^T \quad (6.15)$$

Given \mathbf{V} , \mathbf{A} , we want to estimate the array calibration errors \mathbf{U} . Perform an initial step by subtracting out the known line components.

$$\mathbf{Y} = \mathbf{X} - \mathbf{V}\mathbf{A} = \mathbf{U}\mathbf{A} + \mathbf{N} \quad (6.16)$$

Before continuing we'll make the following assumptions:

- The array calibration errors, \mathbf{u}_k , are non-random but unknown, and are different for each source, $k = 1 \dots K$.
- The noise terms are zero mean and independent of the array manifold responses and signal amplitudes, with covariance, $E \{ \mathbf{n}_m \mathbf{n}_m^H \} = \mathbf{R}_n$.
- The snapshots for different sample indices, m , are independent.
- $\text{rank}(\mathbf{A}) = K$. Later we will consider the effects of $\text{rank}(\mathbf{A}) < K$. This rank deficient situation will occur if two signals are perfectly correlated with one another (the magnitude of the correlation coefficient is unity), or the number of interferers exceeds the number of snapshots, $K > M$.

We are interested in a linear processor that can be used to estimate the array manifold response error vectors from the observations. For each error vector (or all $\hat{\mathbf{u}}_k$ simultaneously)

$$\hat{\mathbf{u}}_k = \mathbf{Y}\mathbf{w}_k, \quad \hat{\mathbf{U}} = \mathbf{Y}\mathbf{W} \quad (6.17)$$

where the matrices are $\mathbf{W} = [\mathbf{w}_1, \mathbf{w}_2, \dots, \mathbf{w}_K]$, $\hat{\mathbf{U}} = [\hat{\mathbf{u}}_1, \hat{\mathbf{u}}_2, \dots, \hat{\mathbf{u}}_K]$. We design the processor to be unbiased, so $E \{ \hat{\mathbf{u}}_k \} = \mathbf{u}_k$, $E \{ \hat{\mathbf{U}} \} = \mathbf{U}$. Expanding out the expectation

$$E \{ \hat{\mathbf{u}}_k \} = E \{ \mathbf{Y}\mathbf{w}_k \} = \mathbf{U}\mathbf{A}\mathbf{w}_k \quad (6.18)$$

This implies that to be unbiased $\mathbf{U}\mathbf{A}\mathbf{w}_k = \mathbf{u}_k$, or

$$\mathbf{A}\mathbf{w}_k = \mathbf{e}_k, \text{ or } \mathbf{A}\mathbf{W} = \mathbf{I} \quad (6.19)$$

where \mathbf{e}_k is the elementary vector which is all zeros with a 1 in the k^{th} position. This places K constraints on each weight vector, \mathbf{w}_k . Written out explicitly using the row definition of \mathbf{A}

$$\alpha_j^T \mathbf{w}_k = \delta[j - k] \quad (6.20)$$

where $\delta[j - k]$ is the Kronecker delta. We want to minimize the estimation error variance at the output for each filter, \mathbf{w}_k , given by

$$\sigma_{\mathbf{w},k}^2 = E \left\{ (\mathbf{u}_k - \hat{\mathbf{u}}_k)^H (\mathbf{u}_k - \hat{\mathbf{u}}_k) \right\} \quad (6.21)$$

Using (6.17) in (6.21), the expression for the variance reduces to

$$\sigma_{\mathbf{w},k}^2 = \mathbf{w}_k^H E \{ \mathbf{N}^H \mathbf{N} \} \mathbf{w}_k \quad (6.22)$$

To find $E \{ \mathbf{N}^H \mathbf{N} \}$ recall that $\mathbf{N} = [\mathbf{n}_1, \mathbf{n}_2, \dots, \mathbf{n}_M]$, where the individual \mathbf{n}_m are i.i.d. with covariance, \mathbf{R}_n .

$$\begin{aligned} E \{ \mathbf{N}^H \mathbf{N} \} &= E \left\{ \begin{bmatrix} \mathbf{n}_1^H \mathbf{n}_1 & \mathbf{n}_1^H \mathbf{n}_2 & \mathbf{n}_1^H \mathbf{n}_M \\ \mathbf{n}_2^H \mathbf{n}_1 & \mathbf{n}_2^H \mathbf{n}_2 & \\ \mathbf{n}_M^H \mathbf{n}_1 & & \mathbf{n}_M^H \mathbf{n}_M \end{bmatrix} \right\} \\ &= \text{tr}(\mathbf{R}_n) \mathbf{I} \end{aligned} \quad (6.23)$$

Inserting (6.23) into (6.22) gives the noise output power.

$$\sigma_{\mathbf{w},k}^2 = \text{tr}(\mathbf{R}_n) \mathbf{w}_k^H \mathbf{w}_k \quad (6.24)$$

We can now set up the constrained optimization problem to find the individual weights, \mathbf{w}_k .

$$\arg \min_{\mathbf{w}_k} \text{tr}(\mathbf{R}_n) \mathbf{w}_k^H \mathbf{w}_k \quad \text{subject to} \quad \boldsymbol{\alpha}_j^T \mathbf{w}_k = \delta_{jk} \quad (6.25)$$

Using the method of Lagrange multipliers we set up the following cost function to be minimized [60].

$$J(\mathbf{w}_k) = \text{tr}(\mathbf{R}_n) \mathbf{w}_k^H \mathbf{w}_k + \sum_{l=1}^K \lambda_{kl} (\boldsymbol{\alpha}_l^T \mathbf{w}_k - \delta_{lk}) + \sum_{l=1}^K \lambda_{kl}^* (\mathbf{w}_k^H \boldsymbol{\alpha}_l^* - \delta_{lk}) \quad (6.26)$$

Taking the gradient w.r.t. \mathbf{w}_k and setting to 0

$$\left. \frac{\partial}{\partial \mathbf{w}_k} J(\mathbf{w}_k) = 0 \right|_{\mathbf{w}_k = \mathbf{w}_{k,opt}} \quad (6.27)$$

yields the following expression

$$\mathbf{w}_k^H = -\frac{1}{\text{tr}(\mathbf{R}_n)} \sum_{l=1}^K \lambda_{kl} \boldsymbol{\alpha}_l^T \quad (6.28)$$

Defining the vector $\boldsymbol{\lambda}_k$ and matrix $\boldsymbol{\Lambda}$ respectively,

$$\boldsymbol{\lambda}_k = [\lambda_{k,1}, \lambda_{k,2}, \dots, \lambda_{k,K}], \quad \boldsymbol{\Lambda} = [\boldsymbol{\lambda}_1^T, \boldsymbol{\lambda}_2^T, \dots, \boldsymbol{\lambda}_K^T]^T \quad (6.29)$$

then (6.28) can be written as

$$\mathbf{w}_k^H = -\frac{1}{\text{tr}(\mathbf{R}_n)} \lambda_k \mathbf{A} \quad (6.30)$$

We can express the entire solution for all k simultaneously as

$$\mathbf{W}^H = -\frac{1}{\text{tr}(\mathbf{R}_n)} \mathbf{\Lambda} \mathbf{A} \quad (6.31)$$

Inserting (6.31) into the constraint equation (6.19), and solving for the constraint matrix, $\mathbf{\Lambda}$, we have

$$\mathbf{\Lambda} = -\text{tr}(\mathbf{R}_n) (\mathbf{A} \mathbf{A}^H)^{-1} \quad (6.32)$$

Our earlier assumption that $\text{rank}(\mathbf{A}) = K$ implies that $(\mathbf{A} \mathbf{A}^H)^{-1}$ exists. Inserting (6.32) back into (6.31) produces the overall solution for the weights.

$$\mathbf{W} = \mathbf{A}^H (\mathbf{A} \mathbf{A}^H)^{-1} \quad (6.33)$$

which we recognize as the Moore-Penrose pseudo-inverse of \mathbf{A} [72]. Using (6.33) in (6.17), the minimum variance unbiased linear estimate of the non ideal array manifold response error vectors is

$$\hat{\mathbf{U}} = \mathbf{Y} \mathbf{W} = \mathbf{Y} \mathbf{A}^H (\mathbf{A} \mathbf{A}^H)^{-1} \quad (6.34)$$

In situations where $M < K$, then $\text{rank}(\mathbf{A}) < K$ and the inverse $(\mathbf{A} \mathbf{A}^H)^{-1}$ does not exist. As an ad-hoc solution in this situation, we can choose to restrict the processing to estimate a subset of the array manifold error vectors, $\hat{\mathbf{u}}_k$, corresponding to the M largest sources. In practice this may still have issues with the conditioning of the matrix $\mathbf{A} \mathbf{A}^H$ and a value less than M may work better numerically. Performance will degrade in these scenarios compared to an optimal adaptive beamformer because there is not enough snapshot information to

estimate all the random error vectors from the data.

6.4.3 Maximum Likelihood Estimate of Calibration Errors

In Section 6.4.2, we found the minimum mean square error linear unbiased estimate of the array manifold response error vectors. This required knowledge of the number of point source signals, K , the signal amplitudes, \mathbf{A} , and the ideal array manifold response vectors, \mathbf{V} . Additionally, we assumed that the snapshots were independent. The solution did not require definition of the statistics of the noise term, \mathbf{n}_m , other than state the noise was independent of the other quantities in the data. In this section we derive the maximum likelihood estimation of the array manifold response error vectors. We make the same assumptions as in Section 6.4.2, and additionally specify the noise terms as complex Gaussian, $\mathbf{n}_m \stackrel{d}{\rightarrow} CN_N(\mathbf{0}, \mathbf{R}_n)$. The individual snapshots

$$\mathbf{x}_m = (\mathbf{V} + \mathbf{U}) \mathbf{a}_m + \mathbf{n}_m \quad (6.35)$$

are complex Gaussian random vectors, with non-zero mean, $\mathbf{m}_m = [\mathbf{V} + \mathbf{U}] \mathbf{a}_m$

$$\mathbf{x}_m \stackrel{d}{\rightarrow} CN_N(\mathbf{m}_m, \mathbf{R}_n) \quad (6.36)$$

Grouping all snapshots, $\mathbf{X} = [\mathbf{x}_1, \mathbf{x}_2, \dots, \mathbf{x}_M]$ and amplitude values, $\mathbf{A} = [\mathbf{a}_1, \mathbf{a}_2, \dots, \mathbf{a}_M]$, the complex Gaussian random matrix \mathbf{X} has non-zero mean $\mathbf{M} = (\mathbf{V} + \mathbf{U}) \mathbf{A}$. With the snapshots being independent, the probability density for \mathbf{X} is [87]

$$f_{\mathbf{X}}(\mathbf{X}) = \pi^{-NM} \det(\mathbf{R}_n)^{-M} \exp\left(-\sum_{m=1}^M (\mathbf{x}_m - \mathbf{m}_m)^H \mathbf{R}_n^{-1} (\mathbf{x}_m - \mathbf{m}_m)\right) \quad (6.37)$$

Eqn. (6.37) can be expressed using the trace operator, $\text{tr}()$.

$$f_{\mathbf{X}}(\mathbf{X}) = \pi^{-NM} \det(\mathbf{R}_n)^{-M} \exp\left(-\text{tr}\left[(\mathbf{X} - \mathbf{M})^H \mathbf{R}_n^{-1} (\mathbf{X} - \mathbf{M})\right]\right) \quad (6.38)$$

For the available snapshot data, the likelihood function for a given estimate of the array manifold errors is

$$f_{\mathbf{X}|\hat{\mathbf{U}}}(\mathbf{X}|\hat{\mathbf{U}}) = \pi^{-NM} \det(\mathbf{R}_n)^{-M} \exp\left(-\text{tr}\left[(\mathbf{X} - \mathbf{M}(\hat{\mathbf{U}}))^H \mathbf{R}_n^{-1} (\mathbf{X} - \mathbf{M}(\hat{\mathbf{U}}))\right]\right) \quad (6.39)$$

The maximum likelihood estimate of the array manifold error vectors, $\hat{\mathbf{U}}_{ML}$, is the matrix that maximizes $f_{\mathbf{X}|\hat{\mathbf{U}}}(\mathbf{X}|\hat{\mathbf{U}})$.

$$\hat{\mathbf{U}}_{ML} = \arg \max_{\hat{\mathbf{U}}} f_{\mathbf{X}|\hat{\mathbf{U}}}(\mathbf{X}|\hat{\mathbf{U}}) \quad (6.40)$$

To find $\hat{\mathbf{U}}_{ML}$ we begin with the log-likelihood function, $\ell_{\mathbf{X}|\hat{\mathbf{U}}}(\mathbf{X}|\hat{\mathbf{U}}) = \ln f_{\mathbf{X}|\hat{\mathbf{U}}}(\mathbf{X}|\hat{\mathbf{U}})$.

$$\ell_{\mathbf{X}|\hat{\mathbf{U}}}(\mathbf{X}|\hat{\mathbf{U}}) = C_1 + C_2 - \text{tr}\left[(\mathbf{X} - \mathbf{M}(\hat{\mathbf{U}}))^H \mathbf{R}_n^{-1} (\mathbf{X} - \mathbf{M}(\hat{\mathbf{U}}))\right] \quad (6.41)$$

where the constants C_1 , C_2 are not functions of $\hat{\mathbf{U}}$. Because it is a maximum of $\ell_{\mathbf{X}|\hat{\mathbf{U}}}(\mathbf{X}|\hat{\mathbf{U}})$

$$\left. \frac{\partial}{\partial \hat{\mathbf{U}}} \ell_{\mathbf{X}|\hat{\mathbf{U}}}(\mathbf{X}|\hat{\mathbf{U}}) \right|_{\hat{\mathbf{U}}=\hat{\mathbf{U}}_{ML}} = 0 \quad (6.42)$$

Expanding out terms in (6.41), and applying the partial derivative through the $\text{tr}()$, we arrive at

$$\hat{\mathbf{U}}_{ML} = \mathbf{X}\mathbf{A}^H (\mathbf{A}\mathbf{A}^H)^{-1} - \mathbf{V} \quad (6.43)$$

Alternatively, if we start with

$$\mathbf{Y} = \mathbf{X} - \mathbf{V}\mathbf{A} \quad (6.44)$$

and apply the same procedure, we have

$$\hat{\mathbf{U}}_{ML} = \mathbf{Y}\mathbf{A}^H (\mathbf{A}\mathbf{A}^H)^{-1} \quad (6.45)$$

Eqn. (6.45) matches the result (6.34) in Section 6.4.2.

6.4.4 Comments

It is not surprising that the MMSE linear unbiased estimator has the same form as the ML solution for Gaussian noise. Note that the covariance of the noise term \mathbf{n}_m does not have an impact on the solution. This is particularly useful, since the noise covariance is not known at this point in the processing. Also, it establishes that we should not encounter problems if the underlying noise is non-white.

Where a non-white noise may still cause issues is in situations where the dynamic range of the noise, spectrally, is very large. This could be the case when operating below design frequency where the isotropic noise component is much larger than the sensor noise component. The apparent increase in noise floor due to the effects of array manifold response errors accumulated by the spatially spread isotropic noise process may mask the true sensor noise components. Since we make no attempt to determine the error vectors attributed to the spatially spread process we would expect a loss in performance. Looking ahead, Figure 6.8 shows an example of this type of scenario, where the total contribution of error vectors due to the isotropic noise component mask the sensor noise, even though the point source error vectors are managed.

6.4.5 Procedure

This section describes the procedure to use the results from Sections 6.4.2 and 6.4.3 to supplement the CSS with MTSE approach with additional non-ideal array manifold response error vector information. The dominant sources of normalized SINR loss are the error vectors associated with the high *INR* point sources in the data. We use the term partially structured to indicate that some observation of the underlying structure remains observable. The figures in Section 6.3 showed how this “looked” in the estimated wavenumber spectrum. Fundamentally, being partially structured implies that the high *INR* line components in the spectrum can still be detected via the MTSE harmonic analysis process. In general, this requires some amount of positive *SNR* of the line component above the raised noise floor caused by the array manifold errors.

The following procedure is used to incorporate non-ideal array manifold response error vector information into the overall covariance matrix estimate.

1. Use MTSE harmonic analysis to detect and estimate the number of line components, K , and their parameters, \mathbf{v}_k , and $a_k(m)$.
2. Use (6.44) and (6.45) to estimate array calibration error vectors, \mathbf{u}_k , for these line components.
3. Subtract the discrete components from the snapshot data to form the residual, $\mathbf{X}_{res} = \mathbf{X} - (\mathbf{V} + \mathbf{U}) \mathbf{A}$.
4. (optionally) Iterate steps 1,2,3.
5. Estimate the final residual “continuous” background spectrum, $\hat{P}_{res}(\cdot)$, and form $\mathbf{R}_{MTSE,res}$.
6. Form an overall estimate of the covariance matrix

$$\mathbf{R}_{TOTAL} = \sum_{k=1}^K (\mathbf{v}_k + \mathbf{u}_k) (\mathbf{v}_k + \mathbf{u}_k)^H \frac{1}{M} \sum_{m=1}^M |a_k(m)|^2 + \mathbf{R}_{MTSE,res} \quad (6.46)$$

6.5 Performance Simulation

Performance of the algorithm described in Section 6.4.5 is assessed via simulation for several scenarios. Processing for random array manifold errors, both at and below design frequency is considered, as well as the two types of deterministic positional errors presented earlier. We continue to focus on performance for the uniform linear array case, with varying interference environments. The primary measure of performance is the normalized SINR loss. We also consider, qualitatively, the estimated wavenumber spectrum in comparison to the corresponding ensemble MVDR spectrum.

6.5.1 Random Errors

Operation At Design Frequency

Simulations are performed for an $N = 32$ uniform linear array with spacing $d = \lambda/2$ operating at the design frequency, i.e., $f = c/\lambda$. We use the simple random error model of Section 6.2.1, and vary the measure σ_g^2/c_h^2 . Initial simulations contain $K = 6$ interferers, each with $INR = 50$ dB. Figures 6.5 and 6.6 show the results for $\sigma_g^2/c_h^2 = -30$ and -10 dB respectively.

The upper portion of each Figure shows two estimated wavenumber spectra. The top most is the MTSE spectrum for the data, with the MTSE parameters $NFPE = 32$, $NW = 2$, $D = 4$ and $\gamma_{TH} = 5$ dB. A single pass of non-ideal response processing is carried out. In regions away from the line components the noise floor is raised due to the sidelobes introduced by the non-ideal array manifold response, similar to the observations in Section 6.3. A key difference here is the each interferer contributes to the raised noise floor, so that the apparent noise floor is

$$\sim INR_{dB} + (\sigma_g^2/c_h^2)_{dB} + 10 \log_{10}(K) \quad (6.47)$$

The lower spectrum is the MTSE spectrum after array manifold response error processing.

In this spectrum the ideal portions, \mathbf{v}_k , of detected components are numerically added to the estimated continuous background spectrum. This estimated background spectrum is computed from the residual snapshot data, where the line components and their associated array manifold response error vectors have been subtracted out. The six interferers are clearly visible, with overall noise floor showing a flat shape, as expected, but biased lower than its actual level at 0 dB. The lower portion of the Figure shows the normalized SINR loss (in blue) for the adaptive beamformer based on the final estimated covariance, \mathbf{R}_{TOTAL} . For comparison, the multistage Wiener filter (MWF) with rank $r = 6$ is shown in red. CSS with MTSE and MWF both operate on the same snapshot data, and both use the ideal array manifold response to generate the steering the vector, \mathbf{s} . Both 50th and 90th percentile are shown in the Figure.

Figure 6.5 shows the case of $\sigma_g^2/c_h^2 = -30$ dB, with a perceived raised noise floor in the range 28-32 dB, near the expected 27.8 dB. Again, the final wavenumber spectrum is reasonable, with the normalized SINR loss tracking well with MWF except near $M = 6$ snapshots. This is a result of the ad-hoc limiting discussed in Section 6.4.2 restricting the number of processed interferers to $M - 1$ to improve condition number of the $\mathbf{A}\mathbf{A}^H$ matrix.

Figure 6.6 shows a more stressful scenario with $\sigma_g^2/c_h^2 = -10$ dB. The elevated noise floor is in the range of 50 dB, near the expected 47.8 dB. The final wavenumber spectrum is reasonable. Here also, normalized SINR loss tracks well with MWF except approaching $M = 6$ snapshots. Also evident is that the 90th percentile curve is starting to show higher loss, indicated that the performance of the technique is starting to break down. Cases with $\sigma_g^2/c_h^2 > -10$ dB showed generally poor performance, indicating that the “partially structured” condition is no longer applicable and the harmonic analysis is unable to consistently detect line components in the data.

The behavior seen here is consistent through all simulation scenarios. When error vector processing works, normalized SINR loss performance tracks with the MWF of appropriate rank. As the non-ideal array manifold response becomes large the line components are not consistently detected and performance degrades. When the non-ideal array manifold

response becomes so large that the line components are undetectable the method does not work.

Iterative Processing

All line components may not be evident in the initial estimated spectrum as the sidelobes due to the strongest interferers may mask them. Depending on the INR of these hidden line components, and the degree of non-ideal response, additional error vector processing may be required. As mentioned in Section 6.4.5, the array manifold error processing may be iterated. Figure 6.7 shows an example of such a situation, with $\sigma_g^2/c_h^2 = -10$ dB. Here, two of the point sources are at $INR = 50$ dB, with the remaining four lowered to $INR = 20$ dB. The original MTSE spectrum only shows the two peaks corresponding to the strongest sources. A single iteration of processing does not account for the lower INR source error vectors. In the figure, two iterations of array manifold error processing are carried out, with the resultant estimated wavenumber spectrum shown in the middle. All components are identified, at appropriate power levels and the spectrum is reasonable. The normalized SINR loss perform tracks similarly to MWF except near $M = 6$ snapshots, a behavior seen in the original $\sigma_g^2/c_h^2 = -10$ dB test case.

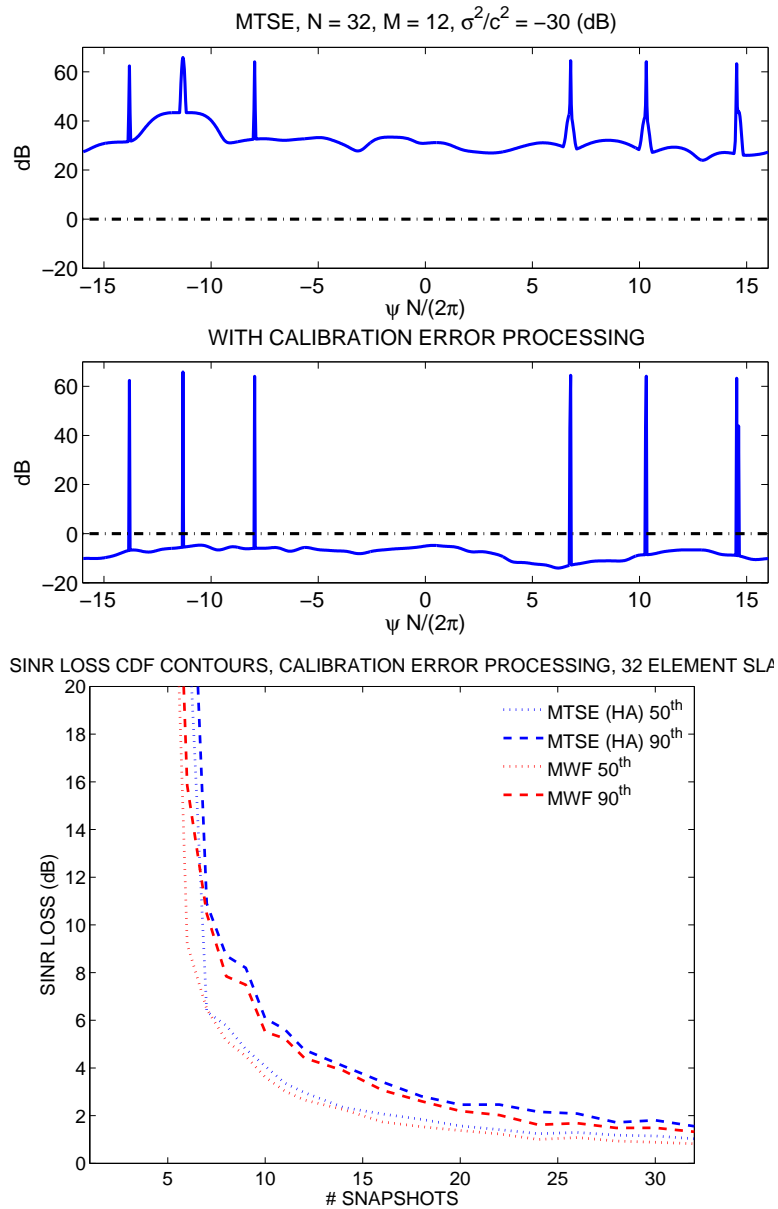


Figure 6.5: $N = 32$, $\sigma_g^2/c_h^2 = -30$ dB, **constant** $INR = 50$ dB: In this test case the impact of the non-ideal array manifold response is clearly visible in the original MTSE spectrum, shown in the upper subplot, as the noise floor is significantly higher than the true noise floor (indicated by the black dash-dot line). After error vector processing the final estimated spectrum is much improved, as seen in the middle subplot. As shown in the lower plot, the normalized SINR loss performance of CSS with MTSE and error vector processing tracks with MWF performance.

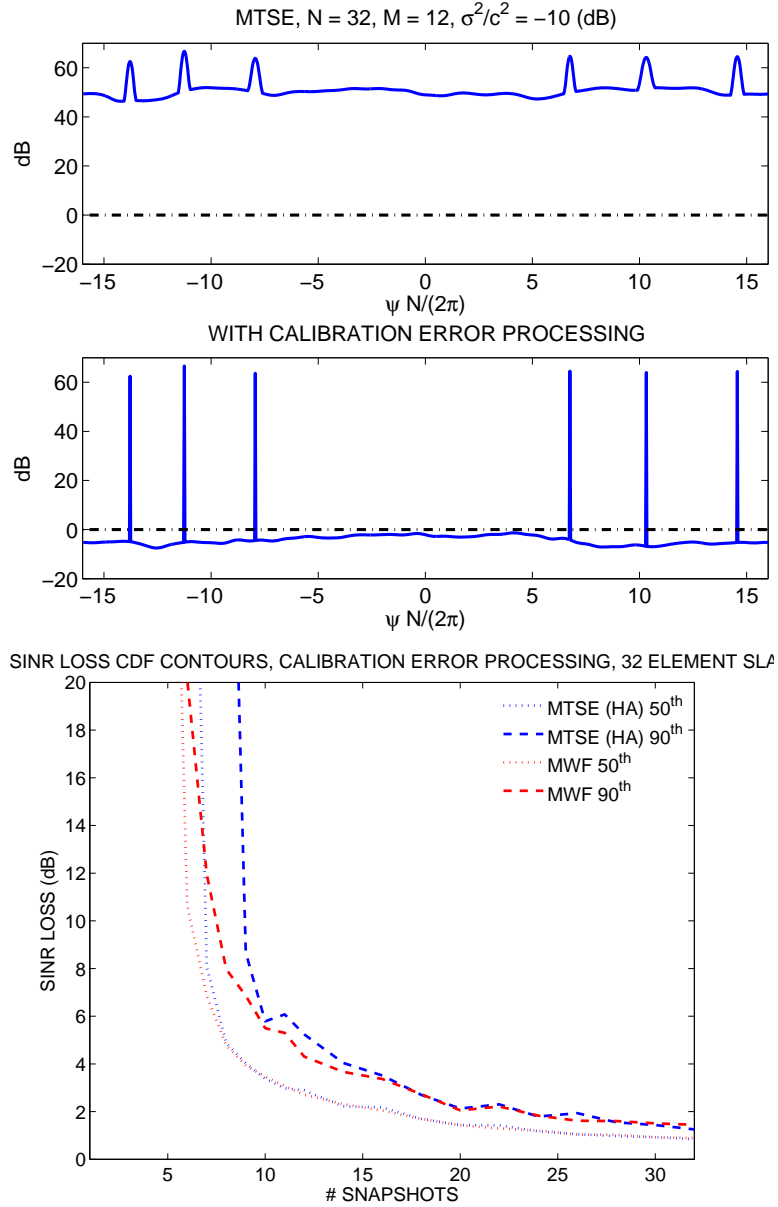


Figure 6.6: $N = 32$, $\sigma_g^2/c_h^2 = -10$ dB, **constant** $INR = 50$ dB: In this test case the large non-ideal array manifold response almost masks the high INR point sources in the original MTSE spectrum, shown in the upper subplot. The noise floor exceeds the true noise floor by 50 dB. After error vector processing the final estimated spectrum is again much improved, as seen in the middle subplot. Normalized SINR loss performance of CSS with MTSE and error vector processing follows MWF performance to $M = 7$ snapshots in the 50th percentile, and to $M = 9$ snapshots in the 90th percentile. This indicates that the magnitude of the non-ideal response is approaching the point where the “partial structure” concept is no longer applicable.

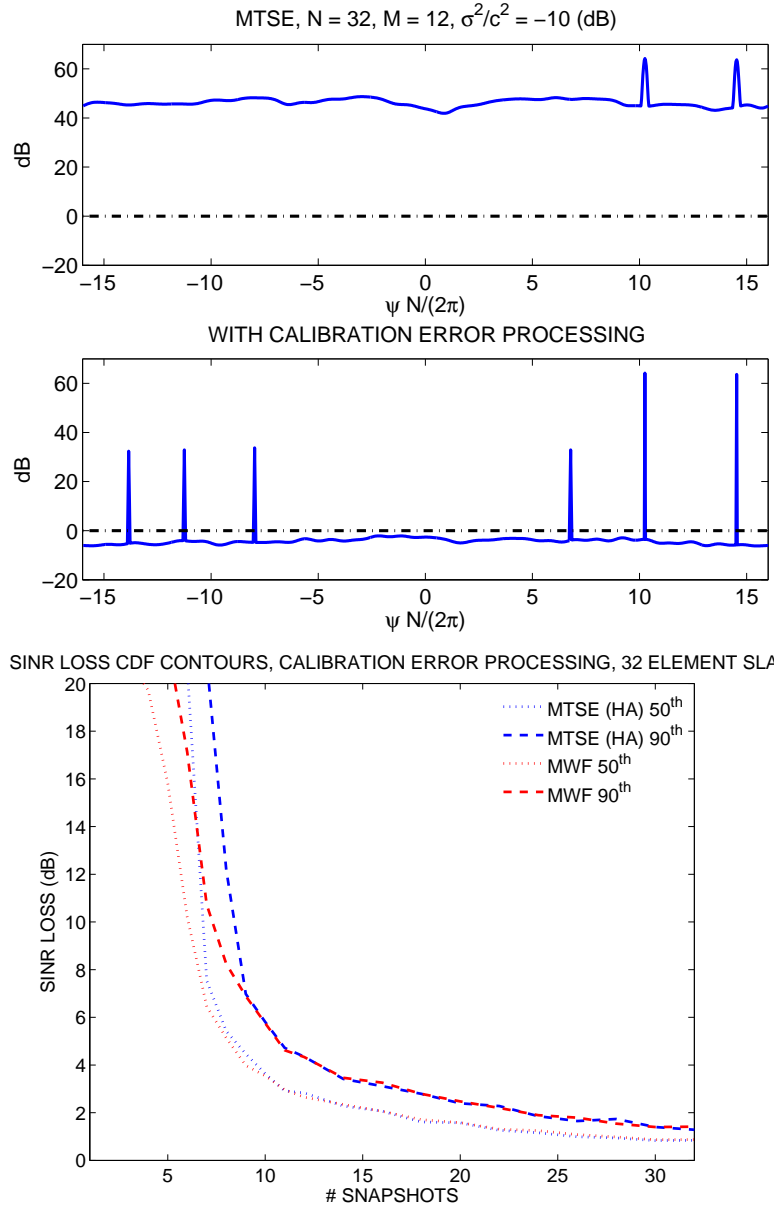


Figure 6.7: $N = 32$, $\sigma_g^2/c_h^2 = -10$ dB, **variable** $INR = [20, 50]$ dB, **2 passes**: The error vectors corresponding to the largest INR line components may mask point sources that are substantially weaker but present. In this example, the sidelobes of the two highest INR sources hide the four lower INR sources. These lower sources also contribute their own array manifold response error vectors. These may require additional processing to progressively peel back the impact of the line components to observe the true noise floor (shown as the black dash-dot line). Two passes of error vector processing accomplish this, as shown in the middle subplot. Overall normalized SINR loss performance tracks well with MWF performance. Without the second pass, the normalized SINR loss is in line with expected [86] as illustrated in Figure 6.2, in this case ~ 16 dB.

Operation Below Design Frequency

To simulate operation below the design frequency several parameters need to be specified. The isotropic noise component, σ_n^2 , must be specified relative to the uncorrelated sensor noise component, σ_w^2 . For simulation we use $\sigma_w^2 = 0$ dB, $\sigma_n^2 = 20$ dB. To properly form the snapshot data for the isotropic noise requires the isotropic noise covariance matrix, \mathbf{R}_n . This is not straightforward using the simple model of Section 6.2.1, but can be done using the explicit model. We use σ_A^2 corresponding to a gain variation in the range ± 3 dB (w.r.t. power) for all sensors, with a phase error of $\sigma_\theta = 15^\circ$. With these set, simulations are run for $\sigma_{\Delta x} = \sigma_{\Delta y} = \sigma_{\Delta z}$ corresponding to 1% and 10% of the interelement spacing, $\lambda_o/2$. The test cases consider operation at one-half the design frequency. To avoid changing the wavenumber resolving capability of the array, which impacts the effectiveness of MTSE harmonic analysis, the uniform linear array has $N = 64$ elements (compared to $N = 32$ used earlier). To maintain similar line component cancellation performance as earlier, we correspondingly lower $NFPE$ to 16 from 32. The remaining MTSE parameters used are $NW = 2$, $D = 4$ and $\gamma_{TH} = 5$ dB. The same constant INR , $K = 6$ interferer test case is used in these scenarios.

Figure 6.8 shows the results for positional errors corresponding to a standard deviation of 10% of the element spacing. The final estimated wavenumber spectrum is still reasonable, but the bias in the noise floor in the virtual region is more apparent. This is a result of the sidelobe contributions from the isotropic noise component, similar to the effect of individual point sources but for a spatially spread process. Normalized SINR loss performance tracks closely with the MWF (rank $r = 6$). Positional errors greater than 12.5% standard deviation begin to rapidly degrade compared to the unconstrained covariance technique. Performance results for 1% standard deviation of position (not shown) similarly track with MWF to $M = 6$ snapshots.

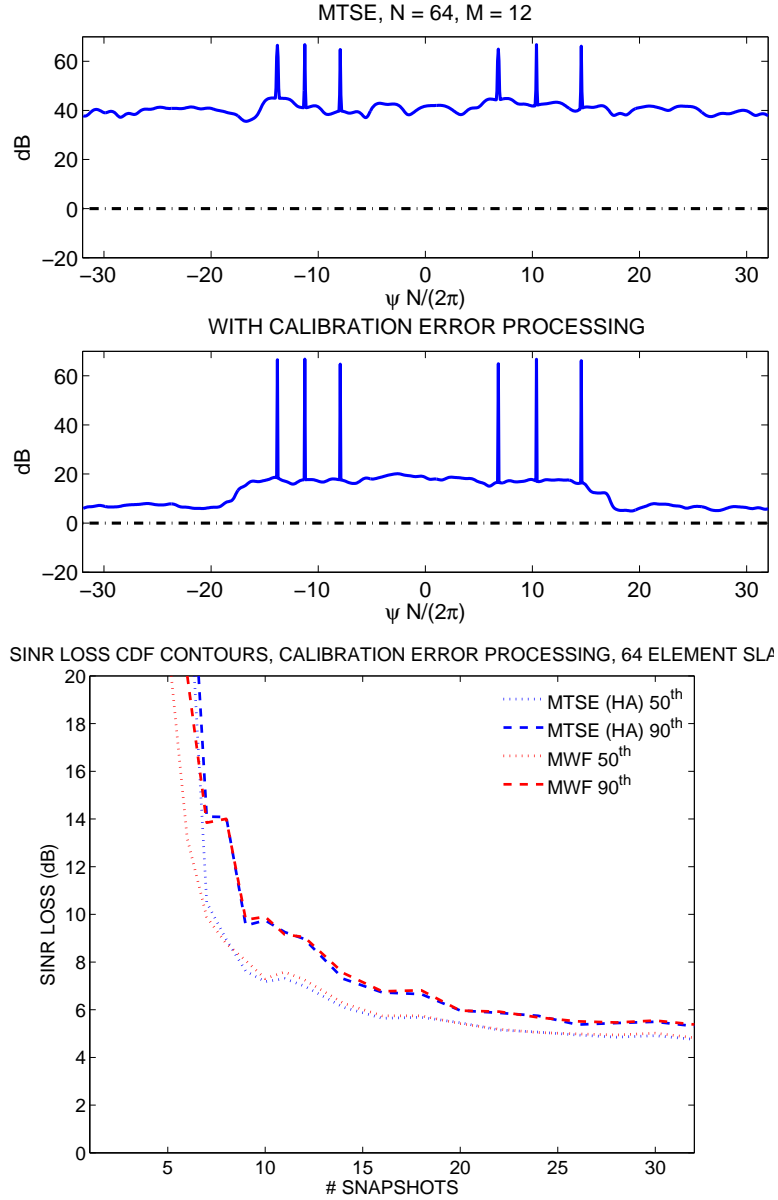


Figure 6.8: $N = 64$, $\sigma_{\Delta x,y,z} = 10\% \cdot \lambda_o/2$, **constant INR = 50 dB, half design frequency**: The large positional errors result in large bias in the virtual region after error vector processing. The algorithm does not attempt to mitigate the effect of non-ideal response attributed to spatially spread noise sources such as the isotropic noise environment, just the line components in the spectrum.

6.5.2 Deterministic Errors

Circular Bow

This section looks at performance of the array manifold error processing algorithm in the situation of a circular bow in the array, as discussed in Section 6.2.2. We use the same $K = 6$ interferer, $INR = 50$ dB test case, and vary the amount of deflection of the array at its center, H , from the nominal line of the array. This is expressed as a percentage of the overall array length, H/L .

Figure 6.9 shows the results for $H/L = 2.0\%$, lower values of H/L indicate smaller array deformation so results are comparable. The original MTSE spectrum shows the impact of the positional errors and 'sidebands' around the location of the sources, similar to that shown in Figure 6.3 for the case of a single interferer. Because of the proximity of the sources with respect to each other, the overall noise floor appears raised, but this is the sum of the contribution of the sidebands. The final estimated wavenumber spectrum after array manifold error processing appears reasonable. The normalized SINR loss performance is comparable to the MWF (rank $r = 6$) processor, with some advantage below the point of $M = 6$ snapshots.

As the value of H/L exceeds 2.0% performance is seen to degrade in the final MTSE spectrum as line components are not reliably detected (not shown). This implies that the error vector processing is not estimating and removing the non-ideal array manifold response as completely as seen in earlier cases, and that the true covariance matrix itself is becoming unstructured compared to the assumed model.

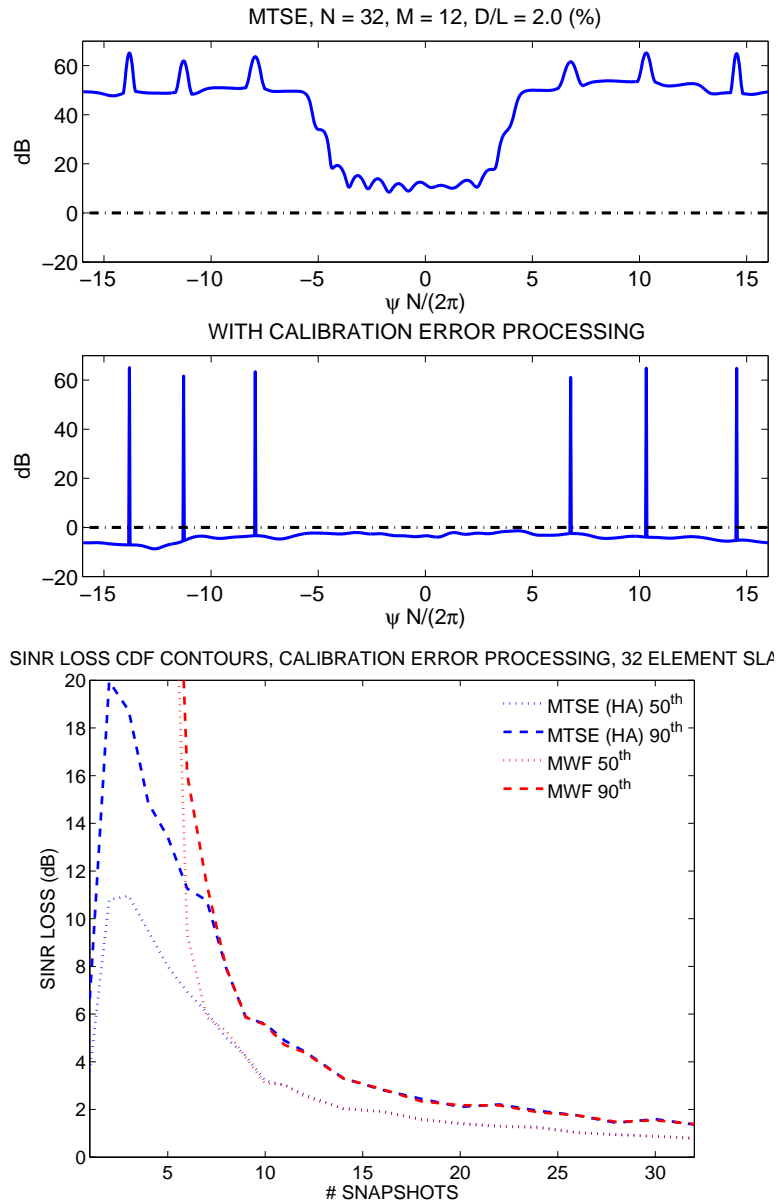


Figure 6.9: **Circular bow in array shape, $N = 32$, $H/L = 2.0\%$, constant $INR = 50$ (dB)**: The array bending occasionally results in one of the point sources failing to be detected in the estimated wavenumber for $M = 12$, shown in the upper subplot. Error vector processing operates on the point sources that are detected. The final wavenumber spectrum, shown in the middle subplot, appears reasonable. The normalized SINR loss performance, shown the bottom plot, is comparable to MWF. Larger circular bow deformity, $H/L > 2.0\%$, results in unacceptable performance.

Partial Circular Bow

This section looks at performance of the array manifold error processing algorithm in the situation of a partial circular bow in the array, as discussed in Section 6.2.2. Because a portion of the array maintains its linear form, performance is more tolerable to a higher deflection, H , from the nominal line of the array. We select the curved portion of the array to span a distance $L_2/L = 25\%$ of the overall array length, and vary the deflection as a percentage of overall array length, H/L . The interference environment is the same $K = 6$ interferer, fixed $INR = 50$ dB test case. Performance was assessed for $H/L = 2.0, 3.0,$ and 4.0% . Below $H/L = 4.0\%$, the error vector processing successfully identifies and accounts for the non-ideal response. Similar to circular bow case, the final MTSE spectrum is reasonable and performance is inline with MWF. Results are not shown as they are comparable to Figure 6.9.

For $H/L = 4.0\%$, Figure 6.10 shows that the final wavenumber spectrum exhibits artifacts, a sign that performance is beginning to degrade. The normalized SINR loss curves are slightly worse than MWF at the 50^{th} percentile. Additionally, the 90^{th} percentile curve is not visible, clearly indicating that algorithm is not performing at all some percentage of the time in this case. For $H/L > 4.0\%$, for $L_2/L = 25\%$, performance continues to degrade. This behavior is similar to that seen in the circular bow case for $H/L > 2.0\%$.

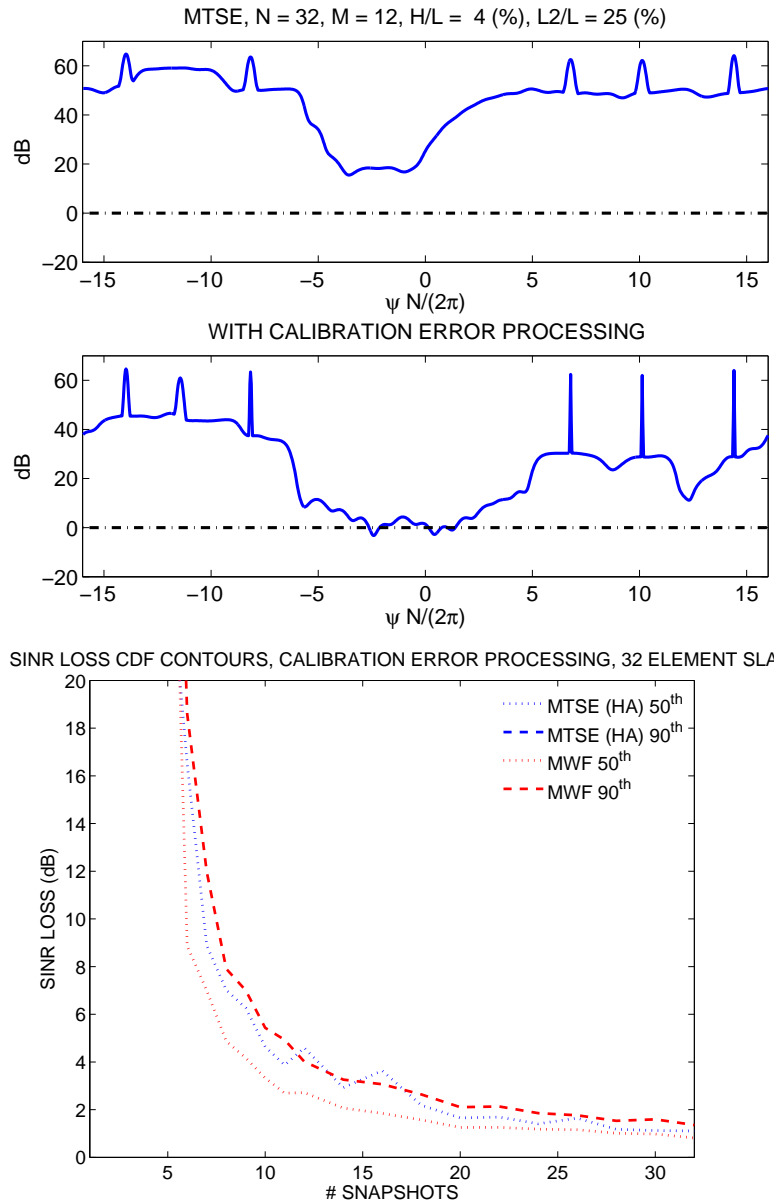


Figure 6.10: **Partial circular bow in array shape, $N = 32$, $H/L = 4.0\%$, $L_2/L = 25\%$, constant $INR = 50$ dB**: The larger array bending in the partial bow results in one of the point sources occasionally failing to be detected in the estimated wavenumber for $M = 12$, shown in the upper subplot (recall this occurred for $H/L = 2.0\%$ in the circular bow case, Figure 6.9). Error vector processing operates on the point sources that are detected and the final wavenumber spectrum, shown in the middle subplot, shows evidence of the impact of the overlooked interferer. Near broadside the estimated noise floor is still reasonably close to the true noise floor, shown as the black dash-dot at 0 dB. The normalized SINR loss performance, shown the bottom plot, is still comparable to MWF. Larger partial circular bow deformity, $H/L > 4.0\%$ results in unacceptable performance for this particular L_2/L .

6.5.3 Impact of Error Processing with Ideal Array Manifold Response

The previous sections showed scenarios where the addition of array manifold error processing improved upon the normalized SINR losses predicted for structured algorithms, with performance in line with that seen using MWF processing. This came at the expense of the fast convergence of the original CSS with MTSE algorithm seen earlier. A remaining question is if there is a penalty incurred for performing this processing in the event the array has an ideal array manifold response.

With no array manifold response errors, the test cases considered represent three scenarios. The first, a constant INR , six interferer test case is shown in Figure 6.11. With MTSE parameters $NFPE = 32$, $NW = 2$, $D = 4$ and $\gamma_{TH} = 5$ dB, the original MTSE spectrum (top) shows the characteristic pedestal behavior due to the accuracy of the discrete component cancellation. Array manifold error processing eliminates the residual components, as seen in the final estimated wavenumber spectrum. This is a beneficial byproduct of the array manifold error processing. The normalized SINR loss curve is only slightly worse performing than MWF for $M > 6$, with improved performance below $M = 6$.

The improved performance below $M = 6$ deserves some discussion. In general, the error vector processing attempts to remove array manifold error vectors from the data when, in fact, there are none. This causes a drop in performance compared to that seen with the original CSS with MTSE algorithm from Chapter 4. Simulations have shown that using a large initial $NFPE$, say ≥ 128 , makes this problem worse due to the improved accuracy in initial harmonic analysis line component cancellation. This makes the error vector estimates more sensitive to numerical issues. Larger $NFPE$ also produces a much lower biased noise floor in the final estimated wavenumber spectrum. For this test case all six point sources are always detected, but when $M \leq 6$ snapshots are available the number of point sources considered is limited to $M - 1$, to maintain appropriate rank of the matrix \mathbf{A} in (6.33). When this happens, by limiting the additional error vector processing the overall processor behaves more like the original algorithm of Chapter 4, which is the more appropriate for the data. At $M = 1$ no additional error vector processing is attempted at all, and the

performance is the same as seen for $M = 1$ in Chapter 4.

Figure 6.12 shows the second test case, identical to the first but with a mix of INR levels. Two iterations of array manifold response error processing are invoked. Overall performance is very similar to the first test case, with normalized SINR loss performance slightly better than MWF, but not by a notable amount.

Figure 6.13 is the test case for operation below the design frequency. MTSE parameters are $NFPE = 16$, $NW = 2$, $D = 4$ and $\gamma_{TH} = 5$ dB. The array manifold response error processing does produce a good final estimate of the wavenumber spectrum, in both the visible and virtual regions. The normalized SINR loss performance follows a similar convergence trajectory as MWF.

In all cases, implementing additional error vector processing results in performance that is driven by the number of snapshots, M , and interferers, K . The rapid convergence with near optimal performance of the original CSS with MTSE when applied to ideal array manifold response data is not exhibited.

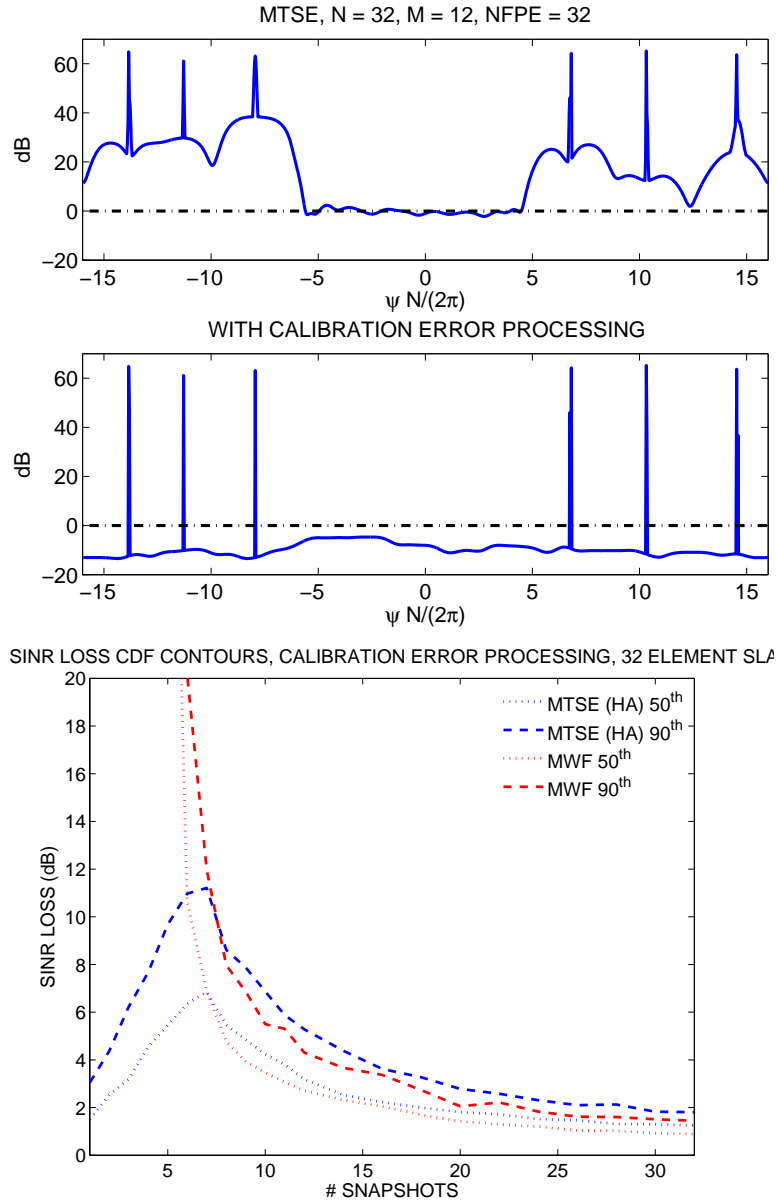


Figure 6.11: **Impact of error processing for ideal manifold response, fixed INR:** This test case measures the impact of error vector processing when the array manifold response is in fact ideal, for the $N = 32$ with constant $INR = 50$ (dB) scenario. Above $M = 6$ snapshots, performance follows the MWF trajectory within 1 dB. Below $M = 6$ snapshots performance is better. This is a resultant of the algorithm constraining the error vector processing due to the limited snapshots versus number of interferers. By limiting error vector processing, the algorithm behaves more like the basic CSS with MTSE of Chapter 4, which is the appropriate algorithm for the data. Therefore, as the error vector processing is “phased out”, performance improves.

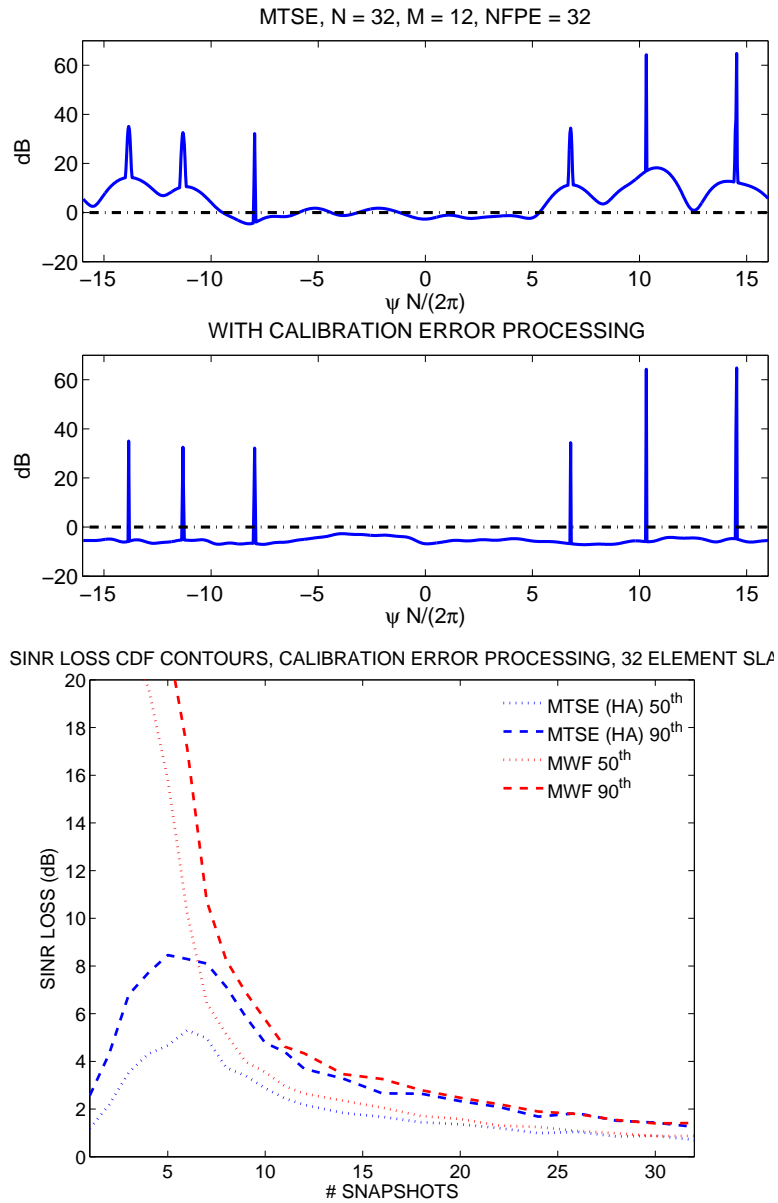


Figure 6.12: **Impact of error processing for ideal manifold response, mixed INR, two pass processing:** This test case measures the impact of error vector processing when the array manifold response is, in fact, ideal for the $N = 32$, mixed $INR = 20$, 50 dB scenario. Two passes of error vector processing are used, although performance is identical to single pass processing as all line components are detected in the first pass. Above $M = 7$ snapshots, performance is slightly better than the MWF trajectory. Below $M = 7$ snapshots performance is noticeably better due to the “phasing out” of the error vector processing described earlier.

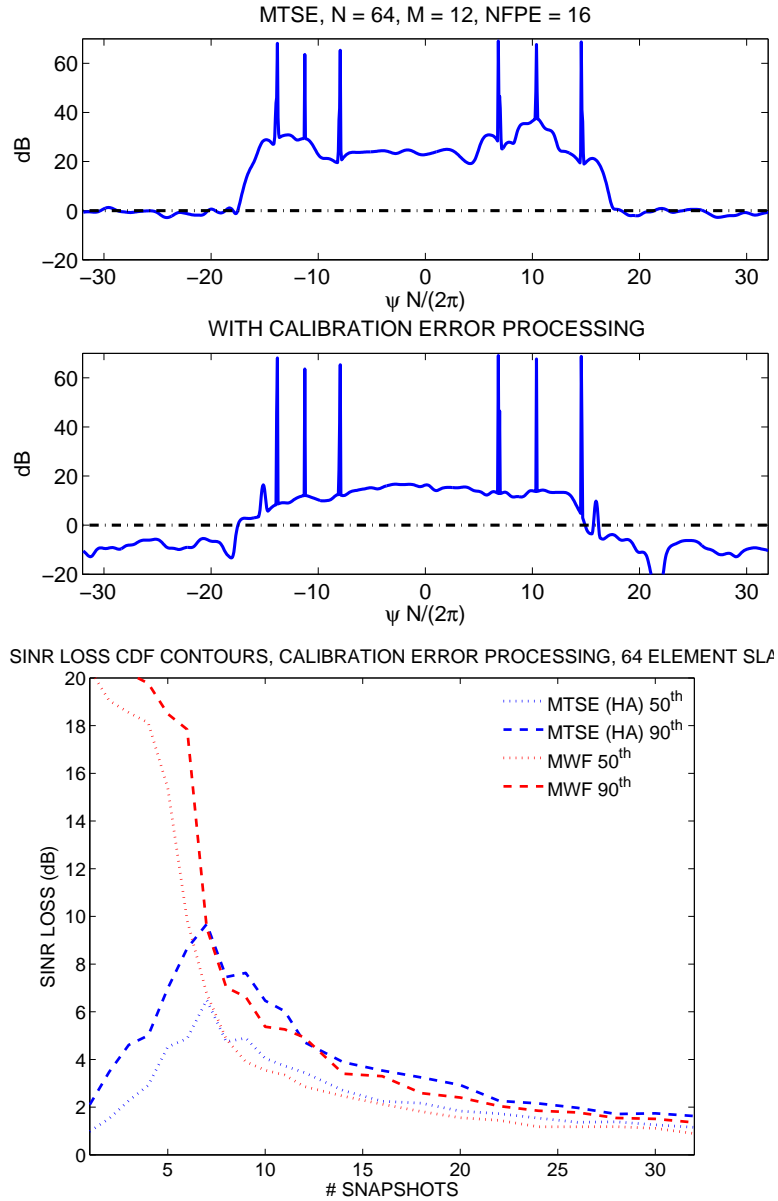


Figure 6.13: **Impact of error processing for ideal manifold response, below design frequency:** This test case measures the impact of error vector processing when the array manifold response is, in fact, ideal and operation is below the design frequency of the array. In this case, $N = 64$, $INR = 50$ dB, and operational frequency is one-half design frequency, $f/f_o = 1/2$. Error vector processing can be seen impacting noise floor estimation in the virtual region, as seen in the difference in the MTSE spectrum before (top subplot) and after processing (middle subplot). This is attributable to estimation errors, as the algorithm forces a subtraction of what it estimates as the non-ideal response. Performance for $M < 6$ is consistent with the other cases considered.

6.5.4 Performance Simulation Recap

Sections 6.5.1 through 6.5.3 looked at performance of the various combinations of ideal array manifold response, non-ideal array manifold response, and whether or not additional array manifold response error vector processing was used to supplement the original CSS with MTSE algorithm of Chapter 4. If the array manifold response was non-ideal, and no additional processing was done, the normalized SINR loss was degraded predictably [86] as shown in Figure 6.2. The algorithm of Section 6.4.2 was implemented and different array manifold response test scenarios were simulated. In general when the algorithm was able to operate successfully the performance followed a consistent behavior. This was the case as long as the line components were detectable above the perceived raised noise floor. As a point of reference, the original CSS with MTSE algorithm applied to ideal array manifold response data always exhibits better performance. Figure 6.14 recaps the relative performance that has been observed.

6.5.5 Comparison - MTSE and MVDR Spectra

The error vector processing is a technique for adapting the CSS with MTSE approach to handle non-ideal array manifold response, where the response retains sufficient “likeness” to the ideal that the parameters of the large discrete components in the spectrum can be estimated. Using this information, the error vector(s) can be estimated and used in the formulation of the final estimate of covariance. The previous sections showed several examples where this processing was effective and the overall normalized SINR loss was equivalent to reduced rank processing of the data using MWF. In each scenario, the array manifold error could be made large enough so that the covariance matrix was effectively unstructured w.r.t. the assumed model, and the technique was ineffective. So the array manifold error processing is not a replacement for unconstrained covariance and reduced rank techniques, but offers a way to extend the basic CSS with MTSE processing based on available data products to address the issue of non-ideal response.

An additional byproduct of this processing is a final MTSE wavenumber spectrum with

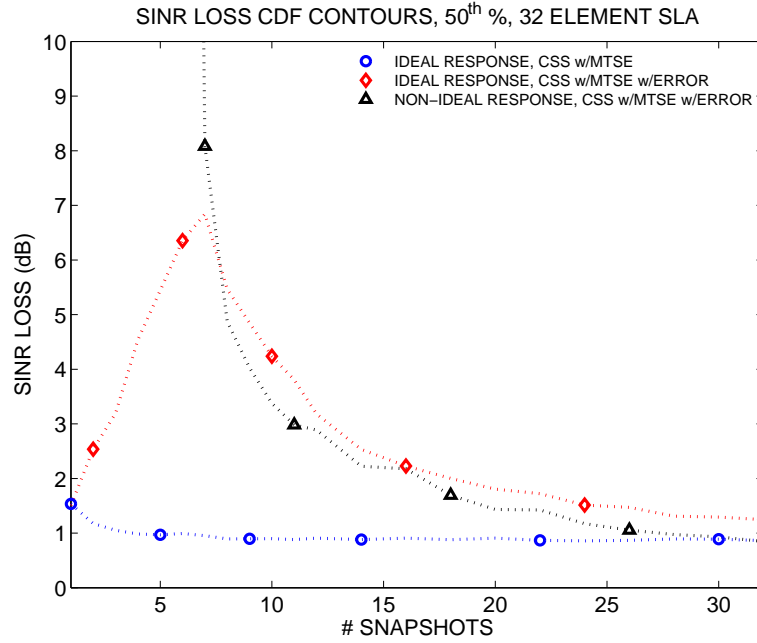


Figure 6.14: **Performance comparison with/without non-ideal response processing:** Sections 6.5.1 through 6.5.3 looked at performance of the non-ideal error vector estimation algorithm on overall adaptive beamformer performance. When the algorithm is able to operate successfully the normalized SINR loss performance generally follows a consistent behavior as illustrated in this figure, shown for the $K = 6$ fixed INR test case. When the array manifold response is ideal, and the original CSS with MTSE algorithm of Chapter 4 is applied the best overall performance results, show as the blue circle trace. When CSS with MTSE and error vector processing is applied to this data, as shown in red diamond, performance follows that of MWF (a representative reduced rank algorithm) above $M = K$ snapshots. Below $M = K$, performance improves as the algorithm constrains itself to remove fewer and fewer estimated error vectors, based on the number of available snapshots. This performance converges at $M = 1$ to the original algorithm, since the error vector processing is disabled at this point. When the array manifold response is in fact non-ideal, and the CSS with MTSE and error vector processing is applied, performance generally tracks with the MWF, shown in black triangle.

the influence of the error vectors for the large discretized removed. One can qualitatively compare the utility in this final estimate of the spectrum to MVDR spectra computed using the ensemble covariance matrix. Figures 6.15 - 6.18 show this comparison for the test cases used thus far, and also include an additional example (Figure 6.17). In each figure, three test cases are considered for the scenario corresponding to increasing the amount of array manifold errors. The green trace is the least error, red a medium amount, and blue a large amount (but not so large that the processing fails). The traces are offset slightly in the x-axis to help in being able to interpret the plots. Without this offset the traces overlap too much and make a visual comparison difficult. In the top left of each figure the initial MTSE spectra are shown. This is before any array manifold response error processing, and represents what the standard MTSE processing will produce given the snapshot data. In the top right of each figure, the corresponding traces are shown for the final MTSE spectra after all array manifold error processing is complete. Each MTSE plot represents one realization for $M = 50$ snapshots. In the lower left of each figure is the MVDR wavenumber spectrum using the ensemble matrix for the problem, with array manifold response errors included. In the lower right of each figure is the corresponding MVDR spectrum using the ensemble matrix as if the array manifold response is ideal. The figure captions describe the scenarios in greater detail.

Although each test case is different, the behavior observed is consistent. The original MTSE spectrum is degraded by the non-ideal array manifold response, as evidenced by the raised noise floor which potentially masks other line components in the spectrum. After error vector processing, the final MTSE spectrum recovers the true noise floor, or close to it, and represents the line components with the correct relative power levels. This is contrasted to an MVDR spectrum, given the ensemble covariance matrix for the data, including the non-ideal array manifold response. The MVDR spectrum provides the correct locations for line components, but their relative strength is affected by the array manifold errors. The final MTSE spectrum is more comparable to an MVDR spectrum for an ensemble covariance with ideal array manifold response. Effectively, after error vector processing, the

MTSE spectrum is providing a picture of what the environment looks like if the array were “fixed” and ideal array manifold response restored.

6.6 Summary

This chapter investigated the impacts to CSS performance when the array manifold response encountered was non-ideal. Normalized SINR loss degrades in a predictable manner, and quickly becomes unacceptable depending on the severity of the non-ideal response. A technique was developed to estimate the error vectors associated with the strongest *INR* line components in the data using the detection and estimation parameters available from harmonic analysis. Through simulation, this technique was seen to improve performance in the face of non-ideal array manifold response, and normalized SINR loss was seen to be comparable to reduced rank techniques provided the harmonic analysis could reliably detect the line components. The extremely fast convergence of the original CSS when encountering ideal array manifold response data is no longer seen. This is a result of the error vector estimation performance being tied to the amount of data averaging provided. As a beneficial byproduct, MTSE could be made to produce an estimate of the wavenumber spectrum as if the array manifold had been restored to ideal.

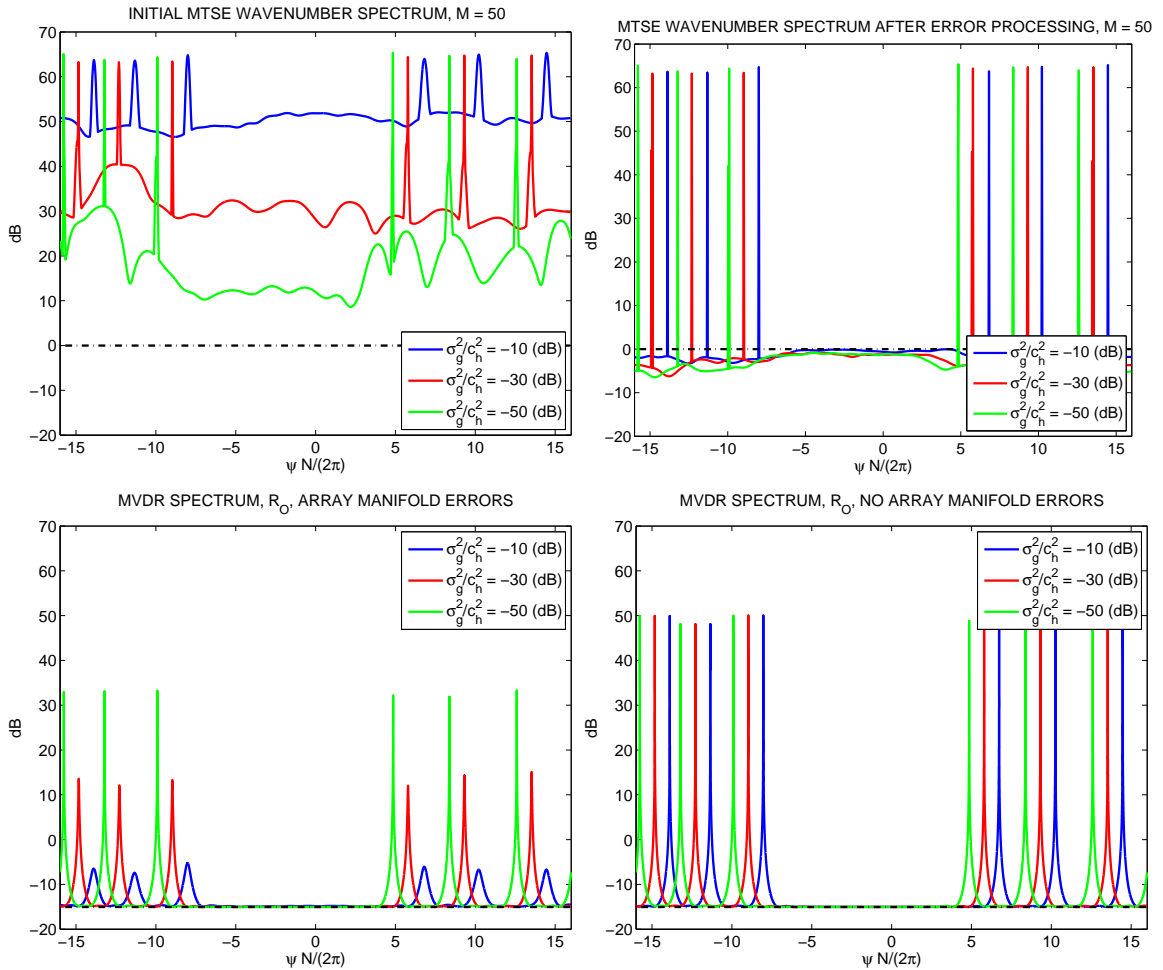


Figure 6.15: **Comparison of final MTSE and MVDR spectra, fixed INR case:** Compare the final MTSE spectra (upper right) to the MVDR spectra given the ensemble covariance for the data (lower left). While MVDR indicates the line components, their relative strength is proportional to the magnitude of non-ideal response present. The final MTSE spectrum (upper right) shows all line components with the correct power. This is similar to an MVDR spectrum based on an ensemble covariance as if the array manifold response were ideal (lower right). For all plots the blue, green, and red traces are all for the same underlying point source locations, but are staggered in the display for visual clarity.

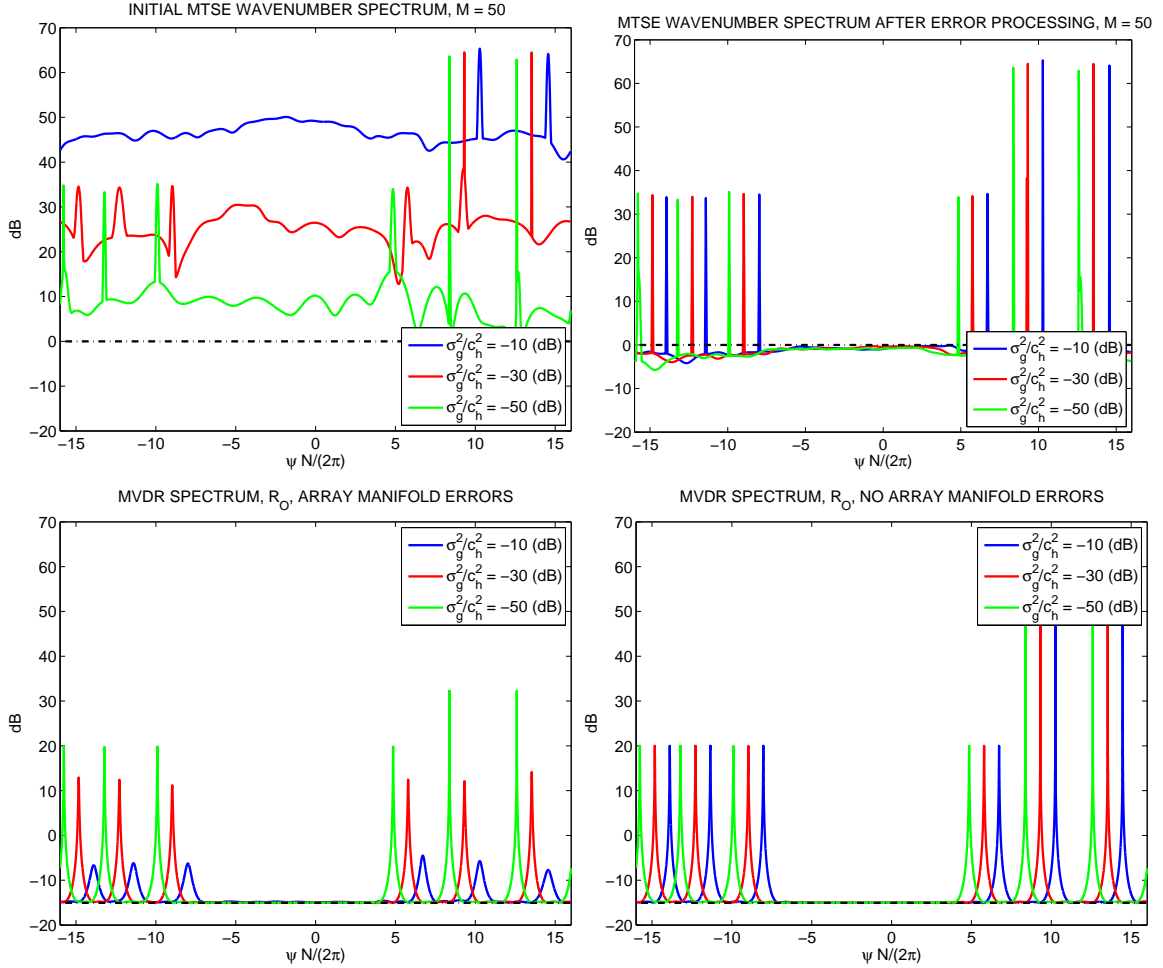


Figure 6.16: **Comparison of final MTSE and MVDR spectra, mixed INR case:** In cases where individual *INR* is mixed, large point sources may mask out lower *INR* point sources, as seen in the initial MTSE spectra (upper left) in blue. These lower *INR* sources may also be strong enough to mask the true noise floor. Two passes of error vector processing are used to address this. The final MTSE spectra (upper right) produces a correct spectrum. Compare this to the MVDR spectra given the ensemble covariance for the data (lower left). While MVDR indicates the line components, their relative strength is impacted by the non-ideal response. The final MTSE spectrum is more like the MVDR spectrum based on an ensemble covariance for an ideal array manifold response (lower right). For all plots the blue, green, and red traces are all for the same underlying point source locations, but are staggered in the display for visual clarity.

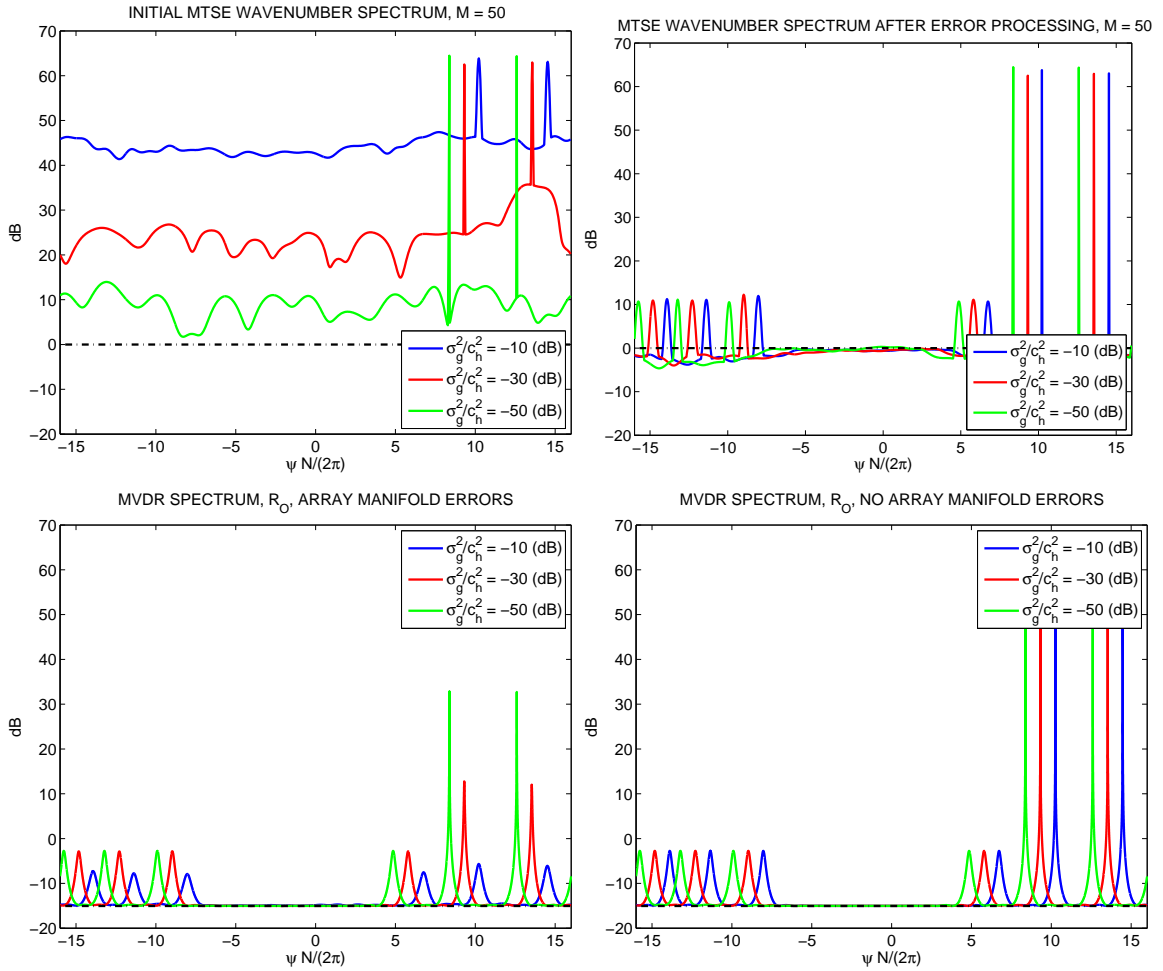


Figure 6.17: **Comparison of final MTSE and MVDR spectra, wide range INR case:** This test case extends the scenario of Figure 6.16 by making the separation between the strong and weak point sources even larger, 50 dB and -3 dB (per element). Final MTSE spectra performance is similar to other examples, and corrects for the non-ideal array manifold response. For all plots the blue, green, and red traces are all for the same underlying point source locations, but are staggered in the display for visual clarity.

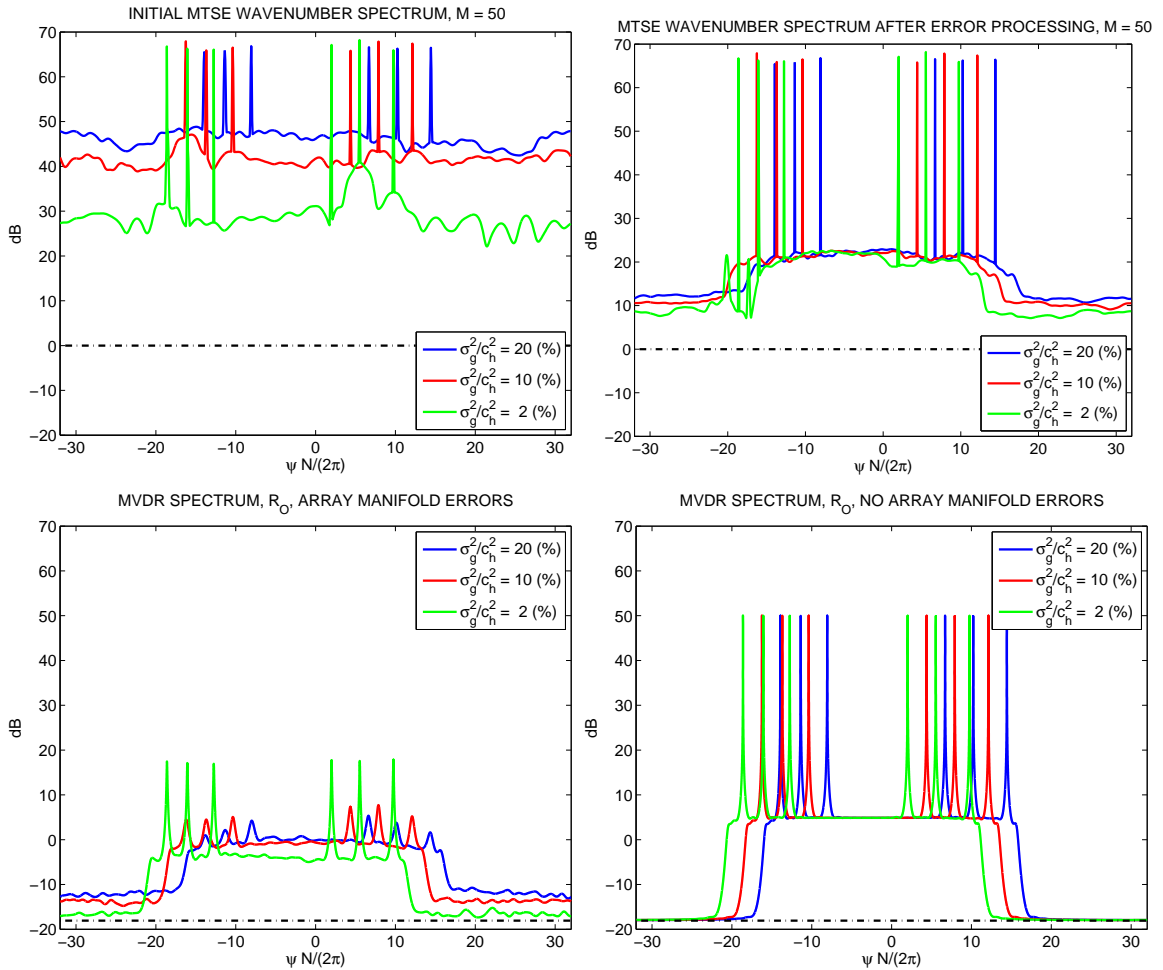


Figure 6.18: **Comparison of final MTSE and MVDR spectra, $\frac{1}{2}$ design frequency:** Operation below design frequency introduces challenges when the impact of the non-ideal array manifold and the environmental, e.g. isotropic, noise combine to exceed the sensor noise in the virtual region. CSS with MTSE and error vector processing addresses only the non-ideal array manifold response for the detected line components, not the spatially spread isotropic noise. As a result, the final MTSE spectra, shown in the upper right, contains residual bias in the virtual region. The relative power of the line components in the visible region is correct, though, compared to MVDR based on the ensemble covariance for the data (lower left). For all plots the blue, green, and red traces are all for the same underlying point source locations, but are staggered in the display for visual clarity.

Chapter 7: Extensions for Arbitrary Geometry

7.1 Introduction

Arrays with a regular element spacing lend themselves to a convenient simultaneous estimation of visible space components of the space-time process and virtual space sensor noise using classical spectral estimation techniques and efficient FFT computation. For arbitrary array geometries, proper estimation of the virtual space sensor noise may require more effort. This chapter develops an approach for doing this based upon analyzing the covariance for isotropic noise. The CSS with MTSE techniques are then extended for application to arbitrary arrays. Performance is assessed for the particular case of a uniform circular array.

7.2 Sensor Noise with Arbitrary Array Geometry

The covariance matrix of interest, \mathbf{R}_x , consists of two subspaces corresponding to visible and virtual regions.

$$\langle \mathbf{R}_x \rangle = \langle \mathbf{R}_{vs} \rangle + \langle \mathbf{R}_{vr} \rangle \quad (7.1)$$

where the notation $\langle \mathbf{A} \rangle$ indicates the span of the column space of the matrix \mathbf{A} . We may assume that the subspaces, $\langle \mathbf{R}_{vs} \rangle$ and $\langle \mathbf{R}_{vr} \rangle$ are approximately orthogonal, although due to the array geometry the transition between the two may not be so sharp. The visible region subspace is approximately the subspace defined by the covariance associated with 3D isotropic noise.

$$\langle \mathbf{R}_{vs} \rangle \approx \langle \mathbf{R}_{iso} \rangle \quad (7.2)$$

This is convenient for two reasons. First, the 3D isotropic noise is specified in terms of angle of arrival to the array. This has an intuitive physical interpretation regardless of array geometry. Second, from (3.31) the contribution of the sensor noise component appeared as a 3D isotropic noise component when restricting attention to the visible region only. This will be useful later when considering the positive definiteness of the estimated covariance.

Because of the spatial stationarity of the 3D isotropic noise, the covariance is a function of the difference in position only, $\Delta \mathbf{p}$. This difference can be expressed in cartesian $\{ \Delta p_x, \Delta p_y, \Delta p_z \}$ or spherical coordinates $\{ s, \gamma, \zeta \}$.

$$\Delta \mathbf{p} = \begin{bmatrix} \Delta p_x \\ \Delta p_y \\ \Delta p_z \end{bmatrix} = \begin{bmatrix} s \sin \gamma \cos \zeta \\ s \sin \gamma \sin \zeta \\ s \cos \gamma \end{bmatrix} \quad (7.3)$$

The covariance between two omnidirectional sensors in 3D isotropic noise has a known form [1, 54]

$$R_{\text{iso}}(s, \gamma, \zeta) = R_{\text{iso}}(s) = \frac{\sin(\omega s/c)}{\omega s/c} \quad (7.4)$$

The covariance matrix for an array of sensors is populated by values of this function where the relative position is $\Delta \mathbf{p} = \mathbf{p}_r - \mathbf{p}_c$.

$$\mathbf{R}_{\text{iso}} = ((R_{\text{iso}}(\Delta \mathbf{p})))_{r,c} = ((R_{\text{iso}}(s)))_{r,c} \quad (7.5)$$

We use (7.4) in (7.5) to compute \mathbf{R}_{iso} , and perform an eigendecomposition of the matrix. The decomposition is ordered according to decreasing eigenvalues.

$$\mathbf{R}_{\text{iso}} = \mathbf{Q}_{\text{iso}} \mathbf{\Lambda}_{\text{iso}} \mathbf{Q}_{\text{iso}}^H = \sum_{n=0}^{N-1} \lambda_n \mathbf{q}_n \mathbf{q}_n^H \quad (7.6)$$

The eigenvalues, λ_n , for \mathbf{R}_{iso} are a measure of the concentration of each eigenvector within the visible region subspace. We divide the eigenvectors into two sets, the first set being those with large eigenvalues meaning they are mostly concentrated in the visible region. Those with low concentration, meaning those with eigenvalues near zero, are assigned to the virtual region subspace. The boundary is somewhat arbitrary but may be immediate from inspection of the eigenvalues. The upper plot in Figure 7.1 shows the eigenvalues for an $N = 32$ uniform linear array operated at and below the design frequency f_o . The distinction between the visible and virtual region is obvious in this case. The eigenvalues in the Figure show a rapid drop off as $n/N > f/f_o$. Also evident is that there is no virtual space when operating at design frequency, as the eigenvalues are all equal. The visible and virtual regions are less clearly defined for a uniform circular array. The lower plot in Figure 7.1 shows the eigenvalues for an $N = 50$ uniform circular array. Changing the operational frequency changes the size of the radius as measured in wavelengths. In Figure 7.1, the results are provided for a radius of $R_\lambda = 5\lambda_o, 3.75\lambda_o, 2.5\lambda_o,$ and $1.25\lambda_o$. The cases of $3.75\lambda_o, 2.5\lambda_o,$ and $1.25\lambda_o$ show a rapid drop off similar to the ULA, but not immediately at the point $n/N > R_\lambda/5$. Also, even for operation at the design frequency the eigenvalues are not all equal valued, showing a gradually decrease from 0 to -3 dB.

Indicating the number of eigenvectors determined to be in the visible space as N_{vs} , show the explicit make up of \mathbf{R}_{iso} .

$$\mathbf{R}_{\text{iso}} = \sum_{n=0}^{N_{\text{vs}}-1} \lambda_n \mathbf{q}_n \mathbf{q}_n^H + \sum_{n=N_{\text{vs}}}^{N-1} \lambda_n \mathbf{q}_n \mathbf{q}_n^H \quad (7.7)$$

The visible region subspace is approximately the subspace spanned by the first N_{vs} eigenvectors.

$$\langle \mathbf{R}_{\text{vs}} \rangle \approx \langle \mathbf{q}_0, \mathbf{q}_1, \dots, \mathbf{q}_{N_{\text{vs}}-1} \rangle \quad (7.8)$$

The eigenvectors, \mathbf{Q}_{iso} , make a complete orthonormal set for $\langle \mathbb{C}^{NxN} \rangle$. The covariance

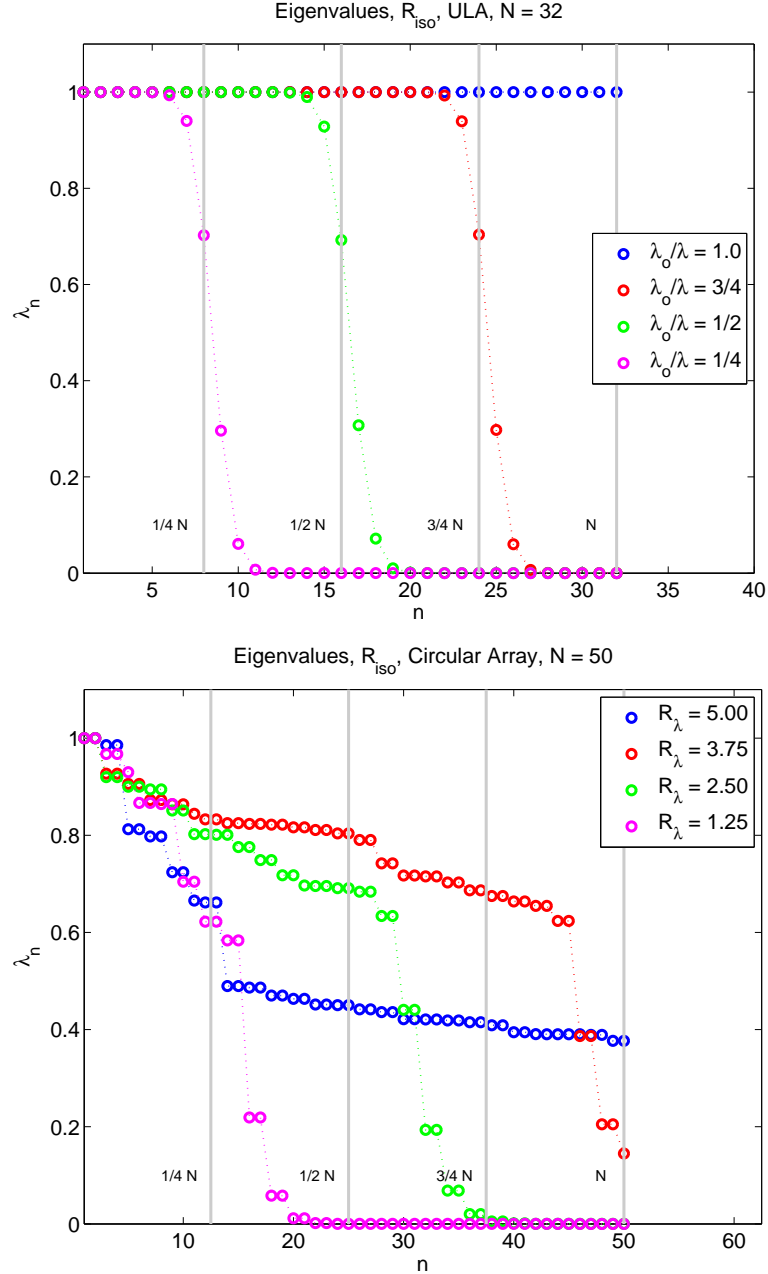


Figure 7.1: **Eigenvalues for \mathbf{R}_{iso} , various arrays:** Analysis of the eigenvalues of the covariance for 3D isotropic noise, \mathbf{R}_{iso} , for an array and operational frequency can be used to determine the visual region and virtual region subspaces. In the top plot, the eigenvalues for a uniform linear array show a sharp drop off as $n/N > f/f_o$. This makes sense as the space-time process at lower operational frequencies, f , is spatially oversampled. The eigenvalues for a uniform circular array, shown in the lower plot, follow a similar trend but the transition point must be found by inspection. In both cases for operation at the design frequency, the eigenvalues show that virtual region subspace effectively does not exist, as the visible region subspace occupies the entire space, $\langle \mathbb{C}^{N \times N} \rangle$.

matrix \mathbf{R}_x is full rank, so from $\langle \mathbf{R}_x \rangle = \langle \mathbb{C}^{N \times N} \rangle = \langle \mathbf{Q}_{\text{iso}} \rangle$. So we have

$$\langle \mathbf{R}_{\text{vr}} \rangle \approx \langle \mathbf{q}_{N_{\text{vs}}}, \mathbf{q}_{N_{\text{vs}}+1}, \dots, \mathbf{q}_{N-1} \rangle \quad (7.9)$$

Grouping the appropriate eigenvectors together for the visible and virtual region subspaces,

$$\mathbf{Q}_{\text{vs}} = [\mathbf{q}_0, \mathbf{q}_1, \dots, \mathbf{q}_{N_{\text{vs}}-1}], \quad \mathbf{Q}_{\text{vr}} = [\mathbf{q}_{N_{\text{vs}}}, \mathbf{q}_{N_{\text{vs}}+1}, \dots, \mathbf{q}_{N-1}] \quad (7.10)$$

we form projection matrices for those subspaces

$$\mathbf{P}_{\text{vs}} = \mathbf{Q}_{\text{vs}} \mathbf{Q}_{\text{vs}}^H, \quad \mathbf{P}_{\text{vr}} = \mathbf{Q}_{\text{vr}} \mathbf{Q}_{\text{vr}}^H = \mathbf{I} - \mathbf{Q}_{\text{vs}} \mathbf{Q}_{\text{vs}}^H \quad (7.11)$$

Let $N_{\text{vr}} = N - N_{\text{vs}}$. The sensor noise power component within the virtual region subspace can be estimated from the available snapshots as

$$\hat{\sigma}_w^2 = \frac{1}{M} \cdot \frac{1}{N_{\text{vr}}} \sum_{m=1}^M \mathbf{x}_m^H \mathbf{P}_{\text{vr}} \mathbf{x}_m \quad (7.12)$$

From the form of the projection matrix, \mathbf{P}_{vr} , the sensor noise power estimate in (7.12) is equivalent to

$$\hat{\sigma}_w^2 = \frac{1}{M} \cdot \frac{1}{N_{\text{vr}}} \sum_{m=1}^M \sum_{n=N_{\text{vs}}}^{N-1} |\mathbf{x}_m^H \mathbf{q}_n|^2 \quad (7.13)$$

Eqn. (7.13) shows $\hat{\sigma}_w^2$ is just the average power across each of the orthonormal basis vectors, \mathbf{q}_n , in the virtual subspace. The overall estimate for the covariance \mathbf{R}_x then uses this estimate as

$$\hat{\mathbf{R}}_x = \hat{\mathbf{R}}_{\text{vs}} + \hat{\sigma}_w^2 \mathbf{P}_{\text{vr}} \quad (7.14)$$

Use of the projection matrix \mathbf{P}_{vr} in (7.14) avoids double counting the sensor noise component

measured in the visible region subspace and contained in $\hat{\mathbf{R}}_{\text{vs}}$. If the sensor noise is significantly below the continuous background noise component of the space-time process throughout the visible region, one could use the simpler expression

$$\hat{\mathbf{R}}_x = \hat{\mathbf{R}}_{\text{vs}} + \hat{\sigma}_{w,\text{vr}}^2 \mathbf{I} \quad (7.15)$$

directly at the expense of double counting the sensor noise in the visible region. In either case some representation of the sensor noise in the virtual region is required.

7.3 Positive Definiteness

The estimated covariance is required to be positive definite to be meaningful for array processing. Chapter 3 showed that for regularly spaced arrays this requirement is satisfied under the conditions that the estimated frequency-wavenumber spectrum, $\hat{P}(\mathbf{k})$, and the estimated sensor noise, $\hat{\sigma}_w^2$, are > 0 . This section shows the estimated covariance is also positive definite for arbitrary geometry arrays, where the covariance is estimated as the sum of the visible space covariance, $\hat{\mathbf{R}}_{\text{vs}}$, and the sense noise in the virtual space as in Section 7.2. As in Chapter 3, it is necessary that the estimate of the frequency-wavenumber spectrum, $\hat{P}_{\text{vs}}(\mathbf{k})$, and the estimate for the sensor noise, $\hat{\sigma}_{w,\text{vr}}^2$, are > 0 .

7.3.1 Method 1

Eqn. (7.14) provided the more accurate method for accounting for the sensor noise in the covariance matrix.

$$\hat{\mathbf{R}}_x = \hat{\mathbf{R}}_{\text{vs}} + \hat{\sigma}_w^2 \mathbf{P}_{\text{vr}} \quad (7.16)$$

The estimate for the covariance corresponding to the visible region of the array is

$$\hat{\mathbf{R}}_{\text{vs}} = (2\pi)^{-C} \int \dots \int_{\text{vs}} \hat{P}_{\text{vs}}(\mathbf{k}) \mathbf{v}(\mathbf{k}) \mathbf{v}^H(\mathbf{k}) d\mathbf{k} \quad (7.17)$$

We assume that the estimate of the wavenumber spectrum in the visible region is greater than zero, $\hat{P}_{\text{vs}}(\mathbf{k}) > 0$. This allows us to express it as consisting of an estimate of the wavenumber spectrum of the observed process, $\hat{P}_f(\mathbf{k}) \geq 0$, and an estimate of the sensor noise seen in the visible region, $\hat{\sigma}_{w,\text{vs}}^2 > 0$.

$$\hat{P}_{\text{vs}}(\mathbf{k}) = \hat{P}_f(\mathbf{k}) + \hat{\sigma}_{w,\text{vs}}^2 \quad (7.18)$$

Using (7.18) and (7.17) in the quadratic expression for positive definiteness, we have

$$\mathbf{x}^H \hat{\mathbf{R}}_x \mathbf{x} = \mathbf{x}^H \left((2\pi)^{-C} \int \dots \int_{\text{vs}} \left[\hat{P}_f(\mathbf{k}) + \hat{\sigma}_{w,\text{vs}}^2 \right] \mathbf{v}(\mathbf{k}) \mathbf{v}^H(\mathbf{k}) d\mathbf{k} + \hat{\sigma}_w^2 \mathbf{P}_{\text{vr}} \right) \mathbf{x} \quad (7.19)$$

Carrying out the integration, this simplifies to

$$\mathbf{x}^H \hat{\mathbf{R}}_x \mathbf{x} = \mathbf{x}^H \hat{\mathbf{R}}_f \mathbf{x} + \mathbf{x}^H \left(\hat{\sigma}_{w,\text{vs}}^2 \mathbf{R}_{\text{iso}} + \hat{\sigma}_w^2 \mathbf{P}_{\text{vr}} \right) \mathbf{x} \quad (7.20)$$

The covariance estimate for the space-time process is positive semidefinite, $\hat{\mathbf{R}}_f \geq 0$. This follows from

$$\mathbf{x}^H \hat{\mathbf{R}}_f \mathbf{x} = (2\pi)^{-C} \int \dots \int_{\text{vs}} \hat{P}_f(\mathbf{k}) \left| \mathbf{x}^H \mathbf{v}(\mathbf{k}) \right|^2 d\mathbf{k} \quad (7.21)$$

where $\hat{P}_f(\mathbf{k}) \geq 0$ and $\left| \mathbf{x}^H \mathbf{v}(\mathbf{k}) \right|^2 \geq 0$. For the terms relating to the noise estimates we replace \mathbf{R}_{iso} with its eigendecomposition.

$$\hat{\sigma}_{w,\text{vs}}^2 \mathbf{R}_{\text{iso}} + \hat{\sigma}_w^2 \mathbf{P}_{\text{vr}} = \hat{\sigma}_{w,\text{vs}}^2 \left[\sum_{n=0}^{N-1} \lambda_n \mathbf{q}_n \mathbf{q}_n^H \right] + \hat{\sigma}_w^2 \mathbf{P}_{\text{vr}} \quad (7.22)$$

The matrix \mathbf{P}_{vr} is also defined in terms of the eigendecomposition of \mathbf{R}_{iso}

$$\hat{\sigma}_{w,vs}^2 \mathbf{R}_{\text{iso}} + \hat{\sigma}_w^2 \mathbf{P}_{\text{vr}} = \sum_{n=0}^{N_{\text{vs}}-1} \hat{\sigma}_{w,vs}^2 \lambda_n \mathbf{q}_n \mathbf{q}_n^H + \sum_{n=N_{\text{vs}}}^{N-1} (\hat{\sigma}_{w,vs}^2 \lambda_n + \hat{\sigma}_w^2) \mathbf{q}_n \mathbf{q}_n^H \quad (7.23)$$

Define the combined eigenvalues, λ'_n , as

$$\lambda'_n = \begin{cases} \hat{\sigma}_{w,vs}^2 \lambda_n & 0 \leq n \leq N_{\text{vs}} \\ \hat{\sigma}_{w,vs}^2 \lambda_n + \hat{\sigma}_w^2 & N_{\text{vs}} \leq n < N \end{cases} \quad (7.24)$$

By the selection methods outlined in Section 7.2, the eigenvalues λ_n for $0 \leq n < N_{\text{vs}}$ are greater than zero, such that all λ'_n are real-valued and greater than zero. Defining $\mathbf{\Lambda}' = \text{diag}(\lambda'_0, \lambda'_1, \dots, \lambda'_{N-1})$, we have

$$\mathbf{x}^H (\hat{\sigma}_{w,vs}^2 \mathbf{R}_{\text{iso}} + \hat{\sigma}_w^2 \mathbf{P}_{\text{vr}}) \mathbf{x} = \mathbf{x}^H \mathbf{Q}_{\text{iso}} \mathbf{\Lambda}' \mathbf{Q}_{\text{iso}}^H \mathbf{x} \quad (7.25)$$

The matrix \mathbf{Q}_{iso} is unitary, therefore $|\mathbf{Q}_{\text{iso}}^H \mathbf{x}|^2 = |\mathbf{x}|^2 \neq 0$ for $|\mathbf{x}|^2 \neq 0$. With positive, real-valued entries on the diagonal of $\mathbf{\Lambda}'$, we have

$$\mathbf{x}^H (\hat{\sigma}_{w,vs}^2 \mathbf{R}_{\text{iso}} + \hat{\sigma}_w^2 \mathbf{P}_{\text{vr}}) \mathbf{x} > 0 \quad (7.26)$$

The overall matrix $\hat{\mathbf{R}}_x$ is the sum of a positive semidefinite matrix, $\hat{\mathbf{R}}_f$, and a positive definite matrix, $\mathbf{x}^H (\hat{\sigma}_{w,vs}^2 \mathbf{R}_{\text{iso}} + \hat{\sigma}_w^2 \mathbf{P}_{\text{vr}}) \mathbf{x}$, and therefore is positive definite, $\hat{\mathbf{R}}_x > 0$.

7.3.2 Method 2

The simpler method for an arbitrary array geometry is

$$\hat{\mathbf{R}}_x = \hat{\mathbf{R}}_{\text{vs}} + \hat{\sigma}_{w,\text{vr}}^2 \mathbf{I} \quad (7.27)$$

Following Method 1, we have $\hat{\mathbf{R}}_{\text{vs}} = \left(\hat{\mathbf{R}}_f + \hat{\sigma}_{w,\text{vs}}^2 \mathbf{R}_{\text{iso}} \right) \geq 0$. The matrix $\mathbf{I} > 0$ and so directly $\hat{\mathbf{R}}_x > 0$.

7.4 Covariance from Spatial Spectra (CSS) with MTSE

This section outlines the adaptation of the CSS with MTSE algorithm presented in Chapter 4 for application to arbitrary geometry arrays. All steps translate directly in concept, with the main difference centering on the need to carry out explicit calculations without the computational benefits of FFT processing.

7.4.1 Design of the Tapers

For arbitrary array geometry the design of the multiple tapers for spectral estimation is done by dividing the visible region into a search grid, where each grid point defines a region of analysis as illustrated in Figure 7.2. For convenience, we do this in the angle domain, (θ, ϕ) , although it may also be specified in wavenumber. In its most general form, the search grid covers the sphere, $0 \leq \theta \leq \pi$, $0 \leq \phi \leq 2\pi$, although the array characteristics may be exploited to reduce this. For example, a planar array in the $x - y$ plane cannot measure wavenumber in the z direction. Because of this, its search grid can be restricted to the hemisphere, $0 \leq \theta \leq \pi/2$, $0 \leq \phi \leq 2\pi$, as the lower hemisphere is identical due to the ambiguity and provides no additional information.

One approach is to design a set of tapers at each grid location, $(\theta_o \pm \Delta\theta, \phi_o \pm \Delta\phi)$, based on an eigendecomposition of the matrix

$$\begin{aligned} \mathbf{R}_{\theta_o, \phi_o} &= \frac{1}{4\pi} \int_{\theta_o - \Delta\theta}^{\theta_o + \Delta\theta} \int_{\phi_o - \Delta\phi}^{\phi_o + \Delta\phi} \mathbf{v}(\theta, \phi) \mathbf{v}^H(\theta, \phi) \sin\theta d\theta d\phi \\ &= \mathbf{Q}_{\theta_o, \phi_o} \mathbf{\Lambda}_{\theta_o, \phi_o} \mathbf{Q}_{\theta_o, \phi_o}^H \end{aligned} \tag{7.28}$$

where $\mathbf{v}(\theta, \phi)$ is the array manifold response vector. The multi-tapers are selected as the

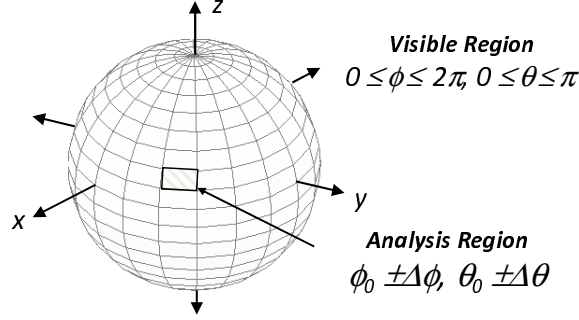


Figure 7.2: **Partition of the visible region for multi-taper design, arbitrary array geometry**: For arbitrary array geometry, the multiple tapers necessary for harmonic analysis and multi-taper spectral estimation can be designed for each area designated in the search grid defined throughout the visible region. Alternatively, a single set of tapers can be designed and steered through out the visible angle space.

eigenvectors corresponding to the D largest eigenvalues of $\mathbf{R}_{\theta_o, \phi_o}$.

$$\mathbf{w}_{\theta_o, \phi_o, d} = \mathbf{q}_{\theta_o, \phi_o, d-1}, \quad d = 1, \dots, D \quad (7.29)$$

Alternatively, one may design a single set of tapers, $\mathbf{w}_{o, d}$, perhaps at broadside for the array, and steer the main response axis (MRA) of this fixed set of weights through angle space.

$$\mathbf{w}_{\theta_o, \phi_o, d} = \mathbf{w}_{o, d} \odot \mathbf{v}(\theta_o, \phi_o), \quad d = 1, \dots, D \quad (7.30)$$

7.4.2 Discrete Line Component Processing (Harmonic Analysis)

Defining the multi-taper weight matrix,

$$\mathbf{W}(\theta_o, \phi_o) = [\mathbf{w}_{\theta_o, \phi_o, 1}, \mathbf{w}_{\theta_o, \phi_o, 2}, \dots, \mathbf{w}_{\theta_o, \phi_o, D}] \quad (7.31)$$

the eigencoefficients are computed for each snapshot, \mathbf{x}_m , as

$$\mathbf{y}_m(\theta_o, \phi_o) = \mathbf{W}^H(\theta_o, \phi_o) \mathbf{x}_m \quad (7.32)$$

The eigencoefficient output for a line component at (θ_o, ϕ_o) is given by

$$\mathbf{q}_{\theta_o, \phi_o} = \mathbf{W}^H(\theta_o, \phi_o) \mathbf{1} \quad (7.33)$$

where $\mathbf{1}$ is the all one's vector. This vector defines the subspaces used for computing the detection statistic.

$$\mathbf{P}_{\theta_o, \phi_o} = \mathbf{q}_{\theta_o, \phi_o} (\mathbf{q}_{\theta_o, \phi_o}^H \mathbf{q}_{\theta_o, \phi_o})^{-1} \mathbf{q}_{\theta_o, \phi_o}^H, \quad \mathbf{P}_{\theta_o, \phi_o}^\perp = \mathbf{I} - \mathbf{P}_{\theta_o, \phi_o} \quad (7.34)$$

The detection statistic is computed as before

$$F(\theta_o, \phi_o) = \frac{\sum_{m=1}^M \mathbf{y}_m^H(\theta_o, \phi_o) \mathbf{P}_{\theta_o, \phi_o} \mathbf{y}_m(\theta_o, \phi_o)}{\sum_{m=1}^M \mathbf{y}_m^H(\theta_o, \phi_o) \mathbf{P}_{\theta_o, \phi_o}^\perp \mathbf{y}_m(\theta_o, \phi_o)} \underset{H_0}{\overset{H_1}{\gtrless}} \gamma_{TH} \quad (7.35)$$

K is the number of detected line components. Each has its parameters estimated, $(\hat{\theta}_k, \hat{\phi}_k, \hat{a}_k(m))$, and these are used to subtract the line component from the data. The projection or subtraction methods of Section 4.2.4 are applicable. The variance for each line component is estimated as

$$\hat{\sigma}_k^2 = \frac{1}{M} \sum_{m=1}^M |\hat{a}_k(m)|^2 \quad (7.36)$$

and is used in the formation of the covariance matrix. This process may be iterated to successively process multiple line components in the data. The final residual snapshot data, $\mathbf{x}_{b,m}$, contains only the smooth, continuous background content

7.4.3 Background / Continuous Spectrum

Once harmonic analysis is complete the residual snapshot data, $\mathbf{x}_{b,m}$, is used to compute the final smooth, continuous background spectrum. The eigencoefficients are computed

$$\mathbf{y}_{b,m}(\theta_o, \phi_o) = \mathbf{W}^H(\theta_o, \phi_o) \mathbf{x}_{b,m} = ((y_{b,m}^{(d)}(\theta_o, \phi_o)))_d \quad (7.37)$$

The eigencoefficients are used to produce the individual eigenspectra.

$$\hat{P}_b^{(d)}(\theta_o, \phi_o) = \left| y_{b,m}^{(d)}(\theta_o, \phi_o) \right|^2 \quad (7.38)$$

The individual eigenspectra are then linearly combined according to a set of weights

$$\hat{P}_{b,x}(\theta_o, \phi_o) = \sum_{d=1}^D h_d(\theta_o, \phi_o) \hat{P}_b^{(d)}(\theta_o, \phi_o) \quad (7.39)$$

The weights, $h_d(k)$, may be fixed, which is optimal for an underlying white spectrum, or determined adaptively. Adaptive weighting algorithms are detailed in [52, 56].

7.4.4 Estimate Sensor Noise in Virtual Region

Section 7.2 outlined the process for analyzing the covariance matrix of isotropic noise to determine an appropriate subspace for the virtual region for the array. This analysis provides a dimension, N_{vr} , and projection matrix for that subspace, \mathbf{P}_{vr} . The sensor noise is estimated from the residual snapshot data, $\mathbf{x}_{b,m}$, as

$$\hat{\sigma}_w^2 = \frac{1}{M} \cdot \frac{1}{N_{\text{vr}}} \sum_{m=1}^M \mathbf{x}_{b,m}^H \mathbf{P}_{\text{vr}} \mathbf{x}_{b,m} \quad (7.40)$$

7.4.5 Covariance Matrix Estimate

The final estimate of the covariance matrix is formed from the estimated line components, the covariance from spatial spectrum of the residual continuous background, and the sensor noise component as

$$\hat{\mathbf{R}}_{CSS} = \hat{\mathbf{V}}\hat{\mathbf{R}}_a\hat{\mathbf{V}}^H + (4\pi)^{-1} \int_0^\pi \sin \theta d\theta \int_\pi^\pi \hat{P}_{b,x}(\theta, \phi) \mathbf{v}(\theta, \phi) \mathbf{v}^H(\theta, \phi) d\phi + \sigma_w^2 \mathbf{P}_{\text{vr}} \quad (7.41)$$

where

$$\hat{\mathbf{R}}_a = \text{diag}(\hat{\sigma}_1^2, \hat{\sigma}_2^2, \dots, \hat{\sigma}_K^2) \quad (7.42)$$

and

$$\hat{\mathbf{V}} = \left[\mathbf{v}(\hat{\theta}_1, \hat{\phi}_1), \mathbf{v}(\hat{\theta}_2, \hat{\phi}_2), \dots, \mathbf{v}(\hat{\theta}_K, \hat{\phi}_K) \right] \quad (7.43)$$

7.5 Performance Simulation

This section assesses performance of CSS with MTSE using (7.41), as applied to a $N = 50$ uniform circular array in 3D isotropic noise. Three point sources are in the environment as detailed in Table 7.1. This environment is similar to [24], but does not include the Gaussian spreading of the line components. To highlight the importance of considering the virtual space component as discussed in Section 7.2, two different values are used for the array radius normalized by the wavelength, R_λ . For a value of $R_\lambda = 5$, there is no virtual region, while for $R_\lambda = 2.5$ we set the virtual to have a dimension of $N_{\text{vr}} = 15$. This can be seen by inspection of Figure 7.1.

The multi-tapers are developed from a single multi-taper set that is steered in angle space. The reference set of tapers is found as the eigenvectors for the D largest eigenvalues of the matrix

$$\mathbf{R}_{MT} = \int_0^{\Delta\theta} \sin \theta d\theta \int_0^{2\pi} \mathbf{v}(\theta, \phi) \mathbf{v}^H(\theta, \phi) d\phi \quad (7.44)$$

This corresponds to a region steered at broadside to the array, symmetric in azimuth and

Table 7.1: Environment parameters, uniform circular array example

component	u_x	u_y	(θ, ϕ)	$SNR, R_\lambda = 5$	$SNR, R_\lambda = 2.5$
source 1	0.500	0.00	$(30^\circ, 0^\circ)$	12 (dB)	15 (dB)
source 2	-0.275	0.476	$(33.3^\circ, 120^\circ)$	9 (dB)	12 (dB)
source 3	-0.175	-0.476	$(30.5^\circ, -110^\circ)$	6 (dB)	9 (dB)
isotropic noise	NA	NA	NA	20 (dB)	20 (dB)
sensor noise	NA	NA	NA	0 (dB)	0 (dB)

Table 7.2: Array and CSS parameters, uniform circular array example

R_λ	M	D	$\Delta\theta$	N_θ	N_ϕ	γ_{TH}
2.5	5	7	18.0°	30	180	0.70
2.5	10	7	18.0°	30	180	0.50
2.5	20	7	18.0°	30	180	0.40
5.0	5	9	11.6°	45	180	0.55
5.0	10	9	11.6°	45	180	0.40
5.0	20	9	11.6°	45	180	0.35

extending down from $\theta = 0$ to $\Delta\theta$. Since it is a planar array, the visible region search grid is defined as N_ϕ locations uniform in azimuth, $0 \leq \phi \leq 2\pi$, and N_θ locations uniform in elevation, $0 \leq \theta \leq \pi/2$. Simulations are performed for $M = 5, 10$, and 20 snapshots. MTSE parameters for the different test cases are summarized in Table 7.2.

7.5.1 $N = 50$ Element Uniform Circular Array, $R_\lambda = 5.0$

The MVDR spectrum for the ensemble covariance described by the parameters in Table 7.1 for $R_\lambda = 5$ is shown in Figure 7.3. The three point sources are evident in the spectrum. For this test case the array radius in wavelengths is $R_\lambda = 5$. For circular arrays, from Van Trees [1], when $N < 4\pi R_\lambda \sim 63$ there will be aliasing effects in the beampattern due to the spatial sampling. This is evident in the Figure as the rise in the noise floor near the ring $u_x^2 + u_y^2 = 1$, which is the boundary of the visible region, and outside.

Simulation results for $M = 5, 10$, and 20 snapshots are shown in Figures 7.4, 7.5, and 7.6. At the lowest amount of snapshot support, the weakest source is not consistently detected during harmonic analysis. The analysis region width is large enough that the component is smoothed out in the residual background spectrum. As a result, the average

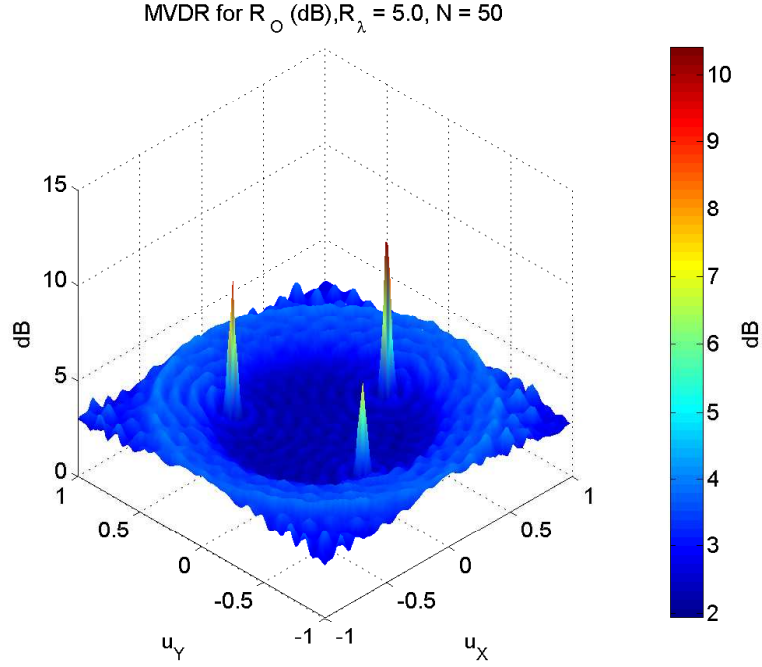


Figure 7.3: **MVDR spectrum for ensemble covariance**, $N = 50$, $R_\lambda = 5$ **circular array**: The low, medium, and high SNR peaks are clearly visible. The number of elements, N , is not greater than $4\pi R_\lambda$, resulting in aliasing effects due to the spatial sampling [1]. This explains the elevated noise floor in the range $u_x^2 + u_y^2 = 1$ and towards the corners of the plot.

MVDR spectrum for the covariance estimated using (7.41) is biased low for this signal. This steadily improves with increasing snapshots, and at $M = 20$ the average estimated spectrum and the ensemble are very close. Average normalized SINR loss, ξ , shown as $\xi_{dB} = -10 \log_{10} \xi$ in the figures, is less than 0.6 dB in most of the visible region even for $M = 5$. Increased loss occurs near the point sources, likely due to mismatch of the estimated point source parameters $(\hat{\theta}_k, \hat{\phi}_k, \hat{\sigma}_k^2)$. This effect is proportional to source strength, so the 12 dB source has the largest loss, $\xi_{dB} = 1.6$ to 1.8 dB. Of course, due to its greater SNR this is likely less of an issue, unless the processor is attempting detection nearby to this source. While comparative performance for another processor is not shown, the performance indicated in the figures is better than the 3dB within $M = 2K = 6$ snapshots rule of thumb.

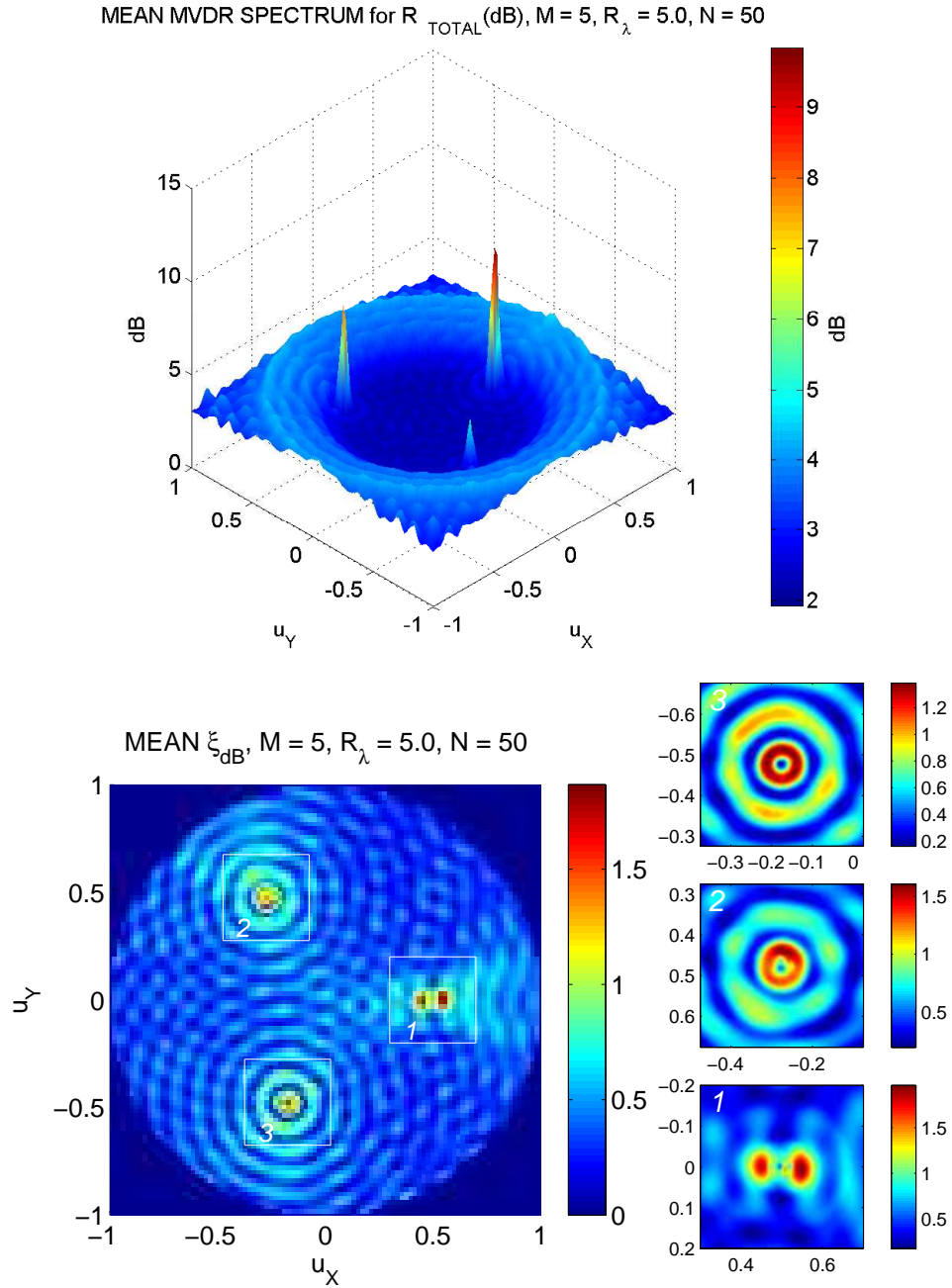


Figure 7.4: **CSS performance, $N = 50$, $R_\lambda = 5$ circular array, $M = 5$ snapshots:** The upper plot shows the average MVDR spectrum for the covariance estimated using (7.41). The weak source is biased low in the average, a result of inconsistent detection of the source in the individual trials. The average normalized SINR loss, ξ_{dB} , shown in the lower plot is less than 0.8 dB in most of the visible region. Mismatch occurs near the point sources, resulting in elevated ξ_{dB} as highlighted in the zoomed insets on the right. Mismatch is worst for the strongest source (bottom inset), but never higher than 1.8 dB (mean value).

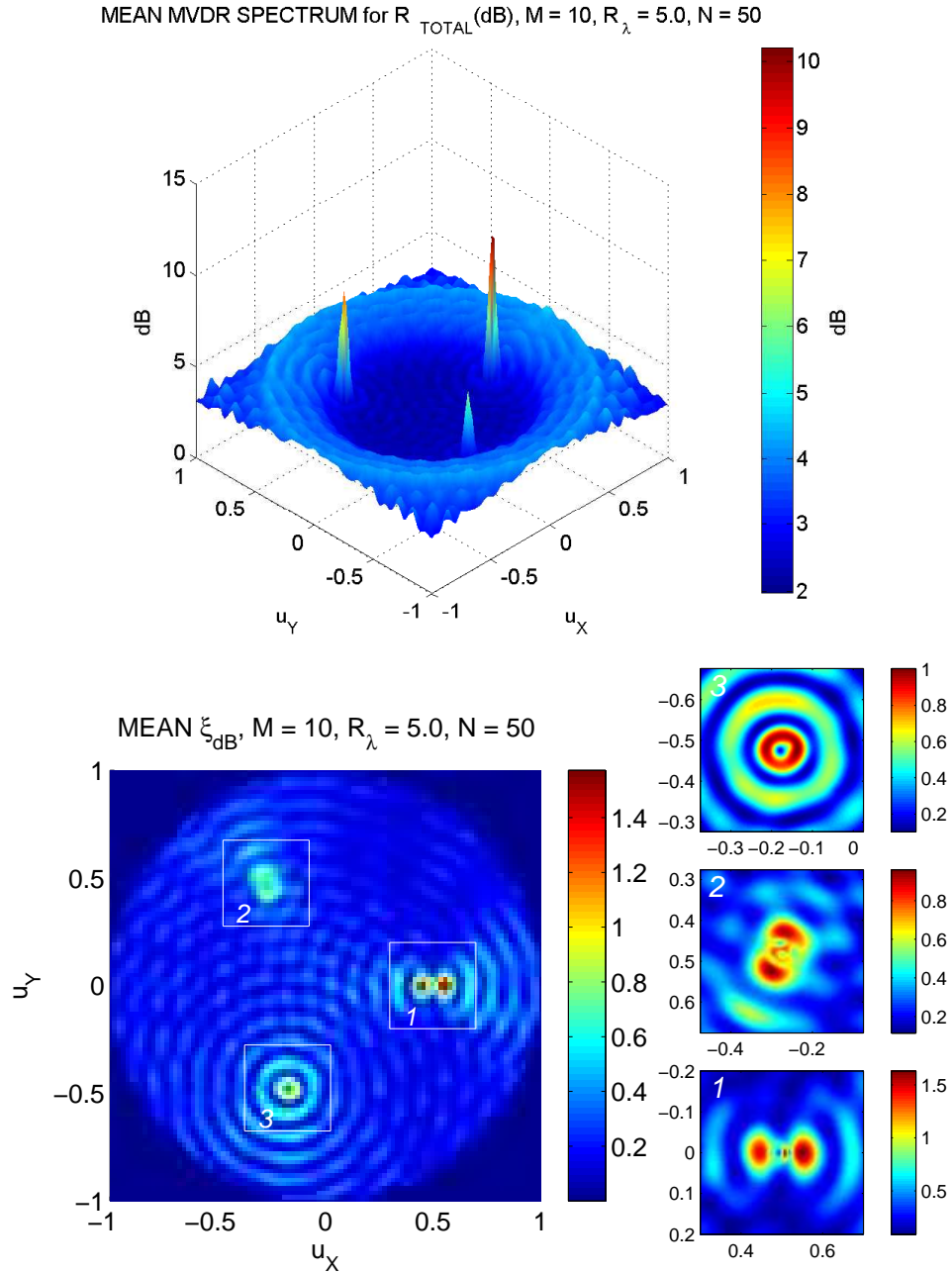


Figure 7.5: **CSS performance, $N = 50$, $R_\lambda = 5$ circular array, $M = 10$ snapshots:** The upper plot shows the average MVDR spectrum for the covariance estimated using (7.41). The weak source is more visible than the $M = 5$ case, but still lower than shown in the ensemble, Figure 7.3. Detection performance as part of harmonic analysis improves with more snapshots. The average normalized SINR loss, ξ_{dB} , shown in the lower plot, improves over the $M = 5$ case with peak of 1.6 dB and less than 0.3 dB in most of the visible region. Again, peak ξ_{dB} occurs in the near vicinity to the point sources, due to estimation mismatch.

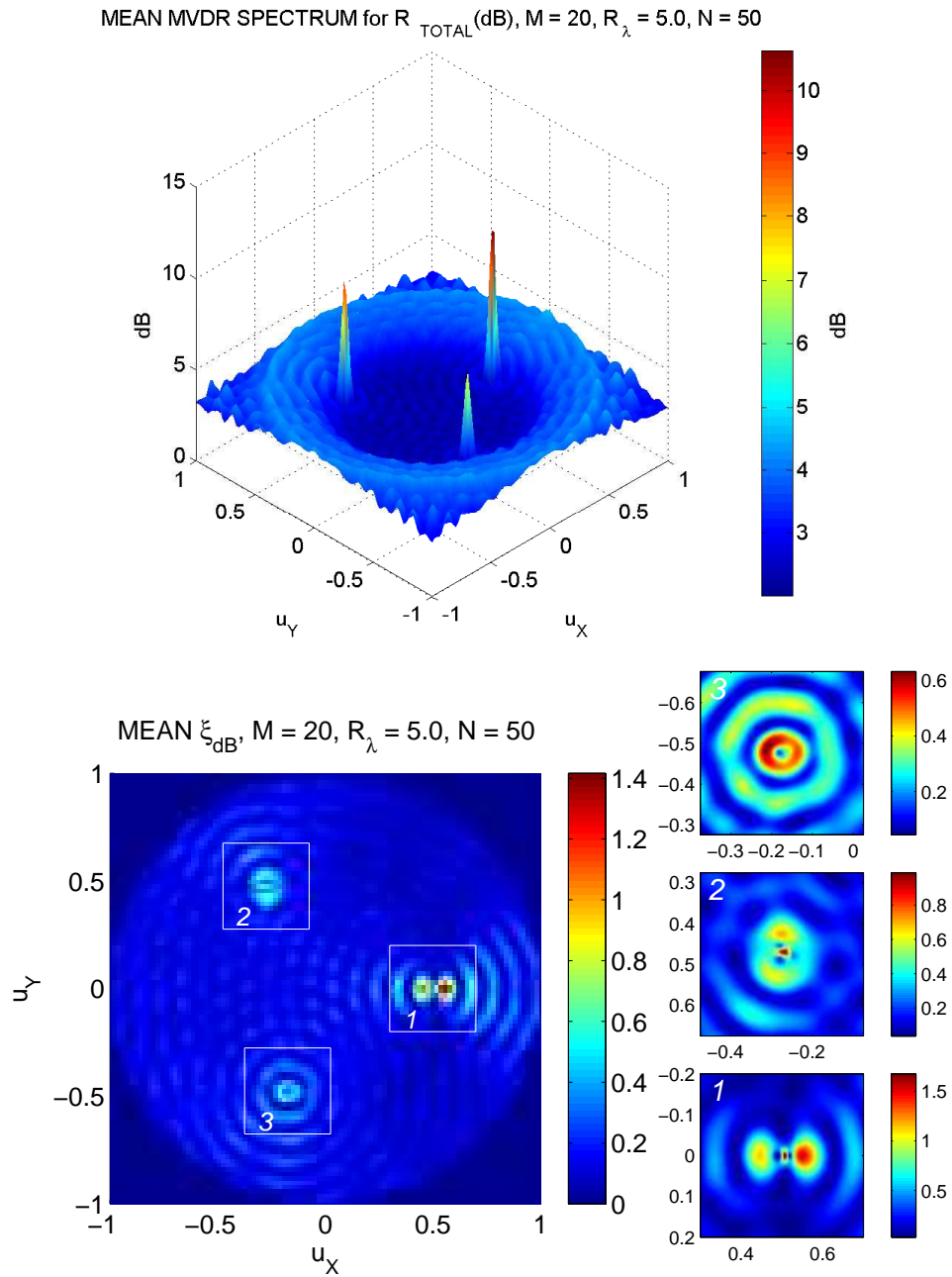


Figure 7.6: **CSS performance**, $N = 50$, $R_\lambda = 5$ **circular array**, $M = 20$ **snapshots**: The average MVDR spectrum in the upper plot is very close to the ensemble spectrum of Figure 7.3. Average normalized SINR loss, ξ_{dB} , continues to improve over the $M = 10$ case, however, values at this point are tenths of a dB from optimal. Mismatch still occurs in the neighborhood of the point sources but is approaching the order of a dB or less.

7.5.2 $N = 50$ Element Uniform Circular Array, $R_\lambda = 2.5$

The MVDR spectrum for the ensemble covariance described by the parameters in Table 7.1 for $R_\lambda = 2.5$ is shown in Figure 7.7. The three point sources are increased by 3 dB for this scenario. The isotropic noise power per sensor has remained constant, but due to the lower operational frequency the noise is concentrated in a smaller wavenumber bandwidth. This is the reason for increasing the power of the point sources. They appear wider due to the lower resolution of the array. For this test case the array radius in wavelengths is $R_\lambda = 2.5$, which should result in no aliasing artifacts due to spatial sampling as $N > 4\pi R_\lambda \sim 32$ [1]. This is clear in the Figure by the sharp transition between visible and virtual space at the boundary $u_x^2 + u_y^2 = 1$.

Simulation results for $M = 5, 10,$ and 20 snapshots are shown in Figures 7.8, 7.9, and 7.10. At the lowest amount of snapshot support, the weakest source goes mostly undetected. The average MVDR spectrum for the covariance estimated using (7.41) reflects this and the source is barely visible. This steadily improves with increasing snapshots, and at $M = 20$ the average estimated spectrum and the ensemble are very close. Average normalized SINR loss, ξ , shown as $\xi_{dB} = -10 \log_{10} \xi$ in the figures, is less than (0.9, 0.5, 0.4) dB in most of the visible region for $M = (5, 10, 20)$ snapshots. As seen earlier, increased performance loss occurs near the point sources, and is proportional to source strength. The largest average loss incurred is $\xi_{dB} = (1.5, 1.1, 1.0)$ dB for $M = (5, 10, 20)$ snapshots. While comparative performance for another processor is not shown, the performance indicated in the figures is better than the 3dB within $M = 2K = 6$ snapshots rule of thumb.

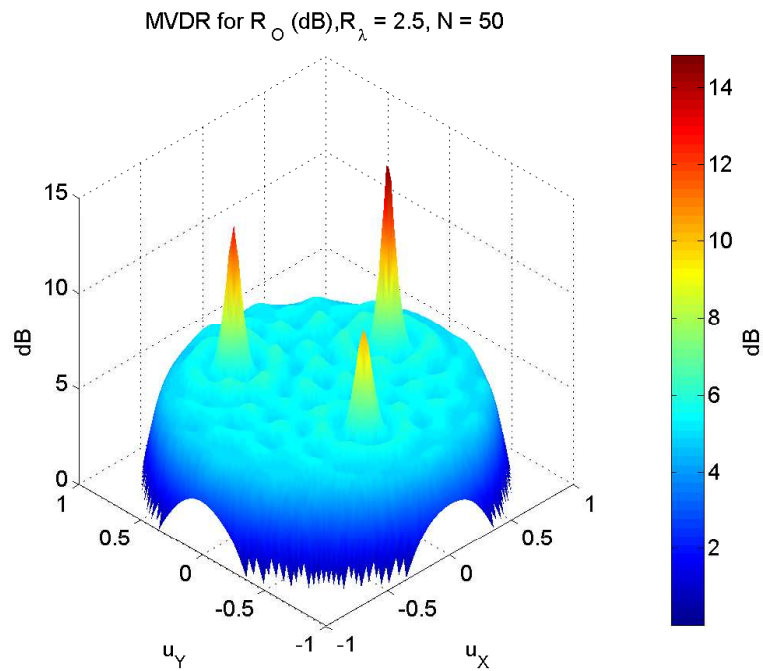


Figure 7.7: **MVDR spectrum for ensemble covariance, $N = 50$, $R_\lambda = 2.5$ circular array:** The low, medium, and high SNR peaks are clearly visible. The number of elements, N , is greater than $4\pi R_\lambda$, so aliasing effects due to the spatial sampling are negligible [1]. The drop off in the transition from the edge of the visible region occupied with isotropic noise to the virtual region containing only sensor noise is clear at the ring $u_x^2 + u_y^2 = 1$.

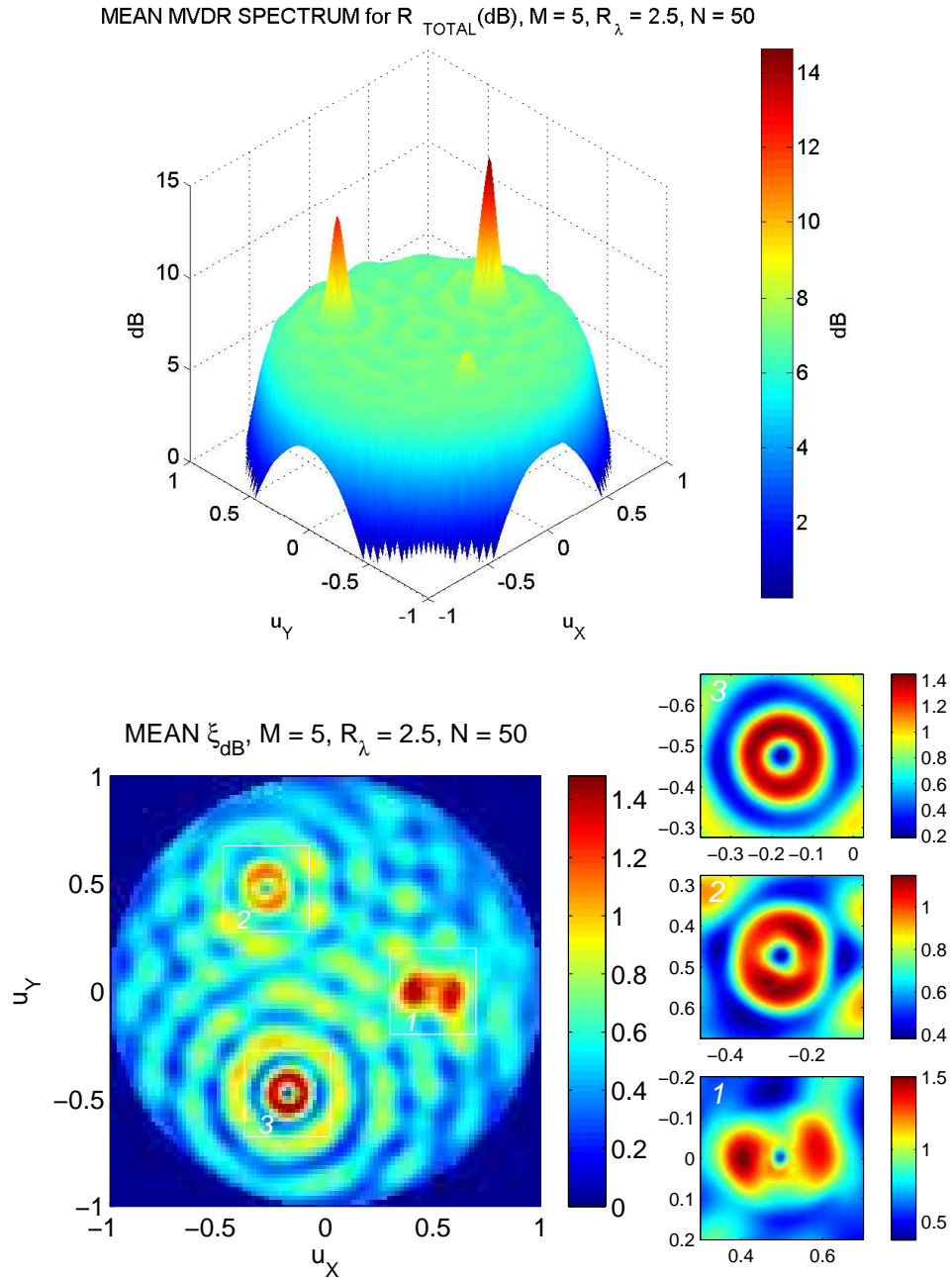


Figure 7.8: **CSS performance, $N = 50$, $R_\lambda = 2.5$ circular array, $M = 5$ snapshots:** The upper plot shows the average MVDR spectrum for the covariance estimated using (7.41). The weak source is barely visible in the average. This is a result limited detection of the source in the individual trials. The average normalized SINR loss, ξ_{dB} , shown in the lower plot is less than 1.0 dB in most of the visible region. Mismatch occurs near the point sources, resulting in elevated ξ_{dB} as highlighted in the zoomed insets on the right. Mismatch is worst for the strongest source (bottom inset) but nearly the same in vicinity of the poorly detected weak source. ξ_{dB} is never higher than 1.5 dB (mean value).

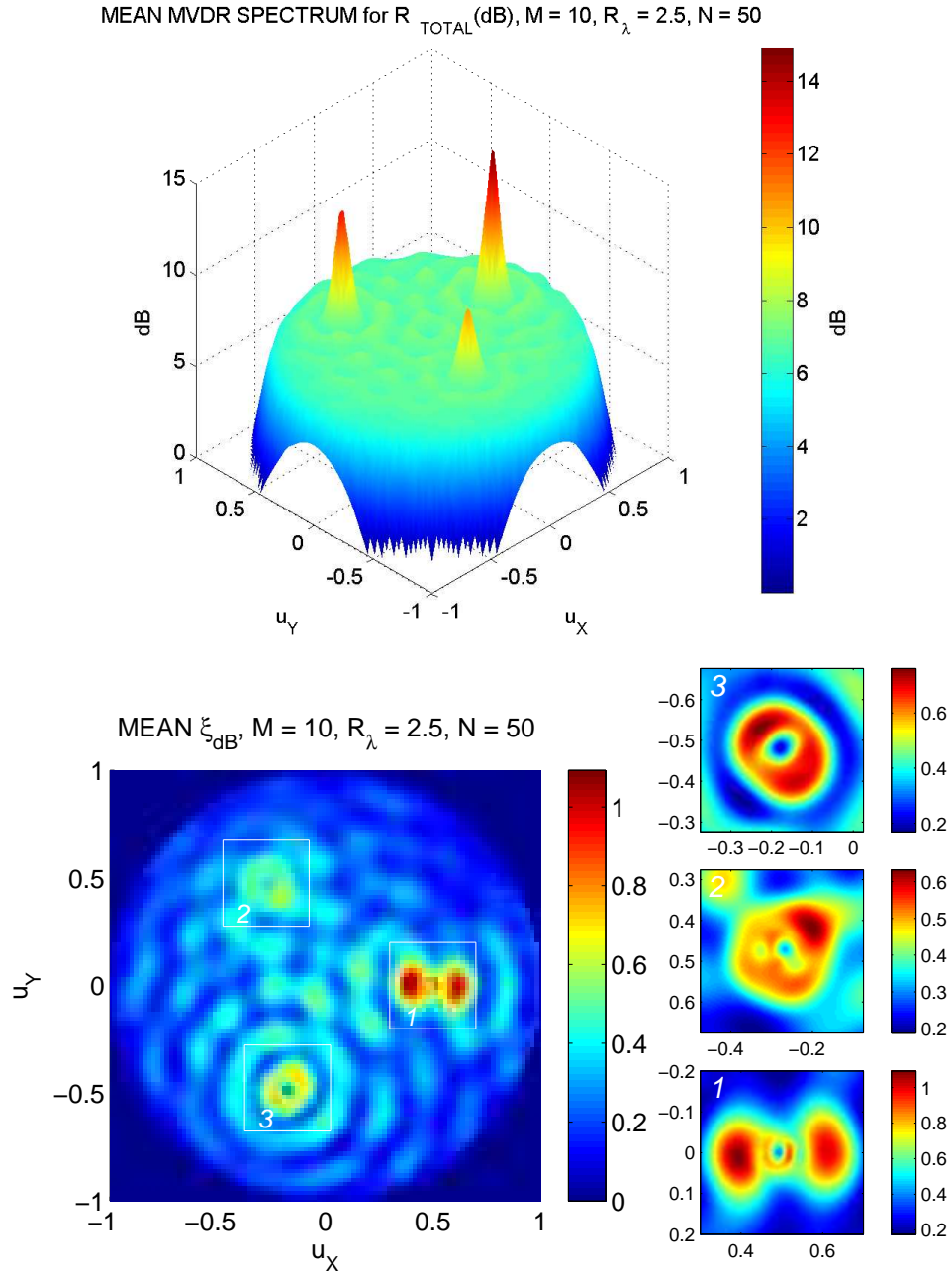


Figure 7.9: **CSS performance**, $N = 50$, $R_\lambda = 2.5$ **circular array**, $M = 10$ **snapshots**: The upper plot shows the average MVDR spectrum for the covariance estimated using (7.41). The weak source is much more visible than the $M = 5$ case, but still somewhat lower than shown in the ensemble, Figure 7.7. Detection performance as part of harmonic analysis improves with more snapshots. The average normalized SINR loss, ξ_{dB} , shown in the lower plot, improves over the $M = 5$ case with peak of 1.1 dB and less than 0.5 dB in most of the visible region. Again, peak ξ_{dB} occurs in the near vicinity to the point sources, due to estimation mismatch.

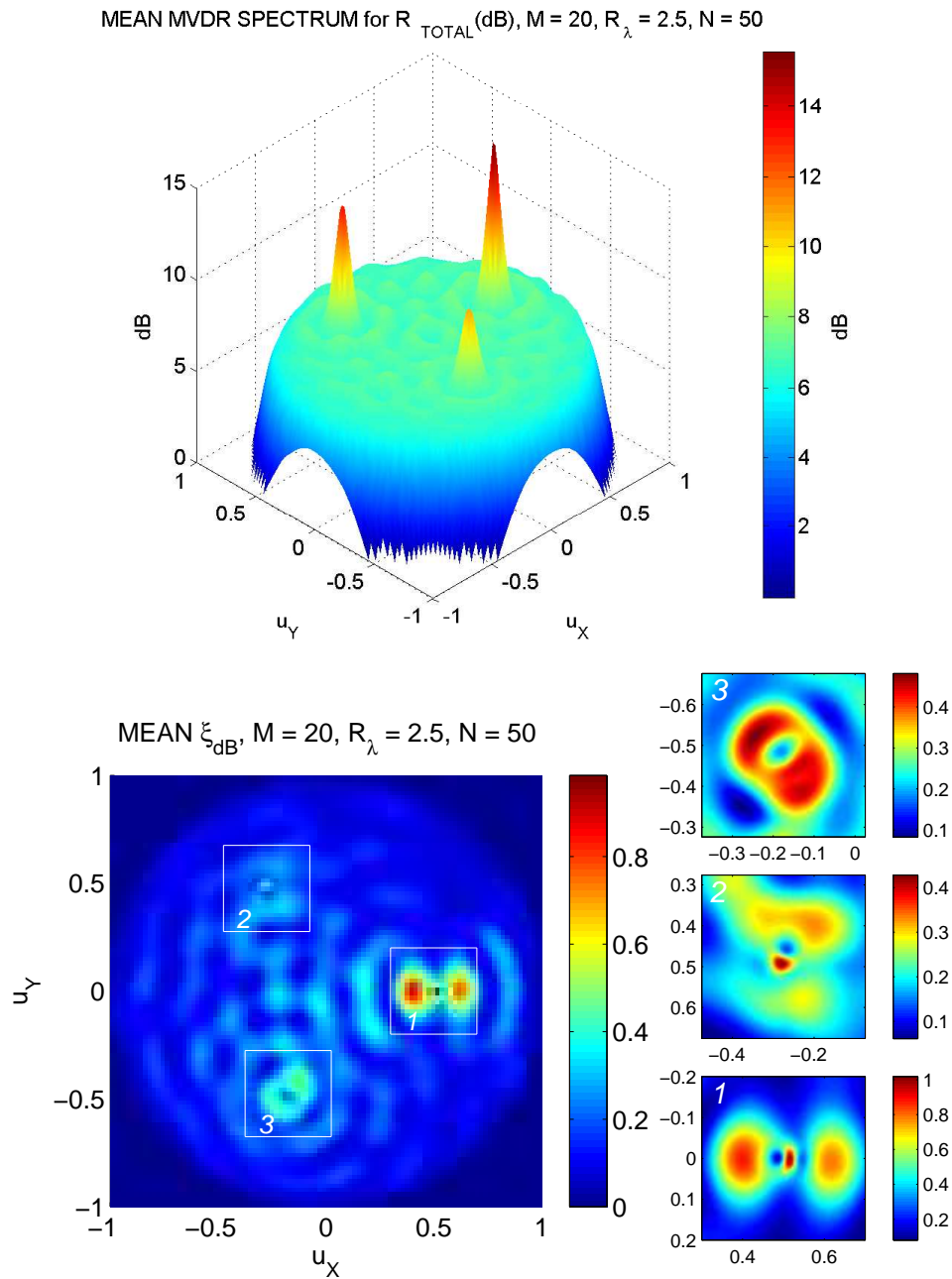


Figure 7.10: **CSS performance**, $N = 50$, $R_\lambda = 2.5$ **circular array**, $M = 20$ **snapshots**: Performance improvement is slight, but visible, compared to the already good results for the $M = 10$ case. The average MVDR spectrum in the upper plot is very close to the ensemble spectrum of Figure 7.7. Average normalized SINR loss, ξ_{dB} , values are tenths of a dB from optimal over most of the visible region. Mismatch still occurs in the neighborhood of the point sources but is approaching the order of a dB or less.

7.5.3 Importance of $\hat{\sigma}_w^2 \mathbf{P}_{\text{vr}}$

To reinforce the importance of estimation and inclusion of the sensor noise component in the virtual region, we consider an example where the $\hat{\sigma}_w^2 \mathbf{P}_{\text{vr}}$ term in (7.41) is not included. Section 3.3.2 discussed why this term is important, and provided an illustration for a uniform linear array. Here we use the uniform circular array described in Section 7.5.2. From the analysis in Figure 7.1, this particular array has a virtual subspace with dimension $N_{\text{vr}} = 15$. One of the side-effects of this is the distinct drop off in noise power at the isotropic to sensor noise transition at the boundary of the visible and virtual regions. This effect is illustrated in Figure 7.11, where it is clear that the estimated covariance accurately represents the visible region for the problem. The average normalized SINR loss, ξ , shown as $\xi_{dB} = -10 \log_{10} \xi$ in the Figure, shows the degradation in performance for neglecting the noise term compared to Figure 7.10. This is a result of poor adaptive beamformer sidelobe behavior in the virtual region that results in undesired noise amplification. As shown in the Figure, this affect is particularly pronounced at the boundary between visible and virtual space, the ring $u_x^2 + u_y^2 = 1$.

7.6 Summary

This chapter applied the CSS technique to arrays with arbitrary geometry. The importance of proper estimation and accounting of the sensor noise component in virtual space was emphasized, and a method for doing so based on the covariance matrix of 3D isotropic noise was developed. An example of the application to uniform circular arrays was provided. Uniform circular arrays maintain a certain structure, and are not strictly speaking arbitrary, but do result in a covariance matrix which is not Toeplitz. Normalized SINR loss performance and average MTSE spectra were assessed via simulation. Performance was generally seen to be very close to optimal with very little snapshot support, with some losses encountered near line components due to mismatch, and for weak *INR* line components at very low snapshot support due to inconsistent detection within harmonic analysis.

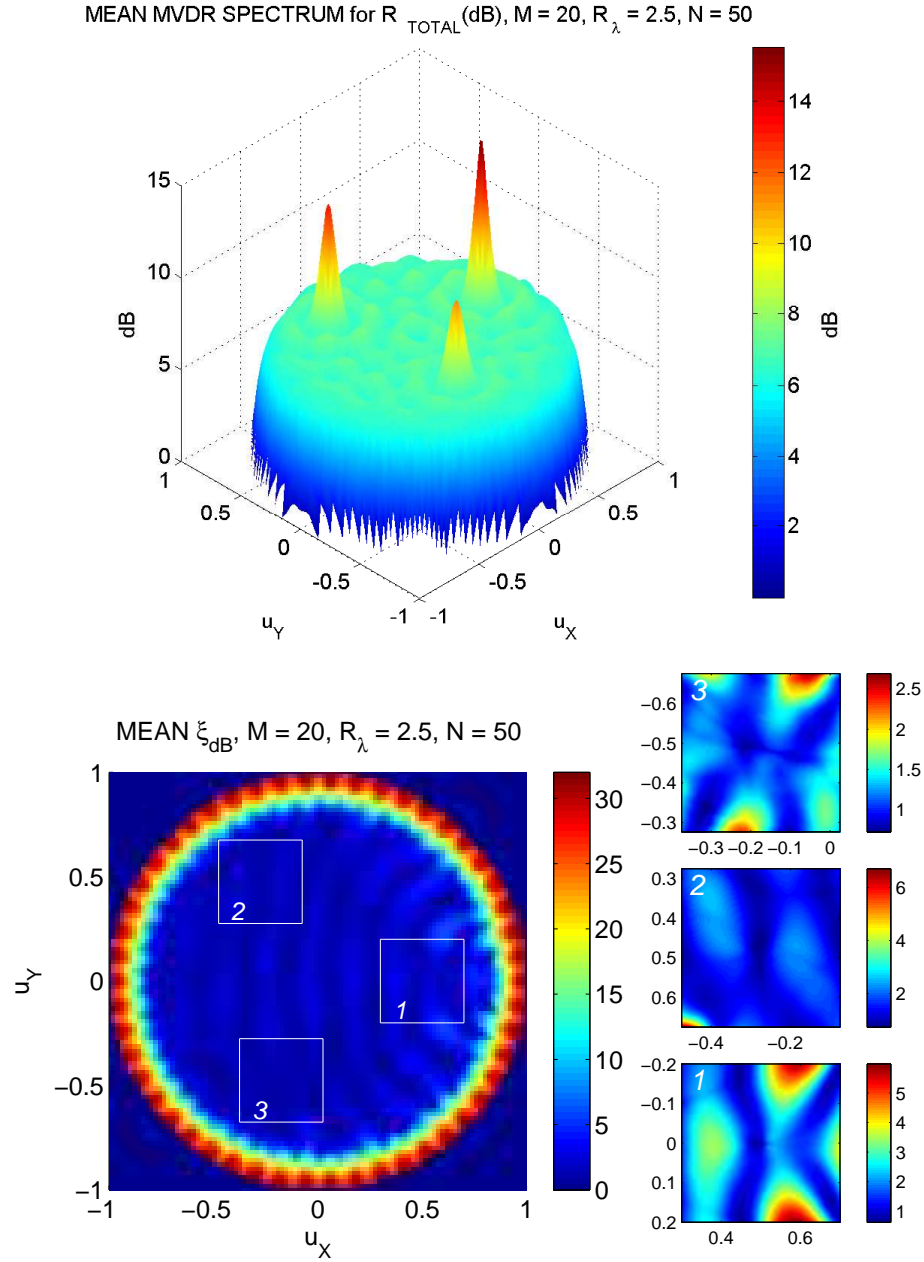


Figure 7.11: **Impact of covariance estimated from visible space only:** In this example, $R_\lambda = 2.5$, so the virtual subspace exists and has dimension $N_{\text{vr}} = 15$. The $\hat{\sigma}_w^2 \mathbf{P}_{\text{vr}}$ term is not included in (7.41). The estimated wavenumber spectrum, shown in the upper plot, is correct in representing the visible region of the array. However, the average normalized SINR loss, ξ , expressed in dB as $\xi_{dB} = -10 \log_{10} \xi$, shown in the lower plot exhibits poor performance, in particular near the ring $u_x^2 + u_y^2 = 1$ (low elevations w.r.t. the plane of the array). Even at higher elevations from the array plane, ξ_{dB} shows significant ripples with peaks in the 5 to 6 dB range. This plot should be compared to Figure 7.10, which is the performance using the same amount of snapshots and properly accounting for the $\hat{\sigma}_w^2 \mathbf{P}_{\text{vr}}$ term.

Chapter 8: Summary and Future Work

In summary, the estimation of covariance from the corresponding spatial spectrum is a valuable technique for adaptive array processing that addresses low snapshot support and correlated signal and interference conditions. Inherently, spectral estimation enforces a wide sense stationary model for the data and uses the knowledge of the array geometry in its development. This defines the structure in the underlying problem, making estimation of covariance from spatial spectrum (CSS) a structured covariance algorithm. The transform relationship between spectrum and covariance is well established. The contribution of this work is in developing an understanding of the performance and limitations of the technique for adaptive array processing, and developing extensions to the basic techniques to provide better performance across a broader range of conditions including mixed spectra environments and non-ideal array manifold response.

The first major contribution of the work is in the area of application of CSS to the narrowband wide sense stationary space-time process. The main line of development focused on application to the uniform line array. This allows the use of results and relationships from uniform sampled time series analysis. In particular, the estimate of the space-time process covariance and sensor noise component can be done simultaneously using fast Fourier transform techniques. While the covariance from power spectrum result is immediately obvious when considering the problem from a time series perspective, we highlighted the distinction between the individual contributions of the space-time process within the visible region of the array and the sensor noise component occupying both visible and virtual space. This distinction is important when adapting the technique to non-uniformly spaced arrays. To be meaningful for adaptive beamforming, the estimated covariance matrix must be positive definite. The estimated CSS covariance was shown to be positive definite when the power spectral estimate is real-valued and greater than zero. This is a reasonable assumption

for most spectral estimation algorithms when the uncorrelated sensor noise component is present. Initial performance analysis considered using classical spectral estimation techniques - the averaged windowed periodogram, as the basis for the algorithm. It was shown this was equivalent to a diagonal sum replace operation, referred to as $DSR(\cdot)$, on the sample covariance matrix of the windowed snapshots and produces a biased estimate of the covariance matrix. For a single interferer in spatially white noise, the normalized SINR loss performance is within 1 dB of optimal provided that the interferer is sufficiently separated from the desired steering vector, and the sidelobe level of the chosen window sufficiently suppresses the interference. Neither of these conditions can be guaranteed in practice. This motivates the introduction of a harmonic analysis process into the operation. The purpose of this process is to successively detect, estimate, and subtract the influence of discrete line components from the data. Thomson's multitaper spectral estimation (MTSE) neatly combines a non-parametric spectral estimation algorithm with the required harmonic analysis in low snapshot support algorithm.

The procedure for using Thomson's approach with harmonic analysis as the spectral estimation algorithm was then specified and labeled CSS with MTSE. Being a structured covariance algorithm, the normalized SINR loss performance prediction maintains a dependence on the true underlying covariance. In other words, every situation encountered is its own problem when it comes to performance. To this end, performance of CSS with MTSE was assessed in several relevant interference and noise environments. Performance was demonstrated to be near optimal in very few snapshots for spatially spread interference, line component interference and mixed spectra interference as long as the array could resolve the individual line components (if they existed) within the spectrum. This is one of the features that makes this technique especially attractive for long aperture arrays with large numbers of sensors, as these have good resolution properties. Performance is consistently better than other reduced rank techniques or optimal diagonal loading in terms of normalized SINR loss and convergence time. The sample covariance matrix based techniques ultimately approach optimal as the number of snapshots approaches infinity. In fact, their

performance is predictable in closed form based on the number of interferers and snapshots. On the other hand, CSS with MTSE is biased due to the limits of spectral estimation and does not converge to the optimal result in general. However, CSS with MTSE does converge to near optimal extremely fast, typically within two to three snapshots. For the uniform linear array case, the CSS technique can be represented in terms of the $DSR(\cdot)$ operation, where values in the covariance matrix are replaced by the sum of the respective diagonal in the windowed sample covariance matrix. This increases the amount of effective averaging of the data in a manner that sample covariance matrix methods do not.

The second major contribution of the work is in the area of application of CSS to the problem of correlated signal and interference. This type of space-time process is not spatially stationary, as the correlation between disjoint wavenumber bands is not uncorrelated. Still, as the wavenumber spectrum conveys no correlation information we expect CSS to suppress the impact of the correlation in the data. Analysis of the expected value of the CSS covariance showed that it is biased in two ways. The first bias is in a manner similar to the stationary process case and is related to the choice of window function used in the spectral estimation. The second bias is related to the cross-correlation terms between the signals. The overall impact to performance of this second bias was investigated in two ways. The first approach compared the ratio of the contribution of the correlated component within the covariance to the uncorrelated component, as measured using the Froebenius norm squared. While the correlated component is non-zero, its influence is concentrated near the main lobe of the array. For increasing array aperture, the main lobe width steadily decreases and in the limit as the aperture goes to infinity the influence of the correlation disappears. This is helpful in understanding the limiting behavior, but for arrays of practical length the normalized SINR loss is a more valuable measure of performance. It was shown that CSS applied to correlated signal and interference data performs almost identically to CSS applied to the same problem where the signal and interference are uncorrelated. In other words, CSS has a strong suppression effect on the residual correlation reflected in the covariance. This was demonstrated through simulation using the effective SINR

metric. This metric correctly predicts the performance loss of traditional MVDR for signal and correlated interference cases. With an increasing magnitude of correlation coefficient, MVDR degrades while CSS maintains a consistent level of performance. From the analysis of CSS under the correlated signal and interference case using the $DSR(\cdot)$, we are able to relate the work to covariance matrix tapers and redundancy averaging, and show that CSS combines benefits of both algorithms with some of its own - increase in effective sample size due to $DSR(\cdot)$ integration, mitigation of correlated signal and interference, and positive definiteness.

The third major contribution of the work is in the area of application of CSS with conditions of non-ideal array manifold response. Because it is a structured covariance technique CSS relies on knowledge of the array geometry. When the array manifold response is non-ideal the basic CSS approach suffers a predictable degradation in normalized SINR loss performance. This is true for other structured covariance techniques as well. Performance degradation is dominated by the error vectors associated with the largest line components in the data. A linear MMSE (ML in Gaussian noise) estimate of the non-ideal response error vectors was developed so that the error vector information could be incorporated into the covariance. This processing may be applied iteratively as was done for line component processing in the original harmonic analysis. This approach allows the data to be successively peeled back so that initially hidden components can be identified and processed in the data. This technique was applied successfully to random errors in array manifold response, both at and below design frequency, as well as to the case of deterministic array manifold response errors due to array bending. As long as the error vectors are not so large as to prevent detection of the line components the technique works well. Performance is seen to be comparable to the reduced rank multi-stage Wiener filter (MWF). A consequence of the error vector processing is that performance no longer exhibits the rapid converge seen in the ideal array manifold response case. This behavior is also seen when applying the error vector processing if the array manifold response was, in fact, ideal. An important concept for the deterministic error case is that the underlying problem is still a structured

covariance problem as the array displacement does not affect the stationarity of the space-time process. But the structure as defined by the assumed array geometry and its array manifold response is different than what is actually encountered. With proper knowledge of the array geometry the problem reverts back to the ideal array manifold response situation studied earlier. In all cases a beneficial byproduct of the error vector processing was the ability to produce an estimate of the wavenumber spectrum that with the influence of the error vectors removed. This is, effectively, how the situation would appear if we were able to “fix” the array and may be valuable for some applications in its own right.

The final contribution of the work is the extension of the CSS techniques to arbitrary array geometries. This is significant in that some structured covariance algorithms that exploit Toeplitz structure in the covariance for uniform linear arrays are not easily extendable. For an arbitrary geometry, the covariance for the space-time process can be estimated by scanning through the visible space, but this does not typically address the sensor noise in virtual space. A technique for specifically estimating the sensor noise by partitioning the N -dimensional space into visible and virtual subspaces based on the covariance for 3D isotropic noise was proposed. This technique, along with multi-taper spectral estimation with harmonic analysis, was applied to uniform circular arrays. The normalized SINR loss performance was seen to be within one dB of optimal throughout most of the visible space for low numbers of snapshots, with slightly higher loss seen in the vicinity of line components due to mismatch. Specific cases deliberately ignoring the virtual space noise component exhibited much higher normalized SINR loss and reaffirmed the need to address this quantity.

Throughout the work we have focused on representation in the spectral domain, starting with the Cramér spectral representation of the observed space-time process. This has added value in understanding how the operations in the spatial covariance domain have been influenced or impacted the processing. The work has looked at broad concepts that provide a basis for continuing research. In particular, areas that are suitable for continuing research are:

- Convergence time - It was identified that performance could not be reduced to a simple expression based on the number of interferers and snapshots alone, as is the case for sample covariance based methods. Simple arguments demonstrated that CSS techniques provide the equivalent of additional averaging, or the increase in effective sample size, and this was supported by simulation results showing rapid convergence. Further research may pursue predictions of convergence time that explicitly incorporate the number of sensor elements, N .
- Methods to extend CSS processing to arbitrary array geometry were presented, and performance was simulated for a uniform circular array. Further research may look into aliasing due to spatial sampling for arbitrary geometry and its impact on estimation of the wavenumber spectrum, and consequently the CSS covariance.
- For deterministic array manifold response errors, further research may explore integration of the error vector processing with array shape estimation algorithms in a closed loop manner.
- Application of CSS techniques to acoustic mode processing or vector sensor processing.

Appendix A: Circular and Partial Circular Array Bending

A.1 Introduction

This appendix provides further information on the geometry and specification of the two types of deterministic positional errors for uniform linear arrays used in the dissertation.

A.2 Circular Bow

For a linear array with total aperture length, L , the circular bow deformity is shown in Figure A.1. The linear array is deflected from the linear axis at its center by a displacement, H . The resulting arc, of length L , lies on a circle with radius, R , whose center is the point $(0, [H - R])$. The arc subtends an angle, θ , which is related to the arc length by $L = \theta R$. θ can also be computed from $[R - H] = R \cos(\theta/2)$, as

$$\theta = 2 \cos^{-1} \left(\frac{R - H}{R} \right) \quad (\text{A.1})$$

Substituting (A.1) into the expression for arc length

$$L = 2 \cos^{-1} \left(\frac{R - H}{R} \right) R \quad (\text{A.2})$$

which can be rewritten as

$$\cos \left(\frac{L}{2R} \right) + \frac{H}{R} - 1 = 0 \quad (\text{A.3})$$

Equation (A.3) cannot be solved in closed form for R but can be solved numerically, for example using the `fzero()` routine in MATLAB. An initial estimate for R , necessary for some numerical solving routines, can be provided by approximating the chord length, C , as

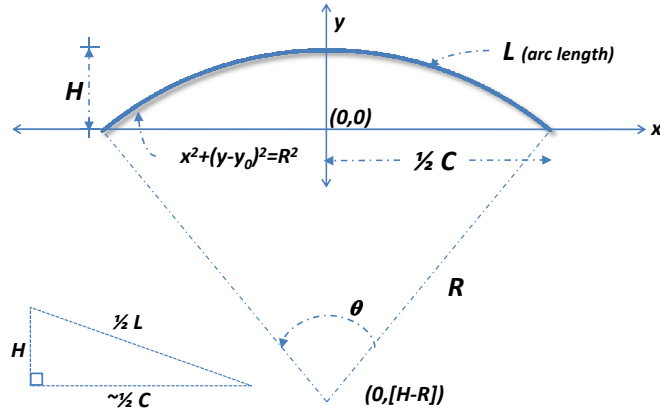


Figure A.1: Definition of a circular bow array deformity

the bottom of the right triangle shown inset in Figure A.1.

$$\hat{C} \approx 2\sqrt{\left(\frac{L}{2}\right)^2 + H^2} \quad (\text{A.4})$$

Using \hat{C} , along with the known versine, H , the initial estimated of R can be computed (via the chord theorem), as

$$\hat{R}_{ini} = \frac{C^2}{8H} + \frac{H}{2} \approx \frac{\hat{C}^2}{8H} + \frac{H}{2} \quad (\text{A.5})$$

A.3 Partial Circular Bow

For a linear array with total aperture length, L , the partial circular bow deformity is shown in Figure A.2. A portion of the array bends in a circular fashion starting from a displacement, H , and joins the linear axis after a distance of L_2 . The remainder of the array lies on the linear axis. The curved portion of the array lies on the circle with radius,

R , whose center is the point $(x_0, y_0) = (0, R)$. The second known point on the circle is $(x_1, y_1) = (-L_2, H)$. Inserting these values into the equation for a circle

$$(x_1 - x_0)^2 + (y_1 - y_0)^2 = R^2 \quad (\text{A.6})$$

we can solve for R

$$R = \frac{L_2^2 + H^2}{2H} \quad (\text{A.7})$$

The remaining steps are to determine the length of the arc, L'_2 , and the length of the linear portion of the array, L_1 . The distance L_a can be found immediately from the provided dimensions, $L_a = \frac{1}{2}\sqrt{H^2 + L_2^2}$. The angle $\theta = 2 \sin^{-1} \left(\frac{L_a}{R} \right)$ subtends the arc, yielding an arc length

$$L'_2 = \theta R = 2 \sin^{-1} \left(H [L_2^2 + H^2]^{-1/2} \right) \frac{L_2^2 + H^2}{2H} \quad (\text{A.8})$$

and linear array portion length of

$$L_1 = L - L'_2 \quad (\text{A.9})$$

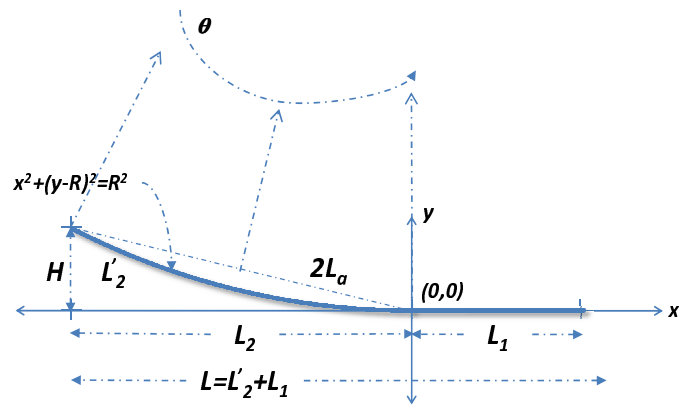


Figure A.2: Definition of a partial circular bow array deformity

Appendix B: Sensitivity of Optimal Beamformer to Model Estimation Errors

B.1 Introduction

This appendix contains the details of the expressions for normalized SINR loss of a model based adaptive beamformer as a function of estimation accuracies of the model parameters, namely wavenumber and interferer to noise ratio (INR). This analysis supports the discussion in Section 3.2.

B.1.1 Interferer to Noise Ratio

For an N element array of isotropic sensors, the quantity β_o in the expression for the covariance matrix inverse is

$$\beta_o = \frac{\sigma_n^2 / \sigma_w^2 \mathbf{v}_o^H \mathbf{v}_o}{1 + \sigma_n^2 / \sigma_w^2 \mathbf{v}_o^H \mathbf{v}_o} \quad (\text{B.1})$$

which is the ratio of the power of the interferer, C , to the total interferer and noise power at the output of the array, $C + W$

$$\beta_o = \frac{C}{C + W} \quad (\text{B.2})$$

where $\mathbf{v}_o^H \mathbf{v}_o = N$, $C = \sigma_n^2 N$, and $W = \sigma_w^2$.

B.1.2 Over/Under-estimate INR , $\Delta INR \neq 0$

Case 1. $\beta_a \approx 1$

This section develops the approximate normalized SINR loss expression for the case of overestimation of INR , or underestimated INR where $(INR)^{-1}(\Delta INR)^{-1} \leq 1$. Starting with the exact expression for the normalized SINR loss

$$\xi = \frac{\mathbf{s}^H \mathbf{R}_a^{-1} \mathbf{s}}{\mathbf{s}^H \mathbf{R}_o^{-1} \mathbf{s}} \cdot \frac{\mathbf{s}^H \mathbf{R}_a^{-1} \mathbf{s}}{\mathbf{s}^H \mathbf{R}_a^{-1} \mathbf{R}_o \mathbf{R}_a^{-1} \mathbf{s}} \quad (\text{B.3})$$

and expanding the matrix and matrix inverse terms, and applying the conditions $\mathbf{P}_{v_a} = \mathbf{P}_{v_o}$ and $\beta_a \approx 1$

$$\xi \approx \frac{\mathbf{s}^H [\mathbf{I} - \mathbf{P}_{v_o}] \mathbf{s}}{\mathbf{s}^H [\mathbf{I} - \beta_o \mathbf{P}_{v_o}] \mathbf{s}} \cdot \frac{\mathbf{s}^H [\mathbf{I} - \mathbf{P}_{v_o}] \mathbf{s}}{\mathbf{s}^H [\mathbf{I} - \mathbf{P}_{v_o}] [\sigma_n^2 / \sigma_w^2 \mathbf{v}_o \mathbf{v}_o^H + \mathbf{I}] [\mathbf{I} - \mathbf{P}_{v_o}] \mathbf{s}} \quad (\text{B.4})$$

Recognizing that $\mathbf{P}_{v_o}^\perp = [\mathbf{I} - \mathbf{P}_{v_o}]$ is a projector on the null space of \mathbf{v}_o , and $\mathbf{P}_{v_o}^\perp = \mathbf{P}_{v_o}^\perp \mathbf{P}_{v_o}^\perp$, we can simplify to

$$\xi \approx \frac{\mathbf{s}^H [\mathbf{I} - \mathbf{P}_{v_o}] \mathbf{s}}{\mathbf{s}^H [\mathbf{I} - \beta_o \mathbf{P}_{v_o}] \mathbf{s}} \cdot \frac{\mathbf{s}^H [\mathbf{I} - \mathbf{P}_{v_o}] \mathbf{s}}{\mathbf{s}^H [\mathbf{I} - \mathbf{P}_{v_o}] [\mathbf{I} - \mathbf{P}_{v_o}] \mathbf{s}} \quad (\text{B.5})$$

which reduces further to

$$\xi \approx \frac{\mathbf{s}^H [\mathbf{I} - \mathbf{P}_{v_o}] \mathbf{s}}{\mathbf{s}^H [\mathbf{I} - \beta_o \mathbf{P}_{v_o}] \mathbf{s}} \quad (\text{B.6})$$

For an N element array of omnidirectional sensors, $\mathbf{s}^H \mathbf{s} = N$, and the final approximation for normalized SINR loss is

$$\xi \approx \frac{N - (1/N) |\mathbf{s}^H \mathbf{v}_o|^2}{N - (\beta_o/N) |\mathbf{s}^H \mathbf{v}_o|^2} \quad (\text{B.7})$$

Case 2. $\beta_a \rightarrow 0$

This is the case where the interferer is weak, and the INR is underestimated. Starting with the exact normalized SINR loss expression

$$\xi = \frac{\mathbf{s}^H \mathbf{R}_a^{-1} \mathbf{s}}{\mathbf{s}^H \mathbf{R}_o^{-1} \mathbf{s}} \cdot \frac{\mathbf{s}^H \mathbf{R}_a^{-1} \mathbf{s}}{\mathbf{s}^H \mathbf{R}_a^{-1} \mathbf{R}_o \mathbf{R}_a^{-1} \mathbf{s}} \quad (\text{B.8})$$

and expanding the matrix and matrix inverse terms, and applying the conditions $\mathbf{P}_{v_a} = \mathbf{P}_{v_o}$ and $\beta_a \approx 0$

$$\xi = \frac{N}{\mathbf{s}^H [\mathbf{I} - \beta_o \mathbf{P}_{v_o}] \mathbf{s}} \cdot \frac{N}{\mathbf{s}^H [\sigma_n^2 / \sigma_w^2 \mathbf{v}_o \mathbf{v}_o^H + \mathbf{I}] \mathbf{s}} \quad (\text{B.9})$$

We recognize the two terms in the denominator as the covariance matrix and its inverse for this problem.

$$\xi = \frac{N}{\mathbf{s}^H \mathbf{R}_o^{-1} \mathbf{s}} \cdot \frac{N}{\mathbf{s}^H \mathbf{R}_o \mathbf{s}} \quad (\text{B.10})$$

This is the normalized SINR loss for the conventional (non-adaptive) beamformer.

B.1.3 Spatial Frequency Offset, $\Delta k \neq 0$

Now we consider the case where the estimate of the interferer wavenumber is non-zero. To focus on the impact of estimation error, Δk , assume that the *INR* is estimated perfectly so that $\beta_a = \beta_o$, and the interferer is strength is high (a high *INR* approximation - we are less concerned with the impact of weak interferers). Starting with the exact expression for the normalized SINR loss,

$$\xi = \frac{\mathbf{s}^H \mathbf{R}_a^{-1} \mathbf{s}}{\mathbf{s}^H \mathbf{R}_o^{-1} \mathbf{s}} \cdot \frac{\mathbf{s}^H \mathbf{R}_a^{-1} \mathbf{s}}{\mathbf{s}^H \mathbf{R}_a^{-1} \mathbf{R}_o \mathbf{R}_a^{-1} \mathbf{s}} \quad (\text{B.11})$$

and expanding the matrix and matrix inverse terms, and applying the condition $\beta_a = \beta_o = 1$ (the high *INR* approximation).

$$\xi = \frac{\mathbf{s}^H [\mathbf{I} - \mathbf{P}_{v_a}] \mathbf{s}}{\mathbf{s}^H [\mathbf{I} - \mathbf{P}_{v_o}] \mathbf{s}} \cdot \frac{\mathbf{s}^H [\mathbf{I} - \mathbf{P}_{v_a}] \mathbf{s}}{\mathbf{s}^H [\mathbf{I} - \mathbf{P}_{v_a}] [\sigma_n^2/\sigma_w^2 \mathbf{v}_o \mathbf{v}_o^H + \mathbf{I}] [\mathbf{I} - \mathbf{P}_{v_a}] \mathbf{s}} \quad (\text{B.12})$$

Using the relationship $\mathbf{P}^\perp = [\mathbf{I} - \mathbf{P}]$ and expanding out terms

$$\xi = \frac{\mathbf{s}^H \mathbf{P}_{v_a}^\perp \mathbf{s}}{\mathbf{s}^H \mathbf{P}_{v_o}^\perp \mathbf{s}} \cdot \frac{\mathbf{s}^H \mathbf{P}_{v_a}^\perp \mathbf{s}}{\sigma_n^2/\sigma_w^2 \mathbf{s}^H \mathbf{P}_{v_a}^\perp \mathbf{v}_o \mathbf{v}_o^H \mathbf{P}_{v_a}^\perp \mathbf{s} + \mathbf{s}^H \mathbf{P}_{v_a}^\perp \mathbf{s}} \quad (\text{B.13})$$

Simplify notation by indicating the magnitude squared of the quadratic terms.

$$\xi = \frac{|\mathbf{P}_{v_a}^\perp \mathbf{s}|^2}{|\mathbf{P}_{v_o}^\perp \mathbf{s}|^2} \cdot \frac{|\mathbf{P}_{v_a}^\perp \mathbf{s}|^2}{\sigma_n^2/\sigma_w^2 |\mathbf{v}_o^H \mathbf{P}_{v_a}^\perp \mathbf{s}|^2 + |\mathbf{P}_{v_a}^\perp \mathbf{s}|^2} \quad (\text{B.14})$$

We leave the left term alone and concentrate on the right. Dividing through the right hand term by $|\mathbf{P}_{v_a}^\perp \mathbf{s}|^2$,

$$\xi = \frac{|\mathbf{P}_{v_a}^\perp \mathbf{s}|^2}{|\mathbf{P}_{v_o}^\perp \mathbf{s}|^2} \cdot \left[\sigma_n^2/\sigma_w^2 \frac{|\mathbf{v}_o^H \mathbf{P}_{v_a}^\perp \mathbf{s}|^2}{|\mathbf{P}_{v_a}^\perp \mathbf{s}|^2} + 1 \right]^{-1} \quad (\text{B.15})$$

For small Δk , the left hand term is approximately unity. We don't expect small changes to the null space of \mathbf{v}_o to substantially change the magnitude squared of the projection of the desired steering vector \mathbf{s} within that space.

$$\xi \approx \left[\sigma_n^2/\sigma_w^2 \frac{|\mathbf{v}_o^H \mathbf{P}_{v_a}^\perp \mathbf{s}|^2}{|\mathbf{P}_{v_a}^\perp \mathbf{s}|^2} + 1 \right]^{-1} \quad (\text{B.16})$$

We now use this expression to determine an acceptable Δk that achieves an acceptable SINR loss, ξ_{OK}

$$\xi_{OK} \leq \left[\sigma_n^2/\sigma_w^2 \frac{|\mathbf{v}_o^H \mathbf{P}_{v_a}^\perp \mathbf{s}|^2}{|\mathbf{P}_{v_a}^\perp \mathbf{s}|^2} + 1 \right]^{-1} \quad (\text{B.17})$$

which simplifies to

$$\frac{|\mathbf{v}_o^H \mathbf{P}_{\mathbf{v}_a}^\perp \mathbf{s}|^2}{|\mathbf{P}_{\mathbf{v}_a}^\perp \mathbf{s}|^2} \leq \frac{1 - \xi_{OK}}{\xi_{OK} \sigma_n^2 / \sigma_w^2} \quad (\text{B.18})$$

Again, for small Δk , assume $|\mathbf{P}_{\mathbf{v}_a}^\perp \mathbf{s}|^2 \approx |\mathbf{P}_{\mathbf{v}_o}^\perp \mathbf{s}|^2$. This concentrates the impact of Δk in a single term.

$$|\mathbf{v}_o^H \mathbf{P}_{\mathbf{v}_a}^\perp \mathbf{s}|^2 \leq |\mathbf{P}_{\mathbf{v}_o}^\perp \mathbf{s}|^2 \frac{1 - \xi_{OK}}{\xi_{OK} \sigma_n^2 / \sigma_w^2} \quad (\text{B.19})$$

This is a general expression for the single interferer in uncorrelated white noise case. To simplify further requires some assumptions about the array geometry. We continue by considering a uniform linear array, and analyze performance in terms of Δk . We assume a desired steering vector corresponding to broadside, however, the analysis in the k domain is invariant to shift in k . Translation back to physical angle of arrival does depend on actual k value. Expanding out $\mathbf{P}_{\mathbf{v}_a}^\perp$ explicitly

$$|\mathbf{v}_o^H \mathbf{s} - \mathbf{v}_o^H \mathbf{P}_{\mathbf{v}_a} \mathbf{s}|^2 \leq |\mathbf{P}_{\mathbf{v}_o}^\perp \mathbf{s}|^2 \frac{1 - \xi_{OK}}{\xi_{OK} \sigma_n^2 / \sigma_w^2} \quad (\text{B.20})$$

Going forward note that for the assumption of the desired steering vector corresponding to broadside, the variable k_o now represents the difference between the interferer location and $k_s = 0$. In k space only the difference matters. Using the following relationships

$$\mathbf{s}^H \mathbf{v}_o |_{\mathbf{s}=\mathbf{1}} = e^{-jk_o d(N-1)/2} \frac{\sin(k_o dN/2)}{\sin(k_o d/2)} \quad (\text{B.21})$$

$$\mathbf{v}_a^H \mathbf{v}_o = \sum_{n=0}^{N-1} e^{j\Delta k d n} = e^{j\Delta k d(N-1)/2} \frac{\sin(\Delta k dN/2)}{\sin(\Delta k d/2)} \quad (\text{B.22})$$

$$\mathbf{v}_a^H \mathbf{v}_a = N \quad (\text{B.23})$$

in (B.20) we can work to simplify the left hand side of the expression. Recall $k_a = k_o + \Delta k$. Eqn. (B.20) becomes

$$\left| e^{jk_o d(N-1)/2} \frac{\sin(k_o dN/2)}{\sin(k_o d/2)} - (1/N) e^{jk_o d(N-1)/2} \frac{\sin(\Delta k dN/2)}{\sin(\Delta k d/2)} \cdot \frac{\sin(k_a dN/2)}{\sin(k_a d/2)} \right|^2 \quad (\text{B.24})$$

For small $\Delta k dN/2$, use the small angle approximation for $\sin()$, $\sin(x) \approx x$, consolidate terms and apply the magnitude squared operations to yield

$$\left[\frac{\sin(k_o dN/2)}{\sin(k_o d/2)} - \frac{\sin([k_o + \Delta k] dN/2)}{\sin([k_o + \Delta k] d/2)} \right]^2 \quad (\text{B.25})$$

We use a first order approximation to this difference. Define the function

$$D(kd) \equiv \frac{\sin(kdN/2)}{\sin(kd/2)} \quad (\text{B.26})$$

Then by the quotient rule

$$\dot{D}(kd) \equiv \frac{d}{d(kd)} D(kd) = \frac{1}{2} \cdot \frac{N \sin(kd/2) \cos(kdN/2) - \sin(kdN/2) \cos(kd/2)}{\sin^2(kd/2)} \quad (\text{B.27})$$

and the difference approximation is

$$\frac{\sin(k_o dN/2)}{\sin(k_o d/2)} - \frac{\sin([k_o + \Delta k] dN/2)}{\sin([k_o + \Delta k] d/2)} \approx \dot{D}(k_o d) \Delta kd \quad (\text{B.28})$$

Inserting this back into (B.20) gives an expression for the required wavenumbe accuracy.

$$\Delta kd \leq \left(\frac{|\mathbf{P}_{v_o}^\perp \mathbf{s}|^2}{\dot{D}^2(k_o d)} \cdot \frac{1 - \xi_{OK}}{\xi_{OK} \sigma_n^2 / \sigma_w^2} \right)^{1/2} \quad (\text{B.29})$$

Substituting in for $|\mathbf{P}_{v_o}^\perp \mathbf{s}|^2$ yields the following expression.

$$\Delta kd \leq \left(\frac{1}{\dot{D}^2(k_o d)} \cdot \left[N - \frac{1}{N} \frac{\sin^2(k_o d N / 2)}{\sin^2(k_o d / 2)} \right] \cdot \frac{1 - \xi_{OK}}{\xi_{OK} \sigma_n^2 / \sigma_w^2} \right)^{1/2} \quad (\text{B.30})$$

Eqn. (B.30) contains oscillations that indicate there are areas in k space that are more tolerant to Δk . These correspond to nulls in the conventional beam pattern. We are interested in a smoother bound for the expression that eliminates oscillations and smoothly spans the lower values. This can be done by substituting

$$\dot{D}(kd) \approx \frac{1}{2} \cdot \frac{N \sin(kd/2)}{\sin^2(kd/2)} = \frac{N}{2 \sin(kd/2)} \quad (\text{B.31})$$

within (B.30). The final expression becomes

$$\Delta kd \leq \frac{2 |\sin(k_o d / 2)|}{N} \left(\left[N - \frac{1}{N} \frac{\sin^2(k_o d N / 2)}{\sin^2(k_o d / 2)} \right] \frac{1 - \xi_{OK}}{\xi_{OK} \sigma_n^2 / \sigma_w^2} \right)^{1/2} \quad (\text{B.32})$$

Appendix C: Table of Variables

Table C.1: Table of Variables - Scalars

Variable Notation	Description
c	speed of propagation
d	uniform linear array element spacing, also multitaper index
f	frequency variable
l	index variable
m	time sample index
n	array element index
r, c	row column indices for a matrix
y	scalar output of array processor
C	dimension of Cartesian space
D	the number of multi-tapers used for MTSE
K	the number of point source interferers
M	the number of available snapshots
N	the number of array sensor elements
N_{FFT}	number of points taken in FFT processing
N_{FPE}	number of free-parameter expansion points
W	half-width of analysis region for multitaper design
γ	scalar normalization constant
γ_{TH}	harmonic analysis detection threshold
θ	angle from vertical in spherical coordinates
λ	wavelength variable, also eigenvalue
ξ	normalized SINR loss
ξ_{dB}	normalized SINR loss in $-10 \log_{10}(\cdot)$
σ_{DL}^2	diagonal loading factor
σ_n^2	variance for single discrete interferer
σ_w^2	variance for uncorrelated sensor noise
σ_k^2	variance for the k^{th} discrete interferer
ϕ	azimuth in spherical coordinates
ψ	normalized wavenumber, $\psi = -kd$
ω	radian frequency
Ω	radian frequency, continuous time

Table C.3: Table of Variables - Scalar functions

Variable Notation	Description
$a_k(m)$	complex amplitude of the k^{th} plane wave component
$h_d(\cdot)$	weighting function for multitaper combining
$w_d[n], \mathbf{w}_d = ((w_d[n]))_n$	d^{th} window or taper function
$f(t, \mathbf{p})$	a space-time process
$\hat{\rho}[n]$	sample autocorrelation
$\rho_{\mathbf{w}}[n]$	sample autocorrelation, deterministic sequence, \mathbf{w}
$y_m^{(d)}(f), \mathbf{y}_m(f) = ((y_m^{(d)}(f)))_d$	MTSE d^{th} eigen-coefficient for m^{th} snapshot
$C_{\mathbf{w}}(\cdot)$	power pattern for window, \mathbf{w}
$F(\cdot)$	harmonic analysis detection statistic
$G(\omega, \theta, \phi), G(\theta, \phi), G(\mathbf{k})$	normalized directional distribution of plane waves
$H(\omega, \theta, \phi)$	directional response of sensor element
$P(\omega, \mathbf{k})$	frequency-wavenumber spectrum
$R(\tau, \Delta \mathbf{p})$	spatial-temporal covariance
$S(\omega, \Delta \mathbf{p})$	cross-spectral density

Table C.5: Table of Variables - Vectors and Matrices

Variable Notation	Description
\mathbf{k}	wavenumber vector
\mathbf{k}_s	wavenumber vector defining the steering vector, \mathbf{s}
$\mathbf{n}_{b,m}$	background noise component, m^{th} snapshot
$\mathbf{n}_{w,m}$	uncorrelated sensor noise component, m^{th} snapshot
\mathbf{p}_n	position of the n^{th} element of an array
$\Delta\mathbf{p}$	difference in position, Cartesian $[\Delta p_x, \Delta p_y, \Delta p_z]^T$ or spherical $[s, \gamma, \zeta]^T$
\mathbf{q}_o	MTSE eigen-coefficient response for plane wave \mathbf{v}_o
\mathbf{s}	adaptive beamformer steering vector
$\vec{\mathbf{u}}$	unit directional vector
\mathbf{u}_k	array manifold response error vector for k^{th} discrete source
\mathbf{v}	array manifold response vector
\mathbf{w}	window function, i.e. taper, used for spectral estimation
\mathbf{w}_{opt}	optimal weight vector
\mathbf{w}_a	an actual weight vector, derived from data or covariance estimate
\mathbf{x}_m	array output snapshot vector
\mathbf{y}_m	tapered/windowed snapshot
$\mathbf{P}_v, \mathbf{P}_v^\perp$	range space and null space projection matrices for subspace defined by \mathbf{v}
\mathbf{R}	covariance matrix
\mathbf{R}_a	covariance of plane wave component amplitudes
\mathbf{R}_b	covariance of background noise component
\mathbf{R}_w	covariance of the uncorrelated sensor noise component
\mathbf{R}_w	sample autocorrelation matrix, deterministic sequence, \mathbf{w}
\mathbf{R}_x	covariance of the array output snapshots
$\hat{\mathbf{R}}_{SCM}$	the sample covariance matrix
\mathbf{V}	matrix of array manifold response vectors

Bibliography

Bibliography

- [1] H. L. Van Trees, *Optimal Array Processing - Part IV of Detection, Estimation, and Modulation Theory*. New York: Wiley-Interscience, 2002.
- [2] N. R. Goodman, "Statistical analysis based on a certain multivariate complex Gaussian distribution," *Ann. Math. Stat.*, vol. 34, pp. 152–177, Mar. 1963.
- [3] A. B. Baggeroer and H. Cox, "Passive sonar limits upon nulling multiple moving ships with large aperture arrays," *Conf. Record of the 33rd Asilomar Conf. Signals, Syst. Comput.*, vol. 1, pp. 103–108, Oct. 1999.
- [4] D. C. Ricks, P. G. Cifuentes, and J. S. Goldstein, "What is optimal for nonstationary data?" *Conf. Record of the 34th Asilomar Conf. Signals, Syst. Comput.*, vol. 1, pp. 656–661, Oct. 2000.
- [5] M. D. Zoltowski, "On the performance analysis of the MVDR beamformer in the presence of correlated interference," *IEEE Trans. Acoustics, Speech, Signal Proc.*, vol. 36, no. 6, pp. 945–947, Jun. 1998.
- [6] J. Capon, "High resolution frequency wavenumber spectrum analysis," *Proc. IEEE*, vol. 57, no. 8, pp. 1408–1418, Aug. 1969.
- [7] H. Cox, "Resolving power and sensitivity to mismatch of optimum array processors," *J. Acoust. Soc. Amer.*, vol. 54, no. 3, pp. 771–785, Sep. 1973.
- [8] S. D. Morgera and D. B. Cooper, "Structured estimation: sample size reduction for adaptive pattern classification," *IEEE Trans. Info. Theory*, vol. IT-23, no. 6, pp. 853–863, Nov. 1977.
- [9] Y. Abramovich, "A controlled method for adaptive optimization of filters using the criterion of maximum SNR," *Radiotekh. Elektron. (Radio Engineering Electronic Physics)*, vol. 26, no. 3, pp. 87–95, 1981.
- [10] Y. Abramovich and A. Nevrev, "An analysis of effectiveness of adaptive maximization of the signal-to-noise ratio which utilizes the inversion of the estimated correlation matrix," *Radiotekh. Elektron. (Radio Engineering Electronic Physics)*, vol. 26, no. 12, pp. 67–74, 1981.
- [11] E. Hung and R. Turner, "A fast beamforming algorithm for large arrays," *IEEE Trans. Aerosp. Electron. Syst.*, vol. 19, no. 4, pp. 598–607, Jul. 1983.

- [12] T. A. Barton and S. T. Smith, "Structured covariance estimation for space-time adaptive processing," *IEEE Int. Conf. Acoustics, Speech, Signal Processing*, vol. 5, pp. 3493–3496, Apr. 1997.
- [13] T. A. Barton, "Covariance estimation for multidimensional data," Ph.D. dissertation, Dept. of Elec. Eng. Washington University, Dec. 1993.
- [14] D. R. Fuhrmann and M. I. Miller, "On the existence of positive-definite maximum-likelihood estimates of structured covariance matrices," *IEEE Trans. Info. Theory*, vol. 34, no. 4, pp. 722–729, Jul. 1988.
- [15] D. R. Fuhrmann, "Correction to 'On the existence of positive-definite maximum-likelihood estimates of structured covariance matrices'," *IEEE Trans. Info. Theory*, vol. 43, no. 3, pp. 1094–1096, May 1997.
- [16] D. R. Fuhrmann and T. A. Barton, "New results in the existence of complex covariance estimates," *Conf. Record of the 26th Asilomar Conf. Signals, Syst. Comput.*, vol. 1, pp. 187–191, Oct. 1992.
- [17] F. C. Robey, "A covariance modeling approach to adaptive beamforming and detection," Ph.D. dissertation, Dept. of Elec. Eng. Washington University, Dec. 1990.
- [18] I. P. Kirsteins and D. W. Tufts, "Adaptive detection using low rank approximations to a data matrix," *IEEE Trans. on Aerosp. Electron. Syst.*, vol. 30, no. 1, pp. 55–67, Jan. 1994.
- [19] J. S. Goldstein and I. S. Reed, "Reduced-rank adaptive filtering," *IEEE Trans. Signal Process.*, vol. 45, no. 2, pp. 492–496, Feb. 1997.
- [20] J. S. Goldstein, I. S. Reed, and L. L. Scharf, "A multistage representation of the Wiener filter based on orthogonal projections," *IEEE Trans. Info. Theory*, vol. 44, no. 7, pp. 2943–2959, Nov. 1998.
- [21] E. L. Santos and M. D. Zoltowski, "Adaptive beamforming with low sample support via indirect dominant mode rejection," *Proc. IEEE Sensor Array Multichannel Signal Processing Workshop (SAM 2004)*, vol. S1-7, pp. 18–21, Jul. 2004.
- [22] —, "IDMR beamforming under direction-independent steering vector mismatch," *ICASSP 2006 Proc.*, vol. 4, pp. 1017–1020, May 2006.
- [23] E. L. Santos, M. D. Zoltowski, and M. Rangaswamy, "Indirect dominant mode rejection: A solution to low sample support beamforming," *IEEE Trans. Signal Process.*, vol. 55, no. 7, pp. 3283–3293, Jul. 2007.
- [24] A. L. Kraay and A. B. Baggeroer, "A physically constrained maximum-likelihood method for snapshot-deficient adaptive array processing," *IEEE Trans. Signal Proc.*, vol. 55, no. 8, pp. 4048–4062, Aug. 2007.
- [25] P. W. Howells, "Explorations in fixed and adaptive resolution at GE and SURC," *IEEE Trans. Antennas Propag.*, vol. 24, no. 5, pp. 575–584, Sep. 1976.

- [26] S. P. Applebaum, "Adaptive arrays," *IEEE Trans. Antennas Propagat.*, vol. 24, no. 5, pp. 585–598, Sep. 1976.
- [27] B. Widrow, P. E. Mantey, L. J. Griffiths, and B. B. Goode, "Adaptive antenna systems," *Proc. IEEE*, vol. 55, no. 12, pp. 2143–2159, Dec. 1967.
- [28] O. L. Frost III, "An algorithm for linearly constrained adaptive array processing," *Proc. IEEE*, vol. 60, no. 8, pp. 926–935, Aug. 1972.
- [29] I. S. Reed, J. D. Mallett, and L. E. Brennan, "Rapid convergence in adaptive arrays," *IEEE Trans. Aerosp. Electron. Syst.*, vol. 10, no. 6, pp. 853–863, Nov. 1974.
- [30] R. A. Monzingo and T. W. Miller, *Introduction to Adaptive Arrays*. New York: Wiley, 1980.
- [31] J. L. Krolik and D. N. Swingler, "On the mean-square error performance of adaptive minimum variance beamformers based on the sample covariance matrix," *IEEE Trans. Signal Proc.*, vol. 42, no. 2, pp. 445–448, Feb. 1994.
- [32] B. Carlson, "Covariance matrix estimation errors and diagonal loading in adaptive arrays," *IEEE Trans. Aerosp. Electron. Syst.*, vol. 24, no. 4, pp. 397–401, Jul. 1988.
- [33] X. Mestre and M. A. Lagunas, "Finite sample size effect on minimum variance beamformers: optimal diagonal loading factor for large arrays," *IEEE Trans. Signal Process.*, vol. 54, no. 1, pp. 69–82, Jan. 2006.
- [34] Y. Kim, S. Pillai, and J. Guerci, "Optimal loading factor for minimal sample support space-time adaptive radar," *Proc. IEEE Int. Conf. Acoustics, Speech, Signal Processing*, vol. 1, pp. 2505–2508, Nov. 1998.
- [35] N. K. Jablon, "Adaptive beamforming with the generalized sidelobe canceller in the presence of array imperfections," *IEEE Trans. Antennas Propag.*, vol. 34, no. 8, pp. 996–1012, Aug. 1986.
- [36] L. Chang and C. Yeh, "Performance of DMI and eigenspace-based beamformers," *IEEE Trans. Antennas Propag.*, vol. 40, no. 11, pp. 1336–1347, Nov. 1992.
- [37] S. J. Yu and J. H. Lee, "The statistical performance of eigenspace-based adaptive array beamformers," *IEEE Trans. Antennas Propag.*, vol. 44, no. 5, pp. 665–671, May 1996.
- [38] P. A. Zulch, J. S. Goldstein, J. R. Guerci, and I. S. Reed, "Comparison of reduced-rank signal processing techniques," *Conf. Record of the 32nd Asilomar Conf. Signals, Syst. Comput.*, vol. 1, pp. 421–425, Nov. 1998.
- [39] B. Widrow, K. M. Duvall, R. P. Gooch, and W. C. Newman, "Signal cancellation phenomena in adaptive antennas: Causes and cures," *IEEE Trans. Antennas Propag.*, vol. 30, no. 3, pp. 469–478, May 1982.
- [40] T. J. Shan and T. Kailath, "Adaptive beamforming for coherent signals and interference," *IEEE Trans. Acoustics, Speech, Signal Process.*, vol. 33, no. 3, pp. 527–534, Jun. 1985.

- [41] S. U. Pillai and B. H. Kwon, "Forward / backward spatial smoothing techniques for coherent signal identification," *IEEE Trans. Acoustics, Speech, Signal Process.*, vol. 37, no. 1, pp. 8–15, Jan. 1989.
- [42] D. A. Linebarger and D. H. Johnson, "The effect of spatial averaging on spatial correlation matrices in the presence of coherent signals," *IEEE Trans. Acoust., Speech and Signal Proc.*, vol. 38, no. 5, pp. 880–884, May 1990.
- [43] V. U. Reddy, A. Paulraj, and T. Kailath, "Performance analysis of the optimum beamformer in the presence of correlated sources and its behavior under spatial smoothing," *IEEE Trans. Acoustics, Speech, Signal Process.*, vol. 35, no. 7, pp. 927–936, Jul. 1987.
- [44] K. J. Raghunath and V. U. Reddy, "Finite data performance analysis of MVDR beamformer with and without spatial smoothing," *IEEE Trans. Signal Proc.*, vol. 40, no. 11, pp. 2126–2136, Nov. 1992.
- [45] M. I. Miller and D. L. Snyder, "The role of likelihood and entropy in incomplete-data problems: Applications to estimating point-process intensities and Toeplitz constrained covariances," *Proc. IEEE*, vol. 75, no. 7, pp. 892–907, Jul. 1987.
- [46] A. Dembo, C. L. Mallows, and L. A. Shepp, "Embedding nonnegative definite Toeplitz matrices in nonnegative definite circulant matrices, with application to covariance estimation," *IEEE Trans. Info. Theory*, vol. 35, no. 6, pp. 1206–1212, Nov. 1989.
- [47] K. C. Indukumar and V. U. Reddy, "A note on redundancy averaging," *IEEE Trans. Signal Proc.*, vol. 40, no. 2, pp. 466–469, Feb. 1992.
- [48] D. A. Linebarger, "Redundancy averaging with large arrays," *IEEE Trans. Signal Proc.*, vol. 41, no. 4, pp. 1707–1710, Apr. 1993.
- [49] J. C. Papp, J. C. Preisig, and A. K. Morozov, "Physically constrained maximum likelihood mode filtering," *J. Acoust. Soc. Am.*, vol. 127, no. 4, pp. 2385–2391, Apr. 2010.
- [50] A. B. Baggeroer, "Space-time processes and optimal array processing," Navy Undersea Center, San Diego, California, Technical Report 506, Dec. 1976.
- [51] J. P. Burg, D. G. Luenberger, and D. L. Wenger, "Estimation of structured covariance matrices," *Proc. IEEE*, vol. 70, no. 9, pp. 963–974, Sep. 1982.
- [52] D. J. Thomson, "Spectrum estimation and harmonic analysis," *Proc. IEEE*, vol. 70, no. 9, pp. 1055–1096, Sep. 1982.
- [53] J. R. Guerci, "Theory and application of covariance matrix tapers for robust adaptive beamforming," *IEEE Trans. Signal Proc.*, vol. 47, no. 4, pp. 977–985, Apr. 1999.
- [54] H. Cox, "Spatial correlation in arbitrary noise fields with application to ambient sea noise," *J. Acoust. Soc. Amer.*, vol. 54, no. 5, pp. 1289–1301, Nov. 1973.
- [55] H. Cramér, "On harmonic analysis in certain functional spaces," *Arkiv för Matematik, Astronomi och Fysik*, vol. 28B, pp. 1–7, 1942.

- [56] D. B. Percival and A. T. Walden, *Spectral Analysis for Physical Applications*. New York: Cambridge University Press, 1993.
- [57] M. B. Priestly, *Spectral Analysis and Time Series*. New York: Academic Press, 1981.
- [58] A. M. Yaglom, *An Introduction to the Theory of Stationary Random Functions*. New Jersey: Prentice-Hall, 1962.
- [59] A. V. Oppenheim, R. W. Schaffer, and J. R. Buck, *Discrete-Time Signal Processing*, 2nd ed. New Jersey: Prentice Hall, 1998.
- [60] T. K. Moon and W. C. Sterling, *Mathematical Methods and Algorithms for Signal Processing*. New Jersey: Prentice Hall, 2000.
- [61] R. O. Schmidt, "Multiple emitter location and signal parameter estimation," *IEEE Trans. Antennas Propagat.*, vol. 34, no. 3, pp. 276–280, Mar. 1986.
- [62] S. M. Kay and S. L. Marple, Jr., "Spectrum analysis - a modern perspective," *Proc. of the IEEE*, vol. 69, no. 11, pp. 1380–1419, Nov. 1981.
- [63] F. J. Harris, "On the use of windows for harmonic analysis with the discrete Fourier transform," *Proc. IEEE*, vol. 66, no. 1, pp. 51–83, Jan. 1978.
- [64] S. Haykin, Ed., *Advances in Spectrum Analysis and Array Processing*. New Jersey: Prentice Hall, 1995.
- [65] B. D. V. Veen and L. L. Scharf, "Estimation of structured covariance matrices and multiple window spectrum analysis," *IEEE Trans. Acoustics, Speech, Signal Proc.*, vol. 38, no. 8, pp. 1467–1472, Aug. 1990.
- [66] T. P. Bronez, "Spectral estimation of irregularly sampled multidimensional processes by generalized prolate spheroidal sequences," *IEEE Trans. Acoustics, Speech, Signal Proc.*, vol. 36, no. 12, pp. 1862–1873, Dec. 1998.
- [67] D. Slepian, "Prolate spheroidal wave functions, Fourier analysis, and uncertainty - v: The discrete case," *Bell Sys. Tech. Jour.*, vol. 57, pp. 1371–1431, May-June 1978.
- [68] T. P. Bronez, "On the performance advantage of multitaper spectral analysis," *IEEE Trans. Signal Proc.*, vol. 40, no. 12, pp. 2941–2946, Dec. 1992.
- [69] L. L. Scharf, *Statistical Signal Processing Detection, Estimation, and Time Series Analysis*. New York: Addison-Wesley Publishing Company, 1991.
- [70] Y. Jin and B. Friedlander, "A CFAR adaptive subspace detector for second-order Gaussian signals," *IEEE Trans. on Signal Process.*, vol. 53, no. 3, pp. 871–884, Mar. 2005.
- [71] R. A. Horn and C. R. Johnson, *Topics in Matrix Analysis*. New York: Cambridge Univ. Press, 1991.
- [72] L. N. Trefethen and D. Bau, III, *Numerical Linear Algebra*. Philadelphia: SIAM, 1997.

- [73] K. E. Wage, "Multitaper array processing," *Conf. Record of the 41st Asilomar Conf. Signals, Syst. Comput.*, vol. 1, pp. 1242–1246, Nov. 2007.
- [74] S. Haykin, Ed., *Adaptive Radar Signal Processing*. New York: John Wiley & Sons, Inc., 2007.
- [75] R. E. Crochiere and L. R. Rabiner, *Multirate Digital Signal Processing*. New Jersey: Prentice-Hall, 1983.
- [76] D. C. Rife, "Single-tone parameter estimation from discrete-time observations," *IEEE Trans. Info. Theory*, vol. IT-20, no. 5, pp. 591–598, Sep. 1974.
- [77] R. J. Urick, *Principles of Underwater Sound for Engineers*. New York: McGraw-Hill, 1967.
- [78] J. J. Schwarzwalder and K. E. Wage, "ABF performance using covariance matrices derived from spatial spectra for large arrays," *Conf. Record of the 43rd Asilomar Conf. Signals, Syst. Comput.*, pp. 1164–1168, Nov. 2009.
- [79] C. J. Tsai, J. F. Yang, and T. H. Shiu, "Performance analysis of beamformers using effective SINR on array parameters," *IEEE Trans. Acoustics, Speech, Signal Process.*, vol. 43, no. 1, pp. 300–303, Jan. 1995.
- [80] L. C. Godara, "Beamforming in the presence of correlated arrivals using structured correlation matrix," *IEEE Trans. Acoustics, Speech, Signal Process.*, vol. 38, no. 1, pp. 1–15, Jan. 1990.
- [81] M. Zatman, "Comments on 'Theory and application of covariance matrix tapers for robust adaptive beamforming'," *IEEE Trans. Signal Proc.*, vol. 48, no. 6, pp. 1796–1800, Jun. 2000.
- [82] F. C. Robey, D. R. Fuhrmann, and M. A. Koerber, "Array calibration and modeling of steering vectors," *Conf. Record of the 35th Asilomar Conf. Signals, Syst. Comput.*, vol. 2, pp. 1121–1126, Nov. 2001.
- [83] P. Gerstoft, W. S. Hodgkiss, W. A. Kuperman, H. Song, M. Siderius, and P. L. Nielsen, "Adaptive beamforming of a towed array during a turn," *IEEE Journal of Ocean Eng.*, vol. 28, no. 1, pp. 44–54, Jan. 2003.
- [84] B. G. Ferguson, "Remedying the effects of array shape distortion on the spatial filtering of acoustic data from a line array of hydrophones," *IEEE Journal of Ocean Eng.*, vol. 18, no. 4, pp. 565–571, Oct. 1993.
- [85] D. E. Wahl, "Towed array shape estimation using frequency-wavenumber data," *IEEE Journal of Ocean Eng.*, vol. 18, no. 4, pp. 582–590, Oct. 1993.
- [86] M. A. Zatman, "ABF limitations when using either Toeplitz covariance estimators or the parametric vector AR technique," *Conf. Record of the 35th Asilomar Conf. Signals, Syst. Comput.*, pp. 1111–1115, Nov. 2001.
- [87] H. H. Anderson, M. Hojbjerre, D. Sorensen, and P. S. Eriksen, *Linear and Graphical Models for the Multivariate Complex Normal Distribution*. New York: Springer-Verlag, 1995.

Curriculum Vitae

Joseph James Schwarzwaldler was born on November 23, 1973 in Camden, NJ. He attended The Catholic University of America in Washington, D.C., where he and his future spouse first met in physics class. He graduated Summa Cum Laude with a Bachelors of Electrical Engineering degree in 1996, receiving the Benjamin T. Rome award for leadership and academic excellence. Continuing education while working, he received a Masters of Science in Electrical Engineering from The Johns Hopkins University in 2001. His professional career has focused on signal processing and communications, both commercial and defense related, which he continues to practice at Argon ST, now part of the Boeing Company, where he has been for some time.